The lukewarm frontier:
Some cosmological consequences of 'low-energy' physics

Thesis by

Daniel Grin

In Partial Fulfillment of the Requirements

for the Degree of

Doctor of Philosophy

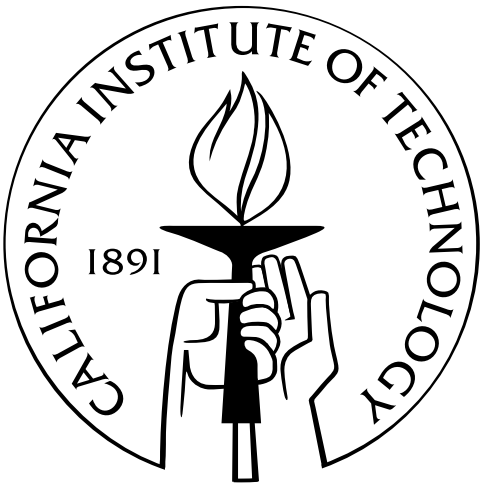

California Institute of Technology

Pasadena, California

2010

(Defended May 28, 2010)

"The effort to understand the universe is one of the very few things that lifts human life a little above the level of farce, and gives it some of the grace of tragedy."

– *Steven Weinberg, 1993 [1]*

"Our knowledge can only be finite, while our ignorance must necessarily be infinite."

– *Karl Popper, 1963 [2]*

Acknowledgments

My journey to and through graduate school was made possible and immeasurably more pleasant by early nourishment, thoughtful mentorship, and the company of fellow travelers.

I begin by thanking my advisor, Prof. Marc Kamionkowski. Marc is rare in his deep curiosity and broad-ranging interests as a cosmologist. I aspire to his scientific taste, to his example of how to choose and solve problems. He has been a thoughtful advisor, pointing me to research problems that are pedagogically and scientifically valuable, guiding me to cogent solutions, and reading my manuscripts to help shape them into clear explanations of our work. He has been generous with his time and his resources, allowing me to travel to fascinating conferences and summer schools. In this difficult year for our department, he has exemplified availability and provided solace.

In the last two years, I have had the pleasure of collaborating with Prof. Chris Hirata, who has generously shared his time, patience, and insight with me. Chris has acquainted me with the beauty and cosmological utility of atomic physics and radiative transfer. Chris's attention to detail and ability to connect seemingly disparate areas of physics have inspired and guided me.

I thank my dedicated collaborators in the research presented in this thesis: Yacine Ali-Haïmoud, Andrew Blain, Robert Caldwell, Giovanni Covone, Chris Hirata, Eric Jullo, Marc Kamionkowski, Jean-Paul Kneib, and Tristan Smith.

I thank Andrew Benson for introducing me to the rich physics behind dark matter halo and galaxy formation, and for being a constructive sounding board for ideas and numerical experiments.

My father Leonid, mother Marina, and sister Rada never ceased believing in me, and I am deeply grateful for their unwavering support, good humor, and reliable willingness to help. My earliest memories involving science are of discovering science fiction, model rockets, and the night sky with Marc Hoag, now my friend of 26 years. Marc lent me a copy of Kip Thorne's book *Black Holes and Time Warps* [3], planting my fascination with astrophysics. Thank you Kip for writing such an inviting book. Kip's lectures on general relativity and classical physics at Caltech were a paragon of simplicity and clarity. It was a treat to TA for him. The teachers at Germantown Friends School taught me the value of systematic thinking and hard work. My ninth grade biology teacher in Los Gatos, John McDonald, taught me to embrace failure and strive for humility. My high-school

calculus teacher Jeanne-Marie Rachlin was exceptionally clear and supportive, helping me to begin university math/physics courses with a running start. I've been lucky to call David Hembry a friend for seventeen years. I continue to profit from thoughtful discourse with him about science, politics, literature, and he has been a caring and supportive friend throughout. His diverse interests and wide ken continue to inspire me. Aaron Silberstein has helped me to stay light-hearted and to appreciate the fortune of my circumstances.

My professors and fellow physics students at Princeton helped lay the foundation for the fun I had in graduate school. Zigmund Kermish taught us about the power of physical intuition (Ziggy is always right) and was generous with his friendship. Tom Jackson relieved us with his understated and brilliant humor. Erik Encarnacion (meta-physicist) never let us forget that a world of strife and moral complexity exists outside the realm of *gedankenexperimenten* and laboratories.

Adrienne Erickcek and I did not finish squabbling over couch space at problem sessions during our undergraduate years, so we followed one another to Great Britain and then Caltech. She has been an attentive, caring, and insightful friend for eleven years, has cheered me at my best, buttressed me at my worst, and taught me to advocate for myself. I aspire to her diligence and insight as a cosmologist. No one could ask for more from a friend or colleague.

Others at Caltech have contributed significantly to my well-being and academic progress. Tristan Smith (the Park Ranger) has been a steadfast friend and a terrific travel partner in the Southwest. He has been the first person I go to when I want to discuss a scientific idea or question. He has always been willing to exchange new ideas and book suggestions, scientific and humanistic. I have wonderful officemates. Nate Bode has shared wisdom, life experience, and stories of his gallant voyages. Conversations with Nate are wonderful, be they about physics, music, or anything else, because Nate doesn't stop asking questions 'till he gets at the heart of the matter. Nate has also made sure that I remember to occasionally look out the window. Yacine Ali-Haïmoud has taught me to never give up in the quest for an analytic solution, and I've enjoyed discussing the gory details of recombination with him. He has been a good friend and brought levity to the office. Anthony Pullen has been a model of diligence and efficiency, a fun study partner in first-year courses, and a good-humored friend.

Anthony 'Badgie' Miller was a terrific roommate, tolerant of my forgetfulness, and indulgent of my eccentricities. We enjoyed blasting classical music on his speakers and learned to love Los Angeles together. Vaclav Cvicek followed in his stead, and he has kept me on my toes with late night discussions in which I have to justify all of cosmology in five sentences or less. He's also put up with

my catastrophes in the kitchen, tumbling heavy objects, and has been a steadfast friend. Above all, he has introduced me to Jara Cimrman's externism.

I am thankful for the open-mindedness, and humility of Daniel Babich. Dan regularly took time to share his problem-solving acumen and company with the graduate students in 158 Bridge.

I have enjoyed the wit and company of Hernan Garcia, Anusha Narayan, Jenny Roizen, usually over lunch. I thank them for their patience with the etymological squabbles between Nate Bode and me.

I am thankful for the friendship of all my fellow astronomy graduate students at Caltech. Special thanks go to my incoming class: Ann Marie-Cody, Thiago Gonçalves, and Hilke Schlichting. It was always a pleasure to encounter Milan Bogosavljević in the hallway. He reminded me to laugh at myself with regularity. Karín Menéndez-Delmestre has always taken the time to check in and say a kind word.

Insofar as I am still sane, it is thanks to the distraction of music. Delores Bing runs a great chamber music program at Caltech with grace and patience. It has been a privilege to perform music of Beethoven, Brahms, Dvorak, Martinu, Messiaen, and Schubert in Dabney Lounge. I shared this musical fun with my friends Jenelle Bray, Kevin Engel, Adrienne Erickcek, Nicholas Fette, George Hines, Chris Kovalchick, Calvin Kuo, Yousi Ma, Anthony Miller, Hui Khoon Ng, Angela Shih, Jing Shen, Lisa Tracy, Christina Vizcarra, Lillian Wang, Jackson Wang, Tina Wang, and June Wicks. Delores has coached our chamber groups to successful performances many times over. The staff at KUSC FM (above all Jim Svejda) have broadened my musical horizons and gotten me through many a work-harried evening (and sunrise) with their thoughtful choices and commentary.

I am grateful to many others for their friendship during my time at Caltech: Lotty Ackerman, Esfandiar Alizadeh, Mustafa Amin, Michael Armen, Doron Bergman, Laura Book, Mike Boyle, Justus Brevik, Geoff Chang, Michael Cohen, Ben Collins, Nicole Czakon, Chaim Danzinger, Natalie Deffenbaugh, Tudor Dimofte, Olivier Doré, Vera Glusćevic, Leo Goldmakher, Daniel Haas, Lynn Kamerlin, David Kantor, Jeff Kaplan, Matthew Kelley, Mike Kesden, David Kopp, Neil Halelamien, Chaim Hanoka, Peggy Hsu, Elisabeth Krause, Zuli Kurji, Andy Lamperski, Nicholas Law, Sam Lee, Michael Mendenhall, Diana Negoescu, David Nichols, Evan O'Connor, Rory Perkins, Annika Peter, Harald Pfeiffer, Prof. Sterl Phinney, Paige Randall, Jonathan Pritchard, Christine Romano, John Saunders, Prof. Re'em Sari, Iggy Sawicki, Mark Scheel, Kevin Setter, Kai Shen, Kris Sigurdson, Brian Standley, Jenn Stockdill, Eve Stenson, Sherry Suyu, Aileen Tang, Kana Takematsu, Amanda

Tavel, Ryan Trainor, Amy Trangsrud, Sarah Tulin, Sean Tulin, Tristan Ursell, Ramon van Handel, and Todd Zoltan.

My research would grind to a halt were it not for the able and cheerful work of Caltech administrative staff, including Gina Armas, JoAnn Boyd, Helen Ticehurst, and Gita Patel. I owe special thanks to Shirley Hampton, who made sure that recommendation letters arrived on time, and kept the cosmology sub-group of TAPIR smoothly running. Chris Mach keeps the TAPIR computers up and running, and saved me from near oblivion after an "rm -r *" crisis. I am grateful to the staff of the Caltech Health Center, especially Maggie Ateia, Divina Bautista, Helena Kopecky, Alice Sogomanian, and Paulette Theresa.

My deepest thanks go to my fiancée Sarah Tarlow. Her love, patience, and support have been unwavering, unconditional, and indispensable. I will strive to fill our new home with warmth to compensate for the dreary New Jersey weather.

Abstract

In this thesis, we present four projects featuring low characteristic energy scales relative to the scales relevant for supersymmetric dark matter production or inflation. We present a telescope search for decaying relic axions in the $3-8$ eV mass range. We utilize larger telescope exposure and superior cluster mass modeling to improve sensitivity. Our results impose new stringent limits to the two-photon coupling or relic density of axions. We extend these results to non-standard sterile neutrinos.

We then reconsider cosmological constraints to axions. Our understanding of physics before big-bang nucleosynthesis is tenuous, and after arguing that a non-standard thermal history before nucleosynthesis is plausible and perhaps even natural, we calculate the abundance and typical momenta of thermal axions in such scenarios. We generalize existing cosmological constraints to axions, showing that the allowed axion mass range expands significantly in non-standard thermal histories. We then estimate the sensitivity of future experiments to axion masses and reheating temperatures.

We then study the $\sim$ eV-scale physics of cosmological hydrogen recombination, computing the recombination history while resolving all $\sim 10^4$ states of hydrogen up to a maximum $n \sim 250$ and studying the associated convergence problem. We show that the recombination history is sufficiently converged for analysis of microwave anisotropy data from the *Planck* satellite if the maximum $n \sim 128$, and that previously ignored electric quadrupole transitions are indeed negligible to the precision necessary for *Planck*.

We conclude by presenting a new astrophysical limit to effective field theories of gravity in which the graviton propagator is damped at energies greater than a milli-eV.

Contents

List of Figures

List of Tables

Chapter 1
Introduction and Summary

Modern cosmology offers an embarrassment of riches. Thanks to projects like BOOMERANG [12], COBE [13], WMAP [14–17], the 2dF/SDSS surveys [18–21], the High-Z supernova search, and the Supernova Cosmology Project [22–25], cosmology has become a precise science. Our understanding of the universe's contents and history is impressive. We know that the universe is flat, that its matter content is dominated by non-baryonic dark matter, and that its baryonic content suffices to explain light-element abundances. We know that the cosmological energy budget was dominated by radiation for temperatures $T \leq 4$ MeV [26], that the cosmological expansion is accelerating 'today,' and that the initial density perturbations were nearly scale-invariant, Gaussian, and adiabatic. These are the riches of modern cosmology.

They are also its embarrassments. We do not know which (if any) of the particles in the myriad of proposed extensions to the standard model (SM) of particle physics constitutes the dark matter, although axions, weakly interacting massive particles (WIMPs) and sterile neutrinos are a few plausible candidates. We have no firm anchor on the cosmological expansion history prior to big-bang nucleosynthesis (BBN), though the observed spectrum of density fluctuations is consistent with an early inflationary epoch. If the universe inflates, we must still identify the responsible field(s) (the inflatons). There is no satisfying fundamental explanation of the apparent milli-eV energy scale of the current cosmological acceleration.

Fortunately, ongoing and future planned experiments/surveys promise to break this impasse. The ADMX/CAST [27, 28] experiments continue to search for dark matter/solar axions. Telescope axion searches are chipping away at the thermal axion window. Experimental searches based on axion-nucleon couplings and cosmological large-scale structure surveys should probe a wide range of axion masses more definitively. In the case of WIMP dark matter, the trifecta of the Large Hadron Collider (LHC) [29, 30], the Fermi γ-ray space telescope [31], and direct detection experiments like CDMS/ZEPLIN/XENON [32–34] offer the possibility of detecting super-symmetric partners in the lab and then confirming their identity as the dark matter. The recently launched *Planck* satellite will begin to meaningfully test inflationary models through extremely precise measurements of cosmic microwave background (CMB) anisotropies [35].

Much of the mystery and future promise in cosmology has to do with physics at several famous high energy scales:

1. The Planck scale: $m_{\rm pl} \sim 10^{19}$ GeV. This is the putative scale at which string theory (or

any theory of quantum gravity) becomes relevant. The inflaton and cosmologically dominant moduli fields may emerge from string theory.

2. The GUT (grand unified theory) scale: $E_{\rm GUT} \sim 10^{16}$ GeV. This scale may be relevant for inflationary physics and baryogenesis.

3. The Peccei-Quinn scale [36]: 10^7 GeV $\lesssim f_{\rm a} \lesssim 10^{12}$ GeV. If the dark matter is an axion or a saxion, this scale will be relevant for dark matter physics.

4. The electroweak scale: $E \sim 250$ GeV. If the dark matter is a neutralino or a gravitino, this scale will be relevant for understanding the dark matter. This scale may also be important in models of the origin of the cosmic baryon asymmetry.

Experimental and observational leverage on this physics, however, passes to us through a lower energy filter. To understand the axion, inflation, and the CMB, we must deal with the ~ 5 eV energies accessible to optical telescopes, the $\sim 10 - 100$ MeV temperatures preceding BBN (when thermal axions fall out of chemical equilibrium), the $\sim$ eV temperature at matter-radiation equality (when density perturbations begin to grow), and the ~ 0.25 eV temperatures at photon-baryon decoupling. If care is not taken in modeling the recombination of the primordial plasma (the formation of the first hydrogen atoms), inferences about the early universe made using data from *Planck* or other next-generation CMB experiments (e,g., CMBPol [37]) should not be trusted: the experimental error bars will be comparable to or smaller than corrections that result from using a more precise atomic physics model of recombination [38–41]. In the case of the cosmic acceleration, new physics seems to kick in at the milli-eV energy scale.

In this thesis, we present several research projects in which these lower energy scales feature prominently. Results from a new telescope search for decaying thermal axions are presented in Chapter 2, along with extensions to non-standard sterile neutrinos and an implication for the early thermal history of the universe. In Chapter 3, we determine the effect of late-time entropy generation in the range 10 MeV $< T <$ 100 MeV and kination models on thermal axion production and cosmological axion constraints. Chapter 4 features new computations of cosmological hydrogen recombination including $\sim 10^4$ states of the Rydberg atom and a tower of electric quadrupole transitions in atomic hydrogen. We compute and discuss the effects of this physics on CMB anisotropies and parameter estimation, compare our results with other recent work, and describe a series of ongoing and future extensions of this work. In Chapter 5, we present an astrophysical limit to 'fading' effective field theories of gravity.

The bulk of our work in each chapter has been published in refereed journals and is reproduced here with permission: Chapter 2 in Ref. [42], Chapter 3 in Ref. [43], Chapter 4 in Ref. [44], and Chapter 5 in Ref. [45]. Additional pedagogical or introductory material has been added, as have several new results. New material is pointed out at the beginning of each chapter.

Chapter 2
A Telescope Search for Decaying Relic Axions[1]

2.1 Introduction

Axions are an obvious dark-matter candidate in some of the most conservative extensions of the standard model of particle physics. The magnitude of the charge-parity (CP) violating term in quantum chromodynamics (QCD) is tightly constrained by experimental limits to the electric dipole moment of the neutron, presenting the strong CP problem [46–49]. Fine tuning can be avoided through the Peccei-Quinn (PQ) mechanism, in which a new symmetry (the Peccei-Quinn symmetry) is introduced, along with a new pseudoscalar particle, the axion. These ingredients dynamically drive the CP violating term to zero [4, 36, 50]. Via mixing with pions, axions pick up a mass, which is set by the PQ scale [4].

Below a mass of 10^{-2} eV, axions will be produced through coherent oscillations of the PQ pseudoscalar, yielding a population of cold relics that dominate the dark-matter density [50–52]. Above this mass, axions will be in thermal equilibrium at early times [50, 51]. Unless $m_{\rm a} \gtrsim 15$ eV, the resulting relic density is insufficient to account for all the dark matter, but high enough that axions will be a nontrivial fraction of the dark matter and likely constitute a larger fraction of the mass density of the universe than either baryons or neutrinos [50]! In either case, axions might be detectable through their couplings to standard-model particles.

The couplings of the axion are set by the PQ scale and the specific axion model [4, 50, 53]. In the Dine-Fischler-Srednicki-Zhitnitski (DFSZ) axion model, standard-model fermions (quarks *and* leptons) carry PQ charge, and so axions couple to photon pairs both via electrically charged standard-model leptons and via mixing with pions [54, 55]. In hadronic axion models, such as the Kim-Shifman-Vainshtein-Zakharov (KSVZ) axion model [56, 57], axions do not couple to standard-model leptons at tree level. Indeed, in the KSVZ model itself, axions do not even couple to standard model quarks. In KSVZ models, axions couple to gluons through triangle diagrams involving exotic fermions, to pions via gluons, and to photons via mixing with pions.

Constraints to the two-hadron couplings of axions come from stellar evolution arguments, from the duration of the neutrino burst from SN1987a, and from the upper limit to their cosmological

[1]The material in this chapter was adapted from *Telescope search for decaying relic axions*, Daniel Grin and others; Phys. Rev. D **75**, 105018 (2006). Reproduced here with permission, copyright (2006) by the American Physical Society. Additional material has been added in Sec. 2.2 and 2.3.

density [4, 50, 58–62]. Upper limits to the two-photon coupling of the axion come from searches for solar axions [63], from upper limits to the intensity of the diffuse extragalactic background radiation (DEBRA) [51, 64], from stellar evolution arguments [4], from direct searches for cosmic axions [27] and from upper limits to x-ray and optical emission by galaxies and clusters of galaxies [10, 11, 51]. Recent searches for vacuum birefringence report evidence for the existence of a light boson [65–71], though in a region of parameter space already constrained by null solar axion searches [63, 72, 73].

The two-photon coupling of the axion will lead to monochromatic line emission from axion decays to photon pairs. Although the lifetime of the axion is much longer than a Hubble time, the dark-matter density in a galaxy cluster is sufficiently high that optical line emission due to the decay of cluster axions could be detected. This line emission should trace the density profile of the galaxy cluster. Telescope searches for this emission were first suggested in Ref. [74]. In Ref. [51], this suggestion was extended to thermally produced axions. A telescope search for this emission was first attempted in Refs. [10, 11], in which a null search imposed upper limits to the two-photon coupling of the axion in the mass window 3 eV $\leq m_{\rm a} \leq$ 8 eV. Less stringent constraints have been obtained in searches for decaying galactic axions [10, 75].

In the past few years, high-precision cosmic microwave background (CMB) and large-scale-structure (LSS) measurements have become available and allowed new constraints to axion parameters in this mass range. In particular, axions in the few-eV mass range behave like hot dark matter and suppress small-scale structure in a manner much like neutrinos of comparable masses. Reference [6] shows that such arguments lead to an axion-mass bound $m_{\rm a} \leq 1.05$ eV. Still, given uncertainties and model dependences, it is important in cosmology to have several techniques as verification. For example, in extended, low-temperature ($\sim$ MeV) reheating models [76–78], light relics like axions and neutrinos have suppressed abundances, evading CMB/LSS bounds, but may still show up in telescope searches for axion decay lines [43]. Finally, other dark-matter candidates may show up in such searches; the sterile neutrino [79–82] is one example, which we will discuss below. We are thus motivated to re-visit the searches of Refs. [10, 11] and see whether new telescopes, techniques, and observations may yield improvements.

Refs. [10, 11] preceded the advent of observations of gravitational lensing by galaxy clusters, however, and so the cluster mass density profiles assumed were not measured directly, but derived using x-ray data and assumptions about the dynamical state of the clusters. The constraints reported in Refs. [10, 11] depend on these assumptions. Today, gravitational-lensing data can be used to determine cluster density profiles, independent of dynamical assumptions [83]. Thus, by using lensing mass maps and by applying the larger collecting areas of modern telescopes, cluster constraints to axions can both be tightened, and made robust. The high spatial resolution of integral field spectroscopy allows the use of lensing mass maps to extract the component of intracluster emission that traces the cluster mass profile. Cluster mass models can be used to derive an optimal spatial

weighting of the data, thus focusing on parts of the cluster where the highest signal is expected.

To this end, we have conducted a search for optical line emission from the two-photon decays of thermally produced axions.[2] We used spectra of the galaxy clusters Abell 2667 (A2667) and Abell 2390 (A2390) obtained with the Visible Multi-Object Spectrograph (VIMOS) Integral Field Unit (IFU), which has the largest field of view of any instrument in its class [84]. VIMOS is a spectrograph mounted at the third unit (Mélipal) of the Very Large Telescope (VLT), part of the European Southern Observatory (ESO) in Chile [85]. In our analysis, we use mass models of the clusters derived from strong-lensing data, obtained with the Hubble Space Telescope (HST), using the Wide Field Planetary Camera #2 (WFPC-2).

We obtain new upper limits to the two-photon coupling of the axion in the mass window 4.5 eV $\leq m_{\rm a} \leq$ 7.7 eV (set by the usable wavelength range of the VIMOS IFU) of $\xi \leq 0.003 - 0.017$. The two-photon coupling of the axion, ξ, is defined in Eq. (2.13) and discussed in Section 2.2. Although we search a smaller axion mass range than Refs. [10, 11], our upper limits improve on past work by a factor of $2.1 - 7.1$, depending on the candidate axion mass and how the limits of Ref. [10, 11] are rescaled to correct for today's best-fit cosmological parameters and more accurate cluster mass profiles. Our data rule out standard hadronic and DFSZ models in the 4.5 eV $-$ 7.7 eV window. However, *theoretical* uncertainties in quark masses and pion couplings may allow for a much wider range of values of ξ than standard hadronic and DFSZ models allow, as emphasized by Ref. [86], thus motivating the search for axions with smaller values of ξ.

A quick estimate shows that our level of improvement is not unexpected: the collecting area of the VLT is a factor of $(8.1/2.1)^2$ greater than the 2.1m telescope at Kitt Peak National Observatory (KPNO) used in Ref. [11]. Our integration time is a factor of 10.8 ksec/3.6 ksec greater. The IFU allows us to cover 3.4 times as much of the field of view as the spectrographs used at KPNO. Thus we estimate that our collecting area should be a factor of ~ 160 higher than that of Ref. [11]. If there is no signal, and if we are noise limited, we would expect a constraint to flux that is a factor of $\simeq 13$ more stringent than that of Ref. [11], and, since $I_\lambda \propto \xi^2$, upper limits to ξ that are $\simeq 3.5$ times more stringent than those reported in Ref. [11].

We begin by reviewing the relevant theory and proceed to describe our observations. We then summarize our data analysis technique. The new limits to axion parameter space are then discussed along with other constraints. We conclude by pointing out the potential of conducting such work with higher redshift clusters. For consistency with the assumptions used to derive the strong-lensing maps used in our analysis, we assume a ΛCDM cosmology parameterized by $h = 0.71$, $\Omega_{\rm m} = 0.30$, and $\Omega_\Lambda = 0.70$, except where explicitly noted otherwise.

[2]Based on observations made with ESO Telescopes at the Paranal Observatories (program ID 71.A-3010), and on observations made with the NASA/ESA Hubble Space Telescope, obtained from the data archive at the Space Telescope Institute. STScI is operated by the association of Universities for Research in Astronomy, Inc. under the NASA contract NAS5-26555.

2.2 Theory

Axions were postulated in 1977 to solve the 'strong-CP' problem [36, 87, 88]. The weak sector has long been know to violate CP (charge-parity) symmetry, specifically through the decays of neutral kaons and B-mesons. No CP-violation has been detected in the strong sector, although no symmetry (gauge or global) prevents one from adding a term of the form [46, 89]

$$\mathcal{L}_\theta = -\frac{g_s^2}{64\pi^2}\theta\epsilon_{\mu\nu\rho\kappa}G^{\mathrm{p}\mu\nu}G_{\mathrm{p}}^{\rho\kappa} = -\frac{g_s^2}{32\pi^3}\theta G^{\mathrm{p}}\tilde{G}_{\mathrm{p}} \tag{2.1}$$

to the standard model (SM) Lagrangian, where g_s is the strong coupling constant and θ is a dimensionless constant. Here $\epsilon_{\mu\nu\rho\kappa}$ is the usual Levi-Civita tensor and $\tilde{G}^{\mathrm{p}\mu\nu} = \epsilon_{\mu\nu\rho\kappa}G^{\mathrm{p}\rho\kappa}$ is the dual of the gluon field-strength tensor. Roman indices (e.g. p) denote QCD color indices, and a pair of up-down repeated indices denotes a sum, as per the usual Einstein convention. Although such surface terms are irrelevant to the dynamics of Abelian gauge theories, they turn out to correspond to an unconserved current (the axial vector current, to be precise) in theories with a local non-Abelian gauge symmetry, once the theory is regularized [46, 90].

This 'because-we-can' addition to the Lagrangian may seem logically wanting, but it turns out that tunneling between the many degenerate vacua of QCD (which must be formally included when evaluating matrix elements) naturally leads to an effective Lagrangian term of the form in Eq. 2.1, where the physical QCD vacuum is $|\theta\rangle = \sum_{n=-\infty}^{\infty} e^{-in\theta}|n\rangle$ and $0 \leq \theta \leq 2\pi$ [4, 46]. It is a straightforward exercise to see that terms proportional to $F\tilde{F}$ or $G\tilde{G}$ are CP-violating (recall that $\tilde{F}_{\mu\nu} = \epsilon_{\mu\nu\rho\kappa}F^{\rho\kappa}$, where $F_{\rho\kappa}$ is the usual Maxwell field tensor from electromagnetism). It turns out that one physical consequence of a θ-term in QCD is the prediction of a nonzero electric-dipole moment for the neutron, given by $d_{\mathrm{n}} \sim 10^{-15}$ e cm, where e is the charge of of an electron [4, 47, 48]. If we imagine a toy model of a neutron, as two classical oppositely charged current loops, we see that under a CP transformation (switch the charges and reverse the directions of each current), the electric field points in the opposite direction while the magnetic field is unchanged. In other words, a neutron electric dipole moment violates CP, as does any term of the form $\vec{E}\cdot\vec{B}$, as we can see in Fig. 2.1. Experimental limits impose the constraint $d_n \leq 6\times10^{-26}$ e cm, and so $\theta < 10^{-10}$, even though one might naively expect this phase to be of order unity.

Moreover, when the weak-sector quark mass matrix M is diagonalized and made real through $SU(2)$ rotations and phase transformations (to identify physical mass eigenstates), an additional term of the form in Eq. 2.1 results, and so the physical variable relevant to d_n is in fact $\overline{\theta} = \theta - \arg\det M$ [4]. Since θ and M correspond to physics in the distinct strong and weak sectors, respectively, the near-vanishing of $\overline{\theta}$ would require considerable fine tuning. In the spirit of solutions to other fine tuning problems, Peccei and Quinn proposed making $\overline{\theta}$ into a dynamical field ζ, with a degenerate vacuum corresponding to a new global [Peccei-Quinn (PQ)] $U(1)$ symmetry [36].

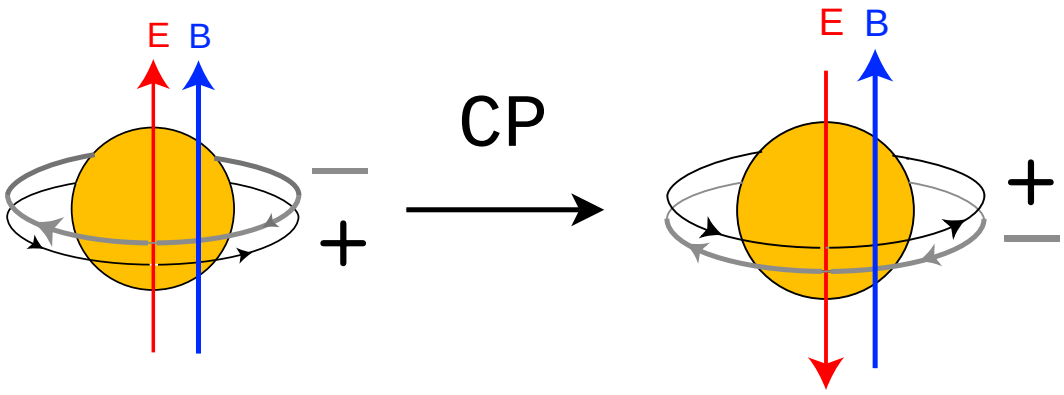

Figure 2.1 Toy model of a neutron as two classical oppositely charged current loops. Under a CP transformation, the electric field flips directions, while the magnetic field stays pointed in the same direction. Thus a neutron electric dipole moment violates CP symmetry.

When the physical vacuum is set by spontaneous symmetry breaking (with vacuum expectation value $v/\sqrt{2}$), we get a new Goldstone boson ϕ corresponding to the phase of the complex scalar [36, 87, 88]. In the free field theory for ζ, ϕ would be an unconstrained flat direction, but couplings of the form $\zeta G\tilde{G}$ will introduce classical dynamics for ϕ that drive the net CP-violating phase to zero. Quantum fluctuations in ϕ would correspond to a new particle, the *axion* [88].

As we shall see below, axion couplings are proportional to f_π/f_a, where f_a is the symmetry-breaking scale. It was originally hoped that the axion might be the Goldstone boson of a two-component Higgs (a very modest extension of the SM), with $f_\mathrm{a} \sim f_\mathrm{EW}$, where the electroweak scale $f_\mathrm{EW} \sim 10^2$ GeV, but this possibility was quickly ruled out by accelerator experiments [4, 91]. In its place, we have the *invisible axion* hypothesis, in which $f_\mathrm{a} \gg f_\mathrm{EW}$, giving the axion extremely weak couplings. Since f_a could *a priori* span the huge range of scales $f_\mathrm{EW} < f_\mathrm{a} < M_\mathrm{Pl}$ (where $m_\mathrm{Pl} \sim 10^{19}$ GeV is the Planck mass), it is hard work to scan through axion parameter space.

Axion decay rates to photons in galaxy clusters will of course depend on the couplings of the axion. We can understand axion couplings (and masses) using hadronic axion models and then generalize to a larger family of models by expanding the set of allowed quantum numbers. In this discussion, we follow closely the formalism for axion couplings laid out in Ref. [89]. In a hadronic axion model, there is a new complex scalar ζ which carries PQ charge 2 and has a potential $V(\zeta)$. There is also a family ψ^i of new Dirac fermions ($i \in \{1, N\}$ for some N), each of which transforms as a triplet under QCD SU(3) (in other words, the new heavy fermions have standard QCD interactions but also carry PQ charge). The new fermions are given mass through Yukawa interaction terms, that is, we have terms of the form $y_i \overline{\psi}^i_L \zeta \psi^i_R$ in the Lagrangian, where the y^i are the Yukawa couplings and $\overline{\psi} \equiv \psi^\dagger \gamma^0$. Here we have the standard Dirac matrices γ^μ from the SM along with $\gamma^5 = i\gamma^0\gamma^1\gamma^2\gamma^3$,

as well as the usual projections onto left and right-handed spinors [90]:

$$\psi_L^i = \frac{1}{2}\left(1-\gamma^5\right)\psi^i,$$
$$\psi_R^i = \frac{1}{2}\left(1+\gamma^5\right)\psi^i. \tag{2.2}$$

The full Lagrangian density for the hadronic model then reads [89]

$$\mathcal{L} = \mathcal{L}_{\rm SM} + \mathcal{L}_{\rm kin} - \sum_i y_i\left(\overline{\psi}_L^i \zeta \psi_R^i + \text{Hermitian conjugate}\right) - V\left(\zeta\right) - \frac{g_s^2}{32\pi^2}\overline{\theta} G^{\mathrm{p}\mu\nu}\tilde{G}_{\mathrm{p}\mu\nu}, \tag{2.3}$$

where $\mathcal{L}_{\rm SM}$ is the complete SM Lagrangian density. When the PQ symmetry is broken, ζ acquires a vacuum expectation value, and so $\zeta = ve^{i\phi/v}/\sqrt{2}$. The kinetic term $\mathcal{L}_{\rm kin}$ has standard contributions from ζ and the PQ-charged fermions. It turns out that a chiral rotation makes the axion's couplings to SM particles clearer:

$$\psi \to e^{i\beta\gamma^5}\psi^i,$$
$$\zeta \to e^{i\beta}\zeta,$$
$$\Delta\mathcal{L} = \frac{g_s^2}{16\pi^2}\beta G^{\mathrm{p}\mu\nu}\tilde{G}_{\mathrm{q},\mu\nu} N \delta_{pq}. \tag{2.4}$$

Here $N \equiv \sum_j X_j$ is the number of Dirac fermion families carrying PQ charge. Choosing $\beta = -\phi/\left(2Nf_{\rm a}\right)$ (where the axion decay constant $f_{\rm a} \equiv v/N$) and taking note of the fact that PQ-charged Dirac fermions may also have electromagnetic (EM) charges under a $U(1)$ symmetry, the following Lagrangian density results after PQ symmetry-breaking:

$$\mathcal{L} = \mathcal{L}_{\rm SM} + \frac{1}{2}\partial_\mu\phi\partial^\mu\phi - \frac{g_{\rm s}^2}{32\pi^2}\frac{\left(\phi + f_{\rm a}\overline{\theta}\right)}{f_{\rm a}} G^{\mathrm{p}\mu\nu}\tilde{G}_{\mathrm{q},\mu\nu} - \frac{e^2}{32\pi^2}\frac{E}{N}\frac{\left(\phi + f_{\rm a}\overline{\theta}\right)}{f_{\rm a}} F^{\mu\nu}\tilde{F}_{\mu\nu}. \tag{2.5}$$

The electric charges Q_j (in units of the fundamental charge e) of all the PQ-charged Dirac fermions enter through the factor $E = 2\sum_j Q_j^2$. Here $F^{\mu\nu}$ is the usual Maxwell tensor from electromagnetism and $\tilde{F}^{\mu\nu} = \epsilon_{\mu\nu\rho\kappa}F^{\rho\kappa}$ is its dual.

Well below the PQ symmetry breaking scale, the $V(\zeta)$ term may be neglected. Close to the QCD phase transition, axions will acquire a mass from interactions with pions, and their classical equations of motion will lead ϕ to have an expectation value, $\langle\phi\rangle = -f_{\rm a}\overline{\theta}$, driving the net CP-violating phase to vanish. There will still be quantum fluctuations about $\langle\phi\rangle$, and these correspond to a new massless particle, the axion. We define the axion field, $A \equiv \phi - \langle\phi\rangle$. To make the axion's coupling to photons transparent, we may perform another chiral rotation, this time on the SM quark fields, $q \to e^{ia\gamma^5/(2\times3)}q$, where the factor of 3 is the number of SM quark flavors, analogous to the

chiral rotation already performed. The quark-axion Lagrangian after this transformation is

$$\begin{aligned}\mathcal{L}_{\rm q,a} &= i\sum_k q_k \not{D} q_k + \frac{1}{2}\left(\partial_\mu A\right)^2 + \frac{1}{6f_{\rm a}}\sum_k \overline{q}^k \gamma^\mu \gamma^5 q^k \partial_\mu A \\ &+ \sum_k \left(\overline{q}^k_L m_k e^{ia/(3f_{\rm a})} q^k_R + \text{Hermitian conjugate}\right) - \frac{e^2}{32\pi^2}\left(\frac{E}{N} - \frac{4}{3}\right)\frac{A}{f_{\rm a}} F^{\mu\nu}\tilde{F}_{\mu\nu}, \quad (2.6)\end{aligned}$$

where k is an index sweeping over light SM quarks and m_k denotes the mass of the $k^{\rm th}$ light SM quark. The slashed covariant derivative is $\not{D} = \gamma^\mu D_\mu$, where D_μ is the standard electro-weak covariant derivative [90]. The axion appears multiplying a CP-violating term in the Lagrangian, and so it must be a pseudo-scalar and not a scalar particle. The classic KSVZ model [56, 57] corresponds to the choice $E/N = 0$, but in fact any choice of quantum numbers is *a priori* possible. The DFSZ [54, 55] model corresponds to a different scenario, where there are no exotic new fermions, but two Higgs doublets which carry PQ charge, as well a new scalar to break the PQ symmetry. As a result, SM quarks *and* leptons interact with the axion. By a similar procedure to the one just outlined, the DFSZ Lagrangian can be transformed into one of the form given in Eq. (2.6), with $E/N = 8/3$, as well as additional terms coupling axions to leptons.

If we are interested in the axion's coupling to two photons $g_{a\to\gamma\gamma}$ at high energies, we may read it off from the last term in Eq. (2.6),

$$g_{\rm a\to\gamma\gamma} = -\frac{e^2}{32\pi^2 f_{\rm a}}\left(\frac{E}{N} - \frac{4}{3}\right). \quad (2.7)$$

Recall that first term resulted from a chiral rotation on the PQ-charged fermions. Physically, if these fermions also carry electromagnetic charge, this results in a contribution to $g_{\rm a\to\gamma\gamma}$. The second term resulted from a chiral rotation which eliminated the axion coupling to gluons. Thus, through the coupling of axions to gluons, and then gluons to SM quarks (which carry EM charge), there is an additional contribution to $g_{\rm a\to\gamma\gamma}$. Of course at low energies below the QCD scale, the relevant degrees of freedom are hadrons (mesons/baryons) and not quarks.

The mesons may be reasonably treated in chiral perturbation theory. A tedious but straightforward calculation then yields the leading-order axion couplings (after dropping terms that are irrelevant below the QCD scale and diagonalizing the relevant mass matrix for the axion-meson system):

$$g_{\rm a\to\gamma\gamma} = \frac{\alpha}{2\pi f_{\rm a}}\left[\frac{E}{N} - \frac{2}{3}\frac{(4+r)}{(1+r)}\right], \quad (2.8)$$

$$m_{\rm a} = \frac{m_\pi f_\pi}{f_{\rm a}}\frac{\sqrt{r}}{1+r}. \quad (2.9)$$

Here $r \equiv m_{\rm u}/m_{\rm d}$ is the ratio of up-down quark masses, $m_\pi \simeq 135$ MeV is the mass of the neutral

pion π^0, $f_\pi = 93$ MeV is the pion decay constant, and α is the usual fine-structure constant.

The first term results from axions coupling to PQ-charged fermions through triangle-anomaly diagrams. Some PQ-charged fermions may also carry electromagnetic charge, and thus couple to photons, yielding the axion-photon coupling diagram shown schematically in Fig. 2.2. The second term results from axions coupling to gluons, which then couple to standard model quarks (e.g. pions). Since pions have a two-photon coupling in chiral perturbation theory, this yields an additional channel for axions to couple to photons, shown schematically in Fig. 2.3. The two terms may interfere, leading to the minus sign in Eq. (2.8). The axion mass results from its mixing with massive pions (this diagram should be generalized to include all manner of additional momentum conserving gluon interactions), shown in Fig. 2.4. This process is relatively ineffective before the QCD phase transition (for $T \gg \Lambda_{\rm QCD}$, where $\Lambda_{\rm QCD}$ is the energy scale of the QCD phase transition), and so the axion mass depends on temperature. Roughly, the axion mass scales as [50, 92]

$$\mathcal{M}_{\rm a}(T) \sim \begin{cases} 0.1 m_{\rm a} \left(\frac{\Lambda_{\rm QCD}}{T}\right)^{3.7} & \text{if } T \gg \Lambda_{\rm QCD}, \\ m_{\rm a} & \text{if } T \ll \Lambda_{\rm QCD}, \end{cases} \tag{2.10}$$

where both this scaling and a more precise value may be obtained from a finite-temperature field theory calculation.

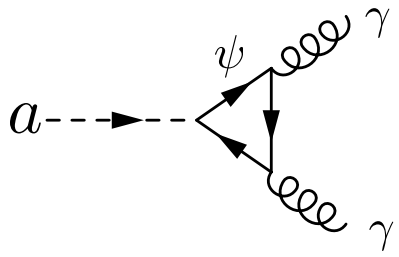

Figure 2.2 Anomaly diagram coupling axions to electromagnetism through new PQ-charged Dirac fermions that also carry electromagnetic charge. Here ψ is a PQ-charged fermion, a is the axion, and γ denotes a photon.

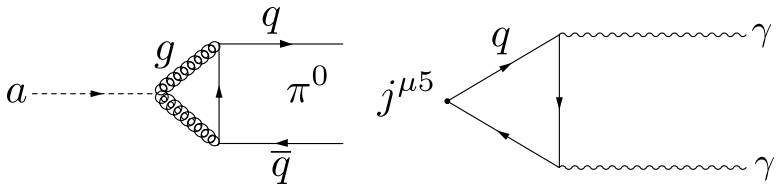

Figure 2.3 Axions couple to pions through the $aG\tilde{G}$ term (gluons are denoted by double curly lines), which then couples to quark pairs. Neutral pions are unstable and couple to electromagnetism. The axial vector current $j^{\mu 5}$ obeys $\partial_\mu j^{\mu 5} = -e^2 \epsilon^{\alpha\beta\mu\nu} F_{\alpha\beta} F_{\mu\nu} / \left(16\pi^2\right)$.

Just from this interaction term in the Lagrangian density, we may estimate the decay rate of

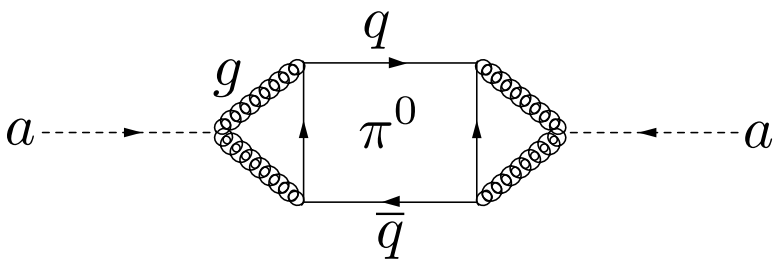

Figure 2.4 Although axions are massless at high energies, they acquire mass through mixing with pions for $E \lesssim \Lambda_{\rm QCD}$.

axions to pairs of photons $\Gamma_{\rm a\to\gamma\gamma}$. From the definition of the electromagnetic stress tensor ($F_{\mu\nu} = \partial_\mu A_\nu - \partial_\nu A_\mu$), we see that the matrix element for the decay diagram is $|M_{\rm a\to\gamma\gamma}| \sim g_{a\gamma\gamma}k^2 = k^2/f_{\rm a} = \alpha k^2 m_{\rm a}/(m_\pi f_\pi)$ (in Fourier space, where Feynman rules are derived, the derivative operator $\partial \to ik_\mu$). For this simple estimate we have neglected pre-factors that depend on specific parameter values of the axion model. The rate is proportional to $|M_{\rm a\to\gamma\gamma}|^2 \sim \alpha^2 k^4 m_{\rm a}^2/\left(m_\pi^2 f_\pi^2\right)$. The only momentum scale in the problem is $k \sim m_{\rm a}$, and we must multiply $|M_{\rm a\to\gamma\gamma}|^2$ by an additional factor of $1/m_{\rm a}$ to get units of energy for the rate, and so

$$\Gamma_{\rm a\to\gamma\gamma} \sim \alpha^2 \frac{m_{\rm a}^5}{m_\pi^2 f_\pi^2}. \tag{2.11}$$

Plugging in numerical values for m_π, f_π and α, we see that $\Gamma \sim 10^{-45}$ GeV$m_{\rm a,eV}^5$, where $m_{\rm a,eV}$ is the axion mass in eV. Converting from natural to cgs units (dividing by $\hbar$), we see that the axion lifetime

$$t = \frac{1}{\Gamma_{\rm a\to\gamma\gamma}} \sim 10^{20} \text{ s}. \tag{2.12}$$

When phase-space factors are properly included [90], the full calculation yields an axion lifetime of [4, 10]

$$\begin{aligned} \tau &= 6.8 \times 10^{24} \xi^{-2} m_{\rm a,eV}^{-5} \text{ s}, \\ \text{where } \xi &\equiv \frac{4}{3}\left(E/N - 1.92 \pm 0.08\right). \end{aligned} \tag{2.13}$$

This will produce a monochromatic axion-decay emission line, with rest frame wavelength [10]

$$\lambda_{\rm a} = c/\nu = \frac{2ch}{m_{\rm a}c^2} = 24,800\text{Å}/m_{\rm a,eV}, \tag{2.14}$$

and a line width dominated by Doppler broadening for the typical kinematic parameters in an astrophysical object.

The values of E and N depend on the axion model chosen, but by parameterizing τ in terms

of ξ, we will be able to probe ξ without prejudice for a particular model, by attempting to observe light from axion decay. The negative sign in Eq. (2.13) comes from interference between the different channels for the two-photon decay of axions. The uncertainty in the theoretical value of ξ comes from uncertainties in the quark masses and pion-decay constant, and may in fact be larger than indicated by Eq. (2.13). A complete cancellation of the axion's two-photon coupling is possible for models in which $E/N = 2$, and even for DFSZ axion models, in which $E/N = 8/3$ [86]. It is thus hasty to claim that an upper limit on ξ truly rules out axions; it always pays to keep looking, though in the long-run, experiments that depend on the non-vanishing hadronic couplings of axions may be more definitive.

To predict the expected intensity of the optical signal due to axion decay, given the mass distribution of a galaxy cluster, we need to know the total mass density in axions. If axions have masses in the eV range, they are kept in thermal equilibrium in the early universe through the reactions $\pi^+\pi^- \rightarrow \pi^0 a$, $\pi^\pm\pi^0 \rightarrow \pi^\pm a$. The relevant chiral Lagrangian is [93]

$$\begin{aligned} \mathcal{L}_{\mathrm{a}\pi} &= C_{\mathrm{a}\pi}\frac{\partial_\mu A}{f_{\mathrm{a}} f_\pi}\left(\pi^0\pi^+\partial_\mu\pi^- + \pi^0\pi^-\partial_\mu\pi^+ - 2\pi^+\pi^-\partial_\mu\pi^0\right), \\ C_{\mathrm{a}\pi} &= \frac{1-r}{3\,(1+r)}. \end{aligned} \tag{2.15}$$

From this Lagrangian the total axion production rate $\Gamma_{a,\pi}$ from pions may be computed, and using the criterion $\Gamma_{a,\pi}\left(T_{\mathrm{F}}\right) = H\left(T_{\mathrm{F}}\right)$ for the axion freeze-out temperature T_{F}, one can show that in the eV mass range, 30 MeV $< T_{\mathrm{F}} <$ 70 MeV [$H\left(T\right)$ is the temperature-dependent Hubble parameter]. We go through this computation in greater detail in Chapter 3.

More generally, axions with $m_{\mathrm{a}} \geq 10^{-2}$ eV do come into chemical equilibrium in the early universe and freeze out while relativistic. Their mass density today is then obtained via standard relativistic freeze-out arguments to be [10, 50, 51]:

$$\Omega_{\mathrm{a}} h^2 = \frac{m_{\mathrm{a,eV}}}{130}\left(\frac{10}{g_{*\mathrm{S,F}}}\right), \tag{2.16}$$

where $g_{*\mathrm{S,F}}$ is the number of relativistic degrees of freedom when axions freeze out. Even if axions are not a thermal relic, they may be quite important cosmologically. If the initial net-CP violating phase $\phi = A_0/f_{\mathrm{a}} \neq 0$, the axion field will coherently oscillate once the axion acquires a mass, obeying the equation of motion [50, 52, 94]

$$\ddot{A}_k + 3H\dot{A}_k + \frac{k^2}{a^2}A_k + \mathcal{M}_{\mathrm{a}}^2\left(T\right) f_{\mathrm{a}} \sin\left(\frac{A_k}{f_{\mathrm{a}}}\right) = 0. \tag{2.17}$$

Here a is the cosmological scale factor, k is the wave number of a Fourier mode A_k of the axion field. If $f_{\mathrm{a}} \gg f_{\mathrm{inf}}$, where f_{inf} is the energy scale of inflation, then inflation will dilute any large

gradients, allowing us to drop the gradient energy term ($k^2 A_k/a^2$). In this case, the axion field is essentially a zero-temperature condensate of coherently oscillating bosons.[3] At times early enough that $T \gg \Lambda_{\rm QCD}$, $\mathcal{M}_{\rm a}(T) \ll H$, and A is constant. Once $\mathcal{M}_{\rm a}(T) \gg H$, the axion may be treated as a harmonic oscillator, and in an appropriate adiabatic limit, the energy density is [50]

$$\rho_{\rm a} \sim \frac{\mathcal{M}_{\rm a}(T)}{a^3}. \tag{2.18}$$

In other words, coherently produced axions behave as cold dark matter (CDM) once $T \ll \Lambda_{\rm QCD}$ [$\mathcal{M}_{\rm a}(T) = m_{\rm a}$], and their relic density is [50, 52, 95]

$$\Omega_{\rm a} h^2 \sim 0.11 \left(\frac{10^{-5}}{m_{\rm a,eV}}\right)^{\frac{7}{6}} \left(\frac{\Lambda_{\rm QCD}}{200\ {\rm MeV}}\right)^{-0.7} f(A_0)\, A_0^2, \tag{2.19}$$

where A_0 is the initial value of the axion field in our causally connected patch and $f(A_0)$ is a function incorporating anharmonic effects and corrections due to the continuous dependence of the axion mass on temperature. After PQ symmetry breaking, $\zeta = v e^{iA/f_{\rm a}}/\sqrt{2}$, and so the initial value of A corresponds to a misalignment of the initial CP-violating phase from 0. As the universe cools and the axion mass grows, the CP-violating phase is driven to zero by the classical dynamics of the axion field, but the initial value A_0 is relevant to setting the axion density today.

Alternatively, PQ symmetry breaking could occur after inflation, that is, $f_{\rm a} \ll f_{\rm inf}$. In this case, the universe today consists of patches with a spectrum of initial phases $A_0/f_{\rm a}$. Naively, the relic density would then be given by Eq. (2.19) using the root-mean-squared (rms) value for A_0, but this neglects the potentially huge contribution of gradient energy due to large inhomogeneities in A_0. These can lead to topological defects (global strings [50, 94, 96–100] and domain walls [94, 101]), which decay into axions at late times and might enhance the density by a factor as high as ~ 200 over that predicted by Eq. (2.19). Precise numerical values for relic densities in this case require computationally intense simulations, and are still a subject of some controversy. In both cases, the resulting axion populations at late time have extremely low velocities today ($v/c < 10^{-13}$ [94]) and are a sensible cold dark-matter candidate. A simple closure constraint ($\Omega_{\rm a} < 1$) yields the limits $m_{\rm a,eV} \gtrsim 10^{-5}$ and $m_{\rm a,eV} \gtrsim 10^{-3}$ in the $f_{\rm a} \gg f_{\rm inf}$ and $f_{\rm a} \ll f_{\rm inf}$ cases, respectively [94].

Since the axion is an energetically sub-dominant, second scalar field during inflation, quantum fluctuations will be imprinted on it, and it will seed iso-curvature perturbations in addition to the canonical inflationary adiabatic perturbations [102]. WMAP data limit iso-curvature perturbations to account for at most 13% of the total primordial density perturbation [103]. This is still consistent with a picture in which axions constitute all the cold dark matter, as long as the ratio $r_{\rm st}$ of the amplitudes of primordial tensor to scalar perturbations $r \lesssim 10^{-12}$, or if one admits the possibility

[3] This is not an abuse of terminology. The occupation number of of 10^{-6} eV axions with zero momentum could be as high as 10^{64} [50]!

of a large amount of entropy generation between 200 MeV and 1 MeV, or a finely tuned initial PQ-violating phase $\overline{\theta}$ [103, 104]. Upcoming CMB polarization experiments will probe the regime $r \gtrsim 10^{-2}$, and thus offer an interesting complementary test of the axion CDM hypothesis. If ADMX detects CDM axions independently [27], one would expect either a null result for tensor modes in any upcoming CMB B-mode polarization experiment, or infer fine-tuning/entropy generation. As we discuss in the next chapter, the latter possibility is broadly consistent with a scenario in which a $1 - 100$ TeV scalar (modulus field) comes to dominate the universe.

In any case, for the remainder of this discussion, we will restrict ourselves to thermal axions, as our optical telescope search for axions lies in the window $4.5 < m_{\mathrm{a,eV}} < 7.7$.

To calculate the expected axion line intensity from a galaxy cluster, we must predict their local mass fraction within a galaxy cluster, $x_{\mathrm{a}} = \rho_{\mathrm{a}}^{\mathrm{cluster}}/\rho_{\mathrm{total}}^{\mathrm{cluster}}$, and not just their global mass fraction $\Omega_{\mathrm{a}}/\Omega_{\mathrm{matter}}$. Thermal relic axions in the mass range probed by our telescope search, which become nonrelativistic when 4.5 eV $\leq T \leq$ 7.7 eV, will have a velocity dispersion today of $\langle v_{\mathrm{a}}^2/c^2\rangle^{1/2} = 4.9 \times 10^{-4} m_{\mathrm{a,eV}}^{-1}$ [4]. For $m_{\mathrm{a,eV}} \sim 1$, $\langle v_{\mathrm{a}}^2\rangle^{1/2} \sim 100$ km s^{-1}. Galaxy clusters have typical velocity dispersions of $\sigma_{\mathrm{3D}} \sim 1000$ km s$^{-1} \gg \langle v_{\mathrm{a}}^2\rangle^{1/2}$, and so it is conceivable that axions might collapse into galaxy clusters [10].

The mass fraction of a light particle in a bound system cannot be arbitrarily high, however, due to phase space limitations. This is the well known Gunn-Tremaine limit [105]. It may be surprising that a similar restriction applies to bosons, as their phase space density is not bounded. In terms of particle number, however, even for bosons, the number density of particles in high occupancy states is actually quite low. A slightly modified version of the Gunn-Tremaine argument thus extends to axions [10, 106, 107], and it is important to verify that galaxy clusters have adequate phase space for a cosmological axion mass fraction.

To make this point clearer, we review the arguments for the Gunn-Tremaine limit and then generalize them to bosons. The phase space density of a single thermalized neutrino species in the early universe is [105]

$$f_\nu\left(\vec{p}\right) = \frac{2}{h^3}\frac{1}{e^{\frac{p}{kT_\nu}}+1}, \tag{2.20}$$

where $\vec{p}$ is the momentum, T_ν is the neutrino temperature, h is the Planck constant, and k is Boltzmann's constant. Neutrinos decouple while relativistic, so even after they freeze out, $f_\nu\left(\vec{p}\right)$ continues to obey Eq. (2.20) with $T_\nu \propto (1+z)$, barring the usual jump $T_\nu \rightarrow \left(\frac{11}{4}\right)^{1/3} T_\nu$ at e^+e^- pair annihilation [50].

Neutrinos are weakly interacting, and thus nearly collisionless. The fine-grained phase space density f_ν thus obeys the collisionless Boltzmann (Vlasov) equation; the fine grained phase density of a comoving fluid parcel is conserved. The coarse grained phase space density q does not obey

[4] This velocity is a typical thermal axion velocity and does **not** obey the $v/c < 10^{-13}$ condition which applies to coherently produced axions.

the Vlasov equation; indeed, by the very definition of coarse graining, regions of high and low phase density will get mixed in with one another as structure forms in the universe. It must, however, be bounded from above by the fine-grained phase-space density. In a virialized halo, the velocity distribution $\tilde{q}_i$ of the species i is reasonably modeled by a Maxwellian [105]:

$$\tilde{q}_i(\vec{r},v)d^3v = \frac{n_i}{\left(2\pi\sigma^2\right)^{3/2}} e^{\frac{\Psi(\vec{r})-v^2/2}{\sigma_i^2}} d^3v, \tag{2.21}$$

where σ_i is the one-dimensional velocity dispersion, $\Psi(\vec{r})$ is the gravitational potential defined with its zero at the cluster center $\vec{r}=0$, and n^i is the central number density of the $i^{\rm th}$ species. The velocity distribution is bounded from above by its value with the argument of the exponent set to zero. The momentum of the $i^{\rm th}$ species is $\vec{p}_i = m_i\vec{v}_i$, and so the momentum space phase space density is $q_i = \frac{1}{m_i^3}\tilde{q}_i$. The central number density $n_i = x_i\rho_0/m_i$, where ρ_0 is the total central mass density of the halo and x_i is a homogeneous mass fraction for i particles. The coarse-grained phase space density thus obeys

$$\begin{aligned} q_i(\vec{r}) &\leq q_i^{\rm max}, \\ q_i^{\rm max}(\vec{r}) &= \frac{\rho_0 x^i}{m_i^4\left(2\pi\sigma_i^2\right)^{3/2}}. \end{aligned} \tag{2.22}$$

Now consider a neutrino species. Its fine-grained phase space density obeys $f_\nu \leq 2/h^3$, and since $q_\nu^{\rm max} \leq f_\nu$, we have [105]

$$m_\nu^4 > \frac{\rho_0 x_\nu h^3}{2\left(2\pi\sigma^2\right)^{3/2}}. \tag{2.23}$$

Assuming that $\rho(\vec{r})$ is described by the relatively simple King profile (just as an example), $\rho_0 = 9\sigma^2/\left(4\pi G r_c^2\right)$ (where r_c is a core radius and σ the velocity dispersion), we may simplify Eq. (2.23) and evaluate it to yield

$$m_\nu > (101\ {\rm eV})\, x_\nu^{1/4}\sigma_{100}^{-1/2} r_{c,{\rm kpc}}^{-1/4}, \tag{2.24}$$

where r_c is the core radius in kpc and $\sigma_{100} = \sigma/\left(1000\ {\rm km\ s^{-1}}\right)$. In other words, if standard thermal neutrinos are to make up the bulk of the dark matter in galaxies, they had better be rather heavy!

Now consider a boson, in particular the axion. The occupation number in a state with energy E is given by the familiar Bose-Einstein distribution [10, 106, 107]:

$$f_{\rm a}(E) = \frac{1}{e^{E/(kT)}-1}. \tag{2.25}$$

There is a critical energy E_* such that $f>1$ for $E<E_*$. The number density of axions in high occupancy states is then given by the usual thermal expressions, but with a smaller domain of

integration:

$$n_{\mathrm{a},>} \equiv \frac{1}{2\pi^2}\int_{E_*}^{\infty}\frac{E^2 dE}{e^{E/(kT)}-1} \simeq 0.08 n_{\mathrm{a}}. \tag{2.26}$$

The Gunn-Tremaine argument then applies for the 92% of axions that are in low-occupancy ($f_{\mathrm{a}} \leq 1$) states, and similarly for a King profile we may obtain a similar constraint:

$$x_{\mathrm{a}} \leq 6.5\times 10^{-3}\sigma_{1000}a_{250}^2 m_{\mathrm{a,eV}}^4. \tag{2.27}$$

For a typical galaxy, $\sigma_{1000}\sim 0.2$ and $a_{250}\sim 0.05$, and so $x_{\mathrm{a}} \leq 3.3\times 10^{-6} m_{\mathrm{a,eV}}^4$. For a 3 eV axion near the lower-frequency end of the optical search window, $x_{\mathrm{a,eV}} < 3\times 10^{-4}$, which is far too small to accommodate a thermal cosmological fraction ($\Omega_{\mathrm{a}}/\Omega_{\mathrm{matter}}\sim 0.15$) of such axions. For a galaxy *cluster* on the other hand, $\sigma_{1000}\sim 1$ and $a_{250}\sim 1$, so for a 3 eV axion, $x_{\mathrm{a}} < 0.53$, a constraint which is more than ample to accommodate a cosmological mass fraction of axions. We note that in this case the phase-space constraint is statistical [106, 107]. Some axions will be in high-occupancy states at early times, and regions of high-occupancy will be be mixed into some galaxy clusters. Thus this 'bosonic Gunn-Tremaine' bound should be taken as a constraint on the *mean* mass fraction of axions in galaxy cluster [106, 107]. The general expression for the line density due to axion decay is [10]

$$I_{\lambda_0} = \frac{\Sigma_{\mathrm{a}}(R)c^3}{4\pi\sqrt{2\pi}\sigma\lambda_{\mathrm{a}}\tau_{\mathrm{a}}(1+z_{\mathrm{cl}})^4} e^{-\frac{(\lambda_0/(1+z_{\mathrm{cl}})-\lambda_{\mathrm{a}})^2}{\lambda_{\mathrm{a}}^2}\frac{c^2}{2\sigma^2}}. \tag{2.28}$$

If the axion has a cosmological density given by Eq. (2.16) and $x_a > \Omega_{\mathrm{a}}/\Omega_{\mathrm{matter}}$, then the observer-frame specific intensity from axion decay is

$$I_{\lambda_o} = 2.68\times 10^{-18}\times \frac{m_{\mathrm{a,eV}}^7 \xi^2 \Sigma_{12}\exp\left[-\left(\lambda_r-\lambda_{\mathrm{a}}\right)^2 c^2/\left(2\lambda_{\mathrm{a}}^2\sigma^2\right)\right]}{\sigma_{1000}(1+z_{\mathrm{cl}})^4 S^2(z_{\mathrm{cl}})}\mathrm{cgs}, \tag{2.29}$$

where λ_{o} denotes wavelength in the observer's rest frame, $\lambda_r = \lambda_o/(1+z_{\mathrm{cl}})$, cgs denotes units of specific intensity (ergs cm^{-2} s^{-1} Å^{-1} arcsec^{-2}), $S(z_{\mathrm{cl}}) \equiv d_a(z_{\mathrm{cl}})/\left[c/\left(100\ \mathrm{km\ s^{-1}\ Mpc^{-1}}\right)\right]$ is a dimensionless angular-diameter distance, and $\Sigma_{12}\equiv \Sigma/\left(10^{12}M_{\odot}\mathrm{pixel}^{-2}\right)$ is the normalized surface mass density of the cluster with a lensing-map pixel size of 0.5 arcsec. If for some reason (e.g., low-temperature reheating [43]), the cosmological axion mass density is lower than indicated by Eq. (2.16), then the intensity in Eq. (2.29) is decreased accordingly.

The cluster mass density was determined by fitting parameterized potentials to the locations of gravitationally lensed arcs. The intensity predicted by Eq. (2.29) is comparable with that of the night-sky continuum, and so it is crucial to obtain a good sky subtraction when searching for an axion-decay line in clusters. Fortunately, the spatial dependence of the cluster density and the expected signal provides a natural way to separate the background from an axion signal, as discussed in Section 2.5.2.

2.3 Constraints in the literature

To understand the state of play in contemporary axion constraints, we show a plot (Fig. 2.5) from one of the many excellent review articles on axions by Georg Raffelt [5], modified to include more recent constraints [5].

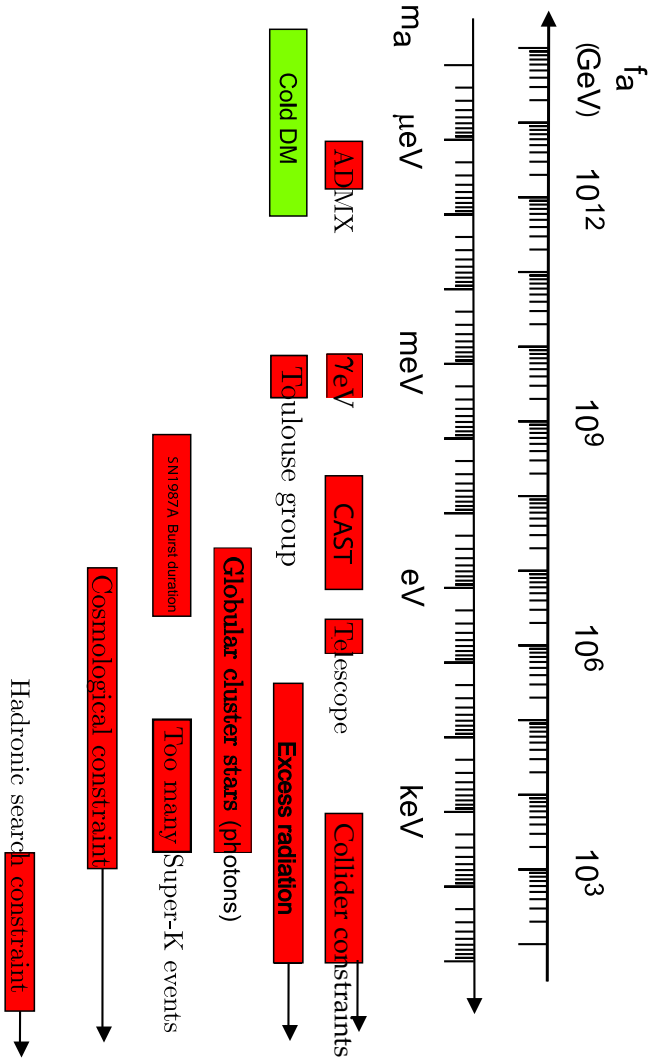

Figure 2.5 Allowed axion parameter space, compiled from many experiments. This plot is a modified version of one in Ref. [5]. Red regions are excluded by the technique indicated, while the green region indicates the axionic dark matter window. See text in Sec. 2.3 for detailed discussion of various limits.

The region of the plot marked CDM indicates a range of masses where the relic density of cold axions would equal or exceed the total dark matter density. As mentioned above, theoretical predictions for the cosmological relic density of cold axions are controversial due to disputes about the importance of topological effects. The rest of this dense plot can be parsed by considering the

different couplings of axions one by one and enumerating some of the relevant experiments. In most cases, we show the most stringent experimental constraint in a given mass window, for the least strongly interacting axion model.

Some of the most robust constraints come from the axion-nucleon-nucleon coupling. In the post-collapse core of a Type II supernova, nucleon axion bremmstrahlung ($NN \rightarrow N\mathrm{a}N$) would cool the neutron-star-to-be. The extra energy-loss channel would shorten the neutrino burst from the supernova (which carries away most of the supernova energy). Fortunately, 19 neutrinos were detected from Supernova 1987A [4], and the duration of this burst excludes the hadronic axion masses of 10^{-2} eV $\rightarrow$ 2 eV in the left grey region of Fig. 2.5. A more restrictive bound applies for the DFSZ model. The bound shown here is for the hadronic axion model. At sufficiently high masses, axions are so strongly interacting that most would get completely trapped in the core of the collapsed star and do not significantly contribute to cooling (see Ref. [50] and references therein). At higher masses still, the few axions that do make their way to us would have strong enough couplings that they would have been directly detected in Super-Kamionkande (see Ref. [50] and references therein), explaining the excluded region on the right in Fig. 2.5 labeled 'Too many Super-K events.'

Most searches for axions rely on their two-photon coupling $g_{\mathrm{a}\rightarrow\gamma\gamma}$. For $m_a \gtrsim 20$ eV, axions would contribute excessively to the UV radiation background, and so this mass range would seem to be excluded. Meanwhile, the limit marked globular cluster stars comes from the fact that axions would be produced in stellar plasmas through the $\mathrm{a} \rightarrow \gamma\gamma$ interaction, leading to an additional cooling channel for stars. This would unacceptably shorten their helium burning lifetimes, and good constraints are obtained from population statistics of HB (horizontal branch), AGB (asymptotic giant branch), and RGB (red giant branch) stars in star clusters [59, 60, 70]. In Chapter 3, we demonstrate how this limit is relaxed when the full model-dependence of $g_{\mathrm{a}\rightarrow\gamma\gamma}$ is considered. DFSZ axions would affect white-dwarf cooling through the coupling of axions to electrons. Recent work has imposed new limits to DFSZ axions in the $\sim$ meV window, using the white-dwarf luminosity function and white-dwarf astroseismology [108, 109]. A less stringent bound may also be obtained from the lifetime of the sun [62]. Constraints from neutron-star lifetimes also exist, but are somewhat unwieldy because of uncertainties in the neutron-star equation of state [110].

In RF (radio-frequency) cavities with strong magnetic fields, cosmological axions would resonantly convert into photons [111]. Experiments based on this principle have been ongoing for years and were first proposed by Pierre Sikivie in 1983. The latest and greatest is the ADMX (Axion Dark Matter eXperiment) experiment [27, 112], and the resulting exclusion range is shown in Fig. 2.5. ADMX is an ongoing experiment: the use of SQUID (Superconducting QUantum INterference Device) amplifiers has recently improved the sensitivity of ADMX to the axion-photon coupling by an order of magnitude [112].

The two-photon interaction term of the axion is $g_{\mathrm{a}\rightarrow\gamma\gamma} a\vec{E}\cdot\vec{B}$, and polarized laser light sent down

an optical cavity would preferentially convert to axions if its polarization were aligned with a strong imposed magnetic field, leading to dichroism (elliptical polarization) and birefringence (rotation of the polarization plane) in a generic polarized beam [66–70, 113]. This technique was used by the PVLAS (Polarizzazione del Vuoto con LASer) group, which claimed tenuous evidence for a new ∼meV pseudoscalar [65] (surprisingly in a region of mass-coupling parameter space that had long ago already been ruled out by stellar evolution arguments, and was not related to the QCD axion hypothesis [72, 73]). The PVLAS result has been tested by experiments utilizing the 'light-shining-through-walls principle' [71, 114]: At the end of the cavity, photons must reflect off the mirror while axions would in principle pass through. If a strongly magnetized cavity was placed down the axion beamline, axions would in principle convert to photons beyond the reach of the first laser beam. Both the γ-eV [115] experiment and an independent experiment in Toulouse [116] have now probed the same axion mass range and found no evidence for a new pseudoscalar, disagreeing with the PVLAS result at 3σ.

A similar idea can be applied to axions that might be streaming towards us from the sun after being produced when x-rays scatter of protons and electrons in the solar plasma. These axions could be converted back into x-ray photons in a magnetized cavity. This is essentially an astronomical 'light-shining-through-walls' experiment. The ongoing CAST (CERN Axion Solar Telescope) experiment [28] has implemented this idea and ruled out the mass range of axions shown in Fig.2.5 for **extremely** strong couplings outside the preferred space of models. The ongoing CDMS experiment would also be sensitive to such solar axions [117], as is the Tokyo Axion helioscope [118].

Longer astronomical baselines for the conversion of photons to axion-like particles may be obtained in the future using the spectra of *Fermi* sources [119, 120]. Anomalous absorption could be a result of $\gamma \rightarrow$ a conversion in a magnetic field. More recently, there have been claims that correlations in quasar polarizations may be the result of conversion from photons to axion-like particles [121]. Those results are still controversial, however, with disagreement about their statistical significance [122].

As we have noted, cosmological thermal relic axions would decay in galaxy clusters to generate a monochromatic emission line. The exclusion region of past telescope searches is marked telescope in the constraint plot. Note that the precise size of this band depends on the axion model assumed and on the value of the up-down quark mass ratio r, as discussed in the preceding section. The up-down quark mass ratio r is surprisingly poorly known, since, as Frank Wilczek put it [123], "Quarks everywhere are born free, but live in chains." The spectrum of mesons does not yield an adequate constraint to infer r, and going from the baryon masses to quark masses requires lattice QCD-based computations; different groups using these techniques still disagree by as much as 50% on the value of r [91]. As a result, there are reasonable parts of parameter space in which the two-photon coupling of the axion would be extremely small, lifting almost all of the astro-physical

constraints [see Eq. (2.8)]. The hadronic axion mass window consistent with ADMX results [27] in this case has been carefully determined in Ref. [89]. We show the allowed axion parameter space in the case of a vanishing two-photon coupling in Fig. 2.6. We see that in this case, the allowed axion mass window is huge, and more definitive experiments must be conducted.

Fortunately, even if the two-photon coupling of axions vanishes, their hadronic couplings will not (they are not as model dependent or sensitive to r), and nuclear resonances in Li, Fe, Kr in the sun would produce a beam of axions detectable via the same resonances on Earth. Preliminary experiments have been conducted and yield upper limits to the hadronic axion mass in the $\sim$ keV range [124–127]. The hadronic couplings of axions are also responsible for the rates keeping them in thermal equilbrium in the early universe, and thus there are cosmological constraints to thermal axions [6, 128–130], shown in Figs. 2.5 and 2.6. These limits are discussed at greater length in Chapter 3.

2.4 Observations

2.4.1 Imaging Data

To construct the lensing models used in our analysis and to mask out IFU fibers corresponding to cluster galaxies and other bright sources, we used images of A2667 and A2390 obtained with the HST and the VLT. The cluster A2667 was observed with HST on October 10-11, 2001, using WFPC-2 in the F450W, F606W, and F814W filters, with total exposure times of 12.0 ksec, 4.00 ksec, and 4.00 ksec, respectively [131]. The cluster A2390 was observed with HST on December 10, 1994, using WFPC-2 in the F555W and F814W filters and total exposure times of 8.40 ksec and 10.5 ksec [132]. After pipeline processing, standard reduction routines were used with both clusters to combine the frames and remove cosmic rays. Figs. 2.7 and 2.8 are images of the cluster cores, with iso-mass contours overlaid from our best-fit lensing models.

On May 30 and June 1, 2001, near-infrared J-band and H-band observations of A2667 were obtained with ISAAC on the VLT [131]. The total exposure times for the J and H band ISAAC data were 7.93 ksec and 6.53 ksec, respectively. The final seeing was $0.51''$ and $0.58''$ in the J and H bands, respectively.

2.4.2 VIMOS Spectra

The massive galaxy clusters A2667 and A2390 were observed with VIMOS, between June 27 and 30, 2003 [131, 132]. The IFU is one of three modes available on VIMOS, and consists of 4 quadrants, each containing 1600 fibers. We used an instrumental setup in which each fiber covered a region of $0.67''$ in diameter. A single pointing covered a $54'' \times 54''$ region of the sky. Roughly 10% of

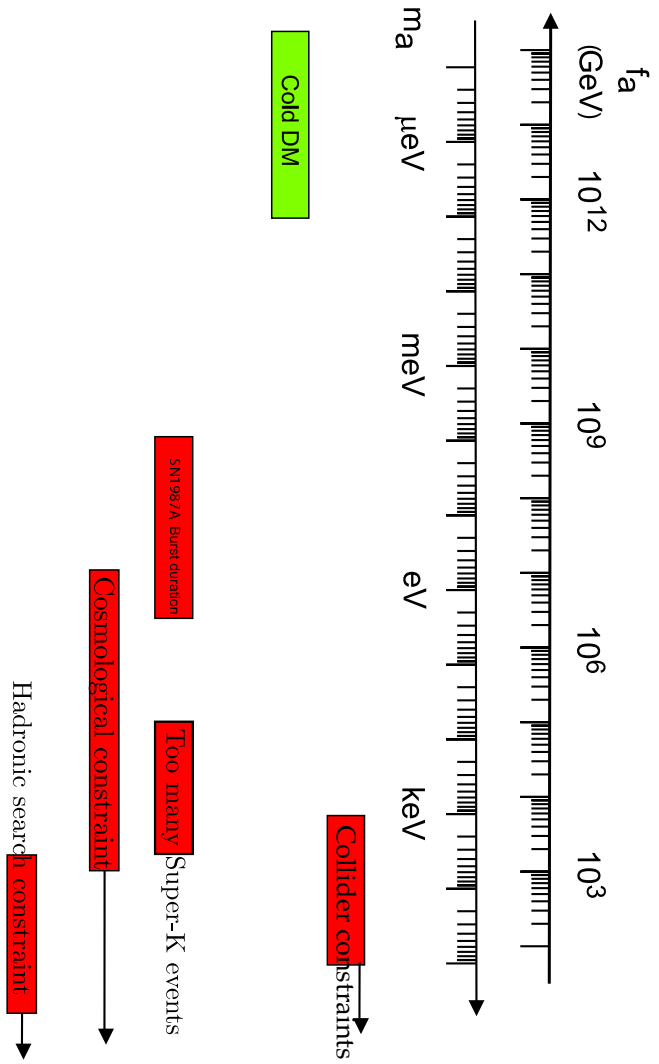

Figure 2.6 Allowed parameter space for hadronic axions if their two-photon coupling constant $g_{a\to\gamma\gamma} = 0$, compiled from many experiments. This plot is a modified version of one in Ref. [5]. Red regions are excluded by the technique indicated, while the green region indicates the axionic dark matter window. See text in Sec. 2.3 for detailed discussion of various limits.

the IFU field of view is unresponsive because of incomplete fiber coverage. A low resolution blue (LR-Blue) grism was used, covering the wavelength range 3500Å to 7000Å with spectral resolution $R \approx 250$ and dispersion 5.355Å/pixel. The FWHM of the axion-decay line is 195Å $\sigma_{1000}\ m_{\rm a,eV}^{-1}$, and so the LR-Blue grism can resolve this line, without spreading a faint signal over too many wavelength pixels. Unfortunately, because spectra from contiguous pseudo-slits (sets of 400 spectra) on the CCD overlap, the first and last 50 pixels on most of the raw spectra are unusable, reducing the spectral range to 4000Å – 6800Å, corresponding to an axion mass-range of $4.5 \leq m_{\rm a,eV} \leq 7.7$ at the nearly identical redshifts ($z \approx 0.23$) of the two clusters.

The total exposure time for each cluster was 10.8 ksec (4×2.70 ksec exposures). Calibration

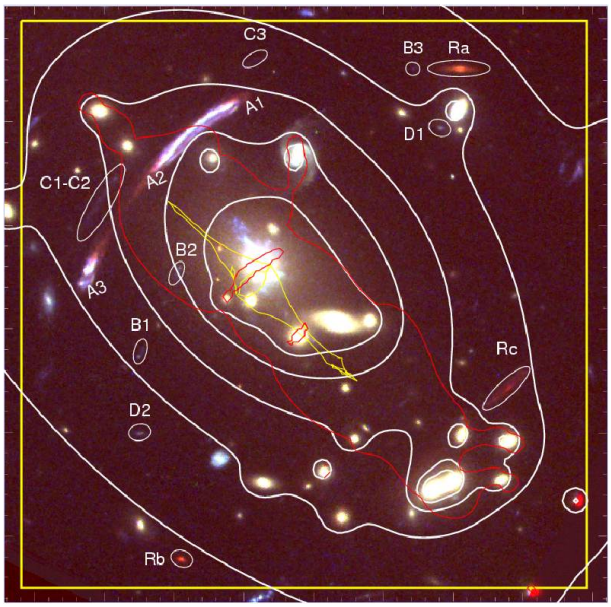

Figure 2.7 Image of the Abell 2667 cluster core imaged with HST in the F450W, F606W, and F814W filters. The white (thin yellow) square shows the IFU field of view, which is 54" × 54". North is to the top and east is to the left. Note the strongly magnified gravitational arc north-east of the central galaxy. The white curves correspond to iso-mass contours from the lens model; the dark gray (red) line is the critical line at the redshift of the giant arc. The field of view is centered on α_{J2000}=23:52:28.4, δ_{J2000}=−26:05:08. At a redshift of $z = 0.233$, the angular scale is 3.661 kpc/arcsec.

frames were obtained after each of the exposures, and a spectrophotometric standard star was observed. In order to compensate for the presence of a small set of bad fibers, we used an offset between consecutive exposures. At a redshift of $z = 0.233$ (A2667), the IFU covers a physical region of 198 kpc × 198 kpc in the plane of the cluster. At a redshift of $z = 0.228$ (A2390), the IFU covers a physical region of 195 kpc × 195 kpc. Further observational details are discussed in Ref. [131].

2.4.3 Reduction of IFU data

If axions exist and are present in the halos of massive galaxy clusters, a distinct spectral feature will appear in VIMOS-IFU data. At a rest-frame wavelength λ_a, we will observe a spatially extended emission line whose intensity traces the projected dark-matter density. Revealing such a faint, spatially extended signal requires great care in correcting for fiber efficiency and in subtracting the sky background, because the instrument itself can impose spatial variation in the sky background through varying IFU fiber efficiency.

The VIMOS-IFU data were reduced using the VIMOS Interactive Pipeline Graphical Interface (VIPGI), and the authors' own routines [133]. References [85, 131] give both a detailed description of the methods and an assessment of the quality of VIPGI data reduction. The reduction steps that

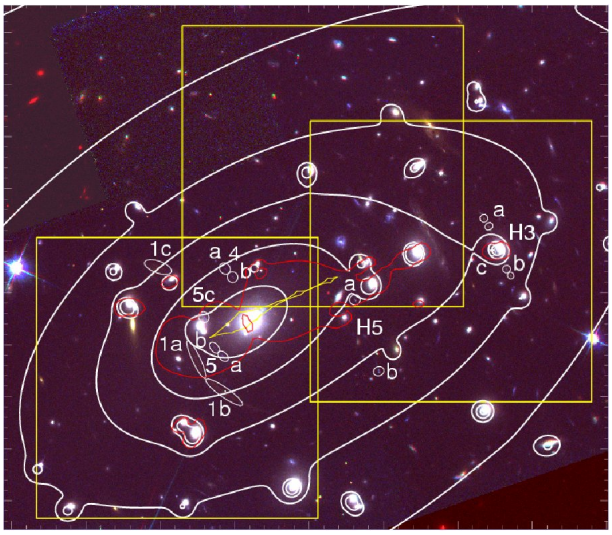

Figure 2.8 Image of the Abell 2390 cluster core imaged with HST in the F450W, F606W, and F814W filters. The white (thin yellow) squares correspond to the IFU field of view in different pointings. The white curves correspond to iso-mass contours from the lens model. The dark gray (red) line is the critical line at the redshift of the giant arc, labelled 1. Each square is 54" × 54". North is to the top and east is to the left. The field of view is centered on α_{J2000}=21:53:36.970, δ_{J2000}=+17:41:44.66. At a redshift of $z = 0.228$, the angular scale is 3.601 kpc/arcsec.

precede the final combination of the dithered exposures into a single data cube are performed on a quadrant by quadrant basis. The main steps are the following [85, 131, 133–135]: extract spectra from the raw CCD data at each pointing, calibrate wavelength, remove cosmic rays, determine fiber efficiencies, subtract the sky background, and calibrate flux.

The exposures were bias subtracted. Cosmic-ray hits were removed with an efficient automatic routine based on a σ-clipping algorithm, which exploits the fact that cosmic-ray hits show strong spatial gradients on the CCD [85], in contrast to the smoother spatial behavior of genuine emission lines. In Ref. [11], spectra were obtained using a limited number of long-slit exposures, so the removal of a small number of incorrectly identified cosmic-ray hits could thwart a search for line emission from decaying axions. An axion-decay line, however, must smoothly track the density profile of the cluster. Our spectra are highly spatially-resolved, and so cosmic-ray hits can be removed safely using our cleaning algorithm. Using the raw CCD spectral traces, we verified that the signals removed by the cleaning algorithm bore the distinctive visual signatures of cosmic-ray hits.

VIPGI usually determines fiber efficiencies by normalizing to the flux of bright sky lines; this technique yielded data cubes with prominent bright and dark patches (each covering $\sim 20 \times 20$ fibers). It is conceivable that an accidental correlation of these patches with the cluster density profile could lead to a spurious axion signal. To avoid this possibility, we measured fiber efficiency using high signal to noise continuum arc-lamp exposures (analogous to flat-fielding for images and henceforth referred to as flat-fielding). The resulting flat-fielded data cubes were much less patchy,

and were thus used for all subsequent analysis.

The VIMOS IFU does not have a dedicated set of fibers to determine the sky-background level. VIPGI usually determines the sky statistically at each wavelength. VIPGI first groups the fibers in each quadrant into three sets according to the shape of a user selected sky-emission line, and then takes the statistical mode of the counts in each set and subtracts it from the counts measured in each fiber in the set [133]. Although axions (and thus their decay luminosity) trace the centrally peaked density profile of the cluster, the average decay luminosity would be wiped out by this procedure, and lead to a spurious depression in measurements of ξ. The sky subtraction implemented in VIPGI is thus unsuitable for our axion search and was not applied. A customized sky-subtraction was applied, as discussed in Section 2.5.2.

Flux is calibrated separately for each IFU quadrant, using observations of a standard star. Finally, the four fully reduced exposures are combined. The final data cube for A2667 is made of 6806 spatial elements, each one containing a spectrum from 3500Å to 7000Å, and covers a sky area of 0.83 arcmin^2, centered 5 arcsec south-west of the brightest cluster galaxy. The final data cube for A2390 is made of $24,645$ spatial elements, each one containing a spectrum from 3500Å to 7000Å, and covers a sky area of 3.11 arcmin^2, centered 15 arcsec north-east of the brightest cluster galaxy. The median spectral resolution is $\simeq 18$Å. For further discussion of the process used to generate the data cubes, see Refs. [85, 131].

After producing data cubes in VIPGI, we passed these data cubes to a secondary routine that searches for emission from axion decay and estimates the noise in our spectra. The most obvious source of error is Poisson counting noise. The number of photons observed at wavelength λ in the j$^{\rm th}$ spatial bin is just $N_{\lambda,j} = E\left[F_{\lambda,j}/(hc/\lambda)\right]\delta t\delta\lambda\delta A$, where $\delta A = 51.2\mathrm{m}^2$ is the collecting area of the Mélipal telescope, $\delta\lambda = 5.355$Å is the dispersion of a single VIMOS spectral pixel, δt is the integration time, $F_{\lambda,j}$ is the flux in the jth pixel at wavelength λ, and E is the end to end mean efficiency of VIMOS mounted at Mélipal. The Poisson counting noise is $\delta N_{\lambda,j} \approx \sqrt{N_{\lambda,j}}$, and so $\delta I_{\lambda,j} \approx I_{\lambda,j}/\sqrt{N_{\lambda,j}}$. A secondary error source is flux contamination from neighboring pixels. To include this error, we use the 5% estimate of Ref. [85], calculate the 'leakage' contribution to noise at each pixel by taking the mean flux of all the nearest neighboring pixels, and multiply it by 5%. We also use time-logged measurements of the CCD bias and dark-current, with the appropriate integration time, to calculate the additional noise from these sources.[5] Finally we estimate the flat-fielding noise using the rms difference between different sets of efficiency tables. These errors are added in quadrature to obtain a data cube of the estimated errors in specific intensity.

In Refs. [10, 11], slit locations were chosen to avoid the locations of known galaxies, as well as regions that showed statistical evidence for faint galaxies [136]. Likewise, we masked out IFU fibers that fell on the locations of individual bright sources. Bright sources were identified in each

[5] `http://www.eso.org/observing/dfo/quality/VIMOS/toc.html`.

cluster image by tagging pixels where the image intensity exceeded the median by more than 1σ and masking IFU fibers that fell on these pixels. Practically, this means that 40% of the fibers in each data cube are left unmasked. The images used to generate this mask are broadband, and so this masking technique will not mask out an axion-decay signal. The accidental inclusion of galaxies could conceivably lead us to erroneously attribute their emission to axion decay. This is unlikely, given that the spectra of cluster galaxies are dominated by continuum emission and line absorption. If we see an indication of emission due to line decay, however, we may have to revise our masking criteria to take account of this possibility. As we shall see later, we imposed upper limits to axion decay, and can safely use the chosen masking criterion. The resulting masks were visually inspected to verify that most of the masked fibers fall near galaxies. To extract the density dependent component of the cluster spectra, we apply a mass map obtained from gravitational lensing observations.

2.5 Analysis

2.5.1 Strong Lensing and Cluster Mass Maps

To model the mass distribution of A2667 and A2390, we used both a cluster mass-scale component (representing the contribution of the dark-matter halo and the intracluster medium) and cluster-galaxy mass components as in Refs. [83, 137]. Cluster galaxies were selected according to their redshift (when available, in the inner cluster region covered with VIMOS spectroscopy) or their color, thus selecting galaxies belonging to the cluster red sequence. For A2667, ISAAC images were used to determine J-H colors, whereas for A2390, HST images were used to determine I-V colors. The lensing contribution from more prominent foreground galaxies was also included, rescaling their lensing properties using the appropriate redshift.

All model components were parameterized using a smoothly truncated pseudo-isothermal mass distribution model (PIEMD) [138], which avoids both the unphysical central-density singularity and the infinite spatial extent of the singular isothermal model.

The galaxy mass components were chosen to have the same position, ellipticity and orientation as their corresponding images. The K-band luminosity of the galaxies was computed, assuming a typical E/S0 spectral energy distribution (redshifted but uncorrected for evolution of constituent stellar populations). Their masses were estimated using the K-band luminosity, calculated assuming a global mass to light ratio (M/L) and the Faber-Jackson relation [139]. The final mass model is made of 70 components, including the large scale cluster halo and the individual galaxies. Using the `LENSTOOL` ray-tracing code [140] with the HST images, we iteratively implemented the constraints from the gravitational lenses. Lensing mass models with $\chi^2 \leq 1$ were found by fitting the ellipticity, orientation, center, and mass parameters (velocity dispersion, core radius, and truncation radius) of the cluster scale component, as well as the truncation radius and velocity dispersion of the ensemble

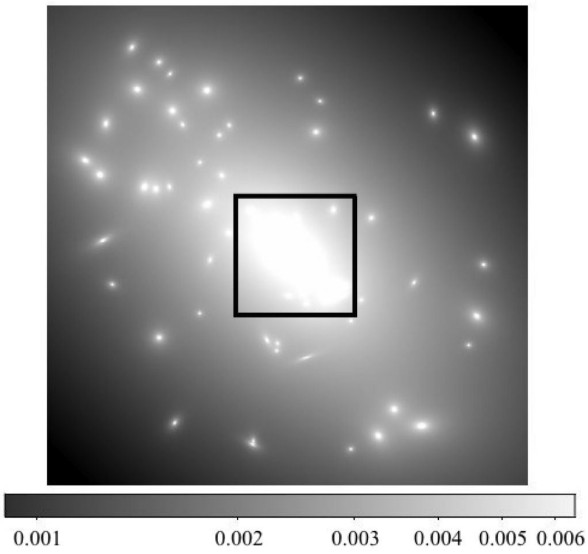

Figure 2.9 Mass map of A2667. The intensity of the image scales with density (in units of $10^{12} M_{\odot}$ pix^{-2}), where 1 pix = 0.50". A density scale is provided on the bottom of the image. The horizontal extent of this map is 222.6". The vertical extent is 200.0". The thick black line indicates the spatial extent of the IFU head on the mass map.

of cluster galaxies, using scaling relations for early-type galaxies [141]. Cluster galaxy redshifts were measured using the IFU data [131]. The bright central galaxy and several galaxies near the locations of strong-lensing arcs were modeled separately from the ensemble. The resulting cluster density maps for A2667 and A2390 are shown in Figs. 2.9 and 2.10 [131, 132]. Statistical errors in the mass model parameters were propagated through the relevant code to produce a fiber by fiber map of statistical errors in Σ. These maps were then used to weight different IFU fibers and thus maximize the signal to noise ratio of any putative line emission from axion decay.

2.5.2 Extraction of One Dimensional Spectra

Using density maps of A2667 and A2390, we can optimally weight averages over fibers to maximize the contribution from high density regions of the cluster. This maximizes the signal to noise ratio of our axion search by emphasizing IFU fibers where maximum signal from axion decay is expected. These maps allow us to separate emission correlated with the mass profile of the cluster, which could be due to axion decay, from a sky background that we assume to be spatially homogeneous. Our technique is an IFU generalization of the long-slit 'on-off' sky-subtraction technique presented in Refs. [10, 11]. The real sky background is certainly not perfectly homogeneous, but by making this assumption, we are being maximally conservative. With our reduction method, any density correlated spatial dependence in the sky background will show up as putative emission from axion

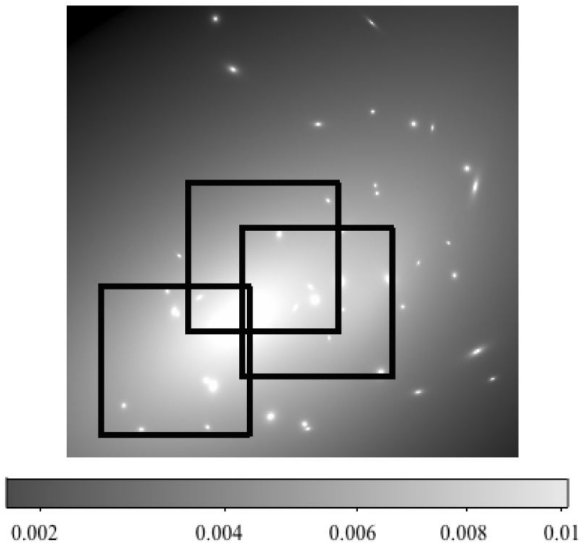

Figure 2.10 Mass map of A2390. The intensity of the image scales with density (in units of $10^{12} M_{\odot}$ pix^{-2}), where 1 pix = 0.50". A density scale is provided on the bottom of the image. The horizontal spatial extent of the map is 157.5". The vertical extent is 150.0". The thick black lines indicate IFU pointings used to construct our data cubes.

decay. If evidence for a signal is seen, we will have to be careful to avoid being confused by sky line emission. The projected surface density of the cluster at the location in the lens plane associated with the i^{th} fiber is denoted $\Sigma_{12,i}$. Assuming that the only spatially dependent signal comes from axions, we can then model the actual intensity $I^{\text{mod}}_{\lambda,i}$ at a given wavelength λ and spatial pixel i as $I^{\text{mod}}_{\lambda,i} = \langle I_{\lambda}/\Sigma_{12}\rangle \Sigma_{12,i} + b_{\lambda}$, where b_{λ} represents the contribution of a spatially homogeneous sky signal, and $I_{\lambda,i}$ is the specific intensity in the i^{th} fiber at wavelength λ. Since the signal from axion decay is bounded from above by the total component of the signal proportional to $\Sigma_{12,i}$, a measurement of $\langle I_{\lambda}/\Sigma_{12}\rangle$ will either provide evidence of axion decay, or impose an upper limit on $\langle I_{\lambda}/\Sigma_{12}\rangle_{\text{axion}}$. Using a simple linear fit to separate the sky background from signal, we extract the array $\langle I_{\lambda}/\Sigma_{12}\rangle$ from each cluster data cube.

At a small number of wavelengths, this yielded negative (unphysical) values for one or both fitted parameters. To avoid this, we fit for $\langle I_{\lambda}/\Sigma_{12}\rangle$ and b_{λ}, subject to the obvious constraints $\langle I_{\lambda}/\Sigma_{12}\rangle \geq 0$ and $b_{\lambda} \geq 0$, estimating errors $\sigma_{\lambda,i}$ as described in Section 2.4.3. Estimated errors in Σ_{12} were also included in the fit. Residuals from the best fit are due to flux noise, imperfect masking of galaxies, and variations in fiber efficiency unaccounted for by the flat-fielding procedure. As can be seen directly from the unconstrained linear-least-squares solutions for the parameters $\langle I_{\lambda}/\Sigma_{12}\rangle$ and b_{λ}, this procedure places higher weights on those VIMOS fibers that fall on higher density portions of the cluster. In essence, we used our knowledge of the cluster density profile to extract only the information that interests us, namely, that part of the emission that is correlated with the

cluster's mass density profile. At some wavelengths, the best fit is $\langle I_\lambda/\Sigma_{12}\rangle = 0$ with very low noise. We verified that these wavelengths coincide with those at which a naive linear fit yielded negative values for $\langle I_\lambda/\Sigma_{12}\rangle$. Thus there is no evidence for density correlated emission at these wavelengths. At these wavelengths, the emission due to axion decay is bounded from above by the brightness of the sky background, and so we used $\langle I_\lambda/\Sigma_{12}\rangle \leq b_\lambda/\langle\Sigma_{12}\rangle$ to obtain a conservative upper limit on the flux. Decaying axions will produce line emission, so it might seem that an additional continuum subtraction might be in order. The continuum component of the sky background, however, is already subtracted using the techniques discussed, and an additional continuum subtraction step would be erroneously aggressive.

As a test of our sky-subtraction technique, we also reimplemented the sky-subtraction technique of Ref. [11] and implemented an 'on-off' subtraction by defining fibers further than $23''$ (A2667) or $72''$ (A2390) from the cluster center (defined by the highest density point in the density maps) as 'sky' fibers, spatially averaging the flux of these sky fibers at each wavelength, and subtracting the resulting sky spectrum from each pixel in the 'on' cluster region. In this case, sky emission was directly estimated from the data rather than modeled. In this case, the best fit for the signal is given by

$$\left\langle \frac{I_\lambda}{\Sigma_{12}} \right\rangle = \frac{\sum_i \frac{I_{\lambda,i}\Sigma_{12,i}}{\sigma^2_{\lambda,i}}}{\sum_i \frac{\Sigma^2_{12,i}}{\sigma^2_{\lambda,i}}}, \tag{2.30}$$

where i is a label for the density at the location of a given IFU fiber, and $\sigma_{\lambda,i}$ is the error in the specific intensity.

In the case of A2667, even the fibers furthest from the cluster center fall on portions of the cluster where emission due to axion decays will be of the same order of magnitude as at the center. The sky-subtraction technique of Ref. [11] is thus entirely inappropriate for our data on A2667, as it will subtract out a substantial fraction of any signal and return unjustifiably stringent limits to emission from axion decay.

For A2390, the effective field of view is much larger, and so the emission expected from axion decays in the outer fibers is much less. Over most of the wavelength range of our data for A2390, the different sky-subtraction techniques agreed to within a factor of two, leading us to believe that our sky-subtraction technique is trustworthy. We used the value for $\langle I_\lambda/\Sigma_{12}\rangle$ obtained using our sky-subtraction technique, as it is desirable to use the same sky-subtraction method for both clusters to be self-consistent. Equation (2.30) and the corresponding best-fit result in the constrained case essentially yield one-dimensional cluster spectra, rescaled by the cluster density, as shown in Figs. 2.11 and 2.12. The specific intensity values in Fig. 2.11 were obtained by multiplying the best-fit values of $\langle I_\lambda/\Sigma_{12}\rangle$ from Eq. (2.30) by the mean $\langle\Sigma_{12}\rangle = \left(\sum_i \Sigma_{12,i}/\sigma^2_{\lambda,i}\right) / \left(\sum_i 1/\sigma^2_{\lambda,i}\right)$. The plotted spectrum is thus not the best-fit spectrum at any particular fiber, but an average cluster spectrum. The signal to noise ratio of the one-dimensional spectrum appears to be higher for A2667

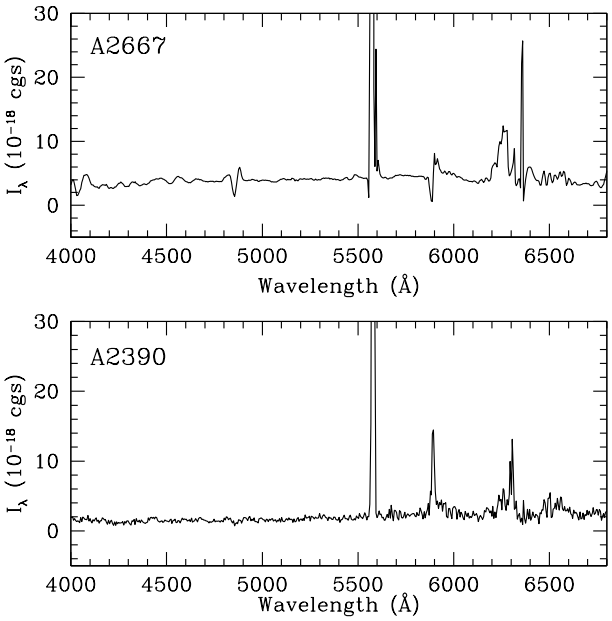

Figure 2.11 Average one-dimensional sky subtracted spectra of clusters A2667 and A2390. Intensity is in units of 10^{-18} ergs cm^{-2} s^{-1} Å^{-1} arcsec^{-2}. Poorly subtracted sky emission lines at 5577Å, 5894Å, and 6300Å have not been removed.

than for A2390, in spite of the lower effective fiber number of the data cube for A2667. We believe that this is the case because the data cube for A2390 was built using four nights of data, with slight variations in sky intensity and efficiency from night to night. The subtraction is poorest around the prominent sky line at 5577Å. There is no obvious candidate for an emission line due to axion decay.

2.5.3 Limits on the two-photon coupling of axions

The expected strength of an axion decay line is set by $m_{\rm a,eV}$ through Eq. (2.29), and the expected Gaussian line profiles are shown on top of our appropriately normalized upper limits to flux in Fig. 2.12 for several candidate axion masses. The narrow feature at 5577Å, present in both panels of Fig. 2.12, arises from the imperfect subtraction of a sky emission line. In the absence of a candidate axion decay line, we proceed to put an upper limit on the coupling strength ξ of an axion to two photons.

Since our best-fit values for $R_\lambda \equiv \langle I_\lambda/\Sigma_{12}\rangle$ at each wavelength come with an error estimate σ_λ, we can calculate a 95%-confidence limit to the line flux. We assume that the distribution of noise peaks is Gaussian, and so the probability that an axion decay associated with a particular value of $R_{{\rm a},\lambda}$ yields a measured best-fit value less than R_λ is

$$P_\lambda = \frac{1}{\sqrt{2\pi}\sigma_\lambda}\int_{-\infty}^{R_\lambda - R_{{\rm a},\lambda}} e^{\frac{-x^2}{2\sigma_\lambda^2}}\,dx. \tag{2.31}$$

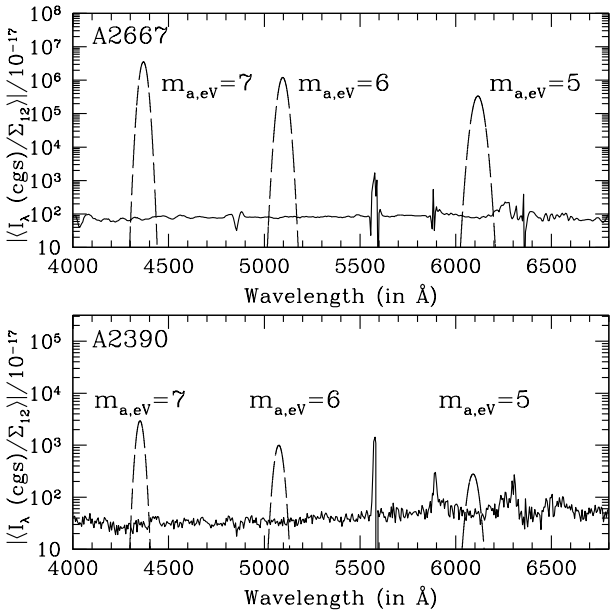

Figure 2.12 Constraints on $\langle I_\lambda/\Sigma_{12}\rangle$ as a function of wavelength λ for A2667 and A2390. CGS units for specific intensity are ergs cm^{-2} s^{-1} Å^{-1} arcsec^{-2}, and $\Sigma_{12} = \Sigma/(10^{12} M_\odot \text{ pix}^{-2})$, where Σ is the projected mass density of the cluster, measured using strong lensing. The over-plotted dashed lines are theoretical Gaussian spectra for axion decays, with central wavelength λ_0, corresponding to an axion mass of $m_{\rm a,eV} = 24,800\text{Å}(1+z)/\lambda_0$. The predicted amplitude is set by Eq. (2.29), and exceeds the measured values in both the top panel ($\xi = 1.0$) and the bottom panel ($\xi = 0.03$).

Eq. (2.31) yields the 95%-confidence limit on intensity from axion decay:

$$R_{\rm a,\lambda} \leq R_\lambda + 1.65\sigma_\lambda. \tag{2.32}$$

At those wavelengths where the best-fit value is $R_\lambda = 0$, we have taken the roughly homogeneous intensity of the sky as a very conservative upper limit on the intracluster emission. This is many σ above the 95%-confidence limit, and so at these wavelengths, we just take $R_{\rm a,\lambda} \leq R_\lambda$ without making our estimate of the upper limit too conservative. Ultimately, we wish to combine the upper limits to flux from the two clusters. One of the advantages of working with two clusters at slightly different redshifts is that rest-frame wavelengths falling near sky lines (where limits to flux are generally quite poor) at one redshift may no longer fall on sky emission lines at the redshift of the second cluster. When this is the case, we excise wavelengths falling on or near sky lines from each spectrum. To account for all the flux in a given candidate axion line, in each cluster spectrum, we calculate the average intensity of non-excised data points in a $24,800\,[(1+z)\sigma/c]$ Å $m_{\rm a,eV}^{-1}$ window around a series of putative line centers spanning the probed axion mass range. We weight the noise in the usual way. Assuming that our spectra uniformly sample this bin and that flux errors are uniform across

the bin, we see by integrating the Gaussian profile given in Eq. (2.29) that

$$R_{\mathrm{a},\lambda} = \frac{2.30 \times 10^{-18}\ \xi^2 m_{\mathrm{a,eV}}^7}{(1+z_{\mathrm{cl}})^4 S^2(z_{\mathrm{cl}})\sigma_{1000}}\ \mathrm{cgs}. \tag{2.33}$$

If axions have the standard thermal-freezeout abundance [Eq. (2.16)], then the limit on the axion coupling is given by

$$\xi \leq \left[\frac{\sigma_{1000}(1+z_{\mathrm{cl}})^4 S^2(z_{\mathrm{cl}}) m_{\mathrm{a,eV}}^{-7}(\lambda) R_{\mathrm{a},\lambda}}{2.30\times10^{-18}\ \mathrm{cgs}}\right]^{1/2}. \tag{2.34}$$

If the cosmological axion abundance takes on some other value $\Omega_{\mathrm{a}}h^2$, then the limit becomes

$$\xi\sqrt{\Omega_{\mathrm{a}}h^2} \leq \left[\frac{\sigma_{1000}(1+z_{\mathrm{cl}})^4 S^2(z_{\mathrm{cl}}) m_{\mathrm{a,eV}}^{-6}(\lambda) R_{\mathrm{a},\lambda}}{3.48\times10^{-16}\ \mathrm{cgs}}\right]^{1/2}. \tag{2.35}$$

Since our real bins are not uniformly sampled (because of the excision of wavelengths that fall on sky emission lines) and since the errors scale with the intensity value at a given wavelength, we make a small correction to this expected value. Specifically,

$$R_{\mathrm{a},\lambda} = \frac{2.68 \times 10^{-18}\ \xi^2 m_{\mathrm{a,eV}}^7}{(1+z_{\mathrm{cl}})^4 S^2(z_{\mathrm{cl}})} \frac{\sum_{j\in T_\lambda} \frac{G_j}{\sigma_j^2}}{\sum_{j\in T_\lambda} \frac{1}{\sigma_j^2}}\ \mathrm{cgs},$$
$$\text{where } G_j = e^{-\frac{(\lambda_j/(1+z_{\mathrm{cl}})-\lambda_{\mathrm{a}})^2 c^2}{2\sigma^2\lambda_{\mathrm{a}}^2}}. \tag{2.36}$$

Here T_λ is the set of all non-excised wavelengths lying within the bin centered at wavelength λ, and j labels wavelengths. The quality of sky background subtraction may vary as a result of spatial and temporal variations in the sky background from night to night. If it is not due to axion decay, the density correlated emission might also genuinely vary between clusters. The quantity $R_{\mathrm{a},\lambda}$, however, will by definition be independent of these factors. A simple error weighted mean of the upper limits obtained from the two clusters would thus erroneously increase the upper limit placed on ξ. If two clusters yield different best-fit values for R_λ, $R_{\mathrm{a},\lambda}$ must be bounded from above by the lesser of these two. By comparing upper limits to R_λ obtained from A2390 with those obtained from A2667 and choosing the lowest value at each wavelength, we obtained the maximum values of $R_{\mathrm{a},\lambda}$ consistent with the data. We then applied Eq. (2.36) to obtain an upper limit on ξ consistent with the spectra of both clusters. To account for variation in the upper limits to ξ arising from systematic errors in the cluster mass profiles, we repeated the preceding analysis, drawing $\Sigma_{12,i}$ from the best-fit NFW (Navarro, Frenk, and White) and King profiles to the cluster mass profiles.

Analytic expressions for the volumetric and surface mass density for NFW and King profiles are reviewed in Appendix A. We determined the mass profile parameters (a and σ for King profiles, c and σ for NFW profiles) by fitting to our strong-lensing density maps. Using these different density profiles and assuming that the mass fraction in axions is $x_{\mathrm{a}} = \Omega_{\mathrm{a}}h^2/(\Omega_{\mathrm{m}}h^2)$, we obtain limits to

ξ. The cluster density at the location of a given IFU fiber varies from profile to profile, and so different fibers receive higher weights when a one-dimensional spectrum is extracted. This explains the variation in upper limits to ξ that arises when different density profiles are assumed. We show the most conservative (with respect to choice of density profile) limit on ξ (assuming the thermal-freezeout abundance of axions) at each candidate axion mass in Fig. 2.13. The upper limits to ξ in adjacent points along the $m_{\rm a,eV}$ axis are correlated due to overlapping bins. The narrow black arrows near $m_{\rm a,eV} = 5.43$ and 4.83 mark sharp night-sky lines at $\lambda = 5577$Å and $\lambda = 6300$Å, where sky subtraction is unreliable and useful limits to ξ cannot be obtained. Limits on ξ and specific intensity at the putative line center are displayed for several candidate masses in Table 2.1. Our data rule out the standard ($E/N = 0$ and $E/N = 2$) hadronic and DFSZ axion models in the mass window $4.5 \leq m_{\rm a,eV} \leq 7.7$, as seen in Fig. 2.14. However, theoretical uncertainties motivate the search for axions with values of ξ smaller than those allowed by the standard hadronic and DFSZ models.

If we relax the assumption that the cosmological axion abundance be given by Eq. (2.16), then our null search implies the bound, shown in Fig. 2.15, to the combination $\xi(\Omega_{\rm a}h^2)^{1/2}$. We see that if $\xi \sim 10^{-1}$, as is the case in the $E/N = 2$ hadronic model, then our results imply an upper limit $\Omega_{\rm a}h^2 \lesssim 10^{-4}$ in our mass range, roughly two orders of magnitude stronger than CMB/LSS limits [6], which probe densities down to $\Omega_{\rm a}h^2 \sim 10^{-2}$. Using Fig. 3.4, we see that if $E/N = 2$ hadronic axions exist, $T_{\rm rh} \ll 10$ MeV, imposing a very stringent constraint on the thermal history of the early universe. We discuss this further in Chapter 3.3.

2.5.4 Revision of past telescope constraints to axions

As can be seen from Eq. (2.29), and from the fact that the mass fraction of the cluster in axions is $x_{\rm a} = \Omega_{\rm a}h^2/(\Omega_{\rm m}h^2)$, the upper limit on ξ derived from a given upper limit on flux depends on the cluster mass model used and the cosmological parameters assumed. References [10, 11] date to a time when the observationally favored cosmology was sCDM (Standard Cold Dark Matter: $h = 0.5$, $\Omega_{\rm m} = 1.0$, $\Omega_\Lambda = 0$). Moreover, the King profiles assumed in those analyses of A2218, A2256, and A1413 were based on available x-ray emission profiles of the chosen clusters [10, 11] (and references therein). The advent of modern x-ray instruments has improved x-ray-derived cluster mass profiles, and gravitational-lensing studies have allowed measurements of cluster mass profiles, free of the dynamical assumptions required to obtain a density profile from an x-ray temperature map. The quoted upper limits of Refs. [10, 11] must thus be rescaled, and we have done so up to an ambiguity in slit placement for A2218; details are discussed in Appendix B and the rescaled limits from past work are shown alongside our own in Fig. 2.13. Our limits improve on the rescaled limits of Ref. [10, 11] by a factor of $2.1 - 7.1$. Our final measurement of $\langle I_\lambda/\Sigma_{12}\rangle$ is only noise limited at a small fraction ($\simeq 10\%$) of the available wavelength range. The dominant uncertainty is systematic and

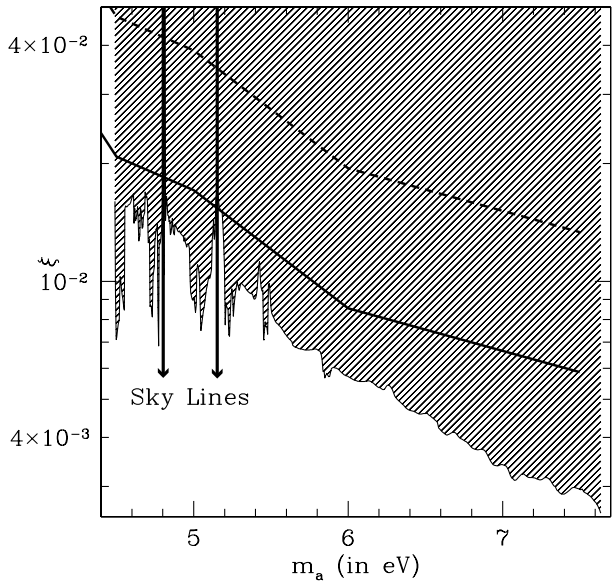

Figure 2.13 Upper limits to the two-photon coupling parameter ξ of the axion, derived directly from upper limits to the intracluster flux of A2667 and A2390. Our data exclude the shaded region. The solid and dashed lines show the upper limits reported in Refs. [10, 11], adjusted (optimistically and pessimistically) for differences between today's best-fit measurements of the cosmological parameters/cluster mass profiles and the assumptions in Refs. [10, 11]. Details are discussed in Appendix B. The mass range 4.5 eV $\leq m_{\rm a} \leq$ 7.7 eV arises from the 4000Å–6800Å usable wavelength range of VIMOS, which is smaller than that of the KPNO spectrograph used in Ref. [11]. The narrow black arrows near 5.43 eV and 4.83 eV mark the sharp night-sky lines at 5577Å and 6300Å, where sky subtraction is unreliable and useful limits to ξ cannot be obtained. The shaded exclusion region is derived by applying the cluster density profile (strong-lensing map, best-fit NFW profile, or best-fit King profile) at each candidate axion mass that yields the most conservative upper limit on ξ.

comes from sky subtraction. The expected improvement estimated in the introduction assumed that we are limited by Poisson noise in the measured flux, and is thus naive.

Previous cluster searches for axions used long-slit spectroscopy. Our use of IFU data is novel, and it is conceivable that peculiarities of the data-reduction techniques used in IFU spectroscopy may affect the sensitivity of our search. To explore this possibility, we have conducted a simulation.

2.5.5 Simulation of Analysis Technique

We simulate axion-decay emission in our data cube for A2667, using Eq. (2.29) and our lensing derived projected density maps. We did this at a range of 10 candidate axion masses spanning the full mass range of our search. We used 3 or 4 different values of ξ at each candidate mass. The first value was chosen to be slightly below $(5-10\%)$ the limit on ξ set by preceding techniques, while the second was chosen to be slightly above the upper limit. The third and fourth values were chosen to be in considerable (factors of 2 and 10, respectively) excess of the upper limit. For all simulated

Table 2.1 Upper limits to central line intensity and ξ at several candidate axion masses, derived directly from sky subtracted spectra of A2667 and A2390.

$m_{\mathrm{a,eV}}$	$\langle I_\lambda/\Sigma_{12}\rangle\,\langle\Sigma_{12}\rangle$ (cgs)	ξ
4.5	1.83×10^{-19}	7.17×10^{-3}
5	6.04×10^{-19}	9.00×10^{-3}
6	8.74×10^{-19}	5.72×10^{-3}
6.5	9.91×10^{-19}	4.60×10^{-3}
7	9.13×10^{-19}	3.41×10^{-3}
7.5	1.11×10^{-18}	2.95×10^{-3}
7.65	8.96×10^{-19}	2.47×10^{-3}

axion masses, visual inspection of the data cube yields clear evidence for the inserted line when ξ exceeds the imposed upper limit. An example is shown in Fig. 2.16. After inspecting the data cubes visually, we applied the routines used for the preceding analysis to produce one-dimensional spectra for each cube. We then applied the same routine used to extract upper limits to ξ to recover the simulated ξ value. When the simulated value of ξ exceeded the upper limit, we recovered the correct answer in all cases to a precision of $5-10\%$. This leads us to believe that our technique is robust and our upper limits reliable. References [10, 11] supplement upper limits to ξ derived directly from flux limits with limits obtained from a cross-correlation analysis. We do the same, using our data on A2667 and A2390.

2.5.6 Cross-Correlation Analysis

If there is an emission line at the same wavelength in the rest frame of both clusters, the function

$$g(l)=\frac{\int I_1(x)I_2(x+l)dx}{\left[\int I_1^2(x)dx\int I_2^2(x)dx\right]^{1/2}}, \tag{2.37}$$

will have a peak at the lag $l_0=\ln\left[(1+z_{\mathrm{a2667}})\,/\,(1+z_{\mathrm{a2390}})\right]$, where $x=\ln\lambda$, $I_1(x)$ and $I_2(x)$ are the specific intensities of galaxy clusters A2667 and A2390, and z_{a2667} and z_{a2390} are their redshifts [10, 11]. A statistically significant peak in $g(l)$ would indicate the existence of an intracluster emission line at unknown wavelength (and correspondingly unknown axion mass), which could then be searched for more carefully in the individual spectra. Peaks due to noise may arise either due to the roughly Gaussian fluctuations in flux of the individual spectra, or due to imperfectly subtracted flux around sharp sky emission lines. It is thus appropriate to mask out bright sky lines. If we assume that the distribution of remaining noise peaks is Gaussian, then the probability that a

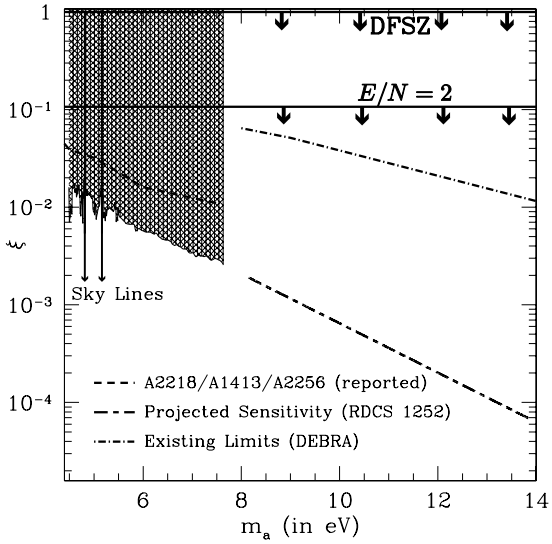

Figure 2.14 Comparison of existing limits to the two-photon coupling of a 4.5 eV − 14 eV axion with the projected sensitivity of our proposed observations of lensing cluster RDCS 1252 ($z = 1.237$). Flux limits and density profiles were assumed to be the same as those of A2667/A2390. The best existing upper limits to ξ in the higher mass window come from limits to the Diffuse Extragalactic Background Radiation (DEBRA), and were rescaled for consistency with today's best-fit ΛCDM parameters and recent measurements [51, 64]. The limits reported in this and previous work, derived using optical spectroscopy of galaxy clusters, are shown for comparison [10, 11]. Regions inaccessible due to night-sky emission lines are marked with narrow black arrows. The two solid horizontal lines indicate the predictions of the $E/N = 2$ hadronic and DFSZ axion models; the downward arrows indicate that ξ is *theoretically* uncertain.

cross-correlation peak with height greater than or equal to s is due to noise is [10, 11]

$$P(\geq s) = \int_s^\infty \frac{e^{-x^2/(4\sigma_g^2)} dx}{\sqrt{\pi}\sigma_g} = 1 - \mathrm{Erf}\left(\frac{s}{2\sigma_g}\right). \tag{2.38}$$

Here, σ_g is the rms value of the antisymmetric component of $g(l)$ and provides an estimate of the correlation due to noise, since a Gaussian signal leads to a symmetric correlation function [10, 142]. Equation (2.38) determines the statistical significance of peaks in $g(l)$. Our analysis of correlated spectra follows the treatment of Ref. [142]. We calculate $g(l)$ using the sky subtracted one-dimensional spectra of A2667 and A2390. With a cross-correlation technique, we are able to perform a blind search for cluster rest-frame emission. We find no statistically significant ($> 2\sigma_g$) cross-correlation peaks, as shown in Fig. 2.17.

We simulate our cross-correlation based search for an intracluster line in order to set alternative upper limits to ξ [10, 11]. The limits reported in Ref. [11] were obtained using this technique. In our simulation, we introduced 'fake' axion decay lines into both spectra and calculated the resulting $g(l)$ for a variety of values $m_{\mathrm{a,eV}}$, thus simulating the cross-correlation search for evidence of intracluster emission. ξ was initially set to a value for which a very significant peak in $g(l)$ appeared, and then

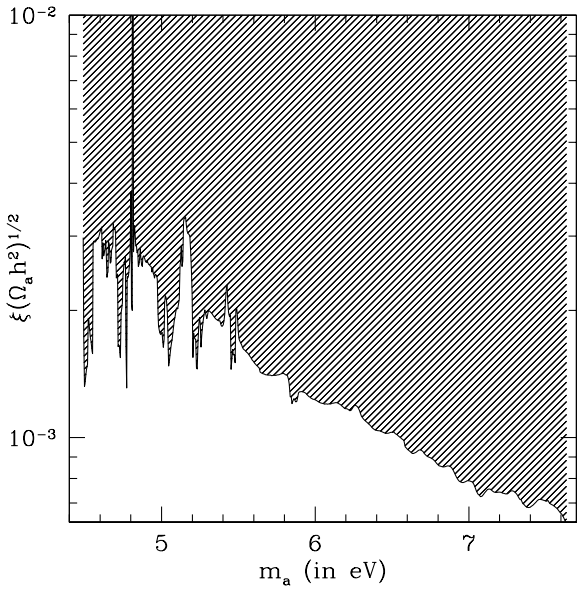

Figure 2.15 Limits on the combination $\xi\left(\Omega_{\rm a}h^2\right)^{1/2}$, derived directly from upper limits to the intracluster flux of A2667 and A2390. Our data exclude the shaded region. Data analysis proceeds as in the thermal case, but appropriate (more general) expressions for the intensity I_λ are used. These constraints do not depend on the assumption that axions are produced thermally at early times.

ramped down until the peak at l_0 ceased to be statistically significant; that is, until $P(s) > 5\%$. At that point, an upper limit on ξ was set. The cross-correlation peaks due to the axion line are well fit by Gaussian curves throughout the $m_{\rm a,eV} - \xi$ parameter space. Since the cross-correlation function includes the contribution of flux away from the line center, rebinning was unnecessary.

To further distinguish between signal and noise peaks, we follow Ref. [10] in using the usual criterion, $|l - l_0| \leq \sigma$, where σ is the width of the best Gaussian fit to $g(l)$ around a cross-correlation peak. We use this criterion in both the simulation and the cross-correlation search [10]. The resulting limits to ξ at a series of candidate axion masses are shown in Table 2.2, and are on average a factor of ~ 1.5 less stringent than those derived directly from flux.

One aspect of the correlation analysis of Ref. [10] is troubling. Two noisy, imperfectly sky subtracted spectra were correlated to search for a signal. The analysis of Ref. [10], however, uses one real spectrum (containing noise and an imperfectly subtracted sky-background signal) with an artificial axion line inserted, and a second, noiseless, template spectrum, containing only the artificial axion line, but no imperfectly subtracted sky component. Thus, the method simulated in Ref. [10] is not the same as the method used to actually search for evidence of an intracluster line, and by artificially reducing the noise budget of the simulation, could lead to artificially stringent constraints. The appropriate way to simulate the cross-correlation analysis is to correlate two real spectra with artificial axion lines inserted, as we have done. Our data also place limits on the decay of other

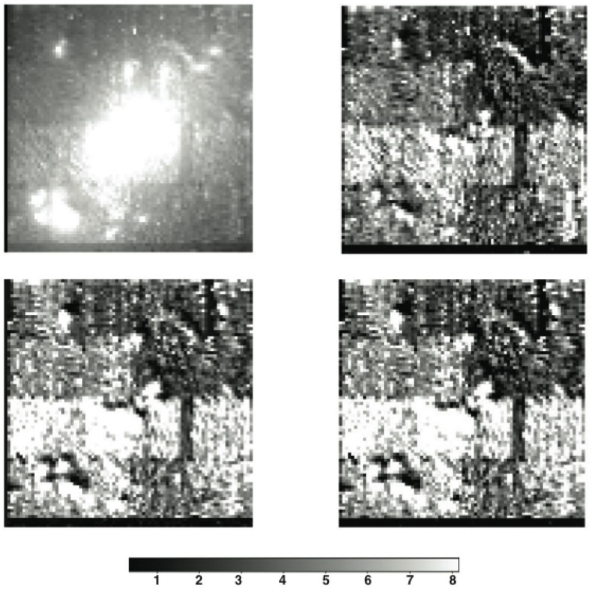

Figure 2.16 The upper left panel of this figure shows a simulated 4255.2Å slice of the A2667 IFU data cube, with an axion-decay emission line inserted corresponding to $m_{\rm a,eV} = 7.2$ and $\xi = 0.011$. The flux scale is in units of 10^{-18} erg s^{-1} cm^{-2} Å^{-1}. This slice, which lies at the expected line center, shows evidence of the inserted axion line. The resulting 'emission' clearly traces the cluster mass density profile. The lower left panel of this figure shows a simulated slice of the same data cube, but at 5267.2Å, well away from the line center. As expected, no signature of axion emission is present this far away in wavelength from the line center. The upper/lower right panels of this figure show 4255.2Å/ 5267.2Å slices, respectively, of the actual A2667 IFU data cube used for our analysis.

relics.

2.5.7 Sterile neutrinos

Our data might also be used to constrain the decay rate of other $\sim$ 5 eV relics, such as sterile neutrinos [79–82]. Although the prevailing paradigm places the sterile-neutrino mass in the keV range, some experimental data can be fit by introducing a hierarchy of sterile neutrinos, at least one of which is in the $1-10$ eV range and could oscillate to produce photons in our observation window [143, 144]. In our notation and in the $m_{e^-,\mu,\tau} \ll m_s$ limit (where m_s is the sterile-neutrino mass), the intensity of this signal is

$$\left\langle \frac{I_{\lambda,\rm s}}{\Sigma_{12}} \right\rangle = 2.4\times10^{-18}\frac{B m_{s,\rm eV}^8 \exp\left[-\left(\lambda_r-\lambda_{\rm s}\right)^2 c^2/\left(2\lambda_{\rm s}^2\sigma^2\right)\right]}{\sigma_{1000}(1+z_{\rm cl})^4 S^2(z_{\rm cl})}{\rm cgs}, \tag{2.39}$$

where B is a model-dependent normalization factor, the oscillation is parameterized by a cumulative mixing angle θ, and the additional power of mass arises from the late-time abundance of sterile

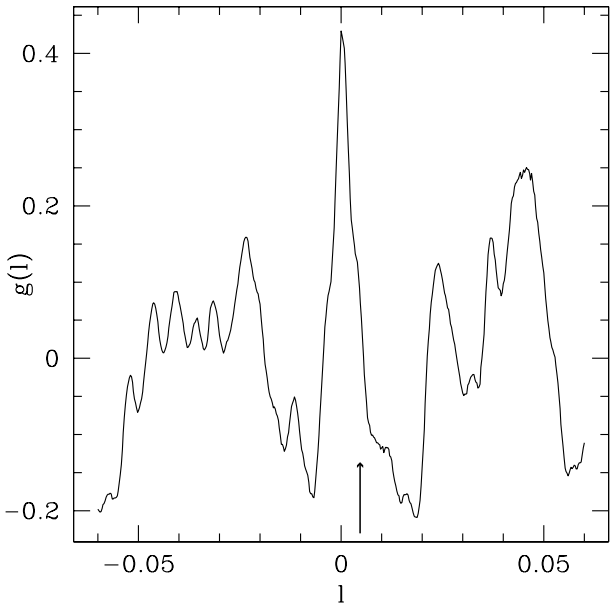

Figure 2.17 Cross-correlation function $g(l)$ between sky subtracted spectra of clusters A2667 and A2390. No peaks with the desired statistical significance were seen, at the desired lag or elsewhere. A single cross-correlation peak is near the expected lag $l = 0.00498$ for an intracluster emission line common to A2667 and A2390. However, it is not statistically significant.

neutrinos [145]:

$$\Omega_{\rm s} h^2 = 0.3 \times m_{s,{\rm eV}}^2 \sin^2 2\theta. \tag{2.40}$$

The flux limits in Table 2.1 impose the constraints $B \leq 8.03 \times 10^{-5},\ 1.14 \times 10^{-4},\ 9.41 \times 10^{-5},\ 3.82 \times 10^{-5},\ 2.28 \times 10^{-5}, 1.16 \times 10^{-5},\ 8.12 \times 10^{-6}$, and 5.61×10^{-6} for sterile-neutrino masses of $m_{s,{\rm eV}} = 4.50,\ 5.00,\ 5.50,\ 6.00,\ 6.50,\ 7.00,\ 7.50$, and 7.65, respectively. In conventional models, $B = \sin^4(2\theta)/10^{11}$. The parameter B encodes the effects of both the early-universe production and the decay of sterile neutrinos, which occurs at the rate $\Gamma_{s\rightarrow\nu+\gamma} = 6.8 \times 10^{-38} s^{-1} m_{s,{\rm eV}}^5 \sin^2 2\theta$ [146–149]. By definition, $B \leq 10^{-11}$, and so optical data only constrain sterile neutrinos if some novel mechanism increases the oscillation rate $\Gamma_{s\rightarrow\nu+\gamma}$ by many orders of magnitude. The sharp disparity between x-ray and optical constraints results from the $\Gamma \propto m_s^5$ scaling of the decay rate.

2.5.8 Ongoing Work

We have demonstrated the utility of applying integral field spectroscopy in concert with lensing data to search for axions in $z \simeq 0.2$ galaxy clusters. Our technique could also be profitably applied to higher redshift galaxy clusters. Although flux falls off as $I_\lambda \propto (1 + z_{\rm cl})^{-4}$, the fact that we are pushing to a higher mass range $m_{\rm a,eV} = 24,800 {\rm \AA}\,(1 + z_{\rm cl})\,/\lambda_{\rm a}$ increases the expected signal. Since $I_\lambda \propto m_{\rm a,eV}^7$, the expected signal actually increases as $I_\lambda \propto (1 + z_{\rm cl})^3$. The most distant known lensing cluster is RDCS 1252, at redshift $z = 1.237$ [150].

Table 2.2 Upper limits to ξ at several candidate axion masses, obtained from a simulation of the cross-correlation method, using spectra of A2667 and A2390.

$m_{\mathrm{a,eV}}$	ξ
4.5	2.73×10^{-2}
5	1.08×10^{-2}
6.0	9.35×10^{-3}
6.5	6.90×10^{-3}
7	4.44×10^{-3}
7.5	4.31×10^{-3}
7.65	2.16×10^{-2}

Using existing weak-lensing mass maps for this cluster [151] and creating our own strong-lensing maps, we should be able to obtain a sky subtracted, spatially weighted spectrum of this cluster, attaining flux levels similar to those we have obtained for A2667 and A2390. We will thus be able to search for emission from decaying axions in the mass window 8 eV $\leq m_{\mathrm{a}} \leq$ 14 eV. Assuming identical cluster density profiles and flux limits, we estimate the range of ξ values accessible with a telescope search for cluster axions in RDCS 1252. The tightest existing constraints to decaying relic axions in this mass window come from limits to the diffuse extragalactic background radiation (DEBRA) [51, 64]. As shown in Fig. 2.14, a VIMOS IFU search for axions in this mass window would detect very weakly coupled axions, or alternatively, improve upper limits to ξ by two orders of magnitude. Applying Eq. (2.16), we see that 8 eV $-$ 14 eV axions would freeze out with abundance $0.12 \leq \Omega_{\mathrm{m}} \leq 0.21$. An axion detection in this mass window could thus account for most of the dark matter; a telescope search in this mass window would provide a useful check of LSS constraints to axion properties. Future discoveries of even higher redshift clusters could allow heavier axion mass windows to be probed with cluster observations. We have obtained 18 hours of IFU data of RDCS 1252 and the raw data have been reduced. At the moment, we are applying the existing parameterized strong-lensing mass model of the cluster conduct a thermal new axion search.

2.6 Conclusions

The axion hypothesis offers attractive solutions to both the strong CP and dark-matter problems. A series of null searches and astrophysical constraints has narrowed down the parameter space of the axion to two mass windows, one between 10^{-5} eV and 10^{-3} eV, and the other between 3 eV and 20 eV. Previous searches for optical emission from decaying axions in galaxy clusters have constrained the two-photon coupling of the axion in the latter window. We have searched for axion-decay light in the galaxy clusters A2667 and A2390, taking advantage of strong-lensing mass maps of A2667/A2390 to free our analysis of dynamical assumptions. Use of the VIMOS IFU allowed an

increase in effective collecting area, thus increasing the sensitivity of our axion search. We observed no evidence for emission from decaying axions in the mass window between 4.5 eV and 7.7 eV.

Conservatively, we improve on constraints to the two-photon coupling ξ of axions by a factor of $\simeq 3$, averaged over the entire mass range we explore. This work presents the first application of IFU spectroscopy to constrain the nature of the dark matter and not just its spatial distribution. To check that the stringency of our constraints is not an artifact of the rather complicated data-reduction techniques inherent to IFU spectroscopy, we have simulated our technique by introducing fake axion lines into our data cubes. Our analysis technique accurately recovers the value of ξ, and the axion's signature fades into the sky-background as ξ is ramped down below our reported upper limits. Our simulations demonstrate the robustness of our technique, and our work highlights the potential of IFU spectroscopy for more sensitive exploration of the axion mass window between 8 eV and 14 eV.

Acknowledgments

The author thanks Giovanni Covone, Jean-Paul Kneib, Marc Kamionkowski, Andrew Blain, and Eric Jullo for their contributions to the research described in this chapter. The author thanks Ted Ressell and Matthew Bershady for helpful discussions. This research was supported by the European Community via the Marie Curie European Re-Integration Grant n.029159, the CNRS, DoE DE-FG03-92-ER40701, NASA NNG05GF69G, the Gordon and Betty Moore Foundation, the Alfred P. Sloan Foundation, and Research Corporation.

Chapter 3
Axion constraints in non-standard thermal histories[1]

3.1 Introduction

The Peccei-Quinn (PQ) solution to the strong-CP problem yields the axion, a dark-matter candidate [36, 47, 48]. If the axion mass $m_{\rm a} \gtrsim 10^{-2}$ eV, axions will be produced thermally, with cosmological abundance

$$\Omega_{\rm a} h^2 = \frac{m_{\rm a}}{130\ {\rm eV}} \left(\frac{10}{g_{*{\rm S,F}}} \right), \tag{3.1}$$

where $g_{*{\rm S,F}}$ is the effective number of relativistic degrees of freedom when axions freeze out [50, 51, 86, 93]. Axions with masses in the $\sim$ eV range would contribute to the total density in roughly equal proportion to baryons.

Axions in the $\sim$ eV mass range are relativistic when they decouple at $T_{\rm F} = 30 - 50$ MeV [93]. Free streaming then erases density perturbations, suppressing the matter power spectrum on scales smaller than the axion free-streaming length [50, 152–154]. Light axions would also contribute to the early integrated Sachs-Wolfe (ISW) effect [155]. Data from large-scale structure (LSS) surveys and cosmic microwave-background (CMB) observations have been used to impose the constraint $m_{\rm a} \lesssim 1$ eV to light hadronic axions [6, 156, 157]. These arguments apply to any particle relativistic at matter-radiation equality or cosmic microwave background (CMB) decoupling, thus imposing the similar constraint $\sum_i m_{\nu,i} \lesssim 1$ eV to the sum of neutrino masses [16, 18, 154, 158–165].

These constraints rely on abundances computed assuming that radiation domination began earlier than the chemical freeze-out of light relics. There is, however, no direct evidence for radiation domination prior to big-bang nucleosynthesis (BBN) [166]. The transition to radiation domination may be more gradual than typically assumed. In such a modified thermal history, two effects may cause relic abundances to change. First, the Hubble expansion rate scales differently with temperature T until radiation domination begins, leading to a different freeze-out temperature. Second, entropy may be generated, suppressing relic abundances.

The universe could have reheated to a temperature as low as $T_{\rm rh} \sim 1$ MeV, with standard

[1] The material in this chapter was adapted from *Axion constraints in non-standard thermal histories*, Daniel Grin, Tristan L. Smith, and Marc Kamionkowski; Phys. Rev. D **77**, 085020 (2008). Reproduced here with permission, copyright (2008) by the American Physical Society. For the thesis, significant amounts of motivation and literature review were added in the introduction of this chapter. The discussion of the model-dependence of globular cluster limits to axion properties is new. The discussions of pion equilibrium and axion production from nucleons were extended as well.

radiation domination proceeding thereafter [26, 77, 78, 167–169]. This low-temperature reheating (LTR) scenario may be modeled simply through the entropy-generating decay of a massive particle ϕ into radiation, with fixed rate Γ_ϕ and initial value H_I of the Hubble parameter. The scalar ϕ may be the inflaton, oscillating as inflation ends and decaying into standard-model particles, or it might be a secondary scalar, produced during preheating [170–174]. This decay softens the scaling of temperature T with cosmological scale factor a, increasing the Hubble parameter $H(T)$ and leading to earlier freeze-out for certain relics. Entropy generation then highly suppresses these relic abundances.

Such low values of T_rh are a far cry from the Planck and GUT (Grand Unified Theory) energy scales of 10^{19} GeV and 10^{16} GeV, respectively. There are, however, several reasons to contemplate such low-reheating temperatures. The first is epistemological. The simple fact is that we have very little direct leverage on the thermal history of the universe before BBN. As long as neutrinos are adequately thermalized and the expansion rate not too perturbed after $T \lesssim 10$ MeV, the successful predictions of BBN may be reproduced. Careful computations show that this constraint requires $T_\mathrm{rh} \geq 4$ MeV [78, 167], but this leaves many orders of magnitude to be explored. It thus behooves us to at least consider the consequences of low reheating temperatures. It is also important not to confuse the reheating temperature T_rh (the temperature of the thermal plasma when radiation domination begins) with T_max, the maximum temperature ever achieved by the plasma after it thermalizes [76, 169, 175, 176]. In a model driven by ϕ decays, T_max may in fact be arbitrarily high for a given value T_rh. As a result, there is still acceptable parameter space for both electroweak baryogenesis (if $T_\mathrm{rh} > 100$ GeV) as well as GUT baryogenesis [76, 169, 176] in models with LTR.

The second reason to seriously consider low values of T_rh is that late-time entropy generation can solve a classical flavor of cosmological problem, the overabundance of some 'dangerous relic.' For example, if gravitinos are thermally produced in the early universe, their relatively late decay could change the expansion history during the sensitive BBN epoch, disassociate light nuclei *after* they form, or inject energy afterwards and distort the CMB blackbody through the addition of a chemical potential. These arguments impose the constraint $T_\mathrm{rh} < 10^9$ GeV [177]. In some areas of supersymmetric parameter space, gravitinos may also be produced non-thermally through gravitational particle production. In that case, one obtains the considerably more stringent constraint $T_\mathrm{rh} \lesssim 100$ GeV [178].

The third reason to seriously consider low values of T_rh relates to the second. Entropy generation suppresses relic abundances *and* temperatures (for the case of thermal relics). The nature of dark matter is as of yet unknown, though the list of candidates includes axions, weakly interacting massive particles (WIMPs) such as neutralinos or gravitinos, heavy sterile neutrinos, and even standard-model (SM) neutrinos. WIMPs are usually considered attractive dark matter candidates, as a simple of order-magnitude estimate of the freeze-out abundance of a weakly-coupled massive

relic is generically close to the total dark matter density. This is the famous "WIMP miracle" [179].

Ongoing experiments, mainly the Large Hadron Collider (LHC), may detect supersymmetric partner particles. They may turn out to have couplings and masses that yield exceedingly high or low relic densities in the conventional thermal history, inconsistent with the usual "WIMP" miracle. In that case, cosmologists might conclude that radiation domination began later than usually assumed and was preceded by an epoch of entropy generation, or that the dark matter was produced non-thermally [180]. It turns out that with an appropriate choice of reheating temperature and direct couplings of the entropy-generating scalar to the SM, nearly any type of neutralino can be made consistent with the total cosmological density of dark matter, $\Omega_{\rm d}h^2 \simeq 0.12$. In other words, the usual cosmological constraints to WIMP properties are considerably relaxed if $T_{\rm rh}$ is allowed to take lower values [180].

Experiments like the LHC could thus drive the allowed values of $T_{\rm rh}$ into a range much lower than favored by conventional wisdom [181]. This could yield meaningful constraints on the very early thermal history of the universe. It turns out that if a wino-like neutralino is detected at the LHC, the demand that it constitute all/most of the dark matter would yield a fairly robust hint of non-thermal dark matter production [180]. In this case of non-thermal dark matter production, there is even a scenario called the 'non-thermal WIMP miracle' [182]. Here, the number density of WIMPs approaches an attractor solution which balances the competing WIMP source of ϕ decays/annihilations with WIMP annihilation. In fact, $\Omega_{\rm d}h^2 \sim 0.12$ is obtained rather generically, contradicting the usual heuristic claim that the standard thermal history provides a more natural framework for obtaining the observed dark matter abundance.

Similarly, experiments like the Axion Dark Matter eXperiment (ADMX) [27] or CERN (Conseil Européen pour la Recherche Nucléaire) Axion Solar Telescope (CAST) [28] may discover an axion with mass $m_{\rm a} < 10^{-2}$ eV, which would be coherently produced in the early universe [111]. If $m_{\rm a}$ is sufficiently low, the relic density of such axions as computed by Eq. (2.19) may drastically exceed $\Omega_{\rm d}$. If the axion is the dark matter, an era of entropy generation may be invoked to adequately dilute these 'misalignment' axions. If, on the other hand, WIMPs constitute the bulk of the dark matter, an era of entropy generation may also be invoked to dilute non-thermal axions to negligible densities. In other words the usual cosmological constraint ($m_{\rm a} \gtrsim 10^{-5}$ eV) to the properties of coherently-produced axions may be considerably relaxed if $T_{\rm rh}$ is allowed to take lower values. More precisely, in the LTR scenario, coherently produced axions (with $f_{\rm a} \gg f_{\rm inf}$) have abundance [76, 183]

$$\Omega_{\rm a}h^2 \sim 2 \times 10^{-7} \left(\frac{m_{\rm a}}{10^{-5}\ {\rm eV}}\right)^{-1.52} \left(\frac{T_{\rm rh}}{\rm MeV}\right)^{1.96}. \tag{3.2}$$

If we saturate the BBN constraint on reheating by choosing $T_{\rm rh} = 4$ MeV, the constraint $\Omega_{\rm a}h^2 < 0.12$ imposes the less stringent constraint that $m_{\rm a} \gtrsim 10^{-8}$ eV, giving experiments searching for coherently

produced axions a few additional orders of magnitude in mass to search.

It is also possible (though depressing to consider) that the LHC, ADMX, CAST, CDMS (Cold Dark Matter Search) [32], and the bevy of other current and future experiments designed to seek super-symmetry or directly detect WIMP/axions will all fail to detect new particles. Other more mundane dark matter candidates may be worth a second look in this case, specifically SM neutrinos. It turns out that $\sim$ keV (warm) SM neutrino dark matter can be made compatible with cosmological constraints if $T_{\rm rh} \sim$ MeV [76, 77]. Heavy, right-handed neutrinos are sometimes invoked to explain SM neutrino masses using the 'seesaw' mechanism [143, 144, 184]. They would mix weakly with SM neutrinos and be non-thermally produced in the early universe [80–82, 145, 185, 186]. Sterile neutrinos in the $\sim$ keV range are a frequently discussed dark matter candidate [79, 148, 187–194], and cosmological constraints on their mixing angles are considerably relaxed in the LTR scenario [195–197].

The fourth reason to consider the LTR scenario is that it is actually quite natural [198]. Light moduli fields abound in many realizations of string theory and M-theory, and their mass may very well lie in the range 10 TeV $\lesssim m_\phi \lesssim$ 100 TeV. These fields are gravitationally coupled, and thus decay with width [198]

$$\Gamma \sim \frac{m_\phi^3}{m_{\rm pl}^2}, \tag{3.3}$$

where $m_{\rm pl}$ is the Planck mass. These scalars may dominate the energy budget of the universe during the epoch following inflation and until radiation-domination. The reheating temperature $T_{\rm rh}$ is then obtained by setting $\Gamma \sim H(T_{\rm rh})$ (We use the standard radiation dominated expression $H\left(T_{\rm rh}\right) \sim T^2/m_{\rm pl}$, as it should be valid at the transition temperature between the entropy-generating and radiation-dominated epochs). The resulting reheating temperature is [182]

$$T_{\rm rh} \sim 10 \text{ MeV} \left(\frac{m_\phi}{100 \text{ TeV}}\right)^{3/2}, \tag{3.4}$$

and so $T_{\rm rh} \sim$ 10 MeV is not as far-fetched as it may naively seem.

Kination models offer another alternative to the standard thermal history, invoking a period of scalar-field kinetic-energy dominance [199], but no entropy production. During kination, $\rho_\phi \propto a^{-6}$, where a is the cosmological scale factor, and $H\left(T\right) \propto T^3$. This behavior is rather generic in quintessential inflation models [200–202], where one scalar field is responsible for both primordial inflation and 'dark energy today.' In these models, reheating typically occurs through gravitational particle production. As the scalar rolls down its potential, it becomes kinetic-energy dominated, and so $\rho_\phi \propto a^{-6}$ damps away. Deep into matter domination, the small residual potential energy density of ϕ becomes important again, relative to the matter density $\rho_{\rm matter}$. In quintessential inflation, this is responsible for the late-time acceleration of a.

Kination has many appealing features, however, that depend in no way on its specific embedding

in a more complete model, but require only an era with $\rho \propto a^{-6}$ [203, 204]. The slightly larger Hubble parameter during kination makes it easier to satisfy the out-of-equilibrium condition required for successful baryogenesis [203]. It has been shown that successful electroweak baryogenesis is possible in cosmologies with a kination epoch [203, 205, 206]. The lack of entropy generation in kination models also means that a successfully generated baryon asymmetry is not diluted away.

Earlier freeze-out of WIMPs and other heavy relics leads to higher relic densities. As in the case of low-temperature reheating, this means that cosmological constraints to WIMP properties are relaxed [207, 208], and that collider experiments can be used to put meaningful constraints on the duration of the kination epoch. One exciting possibility is that for 4 sensible benchmark models in minimal supergravity, the combination of the LHC and ILC (International Linear Collider) will be sufficient to discover a kination epoch preceding BBN (assuming of course, that the supersymmetric particle discovered at colliders is also the dark matter) [29].

Past work has shown that cosmological constraints to neutrinos, weakly interacting massive particles, and non-thermally produced axions are relaxed in the LTR [76, 77, 195] and kination scenarios. Non-thermally produced axions ($m_{\rm a} \lesssim 10^{-2}$ eV) would be produced through coherent oscillations of the PQ pseudoscalar [50–52], as discussed in Sec. 2.2. In this chapter, we obtain **new** constraints to thermally-produced hadronic axions in the kination and LTR scenarios. Thermal axions freeze out while relativistic, and so without entropy generation, their abundances change more modestly than in the LTR case. While kination modestly loosens limits, LTR dramatically changes the cosmologically allowed range of axion masses.

We begin by reviewing these modified thermal histories and calculating axion relic abundances. We then generalize cosmological constraints to axions, allowing for low-temperature reheating and kination. For reheating temperatures $T_{\rm rh} \lesssim 35$ MeV, LSS/CMB limits to the axion mass are lifted; constraints are also relaxed for higher $T_{\rm rh}$. Constraints from the total matter density are also relaxed, but not completely lifted. For $T_{\rm rh} \simeq 10$ MeV, the new constraint is $m_{\rm a} \lesssim 1.4$ keV, while for $T_{\rm rh} \simeq 35$ MeV, we find that $m_{\rm a} \lesssim 43$ eV. If $T_{\rm rh} \gtrsim 170$ MeV, standard results are recovered. We thus see that for sufficiently low $T_{\rm rh}$, thermal axions are a warm dark matter candidate. After estimating the ability of future large-scale-structure surveys to further constrain axion masses for a variety of reheating temperatures, we derive modestly relaxed constraints to axions in the kination scenario. We conclude by considering future possible constraints to the relativistic energy density of axions in a low-temperature reheating model.

3.2 Two non-standard thermal histories: Low-temperature reheating and kination

We now review the low-temperature reheating (LTR) scenario. We consider the coupled evolution of unstable massive particles ϕ, which drive reheating, and radiation R, both in kinetic equilibrium. The relevant distribution functions obey a Boltzmann equation with a decay term, and may be integrated to yield [76, 77, 175]:

$$\frac{1}{a^3}\frac{d\left(\rho_\phi a^3\right)}{dt} = -\Gamma_\phi \rho_\phi, \quad \frac{1}{a^4}\frac{d\left(\rho_R a^4\right)}{dt} = \Gamma_\phi \rho_\phi, \tag{3.5}$$

where ρ_ϕ and ρ_R denote the energy densities in the scalar field and radiation, respectively, Γ_ϕ is the decay rate of the scalar to radiation, and a is the cosmological scale factor. The evolution of the scale factor is given by the Friedmann equation, which is $H^2 = [8\pi/(3M_{\rm pl}^2)]\,(\rho_\phi + \rho_R)$ well before matter or vacuum-energy domination. The reheating temperature $T_{\rm rh}$ is defined by [50, 76, 175]

$$\Gamma_\phi \equiv \sqrt{\frac{4\pi^3 g_{*,\rm rh}}{45}}\frac{T_{\rm rh}^2}{M_{\rm pl}}, \tag{3.6}$$

where $M_{\rm pl}$ is the Planck mass and $g_{*,\rm rh}$ is the effective number of relativistic degrees of freedom when $T = T_{\rm rh}$. In our calculation of the expansion history in LTR, we use g_* calculated using the methods of Refs. [50, 209], as tabulated for use in the DarkSUSY package [210]. We neglect the axionic contribution to g_* for simplicity and assume 3 massless neutrinos. The resulting $\sim 10\%$ error in g_* leads to a comparable fractional error in the resulting axion relic abundance, and is thus negligible at our desired level of accuracy.

We use dimensionless comoving densities [76, 175]:

$$\Phi \equiv \rho_\phi T_{\rm rh}^{-1} T_0^{-3} a^3, \; R \equiv \rho_R a^4 T_0^{-4}, \tag{3.7}$$

where T_0 is the temperature today. At the beginning of reheating, ϕ dominates the energy density and radiation is negligible. Thus, as initial conditions, we use $\rho_R = 0$ and $\rho_\phi = [3/(8\pi)]\,M_{\rm pl}^2 H_{\rm I}^2$, where $H_{\rm I}$ is the initial value of the Hubble parameter. The two physical free parameters in this model are $T_{\rm rh}$ and $H_{\rm I}$. The temperature is related to the radiation energy density by [50]

$$T = \left[\frac{30}{\pi^2 g_*(T)}\right]^{1/4} \rho_R^{1/4}. \tag{3.8}$$

We numerically integrate Eqs. (3.5) to obtain the dependence of T on a, and the results are shown in Fig. 3.1. As the scalar begins to decay, the temperature rises sharply to a maximum at $a_{\rm m} = (8/3)^{2/5}\,a_{\rm I}$, where $a_{\rm I}$ is the initial value of the scale factor, and then falls as $T \propto a^{-3/8}$. This shallow

scaling of temperature with scale factor results from the continual dumping of scalar-field energy into radiation, and yields an unusually *steep* dependence of scale factor on temperature. As shown in Figs. 3.1 and 3.2, when the comoving radiation energy density R overtakes Φ near $T \sim T_{\rm rh}$, the epoch of radiation domination begins, with the usual $T \propto a^{-1}$ scaling.

Well before reheating concludes, Φ is constant and $\rho_{\rm R} \ll \rho_\phi$. If $a_{\rm m} \ll a < a\left(T_{\rm rh}\right)$, an approximate solution of Eqs. (3.5) for $T(a)$ is then [76, 175]

$$\begin{aligned} T &\simeq T_{\rm max} \left(\frac{a}{a_{\rm m}}\right)^{-3/8} \left[\frac{g_*\left(T_m\right)}{g_*\left(T\right)}\right]^{1/4} \\ T_{\rm max} &= 4.2 \text{ GeV } \left[\frac{10 g_{*,\rm rh}}{g_*^2\left(T_{\rm m}\right)}\right]^{1/8} H_{\rm I,eV}^{1/4} T_{\rm rh,MeV}^{1/2}, \end{aligned} \tag{3.9}$$

where $g_{*,\rm rh} = g_*\left(T_{\rm rh}\right)$ and $T_{\rm max}$ is the maximum temperature obtained (see Fig. 3.1). Here $T_{\rm rh,MeV}$ and $H_{\rm I,eV}$ are the reheating temperature and initial value of the Hubble parameter, in units of MeV and eV, respectively.

During reheating, the Hubble parameter is given by [76, 77]

$$H \simeq \left[\frac{5\pi^3 g_*^2\left(T\right)}{9 g_{*,\rm rh}}\right]^{1/2} \left(\frac{T}{T_{\rm rh}}\right)^2 \frac{T^2}{M_{\rm pl}}. \tag{3.10}$$

At a given temperature, the universe thus expands faster during reheating than it would during radiation domination, and the equilibrium condition $\Gamma \equiv n\left\langle\sigma v\right\rangle \gtrsim H$ is harder to establish and maintain. Relics with freeze-out temperature $T_{\rm F} \geq T_{\rm max}$ will thus have highly suppressed abundances because they never come into chemical equilibrium. Relics with $T_{\rm rh} \lesssim T_{\rm F} \lesssim T_{\rm max}$ come into chemical equilibrium, but then freeze out before reheating completes. Their abundances are then reduced by entropy production during reheating. In either case, species with $T_{\rm F} \gtrsim T_{\rm rh}$ have highly suppressed relic abundances.

Less radical changes to abundances follow in kination scenarios. During epochs dominated by the kinetic energy of a scalar field, the energy density ρ scales according to $\rho \propto a^{-6}$ [199]. Thus $H\left(T\right) \propto T^3$ or $H \simeq H_{\rm rad}\left(T\right)\left(T/T_{\rm kin}\right)$, where $H_{\rm rad}\left(T\right)$ is the standard radiation-dominated $H\left(T\right)$ and $T_{\rm kin}$ denotes the transition temperature from kination to radiation domination. Kination yields relic freeze-out temperatures somewhere between the standard and LTR values. There is, however, no entropy generation during kination, leading to a less dramatic change in relic abundances. Note that these conclusions are rather general, as we have not relied on any detailed properties of the kination model, but only on the scaling $H\left(T\right) \propto T^3$ [166].

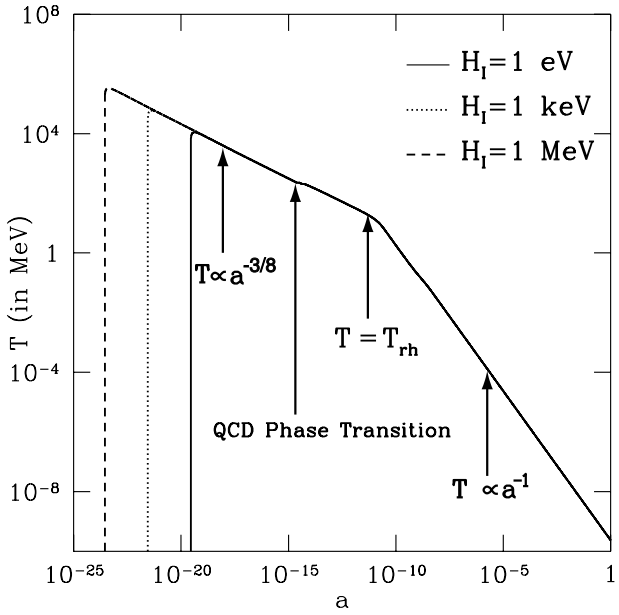

Figure 3.1 This plot shows the evolution of temperature with scale factor in a low-temperature reheating (LTR) scenario with $T_{\rm rh} = 20$ MeV and 3 different initial values for the Hubble parameter $H_{\rm I}$. After a rapid rise due to ϕ decay, $T \propto a^{-3/8}$ until $T \sim T_{\rm rh}$, after which radiation domination begins, and $T \propto a^{-1}$. The small bump near $T \simeq 200$ MeV results from a jump in g_* near the QCD phase transition.

3.3 Axion production in non-standard thermal histories

Axions with $m_{\rm a} \gtrsim 10^{-2}$ eV are thermally produced in the standard radiation-dominated cosmology. We now show that in LTR models, these axions have suppressed abundances. We consider standard hadronic axions, which do not couple to standard-model leptons but do couple to pions and photons through higher order terms [56, 57]. We do not consider flaton models, or other scenarios in which PQ symmetry breaking is related to supersymmetry breaking [211–215]. For temperatures $T \lesssim$ 150 MeV, the dominant channels for axion production are $\pi^+ + \pi^- \to a + \pi^0$, $\pi^+ + \pi^0 \to \pi^+ + a$, and $\pi^- + \pi^0 \to a + \pi^-$ [93]. Axion scattering rates are suppressed relative to particle-number-changing interactions by factors of $T^2/f_{\rm PQ}^2$ and thus decouple very early. Thus, axions stay in kinetic equilibrium because of $\pi + \pi \leftrightarrow a + \pi$, and kinetically decouple when they chemically freeze out.

Nucleonic channels are negligible at these temperatures [93], as we verify below. If pions are in chemical equilibrium and Bose enhancement can be neglected, the axion production rate is obtained

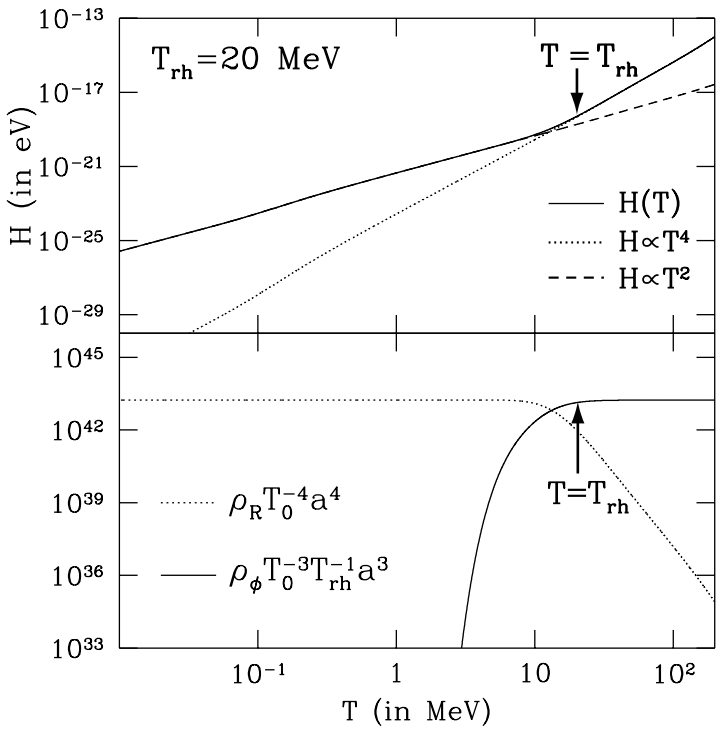

Figure 3.2 The top panel shows the Hubble parameter as a function of temperature in an LTR cosmology with $T_{\rm rh} = 20$ MeV and $H_{\rm I} = 1$ MeV. Initially $H \propto T^4 g_*(T)$, but at temperatures cooler than $T \sim T_{\rm rh}$, $H \propto T^2\sqrt{g_*(T)}$.The second panel shows the comoving radiation energy density $R = \rho_R T_0^{-4} a^4$ and scalar energy density $\Phi = \rho_\phi T_0^{-3} T_{\rm rh}^{-1} a^3$ as a function of temperature. At $T \sim T_{\rm rh}$, R flattens out to a constant and Φ drops off to zero, indicating the conclusion of reheating.

from the Lagrangian in Eq. (2.15) to be [6, 50, 93, 216]

$$\Gamma = \frac{3\zeta(3)T^5 C_{\rm a\pi}^2}{1024\pi^7 f_{\rm a}^2 f_\pi^2}\int dx_1 dx_2 \frac{x_1^2 x_2^2}{y_1 y_2} f(y_1) f(y_2) \int_{-1}^{1} d\mu \frac{\left[s - m_\pi^2\right]^3 \left[5s - 2m_\pi^2\right]}{s^2 T^4},$$
$$C_{\rm a\pi} = \frac{1-r}{3\,(1+r)}, \quad s = 2\left[m_\pi^2 + T^2\,(y_1 y_2 - x_1 x_2 \mu)\right], \tag{3.11}$$

where $x_i = p_i/T$ is the dimensionless pion momentum, $y_i = \sqrt{x_i^2 + m_\pi^2/T^2}$ is the dimensionless pion energy, $f\,(y_i) = 1/\left[\exp\,(y_i) - 1\right]$ is the pion distribution function, $C_{\rm a\pi}$ is the dimensionless axion-pion coupling constant, and $\zeta(x)$ is the Riemann ζ-function. The PQ energy scale is $f_{\rm a}$. The neutral pion mass is $m_\pi \simeq 135$ MeV [91]. The PQ scale can be expressed in terms of the axion mass [87]:

$$f_{\rm a} \simeq \frac{\sqrt{r}}{1+r}\frac{f_\pi m_\pi}{m_{\rm a}}. \tag{3.12}$$

Here $r \equiv m_{\rm u}/m_{\rm d} \sim 0.56$ is the up/down quark mass ratio and $f_\pi \simeq 93$ MeV is the pion decay constant [50, 91].

Evaluating Eq. (3.11) for Γ and numerically solving Eq. (3.5) for $H\,(T)$, we estimate the axion

freeze-out temperature using the condition $\Gamma(T_{\rm F}) \sim H(T_{\rm F})$. As the reheating temperature is lowered, axions freeze out at higher temperatures due to the higher value of H, as shown in Fig. 3.3. As the reheating temperature is increased, the $T \propto a^{-3/8}$ epoch becomes increasingly irrelevant, and the freeze-out temperature of the axion asymptotes to its standard radiation-dominated value. Examining Eq. (3.11), we see that $\Gamma \propto f_{\rm a}^{-2} \propto m_{\rm a}^2$, so higher-mass axions keep up with the Hubble expansion for longer and generally decouple at lower temperatures. Thus, for higher $m_{\rm a}$, a more radical change to the thermal history (even lower $T_{\rm rh}$), is needed to drive $T_{\rm F}$ to a fixed higher value.

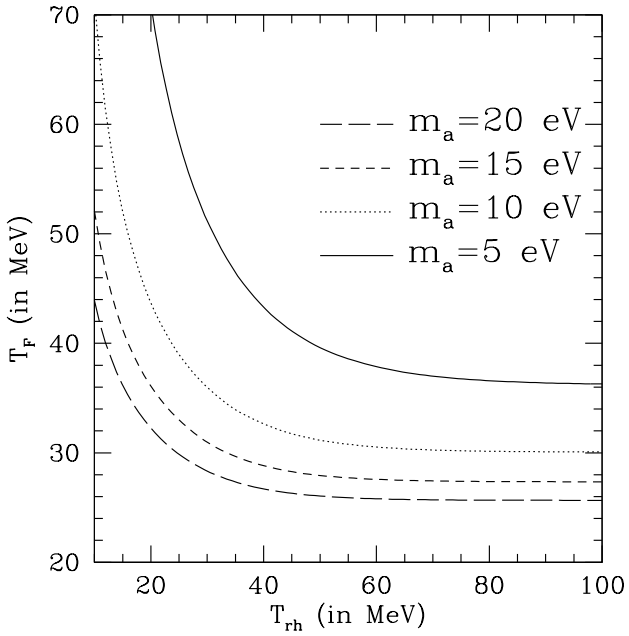

Figure 3.3 Freeze-out temperature of the reactions $\pi^+ + \pi^- \leftrightarrow \pi^0 + a$, $\pi^+ + \pi^0 \leftrightarrow \pi^+ + a$, and $\pi^- + \pi^0 \leftrightarrow \pi^- + a$, shown as a function of the reheating temperature $T_{\rm rh}$, for 4 different axion masses. More massive axions are coupled more strongly, leading to later freeze-out than for lighter axions.

As axions are spin-0 relativistic bosons, their number density at freeze-out is $n_{\rm a}(T_{\rm f}) = \zeta(3) T_{\rm F}^3/\pi^2$. If we assume that axion production ceases at freeze-out, the density of axions at any subsequent time is just $n_{\rm a}(T_{\rm f}) \left[a_{\rm F}/a_0\right]^3$, where $a_{\rm F}$ is the value of the cosmological scale factor at axion freeze-out. The reheating time scale, $t_{\rm rh} \simeq 1/\Gamma$, is much shorter than the Hubble time for $T \lesssim T_{\rm rh}$, and so it is a good approximation to treat the break between the $T \propto a^{-3/8}$ and $T \propto a^{-1}$ epochs as instantaneous at $T = T_{\rm rh}$. Doing so, we apply Eq. (3.9) prior to the completion of reheating and $a \propto T^{-1} g_{*\rm S}^{-1/3}(T)$ afterwards, to obtain

$$\Omega_{\rm a} h^2 = \frac{m_{\rm a,eV}}{130} \left(\frac{10}{g_{*\rm S,F}}\right) \gamma\left(T_{\rm rh}/T_{\rm F}\right),$$

$$\gamma(\beta) \sim \begin{cases} \beta^5 \left(\frac{g_{*,\mathrm{rh}}}{g_{*,\mathrm{F}}}\right)^2 \left(\frac{g_{*\mathrm{S},\mathrm{F}}}{g_{*\mathrm{S},\mathrm{rh}}}\right) & \text{if } \beta \ll 1, \\ 1 & \text{if } \beta \gg 1, \end{cases} \tag{3.13}$$

where m_{a} is the axion mass in units of eV.

Low reheating temperatures drive up the freeze-out temperature. When $T_{\mathrm{rh}} \lesssim T_{\mathrm{F}}$, the present mass density in axions is severely suppressed, because of the sharper dependence of the scale factor a on T during reheating. This is a result of entropy generation. Using the numerical solution for $a\,(T)$ from Sec. 3.2, we obtain Ω_{a}, accounting for the smooth transition between the $T \propto a^{-3/8}$ and $T \propto a^{-1}$ regimes. In Fig. 3.4, we show Ω_{a} normalized by its standard value, Ω_{a}^0, as a function of T_{rh}. At reheat temperatures just a factor of a few below the usual axion freeze-out temperature for a given axion mass, the axion abundance is suppressed by a factor of $10^{-4} - 10^{-3}$. For $T_{\mathrm{rh}} \gg T_{\mathrm{F}}$, the axion abundance asymptotes towards its standard value. We see that the constraints on axion decay from Chapter 2.5.3 then imply a very strict limit $T_{\mathrm{rh}} \ll 10$ MeV if $E/N = 2$ is fixed there, and uncertainties in $m_{\mathrm{u}}/m_{\mathrm{d}}$ are ignored.

In the case of kination, axion freeze-out temperatures are still raised, but there is no additional entropy production. Axion abundances are given by Eq. (3.1), but with the higher $g_{*\mathrm{S},\mathrm{F}}$ values appropriate at higher values of T_{F}.

For the LTR case, our results do not depend on the initial value H_{I} of the Hubble parameter. As seen in Fig. 3.1, changes to H_{I} determine the moment of the fast rise to T_{max}, but have little influence on the expansion history for $T < T_{\mathrm{max}}$. For convenience, we choose $H_{\mathrm{I}} = 1$ MeV for our calculations, corresponding to $T_{\mathrm{max}} \simeq 20$ GeV.

Our calculation is valid only if axions are produced in equilibrium by thermal pions. We check that pions are in chemical equilibrium using the chiral Lagrangian density term for pion-photon interactions, which scales as [217]

$$\mathcal{L}_{\pi\pi\gamma\gamma} \sim \frac{\alpha \pi^0 \pi^0 F_{\mu\nu} F^{\mu\nu}}{f_\pi^2}. \tag{3.14}$$

We use standard expressions for the number density of pions in the non-relativistic regime, and estimate the cross-section for the $\pi\pi \leftrightarrow \gamma\gamma$ reaction accurate to order-of-magnitude level assuming that the photon momentum $k \sim T$. Using the usual $\Gamma\,(T_{\mathrm{F}}) \sim H\,(T_{\mathrm{F}})$ criterion, we estimate that pions stay in equilibrium from the QCD phase transition until long after nucleosynthesis (down to $T \sim$ keV, yielding exponentially suppressed abundances today), and so we may use equilibrium expressions for the number density of pions.

For axion freeze-out to occur during the era where pions have condensed out of the quark-gluon plasma, we must have $T_{\mathrm{rh}} \gtrsim 10$ MeV. Outside this range, our assumptions break down. For sufficiently low values of m_{a} and T_{rh}, pionic cross sections lead to $T_{\mathrm{F}} \gtrsim 200$ MeV, earlier than the quark-hadron phase transition. The absence of hadrons then necessitates the use of quark-axion

production cross sections.

Furthermore, for $T_{\rm rh} \lesssim 10$ MeV, pions will decay before they can come into equilibrium. In both cases, axion abundances are suppressed relative to our calculation. For axion masses saturating our upper limits and $T_{\rm rh} \gtrsim 10$ MeV, we have checked that we are well within the equilibrium regime. We restrict ourselves to this range, noting that for $T_{\rm rh} \lesssim 10$ MeV, more suppressed abundances will lead to an even more dramatic relaxation to cosmological axion limits. Coherent oscillations of the axion field produce a condensate that behaves as cold dark matter [76], but the resulting additional abundance is negligible for $m_{\rm a} \gtrsim 10^{-2}$ eV at all values of $T_{\rm rh}$ under consideration here [76].

It is instructive to verify that production off the ample thermal bath of protons and neutrons for $T \lesssim \Lambda_{\rm QCD}$ is indeed negligible in our regime of interest. In low-energy chiral perturbation theory, the axion-nucleon interaction Lagrangian density is [93]

$$\mathcal{L}_{\rm aN} = \frac{\partial_\mu A}{f_{\rm a}} \left(C_{\rm aN} \overline{n} \gamma^\mu \gamma^5 n + C_{\rm ap} \overline{p} \gamma^\mu \gamma^5 p \right), \tag{3.15}$$

where A is the axion field, $C_{\rm aN}$ is the axion-neutron coupling constant, and $C_{\rm ap}$ is the axion-proton coupling constant. Both coefficients are of order unity. The lowest-order axion-nucleon reactions are NN $\to$ NN a and Nπ $\to$ N a. Using an equilibrium value for the total nucleon density (adequate because the baryon asymmetry is not very relevant until $T \sim 22$ MeV when nucleons freeze out [50]), we obtain the following expression for the ratio of the relevant chemical reaction rate to the Hubble expansion

$$\frac{\Gamma}{H} = \begin{cases} 611 m_{\rm a,eV}^2 \sqrt{\frac{m_{\rm N}}{T}} e^{-\frac{m_{\rm N}}{T}} & \text{if } T < T_{\rm rh}, \\ 6.11 \times 10^{-4} m_{\rm a,eV}^2 \left(\frac{T_{\rm rh}}{\rm MeV} \right)^2 \sqrt{\frac{m_{\rm N}^5}{T^5}} e^{-\frac{m_{\rm N}}{T}} & \text{if } T > T_{\rm rh}. \end{cases} \tag{3.16}$$

Numerically, we find that for the range of $m_{\rm a}$ and $T_{\rm rh}$ considered in this paper, the freeze-out temperature $T_{\rm F}$ of the nucleon-axion chemical reactions lies in the range 100 MeV $\lesssim T_{\rm F} \lesssim$ 200 MeV. Thus, our assumption that the pionic reactions dominate over the nucleonic ones is solid.

3.4 Constraints to axions

Most constraints to the axion mass are obtained from its two-photon interaction. This interaction is parameterized by a coupling constant $g_{\rm a\gamma\gamma}$, given by [4, 10, 11, 28, 42, 50, 51, 53, 74, 75, 218, 219]

$$g_{\rm a\to\gamma\gamma} = -\frac{\alpha}{2\pi f_{\rm a}} \frac{3\xi}{4}, \tag{3.17}$$

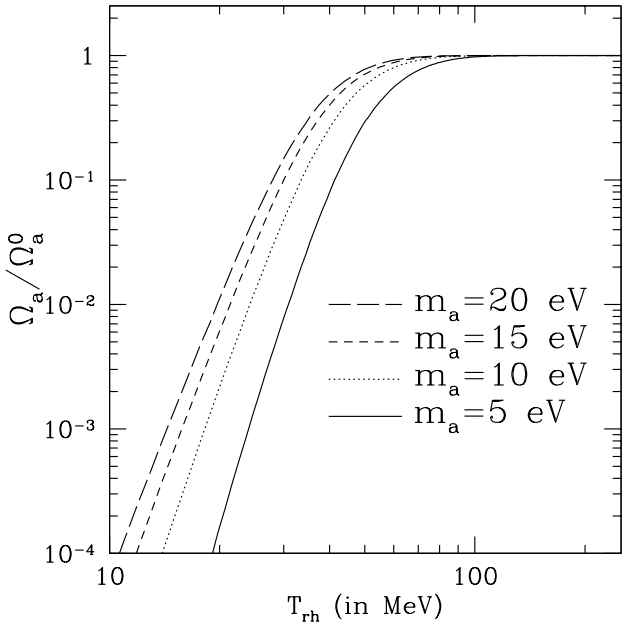

Figure 3.4 Axion abundance $\Omega_{\rm a}$ normalized by its standard value $\Omega_{\rm a}^0$, shown as a function of the reheating temperature $T_{\rm rh}$. Curves are shown for 4 different axion masses. More massive axions freeze out later. As a result, their density is less diluted by entropy production during the reheating epoch, and so they have higher relic densities.

where ξ is a model-dependent parameter and α is the fine-structure constant. The tightest constraint to $g_{\rm a\to\gamma\gamma}$,

$$g_{a\gamma\gamma} \lesssim 0.6 \times 10^{-10}\ {\rm GeV}^{-1}, \tag{3.18}$$

comes from the helium burning lifetime of stars in star clusters [4, 220]. The parameter ξ is given by [4, 53, 89, 218]

$$\xi = \frac{4}{3}\left[\frac{E}{N} - \frac{2}{3}\frac{(4+r)}{(1+r)}\right]. \tag{3.19}$$

Here E and N are weighted sums of the electric and PQ charges of fermions that couple to axions, as discussed in Chapter 2. In existing axion models, $0 \le E/N < 8/3$ [86, 89], while r is poorly constrained and lies in the range [89, 221–223]:

$$0.2 \le r \le 0.8. \tag{3.20}$$

As a result, for any axion model in the range $1.93 \lesssim E/N < 2.39$, there are experimentally allowed r values for which $g_{\rm a\to\gamma\gamma}$ vanishes (see Eq. 3.19), and so constraints to axions from star clusters, helioscope, RF cavity, and telescope searches may all be lifted [86, 89]. These constraints are discussed in detail in Chapter 2. Such a cancellation is fine tuned, but even for other values of E/N, constraints to the axion mass are loosened. In Ref. [89], the authors show that the null results

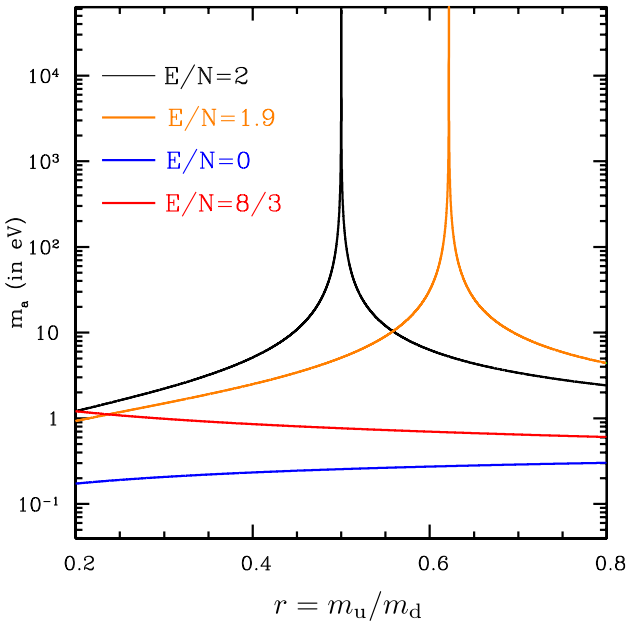

Figure 3.5 Upper limit to the axion mass from the evolution of horizontal branch (HB) stars in globular clusters. Limits are shown as a function of the up/down quark mass ratio $r = m_u/m_d$, for four different axion models, parameterized by the value of E/N. The region above the line is excluded, while below the line is allowed. Limits to $g_{a\to\gamma\gamma}$ are taken from Refs. [4, 5] and generalized to varying r and E/N.

of the ADMX experiment are actually still consistent with all the dark matter in the galactic halo consisting of $E/N = 2$ axions. To further illustrate our point about the lifting of axion constraints based on $g_{a\to\gamma\gamma}$, we show the constraint from globular cluster stellar lifetimes [Eq. (3.18)] generalized to the case of varying r and E/N; to our knowledge, such an illustration does not yet exist in the literature. We see that the globular cluster limit may be significantly relaxed when the full model dependence of $g_{a\to\gamma\gamma}$ is considered.

In contrast, the hadronic couplings do not vanish for any experimentally allowed r values [86]. Axion searches based on these couplings are underway, and have already placed new upper limits to the axion mass in the keV range [124] (and references therein). These couplings also determine the cosmological abundance of axions, and so useful constraints may be obtained from cosmology.

Although the hadronic coupling determines the relic abundance of axions, ξ will determine the lifetime of the axion, which may have implications for cosmological constraints. For the high axion masses allowed by our new constraints and certain values of r and E/N, the decay $a \to \gamma\gamma$ may no longer be negligible on cosmological time scales. Such an axion would be completely unconstrained by limits to $\Omega_a h^2$ from the total matter density or the hot dark matter mass fraction. In the following calculation, we neglect axion decay. Consistent with a vanishing two-photon coupling for $E/N = 2$, we use the value $r = 0.50$. We have verified that our results for $\Omega_a h^2$ vary by only 5% for variations

in r of about 20%, as the dependence of the axion production rate and $T_{\rm F}$ on r is weak (see Eq. 3.11) compared with the dependence on the $e^{-m_\pi/T}$ Boltzmann factor.

3.4.1 Constraints to the axion mass from $\Omega_{\rm m}h^2$

In the standard cosmology, a conservative constraint is obtained by requiring that axions not exceed the total matter density of $\Omega_{\rm m}h^2 \simeq 0.135$ [16], yielding the limit $m_{\rm a} \lesssim 22$ eV, using a concordance value for the dimensionless Hubble parameter $h = 0.73$. In LTR scenarios, axion abundances are highly suppressed, as shown in Eq. (3.13) and Fig. 3.4. Mass constraints to thermal axions from cosmology are thus considerably relaxed.

To obtain abundances in the LTR scenario, we apply the numerical freeze-out and abundance calculation of Section 3.3. Axion mass limits resulting from the requirement that axions not exceed the total dark matter density are shown by the dot-dashed hashed region in Fig. 3.6. If $T_{\rm rh} \lesssim 40$ MeV, constraints are considerably relaxed. For example, if $T_{\rm rh} \simeq 10$ MeV, the axion mass constraint is $m_{\rm a} \leq 1.4$ keV. When $T_{\rm rh} \gtrsim 95$ MeV, we obtain $m_{\rm a} \lesssim 22$ eV, equal to the standard radiation-dominated result. As already discussed, abundances are only slightly changed in the case of kination, so $\Omega_{\rm a}h^2$ imposes the constraint $m_{\rm a} \lesssim 26$ eV if $T_{\rm kin} \simeq 10$ MeV.

3.4.2 Constraints to the axion mass from CMB/LSS data

Axions will free stream at early times, decreasing the matter power spectrum on length scales smaller than the comoving free-streaming scale, evaluated at matter-radiation equality. For sufficiently low masses, axions will also contribute to an enhanced early ISW effect [155] in the CMB. This suppression is given by $\Delta P/P \simeq -8\Omega_{\rm a}/\Omega_m$ if $\Omega_{\rm a} \ll \Omega_m$ [6, 156, 224] (and references therein). The matter power spectrum thus imposes a constraint to $\Omega_{\rm a}h^2$.

First we review the constraints imposed by these effects in a standard thermal history. In this case, both $\Omega_{\rm a}h^2$ and the free-streaming scale, $\lambda_{\rm fs}$, depend only on $m_{\rm a}$ in a hadronic axion model. Using Sloan Digital Sky Survey (SDSS) measurements of the galaxy power spectrum [19] and Wilkinson Microwave Anisotropy Probe (WMAP) [15] $1^{\rm st}$-year measurements of the CMB angular power spectrum, Refs. [6, 156, 224] derived limits of $m_{\rm a} \lesssim 1$ eV. Axions in the mass range of interest ($m_{\rm a} \gtrsim 1$ eV) are non-relativistic at photon-baryon decoupling, and so this constraint essentially comes from measurements of the galaxy power spectrum [158]. As a result, we do not expect that an analysis including more recent WMAP results would make a substantial difference in the allowed axion parameter space. In order to lift this constraint, the relationship between $m_{\rm a}$ and $\Omega_{\rm a}h^2$ or $\lambda_{\rm fs}$ must be changed. More recent results obtained using the WMAP $5^{\rm th}$ and $7^{\rm th}$-year data releases, assuming the standard thermal history [128, 130], confirm this intuition, and the authors even note that the dominant contribution to the axion mass constraint comes from the LSS data.

If $T_{\rm F}$ is allowed to vary freely, the constraints may be relaxed. In particular, using Eq. (3.1) we can see that increasing $g_{*{\rm S},{\rm F}}$ (and thus $T_{\rm F}$) will decrease $\Omega_{\rm a}h^2$. Furthermore, if the free-streaming length of the axion is less than the smallest length scale on which the linear power-spectrum may be reliably measured ($\lambda_{\rm min} \simeq 40\ h^{-1}$ Mpc), its effect on the matter power spectrum is not observable [6, 156, 224]. The comoving free-streaming length scale at matter-radiation equality[2] [50],

$$\lambda_{\rm fs} \simeq \frac{196\ {\rm Mpc}}{m_{\rm a,eV}} \left(\frac{T_{\rm a}}{T_\nu}\right) \left\{1 + \ln\left[0.45 m_{\rm a,eV} \left(\frac{T_\nu}{T_{\rm a}}\right)\right]\right\}, \tag{3.21}$$

is set by the ratio between the axion and neutrino temperatures,

$$\frac{T_{\rm a}}{T_\nu} \approx (10.75/g_{*{\rm S},{\rm F}})^{1/3}, \tag{3.22}$$

so that if $g_{*{\rm S},{\rm F}} \gtrsim 87$ (i.e., if axions freeze out considerably before neutrinos), the constraint to axion masses is lifted [6].

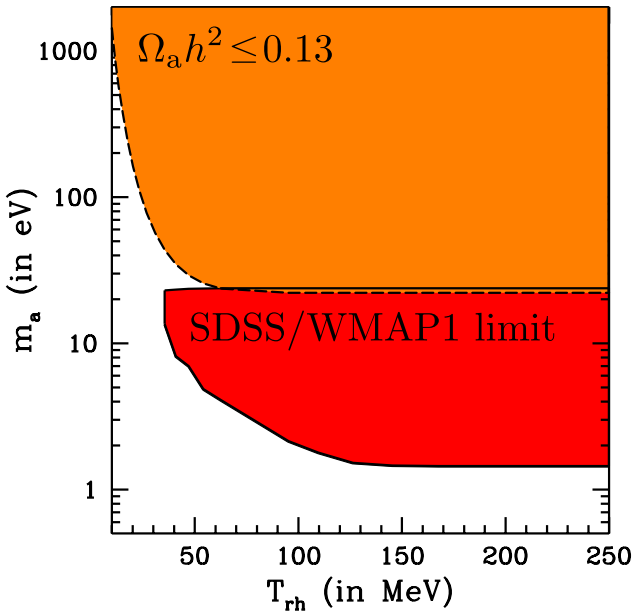

Figure 3.6 Upper limits to the hadronic axion mass from cosmology, allowing the possibility of a low-temperature-reheating scenario. The orange region shows the region excluded by the constraint $\Omega_{\rm a}h^2 < 0.135$ as a function of reheating temperature $T_{\rm rh}$. The red region shows the additional part of axion parameter space excluded by WMAP1/SDSS data. At low reheating temperatures, upper limits to the axion mass are loosened. For $T_{\rm rh} \gtrsim 170$ MeV, the usual constraints are recovered.

In the case of a modified thermal history, the relationship between $T_{\rm F}$ and $m_{\rm a}$ acquires dependence on an additional parameter ($T_{\rm rh}$, in the case of LTR, or $T_{\rm kin}$, in the case of kination) thus allowing us to loosen the constraints. At a series of values of $g_{*{\rm S},{\rm F}}$, Refs. [6, 156, 224] determine the

[2]This differs from the expression in Refs. [154, 224] because we assume, as is the case in our parameter region of interest, that $m > T_{\rm eq}$, the temperature at matter-radiation equality. In Ref. [154], $m < T_{\rm eq}$ is assumed.

maximum values of $\Omega_{\rm a}h^2$ consistent with WMAP measurements of CMB power spectra and SDSS measurements of the galaxy power spectrum, as shown in Fig. 3.7.

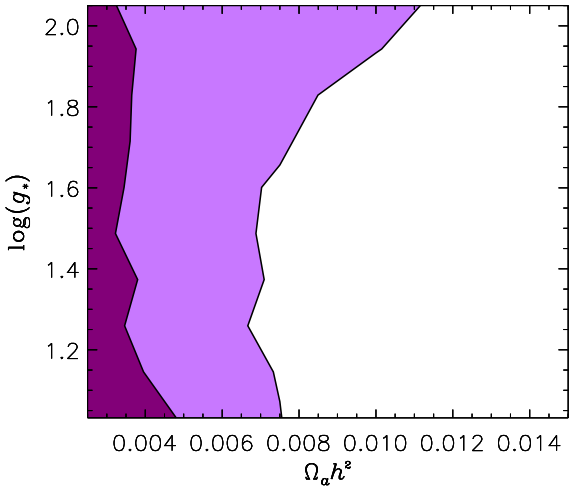

Figure 3.7 Minimum allowed $g_{*\rm S,F}$ for a variety of $\Omega_a h^2$, taken from Ref. [6], reproduced here with permission. The dark area shows the 1σ allowed region, while the region covered by the light and dark areas shows the 2σ allowed region. Taken together with the hadronic freeze-out relationship in a standard radiation dominated universe, these constraints impose the axionic mass bound $m_{\rm a} \lesssim 1.05$ eV.

We begin by mapping those contours (which do not include constraints from the Lyman-α forest), shown in Fig. 3.7), into the $\left(\Omega_a h^2, \lambda_{\rm fs}\right)$ plane. For a fixed $m_{\rm a}$ or $\Omega_{\rm a}$, $\lambda_{\rm fs}$ scales monotonically with $g_{*\rm S,F}$, and thus serves as a proxy for $g_{*\rm S,F}$.

In the domain $10\,{\rm MeV} \leq T_{\rm rh} \leq 250\,{\rm MeV}$ and $0.01\,{\rm eV} \lesssim m_{\rm a} \lesssim 10\,{\rm keV}$, we calculate $\Omega_{\rm a}\left(T_{\rm rh}, m_{\rm a}\right)h^2$ for hadronic axions in LTR, using the full numerical solution described in Sec. 3.3. We also calculate $\lambda_{\rm fs}\left(T_{\rm rh}, m_{\rm a}\right)$. Since axions freeze out while relativistic, their energy will redshift as $E \propto a^{-1}$. They will have temperature $T_{\rm a} = T_{\rm F} a_{\rm F}/a$. Meanwhile, the temperature of the coupled radiation redshifts as $T \propto a^{-3/8}$ until radiation domination begins. Thus entropy generation modifies the relationship between the axion and neutrino temperatures to

$$\frac{T_a}{T_\nu} \simeq \left(\frac{11}{4}\right)^{1/3} \left(\frac{T_{\rm rh}}{T_{\rm F}}\right)^{5/3} \left(\frac{g^2_{*,{\rm rh}} g_{*\rm S,0}}{g^2_{*,{\rm F}} g_{*\rm S,rh}}\right)^{1/3}, \tag{3.23}$$

if $T_{\rm F} > T_{\rm rh}$. To obtain all of our constraints we use the more precise scaling accounting for the smooth transition between the $T \propto a^{-3/8}$ and $T \propto a^{-1}$ regimes. The dominant change to the free-streaming length comes from the modified axion temperature, while the modified expansion rate itself induces negligible fractional changes of order $T_{\rm NR}/T_{\rm rh}$, where $T_{\rm NR}$ is the cosmic temperature at which the axion goes non-relativistic.

For each pair $(T_{\rm rh}, m_{\rm a})$, we calculate $\Omega_{\rm a}h^2$ and $\lambda_{\rm fs}$ to trace out the region forbidden with 95%

confidence. When $\Omega_{\rm a}\left(T_{\rm rh}, m_{\rm a}\right) h^2 > 0.014$, outside the domain of Ref. [224], we extrapolate, assuming that the 95% contour asymptotes to a line of constant axion free-streaming wavelength $\lambda_{\rm fs} = 40\ h^{-1}$ Mpc. Such a trend is noted in Ref. [224], and at the maximum value of $\Omega_{\rm a}h^2$ of the contour obtained from Ref. [6], the maximum allowed free-streaming length is consistent with our assumed asymptote.

We obtain the upper limit to the axion mass as a function of $T_{\rm rh}$, shown in Fig. 3.6. Existing LSS/CMB constraints are severely relaxed in the LTR scenario, and lifted completely for $T_{\rm rh} \lesssim 35$ MeV. For $T_{\rm rh} \lesssim 35$ MeV, $\lambda_{\rm fs} < 40\ h^{-1}$ Mpc for $m_{\rm a} \gtrsim 1$ eV, and so the axion mass is cosmologically constrained only by the condition $\Omega_{\rm a}h^2 \lesssim 0.135$. It will still be subject to phase-space constraints if it is to compose all the dark matter in galactic halos [105–107]. Applying Eq. 2.27, we see that the galactic phase space constraint with $x_{\rm a} = \Omega_{\rm a}/\Omega_m = \Omega_{\rm D}/\Omega_m$ is $m_{\rm a} > 22$ eV. Thus, for $T_{\rm rh} < 35$ MeV, there is an open axion mass window (which actually depends on $T_{\rm rh}$, but we give rough numbers for simplicity) for 20 eV $\lesssim m_{\rm a} \lesssim$ 700 eV, provided other astrophysical constraints may be ignored. In future work, it will be interesting to apply the usual constraints to warm dark matter (WDM) candidates to further constrain such a possibility.

At high reheating temperatures, the constraint from LSS/CMB data ($\Omega_{\rm a}h^2 \lesssim 0.006$) supercedes the constraint $\Omega_{\rm a}h^2 \lesssim \Omega_{\rm m}h^2$. The narrow allowed region between the LSS/CMB and total matter density constraints in Fig. 3.6 (45 MeV $\lesssim T_{\rm rh} \lesssim$ 55 MeV) may be simply understood. Axions in this narrow window are cold and massive enough to evade large-scale structure constraints (i.e., $\lambda_{\rm fs} < \lambda_{\rm min}$), and dilute enough to evade constraints from the total matter density. We note that the CMB/LSS limits asymptote to their standard value of $m_{\rm a} \lesssim 1.4$ eV for $T_{\rm rh} \gtrsim 170$ MeV.

Future instruments, such as the Large Synoptic Survey Telescope (LSST), will measure the matter power-spectrum with unprecedented precision ($\Delta P/P \sim 0.01$) [225, 226]. This order of magnitude improvement over past work [20, 227] will improve the constraint to $\Omega_a h^2$ by an order of magnitude, resulting in the improved sensitivity to axion masses and reheating temperatures shown by the dotted line in Fig. 3.8. To estimate possible constraints to axions from LSST measurements of the power spectrum, we recalculated our limits using the approximate scaling $\Delta P/P \simeq -8\Omega_{\rm a}/\Omega_{\rm m}$, assuming $\Delta P/P \sim 10^{-2}$ for $\lambda > 40\ h^{-1}$ Mpc.

We also estimate the possible improvement offered by including information on smaller scales ($\lambda_{\rm min} \sim 1\ h^{-1}$ Mpc), as may be obtained from measurements of the Lyman-α flux power spectrum [228], also shown in Fig. 3.8. We include this effect by replacing $\lambda_{\rm min}$ with this lower minimum length scale. This is indicated by the dashed line in Fig. 3.8. We can see that more massive axions are probed because of information on smaller length scales, as are lower reheating temperatures.

In the case of kination, a much less severe relaxation of limits to axions is obtained. As there is no entropy generation in the kination case, the abundance and temperature of the axion are still given by Eqs. (3.1) and (3.22), with the value of $g_{*{\rm s,F}}$ appropriate at the new freeze-out temperature.

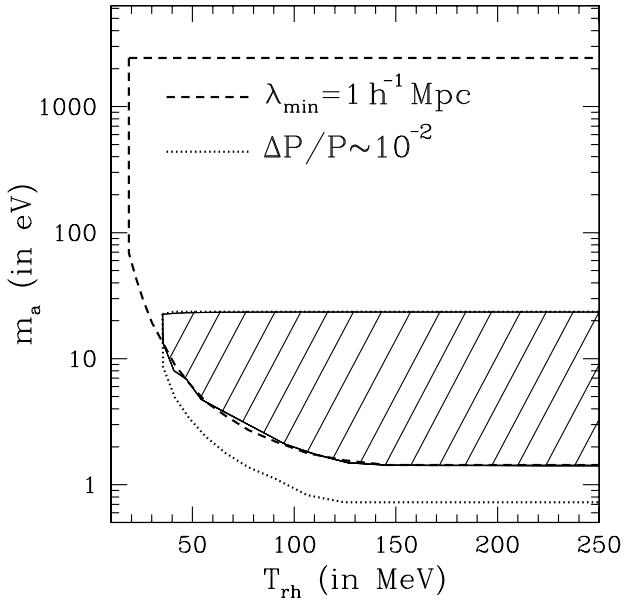

Figure 3.8 Estimated improvement in the accessible axion parameter space from including more precise measurements of the matter power spectrum (region bounded by the dotted line), corresponding to LSST [225, 226], or from measurements of clustering on smaller length scales, corresponding to Lyman-α forest measurements (region bounded by the dashed line) [228]. The hatched region indicates the parameter space excluded by WMAP1/SDSS measurements.

In the range of parameter space explored, 10 MeV $\lesssim T_{\rm F} \lesssim$ 100 MeV, and so the variation in $g_{*{\rm S,F}}$ as a result of kination is $\sim 60\%$. For $T_{\rm kin} \simeq 10$ MeV, the new allowed regions are $m_{\rm a} \lesssim 3.2$ eV and 17 eV $\lesssim m_{\rm a} \lesssim$ 26 eV. These conclusions apply to any non-entropy-generating scenario in which $H \propto T^3$ at some early epoch, and not only to kination [166]. If $T_{\rm rh} \gtrsim 110$ MeV, standard results are recovered.

3.5 Axions as relativistic degrees of freedom at early times

Future limits to axions in the standard radiation-dominated and LTR thermal histories may follow from constraints to their contribution to the energy density in relativistic particles at $T \sim 1$ MeV. Axions are relativistic spin-0 bosons, and so $\rho_{\rm a} \simeq \left(\pi^2/30\right) T_{\rm F}^4 \left(a_{\rm F}/a\right)^4 = \left(\pi^2/30\right) T_{\rm F}^4 \left(a_{\rm F}/a_{\rm rh}\right)^4 \left(a_{\rm rh}/a\right)^4$ [50]. We can express the total relativistic energy density in terms of an effective neutrino number

$$N_\nu^{\rm eff} \equiv \left(\frac{\rho_{\rm a}+\rho_\nu}{\rho_\gamma}\right)\left(\frac{8}{7}\right)\left(\frac{11}{4}\right)^{4/3}, \quad \rho_\gamma = \frac{\pi^2}{15}T^4,$$
$$\rho_\nu = \frac{7}{8}\left(\frac{4}{11}\right)^{4/3} \times 3 \times \left(\frac{\pi^2 T^4}{15}\right). \tag{3.24}$$

Treating the transition between the $T \propto a^{-3/8}$ and $T \propto a^{-1}$ epoch as instantaneous, we solve for the photon and axion temperatures, and then obtain

$$N_\nu^{\rm eff} = 3 + \tfrac{4}{7}\left(\tfrac{43}{4}\right)^{4/3} \Psi\left(T_{\rm F}/T_{\rm rh}\right),$$

The numerical solution is shown in Fig. 3.9.

$$\Psi\left(y\right) \sim \begin{cases} \left[g_{*_{\rm S},{\rm rh}} y^5 \left(\frac{g_{*,{\rm F}}}{g_{*,{\rm rh}}}\right)^2 - 1\right]^{-4/3} & \text{if } y \gg 1, \\ \left[g_{*_{\rm S},{\rm F}} - 1\right]^{-4/3} & \text{if } y \ll 1. \end{cases} \tag{3.25}$$

For sufficiently high masses, the axionic contribution saturates to $\delta N_\nu^{\rm eff} = 4/7$ at high reheating temperatures [93]. In Fig. 3.10, we show $N_\nu^{\rm eff,max}\left(T_{\rm rh}\right)$, the effective neutrino number evaluated at the axion mass which saturates the LSS/CMB bounds, for $T_{\rm rh} \gtrsim 35$ MeV, or saturates the constraint $\Omega_{\rm a} h^2 \sim 0.135$ for lower $T_{\rm rh}$. The behavior of the curve may be readily understood. As can be seen from Fig. 3.6, as we increase $T_{\rm rh}$, the maximum allowed $m_{\rm a}$ decreases. For $T_{\rm rh} \lesssim 20$ MeV, even though the maximum allowed $m_{\rm a}$ is large (which corresponds to a lower $T_{\rm F}$, since $\Gamma \propto m_{\rm a}^2$), the amount of entropy production between $T_{\rm F}$ and $T_{\rm rh}$ leads to a small axionic contribution to $N_{\rm eff}$. As $T_{\rm rh}$ increases, the interval between freeze-out and reheating decreases. This lessens the impact of entropy generation, and leads to the rise in $N_{\rm eff}$. Finally, for $T_{\rm rh} \gtrsim 20$ MeV, the impact of entropy generation is nearly negligible, and $N_{\rm eff}$ falls as the maximum allowed value of $m_{\rm a}$ decreases, as in the standard case (due to earlier freeze-out).

A comparison between the abundance of ^{4}He and the predicted abundance from BBN places constraints to the radiative content of the Universe at $T \sim 1$ MeV [229]; this can be stated as a constraint to $N_\nu^{\rm eff}$. At early times, axions will contribute to the total relativistic energy density (through $N_\nu^{\rm eff}$), and thus constraints to ^{4}He abundances can be turned into constraints on $m_{\rm a}$ and $T_{\rm rh}$, as shown in Fig. 3.10.

In terms of the baryon-number density n_b, we write the primordial ^{4}He abundance as $Y_{\rm p} \equiv 4 n_{\rm He}/n_b$. In order to translate measurements of $Y_{\rm p}$ to constraints on $m_{\rm a}$ and $T_{\rm rh}$ we use the scaling relation [231]

$$\Delta N_\nu^{\rm eff} = \frac{43}{7}\left\{\left(6.25 \Delta Y_p + 1\right)^2 - 1\right\}. \tag{3.26}$$

Constraints to $N_\nu^{\rm eff}$ from direct measurements of Y_p, including a determination of n_b from CMB observations, lead to the 68% confidence level upper limit of $N_\nu^{\rm eff} \leq 3.85$ [232–234]. From Fig. 3.10 and Eq. (3.25), we see that this bound cannot constrain $m_{\rm a}$ or $T_{\rm rh}$. If future measurements reduce systematic errors, constraints to $T_{\rm rh}$ will be obtained for lighter-mass axions.

Constraints to $m_{\rm a}$ and $T_{\rm rh}$ may also follow from indirect CMB measurements of Y_p. The presence of ^{4}He affects CMB anisotropies by changing the ionization history of the universe [235, 236].

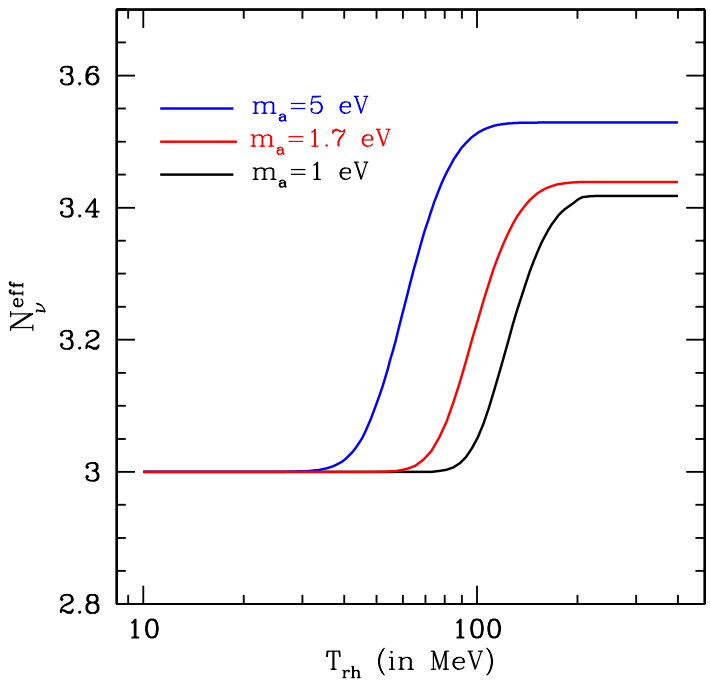

Figure 3.9 Effective neutrino number $N_\nu^{\rm eff}$ as a function of reheating temperature $T_{\rm rh}$ for 3 different axion masses.

Polarization anisotropies are the result of Thompson scattering of a temperature quadrupole. The scattering rate $\sim n_e \sigma_{\rm T} c$, and so changes to the helium abundance will change the level of polarization anisotropy. The Planck satellite is expected to reach $\Delta Y_{\rm p} = 0.013$, yielding a sensitivity of $N_\nu^{\rm eff} \leq 4.04$, while CMBPol (a proposed future CMB polarization experiment) is expected to approach $\Delta Y_p = 0.0039$, leading to the sensitivity limit $N_\nu^{\rm eff} \leq 3.30$ [230, 234, 235, 237]. As shown in Fig. 3.10, for $T_{\rm rh} \gtrsim 15$ MeV, such measurements of $Y_{\rm p}$ may impose more stringent limits on the axion mass. Also, if axions with mass in the eV range are directly detected by CAST or ADMX, Y_p might impose a surprising *upper* limit to $T_{\rm rh}$ [27, 28]. This is another specific example of how a direct detection experiment may be used in concert with cosmological data to meaningfully constrain the early thermal history of the universe.

3.6 Conclusions

The lack of direct evidence for radiation domination at temperatures hotter than 1 MeV has motivated the introduction of kination, low-temperature reheating, and other scenarios for an altered pre-BBN expansion history. In the case of kination, the change in axion abundances and thus cosmological constraints is modest. Low-temperature reheating will suppress the abundance of

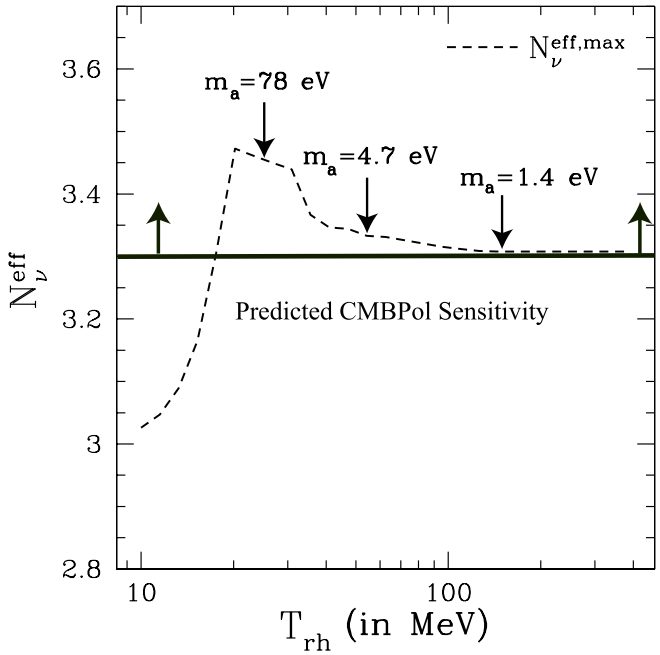

Figure 3.10 Total effective neutrino number $N_\nu^{\rm eff,max}$ for axions with masses saturating the tightest bound on axion masses from Fig. 3.6. The requisite higher temperatures lead to earlier axion freeze out and lower $N_\nu^{\rm eff,max}$. The thick black line indicates the anticipated sensitivity of CMBPol [230] to $N_\nu^{\rm eff}$ through the primordial helium abundance.

thermally-produced hadronic axions, once the reheating temperature $T_{\rm rh} \sim 50$ MeV. This is rather intuitive once we recall that the axion freeze-out temperature in a radiation dominated cosmology is ~ 50 MeV. If the reheating temperature crosses this threshold, axion densities are severely reduced by dramatic entropy production during reheating.

Total density, large-scale structure, and microwave background constraints to axions are all severely loosened as a result, possibly pushing the the axion mass window to very high values; for $T_{\rm rh} \simeq 10$ MeV, the new constraint is $m_{\rm a} < 1.4$ keV. For $T_{\rm rh} \gtrsim 170$ MeV, standard radiation dominated results are recovered. The inclusion of information on smaller scales will probe higher axion masses and lower reheat temperatures. More precise measurements of the matter power spectrum on all scales will probe lower axion masses. Kination also relaxes constraints to axions, though much less markedly. Future probes of primordial helium abundance will either lead to further constraints on axion properties, or, if axions are directly detected, provide a new view into the thermal history of the universe during the epoch 10 MeV $\lesssim T \lesssim$ 170 MeV.

Acknowledgments

The author thanks Tristan Smith and Marc Kamionkowski for their contributions to the research described in this chapter. The author acknowledges helpful discussions with Mark Wise, Stefano

Profumo, Sean Tulin, and Scott Watson. The author thanks Georg Raffelt and Steen Hannestad for permitting the use of a figure from Ref. [6]. This work was supported by DoE DE-FG03-92-ER40701, NASA NNG05GF69G, and the Gordon and Betty Moore Foundation.

Chapter 4
Cosmological hydrogen recombination: The effect of extremely high-n states[1]

4.1 Introduction

Measurements of cosmic microwave background (CMB) temperature anisotropies by the Wilkinson Microwave Anisotropy Probe (WMAP) have ushered in the era of precision cosmology, confirming that the Universe is spatially flat, with a matter budget dominated by dark matter and a baryonic mass fraction $\Omega_b h^2$ [17] in agreement with the measured ratio of deuterium-hydrogen abundances (D/H) [231]. WMAP measurements of large-scale CMB polarization also yield the optical depth τ to the surface of last scattering (SLS), meaningfully constraining cosmological reionization. Together with surveys of supernovae [238, 239], galaxies [240–242], and galaxy clusters [243], WMAP measurements build the case that the Universe's expansion is accelerating, due to "dark energy" or modifications of general relativity [244, 245], and constrain other physical parameters (such as the sum of neutrino masses $\sum_i m_{\nu_i}$ [246–248] and the effective number of massless neutrino species N_ν).

CMB temperature observations (WMAP, BOOMERANG [249], CBI [250] and ACBAR [251]) probe properties of the primordial density field, such as the amplitude A_s, slope n_s, and running α_s of its power spectrum. These observations constrain deviations from the adiabatic, nearly scale free and Gaussian spectrum of perturbations predicted by the simplest models of inflation, but also offer controversial hints of deviations from these models (see Refs. [17, 252] and references therein). Experimental upper limits to B-mode polarization anisotropies (e.g. DASI [253] and BICEP [254]) impose constraints to the energy density of relic primordial gravitational waves [255, 256].

The *Planck* satellite, launched in May 2009, will obtain extremely precise measurements of the CMB temperature anisotropy power spectrum ($C_\ell^{\rm TT}$) up to $\ell \sim 2500$ and the E-mode polarization anisotropy power spectrum ($C_\ell^{\rm EE}$) up to $\ell \sim 1500$ [35]. Robust measurements of the acoustic horizon and distance to the SLS will break degeneracies in dark energy surveys [35, 242, 257, 258]. Polarization measurements will yield the optical depth τ to the SLS [35], further constraining models of reionization and breaking the degeneracy between n_s and τ [35]. Cosmological parameters will

[1]The material in this chapter was adapted from *Cosmological hydrogen recombination: The effect of extremely high-n states*, Daniel Grin and Christopher M. Hirata; Phys. Rev. D **81**, 083005 (2010). Reproduced here with permission, copyright (2010) by the American Physical Society. Discussions of collisions (Sec. 4.5.1.2) and quadrupole results (Sec. 4.5.7) were significantly expanded for this thesis. The discussions of the physicality of high-n states (Sec. 4.3.1), population inversion (Sec. 4.5.2), the visibility function (Sec. 4.5.5.1), line overlap (Sec. 4.2.2.1), and of code comparisons (Sec. 4.5.4) are all new material.

be determined with much greater precision. More precise values of n_s and α_s will be obtained from CMB data alone, helping to robustly constrain inflationary models and alternatives to inflation [35]. The advent of *Planck*, ongoing (SPT [259] and ACT [260]) experiments at small scales, and a future space based polarization experiment like CMBPol [261, 262] all require predictions of primary anisotropy multipole moments C_ℓ with $\mathcal{O}(10^{-3})$ accuracy.

During atomic hydrogen (H) recombination, the Thomson scattering opacity drops, decoupling the baryon-photon plasma and freezing in acoustic oscillations. The phases of acoustic modes are set by the peak location of the visibility function [263, 264], while damping scales [265, 266] and the amplitude of polarization [267, 268] are set by its width. Small-scale CMB anisotropies are also smeared out by free electrons along the line of sight, suppressing power on small scales so that $C_\ell \rightarrow C_\ell e^{-2\tau(\chi_{\rm SLS})}$, where $\tau\left(\chi_{\rm SLS}\right)$ is the optical depth to the SLS [38]. An accurate prediction of the time-dependent free-electron fraction $x_e(z)$ from cosmological recombination is thus essential to accurately predict CMB anisotropies.

Recent work has highlighted corrections of $\Delta x_e(z)/x_e(z) \gtrsim 0.1\%$ to the standard recombination history computed by RecFast [269]. These corrections will propagate through to predictions of anisotropies, and neglecting them would lead to biases and errors in *Planck* measurements of cosmological parameters [41, 270]. The use of the CMB as a probe of the first ionizing sources and of physics at energy scales greater than 10^{16} GeV thus requires an accurate treatment of the $\sim$ eV atomic physics of recombination [271].

Direct recombination to the hydrogen ground state is ineffective because of the high optical depth to photoionization [272, 273]. Recombination proceeds indirectly, first through recombination to a $n \geq 2$ state of H, and then by cascades to the ground state. Because of the optical thickness of the Lyman-n (Lyn) lines, the resulting radiation may be immediately absorbed, exciting atoms into easily ionized states.

There are two ways around this bottleneck [272, 273]. In the first, the sequence of decays from excited H levels ends with a two-photon decay (usually $2s \rightarrow 1s$). The emitted photons may have a continuous range of energies, allowing escape off resonance and a net recombination. In the second, photons emitted in the $np \rightarrow 1s$ transition redshift off resonance due to cosmological expansion, preventing re-excitation and yielding some net recombination. The dominant escape channel is from the $2p \rightarrow 1s$ Lyman-α line. The two-photon recombination channel dominates at high-z, while cosmological expansion driven escape off the $2p \rightarrow 1s$ resonance dominates at low-z. Roughly equal fractions of the neutral hydrogen formed during recombination forms by each channel.

Optically thick resonances like the Lyman series (as well as the optically thin Balmer series and the rest of the tower of resonant transitions in hydrogen) give off line radiation and distort the CMB [274, 275]. It is an open question whether or not these line distortions to the CMB are detectable. The Lyman series causes order unity distortions to the CMB, but is likely totally obscured by the

far infrared background (FIRB), while the remaining resonances likely cause a distortion of just 1 part in $\sim 10^7$ on top of an already-faint CMB blackbody [7].

These distortions have a unique spectral signature, making them in principle easier to detect, but at lower frequencies free-free absorption may consume the signal. At the lowest frequencies, these distortions flatten into an additional continuum on top of the CMB blackbody, and would be extremely challenging to detect. If these distortions are detectable, they may offer our only direct window into the universe behind the screen of the SLS. This would be considerably more feasible if population inversion and amplification yielded masing in the early universe, but that would take a very specific set of physical conditions at early times. It seems unlikely that nature would be so generous, but it is important to properly model recombination to be sure, and to predict $x_e(z)$ for use in CMB data analysis.

Peebles, Sunyaev, Kurt, and Zel'dovich modeled recombination assuming that all net recombination resulted from escaping the $n = 2$ bottleneck [272, 273]. This three-level-atom (TLA) treatment included recombinations to excited states, under the assumption of equilibrium between energy levels n and angular momentum sublevels l for all $n \geq 2$ (note the use of l for atomic angular momentum and ℓ for CMB multipole number). This sufficed until the multi-level-atom (MLA) model of Seager et al. [276], which included hydrogen (H) and helium (He), separately evolved excited states assuming equilibrium between different l, accurately tracked the matter/radiation temperatures $T_{\rm M}/T_{\rm R}$ [277, 278], accounted for line emission using the Sobolev approximation [279], and included H_2 chemistry. This treatment underlies the RecFast module used by most CMB anisotropy codes, including those used for WMAP data analysis [269].

The higher precision of *Planck* requires new physical effects to be considered, among them two-photon transitions from higher excited states in H and He [280–284], other forbidden and semiforbidden transitions in He [285–287], feedback from Lyn lines [288], and corrections to the Sobolev approximation due to a host of radiative transfer effects in H and He resonance lines [39, 284, 289, 290]. Most recent work on recombination has focused in one way or another on the radiative transfer problem. Here we direct our attention to the populations of very high-n states, although we also note ongoing efforts to apply our computational tools to the problem of overlap between Ly lines at high n [291].

One important effect is the breakdown of statistical equilibrium between states with the same value of the principal number n but different angular momenta l. This effect is dramatic at late times. When l sublevels of a level n are resolved, increases in $x_e(z)$ of $\sim 1\%$ at late times result [7, 8]. This changes predicted C_ℓs at a statistically significant level for *Planck*. Highly excited states in hydrogen also change the recombination history at a level significant for *Planck*. While levels as high as $n = 300$ were included in the treatment of Ref. [276] underlying RecFast, l sublevels were not resolved. It is thus important to update cosmological recombination histories to include high-n

states of H while resolving l sublevels, in order to predict the C_ℓs as well as CMB spectral distortions from resonant hydrogen lines during recombination.

Simultaneously including very high n and resolving the l sublevels is computationally expensive, taking nearly a week on a standard workstation for $n_{\rm max} = 100$ [8], using a conventional multilevel-atom recombination code. This becomes prohibitively expensive for higher values of $n_{\rm max}$, unless considerable resources are devoted to the problem. To date, this has prevented a determination of how $x_e(z)$ converges with $n_{\rm max}$ and how high $n_{\rm max}$ must be to predict C_ℓs for *Planck*. The existence of electric dipole selection rules $\Delta l = \pm 1$ means the relevant rate matrices are sparse, and we have used this fact to develop a fast code, RecSparse, to explore convergence with $n_{\rm max}$. While the computation time $t_{\rm comp}$ for standard l-resolving recombination codes scales as $t_{\rm comp} \propto n_{\rm max}^6$, with RecSparse the scaling is $t_{\rm comp} \propto n_{\rm max}^\alpha$, where $2 < \alpha < 3$. With RecSparse, we can calculate recombination histories for $n_{\rm max} = 200$ in 4 days on a standard work-station; this would likely take weeks using a conventional code. For the first time, we have calculated recombination histories for $n_{\rm max}$ as high as 250 *with l sublevels resolved*. More recent work presented in Ref. [9] is in excellent agreement with our results.

While previous computations have included some forbidden transitions, none have included optically thick electric quadrupole (E2) transitions in atomic hydrogen. We include E2 transitions, and find that the resulting correction to CMB anisotropies is negligible.

We find that the correction to CMB C_ℓs due to extremely excited levels is 0.5σ or less if $n_{\rm max} \geq 128$, in the purely radiative case. While we do see some inversion of atomic populations, it is not dramatic enough to deliver a global maser from the recombination process. This work is not the final word on recombination; atomic collisions must be properly included and the effect of levels with $n > n_{\rm max}$ must be included to conclusively demonstrate absolute convergence. The end goal of the present recombination research program is to include all important effects in a replacement for RecFast, as the interplay of different effects is subtle.

In Sec. 4.2, we review the formalism of the multilevel atom (MLA). We then review why extremely high-n states are physical and discuss to we include them in the MLA (Sec. 4.3). We discuss the theory of electric quadrupole transitions and their addition to the MLA in Sec. 4.4. State populations, a discussion of population inversion, a discussion of the effect of collisions, recombination histories, comparisons with other codes, and effects on the C_ℓs are presented in Sec. 4.5. We conclude in Sec. 4.6. We use the same fiducial cosmology as in Ref. [292]: total matter density parameter $\Omega_m h^2 = 0.13$, $\Omega_b h^2 = 0.022$, $T_{\rm CMB} = 2.728$ K, $N_\nu = 3.04$, and helium mass fraction $Y_{\rm He} = 0.24$.

4.2 The standard multilevel atom

We now review the elements of the standard multilevel-atom (MLA) treatment of cosmological recombination. For fundamental constants, we use NIST (National Institute of Standards and Technology) CODATA (Committee on Data for Science and Technology) values everywhere [293]. Unless explicitly noted otherwise, we make the substitution $m_e \rightarrow \mu = m_e m_p / (m_e + m_p)$ in all expressions for the Bohr radius a_0 and the ground-state hydrogen ionization potential $I_{\rm H}$ to correctly account for reduced-mass effects.

4.2.1 Basic framework

CGS units are used except where explicitly noted otherwise. We follow the abundance $x_{n,l} = \eta_{n,l}/\eta_{\rm H}$, where $\eta_{\rm H}$ is the total number density of hydrogen nuclei and $\eta_{n,l}$ is the density of hydrogen in a state with principal quantum number n and angular momentum l (we denote the state $[n, l]$). We evolve these abundances including bound-bound and bound-free radiative, single photon, dipole transitions, as well as the $2s \rightarrow 1s$ two-photon transition, which has rate $\Lambda_{2s,1s} = 8.2245809\ {\rm s}^{-1}$ [294]. Focusing on the effect of single-photon dipole processes at high $n_{\rm max}$, we neglect higher n two-photon processes but note that their effects are large enough that they must be included in a final recombination code [280–283, 285]. Note that we also neglect collisional transitions. We comment on how this may change our conclusions in Sec. 4.5.1.1.

Bound-bound electric dipole processes are described by the equation [272, 276, 283]

$$\dot{x}_{n,l}|_{\rm bb} = \sum_{n' \neq n, l' = l \pm 1} \left(\Gamma^{l,l'}_{n,n'} x_{n',l'} - \Gamma^{l',l}_{n',n} x_{n,l} \right), \tag{4.1}$$

with

$$\Gamma^{l,l'}_{n,n'} = \begin{cases} A^{l,l'}_{n,n'} P^{l,l'}_{n,n'} \left(1 + \mathcal{N}^{+}_{nn'}\right) & \text{if } n' > n, \\ \\ A^{l',l}_{n',n} P^{l',l}_{n',n} \left(g_l / g_{l'}\right) \mathcal{N}^{+}_{n'n} & \text{if } n' < n, \end{cases} \tag{4.2}$$

where $A^{l,l'}_{n,n'}$ is the downward Einstein rate coefficient for decays from $[n', l']$ to $[n, l]$ and $P^{l,l'}_{n,n'}$ is the probability that a photon emitted in the $[n', l'] \rightarrow [n, l]$ line escapes the resonance without being reabsorbed. This probability is calculated in the Sobolev approximation, described in Sec. 4.2.2. For lower l states easily described using the $s, p, d, f...$ orbital notation, we will sometimes use the notation $A^{0,1}_{1,n} = A_{np,1s}$, $P^{0,1}_{1,n} = P_{np,1s}$, and so on to simplify the discussion . The degeneracy of $[n, l]$ is $g_l = 2(2l + 1)$. We explicitly keep track of the angular momentum quantum number l, as this will simplify discussion of our sparse-matrix technique in Sec. 4.3.4.

The photon occupation number blueward/redward of a line transition ($[n', l'] \rightarrow [n, l]$) is denoted

$$\mathcal{N}^{\pm}_{nn'} = \mathcal{N}\left(E_{n,n'} \pm \epsilon, T_{\rm R}\right), \tag{4.3}$$

where $\mathcal{N}\left(E, T_{\rm R}\right)$ is the photon occupation number at photon energy E and radiation temperature $T_{\rm R}$. Here ϵ is an infinitesimal line width and $E_{n,n\prime}$ is the energy of a photon produced in the transition $[n', l'] \rightarrow [n, l]$. The simplest possible assumption for $\mathcal{N}\left(E, T_{\rm R}\right)$ is a blackbody; we discuss further subtleties in Sec. 4.2.2:

$$\mathcal{N}\left(E_{n,n'}, T_{\rm R}\right) = \frac{1}{e^{E_{n,n'}/(kT_{\rm R})} - 1}. \tag{4.4}$$

Here k is the usual Boltzmann constant. The $\left(1 + \mathcal{N}^{+}_{nn'}\right)$ term accounts for stimulated and spontaneous emission.

The two-photon term is [272, 276, 283]

$$\dot{x}_{2s\rightarrow 1s}|_{2\gamma} = -\,\dot{x}_{1s\rightarrow 2s}|_{2\gamma} = \Lambda_{2s\rightarrow 1s}\left[-x_{2s} + x_{1s}e^{-E_{2s,1s}/(kT_{\rm R})}\right], \tag{4.5}$$

where $E_{2s,1s} = E_{2,1}$ and the second term describes two-photon absorption with a rate coefficient obtained by requiring that forward/backward rates satisfy the principle of detailed balance.

The bound-free term is [272, 276, 283]

$$\dot{x}_{n,l}|_{\rm bf} = \int \left[\eta_{\rm H} x_e^2 \alpha_{nl}\left(E_e\right) S\left(S_e, T_{\rm M}, T_{\rm R}\right) - x_{n,l} I\left(E_e, T_{\rm r}\right)\right] dE_e, \tag{4.6}$$

with

$$S\left(E_e, T_{\rm M}, T_{\rm R}\right) = \left[1 + \mathcal{N}\left(E_\gamma, T_{\rm R}\right)\right] P_{\rm M}\left(E_e, T_{\rm M}\right) \tag{4.7}$$

and

$$I\left(E_e, T_{\rm R}\right) = \beta_{nl}\left(E_e\right) \mathcal{N}\left(E_\gamma, T_{\rm R}\right). \tag{4.8}$$

This integral is over the total energy E_e of a recombining electron. The energy of a recombination photon is $E_\gamma = E_e - E_n$, where E_n is the bound-state energy of the recombined electron. The recombination rate in cm^3 s^{-1} of such an electron to the bound state $[n, l]$ is $\alpha_{nl}\left(E_e\right)$ and is discussed in Sec. 4.3.3.2. The ionization rate in s^{-1} is $\beta_{nl}\left(E_e\right)$, and easily shown by detailed balance considerations to be [283]

$$\beta_{nl}\left(E_e\right) = \alpha_{nl}\left(E_e\right) \frac{2^{7/2}\pi\sqrt{E_e \mu^3}}{h^3 g_l}. \tag{4.9}$$

The free-electron abundance is $x_e = \eta_e/\eta_{\rm H}$, where η_e is the free-electron density. We restrict our attention to times after helium recombination, and so the free proton abundance $x_p = x_e$. The net bound-free rate [Eq. (4.6)] includes both spontaneous and stimulated recombination. The electron energy distribution is a Maxwellian with matter temperature $T_{\rm M}$:

$$P_M\left(T_M, E_e\right) = 2\sqrt{\frac{E_e}{\pi\left(kT_{\rm M}\right)^3}}e^{-E_e/(kT_{\rm M})}. \tag{4.10}$$

4.2.2 Radiative transfer and escape probabilities

Numerically solving the radiative transfer problem is computationally intensive, but tremendous simplification can be achieved with the Sobolev escape probability formalism, also known as the Sobolev approximation [279]. The Hubble flow can be used to define a lengthscale over which the bulk flow induces a velocity change equal to the thermal velocity: $L = \sqrt{3kT_{\rm M}/m_{\rm atom}}/H(T_{\rm R})$, where $H\left(T_{\rm R}\right)$ is the value of the Hubble expansion parameter when the radiation has temperature $T_{\rm R}$ and $m_{\rm atom}$ is the mass of an atom [276]. The conditions of the Sobolev approximation are [276, 279, 292]: (i) L is much smaller than the typical length scales over which cosmological quantities vary, (ii) L/c is much smaller than the typical time scales over which cosmological quantities vary, (iii) complete frequency distribution— the rest-frame frequency of an outgoing scattered photon ν does not depend on the incoming frequency ν'— and (iv) no other emission, absorption, or scattering processes occur in the vicinity of the line. Corrections to the Sobolev approximation result from diffusion around resonance lines [295, 296], atomic recoil [292, 297], Thomson scattering near resonances [298, 299], and overlap of the higher Ly series lines, leading to important corrections to cosmological recombination calculations. In this work, however, we work in the Sobolev approximation to focus on other physical effects.

In the Sobolev approximation, the escape probability for photons produced in the downward transition $[n', l'] \rightarrow [n, l]$ is [276]

$$P_{n,n'}^{l,l'} = \frac{1 - e^{-\tau_{n,n'}^{l,l'}}}{\tau_{n,n'}^{l,l'}}, \tag{4.11}$$

where the Sobolev optical depth is given by

$$\tau_{n,n'}^{l,l'} = \frac{c^3\eta_{\rm H}}{8\pi H\nu_{n,n'}^3}A_{n,n'}^{l,l'}\left(\frac{g_{l'}}{g_l}x_{n,l} - x_{n',l'}\right), \tag{4.12}$$

with transition frequency

$$\nu_{n,n'} = \frac{E_{n,n'}}{h} = \frac{I_{\rm H}}{h}\left|\frac{1}{n^2} - \frac{1}{n'^2}\right|. \tag{4.13}$$

Correct expressions for $n' < n$ are obtained by reversing arguments. During cosmological recombination, transitions between excited states are optically thin ($P_{n,n'}^{l,l'} \geq 0.99972$) [283], and so we set

$P^{l,l'}_{n,n'} = 1$ in our calculations for non-Lyman lines. The solution for the radiation field near isolated Lyn lines has the approximate analytic solution [300]

$$\mathcal{N}^{-}_{n1} = \mathcal{N}^{\rm eq}_{n1} + \left(\mathcal{N}^{+}_{n1} - \mathcal{N}^{\rm eq}_{n1}\right) e^{-\tau^{ll'}_{n1}}$$
$$\mathcal{N}^{\rm eq}_{n1} \equiv \frac{x_{np}}{3x_{1s}}. \tag{4.14}$$

Transitions in the Lyman (Ly) series ($n' > n = 1$, $l' = 1$, $l = 0$) are optically thick ($\tau^{l,l'}_{n,n'} \gg 1$) [283], and so $P^{0,1}_{1,n'} \simeq 1/\tau^{0,1}_{1,n'}$. Ly transitions cannot, however, be ignored in the recombination calculation, as the rate at which atoms find their way to the ground state through the redshifting of resonance photons, $P^{0,1}_{1,n'}A^{0,1}_{1,n'}$ is comparable to $\Lambda_{2s\rightarrow 1s}$ and other two-photon rates [283]. Strictly speaking, $\tau^{0,1}_{1,n'}$ depends on $x_{n',1}$, and so one should solve for $x_{n',1}$ and then iteratively improve the solution. The populations of the excited states, however, are very small and the maximum resulting correction to the optical depth is 2×10^{-12} (for $n' = 2, z = 1600$) [283]. We thus drop the second term in Eq. (4.12), simplifying our computation by working in the approximation where the Lyman-n (Lyn) line optical depth depends only on the ground-state population and not on the excited-state populations.

Another aspect of the Lyman-series lines is feedback: a photon that escapes from the Lyn ($np \rightarrow 1s$) line will redshift into the Ly$(n-1)$ line and be reabsorbed. RecSparse has the ability to implement the resulting feedback, using the iterative technique of Ref. [300]. This slows down the code by a factor of a few, however, and so to efficiently focus on the $n_{\rm max}$ problem, we turned feedback off. For the high Lyman lines, feedback is almost instantaneous: the Universe expands by a factor of $\Delta \ln a \approx 2n^{-3}$ during the time it takes to redshift from Lyn to Ly$(n-1)$. In the instantaneous-feedback limit, the Lyn lines do not lead to a net flux of H atoms to the ground state. To approximate this net effect we turned off Lyman transitions with $n > 3$; this leads to a smaller error than would result from leaving these transitions on but disabling feedback. Previous tests using the code of Ref. [292] show resulting errors in the recombination history at the $\approx 1\%$ level; in any case, this should only weakly be related to the $n_{\rm max}$ problem. All of the recombination histories and plots in this chapter were produced by running RecSparse with both feedback and Lyman transitions from $n > 3$ disabled, unless noted otherwise. Using the toolkit provided by RecSparse, we are also exploring extensions to the Sobolev approximation.

4.2.2.1 Line overlap

It is a well known fact that at high n, the separation between adjacent Ly series lines shrink:

$$\nu_{n+1} - \nu_n = \frac{I_{\rm H}}{h}\left[\frac{1}{n^2} - \frac{1}{(n+1)^2}\right] \simeq \frac{2I_{\rm H}}{hn^3}. \tag{4.15}$$

The thermal motion of atoms leads to Doppler broadening of the line, and so it is clear that at any given temperature, there is a transition value $n = n_{\rm o}$ above which neighboring lines overlap. In other words, the fates accessible to a photon produced in the overlapping regime of the Ly-n resonance extend beyond re-absorption by the Ly-n line or escape (until red-shifting brings it into the next Lyman line). This photon may also be immediately re-absorbed by other nearby Ly lines [e.g. Ly-$(n+1)$, Ly-$(n-1)$, and so on]. The Doppler width of a Lyman line is given by

$$\Delta\nu_n = \nu_n \sqrt{\frac{2kT_{\rm M}}{m_p c^2}}, \tag{4.16}$$

where m_p is the proton mass. We can obtain the line-overlap condition by demanding that $\Delta\nu_n \gtrsim \nu_{n+1} - \nu_n$, thus yielding

$$n \gtrsim n_{\rm o} \equiv 44 \left(\frac{T_{\rm M}}{3000\ {\rm K}}\right)^{-1/6} \tag{4.17}$$

as the requirement for overlap of adjacent Ly lines [291]. For yet higher n, high-lying Ly lines will even overlap with the continuum. Similar arguments then lead to the condition

$$n \gtrsim n_{\rm c} \equiv 206 \left(\frac{T_{\rm M}}{3000\ {\rm K}}\right)^{-1/4} \tag{4.18}$$

for Ly line overlap with the continuum. Once this condition kicks in, the large reservoir of ionizing photons could feed the recombination network through an additional channel due to overlap between the continuum and the Lyman series, pumping atoms into excited states, but also providing a new channel to the ground state. Modern recombination codes routinely probe $n > n_{\rm max} = 100$ [7–9, 44]. Indeed, in the work described in this chapter and later work by others, substantial effort was devoted to determining the value of $n_{\rm max}$ required for adequate convergence in the recombination history. Since Ly line overlap becomes important at high n, it is important to properly treat the effect of line overlap on recombination.

Line overlap explicitly breaks assumption iv) of the Sobolev approximation: (iv) no other emission, absorption, or scattering processes occur in the vicinity of the line. Fortunately, the same techniques used to solve for the occupation number $\mathcal{N}\left(E_{n,n'} \pm \epsilon\right)$ in the Sobolev approximation may be readily generalized. The results may be written in a form that lends itself to straightforward numerical integration, as shown in recent work by Y. Ali-Haïmoud [291]. Qualitatively speaking, for $n \gtrsim n_o$ (though it turns out small corrections due to overlap already appear at $n \gtrsim 22$), the solution for the occupation number [Eq. (4.14)] must be replaced with a sum over overlapping Lyman lines, and the portion of the rate matrix corresponding to $np \rightarrow n'p$ transitions must be adjusted to include overlap terms. Using the RecSparse toolkit, we are working on the inclusion of these corrections [291]. Preliminary results indicate that the correction to $x_e\left(z\right) \lesssim 10^{-5}$ for $n \lesssim 150$, leaving most of

the conclusions in this chapter unchanged.

4.2.3 Matter and radiation temperatures

Electrons, though non-relativistic during recombination, interact with photons through Thompson scattering. As a result, they do not follow the simple adiabatic scaling $T_{\rm M} \propto a^{-2}$, where a is the cosmological scale factor. Rather, the matter temperature evolution equation is [277, 278, 301]

$$\dot{T}_{\rm M} = -2HT_{\rm M} + \frac{8x_e\sigma_{\rm T}a_{\rm R}T_{\rm R}^4}{3\left(1+f_{\rm He}+x_e\right)m_ec}\left(T_{\rm R}-T_{\rm M}\right). \tag{4.19}$$

The second term represents the coupling of electrons to photons through Compton scattering. At early times, the second term dwarfs the others and $T_{\rm M} = T_{\rm R}$, while after matter and radiation cease efficiently interacting, $T_{\rm M} \propto a^{-2}$. The Compton equilibration time is

$$t_{\rm comp} = \frac{3\left(1+f_{\rm He}+x_e\right)m_ec^2}{8x_e\left(c\sigma_{\rm T}\right)a_{\rm R}T_{\rm R}^4}. \tag{4.20}$$

When $t_{\rm comp} \ll 1/H(z)$, there is a convenient first-order asymptotic solution, derived in Ref. [283] using an appropriate integrating factor:

$$\frac{T_{\rm M}}{T_{\rm R}} \simeq 1 - \frac{3\left(1+f_{\rm He}+x_e\right)m_ecH}{8x_e\sigma_{\rm T}a_{\rm R}T_{\rm R}^4}. \tag{4.21}$$

Here $\sigma_{\rm T}$ is the Thompson scattering cross section, $a_{\rm R}$ is the radiation constant, $f_{\rm He} = Y_{\rm He}/\left[r\left(1-Y_{\rm He}\right)\right]$ is the He:H ratio by number, and $r = m_{\rm He}/m_{\rm H} \simeq 3.9715$ is the He:H atomic mass ratio. We neglect subdominant processes, such as free-free, line, photo-recombination and collisional ionization cooling, as well as photoionization and collisional recombination heating [276]. RecSparse output for the evolution of the ratio $T_{\rm M}/T_{\rm R}$ is shown for two cases in Fig. 4.1, one for which the asymptotic solution is used at all times, and one for the numerical solution to Eq. (4.19) is used after $z = 500$. We see that the error in the asymptotic solution is less than 10% of $T_{\rm M}/T_{\rm R}$ until $z \sim 200$. It may seem surprising that $T_{\rm M}$ stays so close to T_γ long after Thompson scattering freezes out at the SLS ($z \sim 1100$). After all, this is nominally when photons decouple from electrons. It is important to remember, however, that $\eta_\gamma/\eta_{\rm b} \gg 1$, where η_γ and $\eta_{\rm b}$ are the number densities of photons and baryons today, respectively. Until $z \sim 500$, a free electron can thus easily 'find' a photon, while a photon is unlikely to encounter a free electron. As a result, $T_{\rm M} \sim T_{\rm R}$ long after one might naively expect this to cease being the case. Unless noted otherwise for certain specific illustrative cases, we use the following prescription to evolve $T_{\rm M}/T_{\rm R}$ for the RecSparse results presented in this chapter: for $z \leq 500$, we solve Eq. (4.19) numerically, while for $z > 500$, we apply Eq. (4.21).

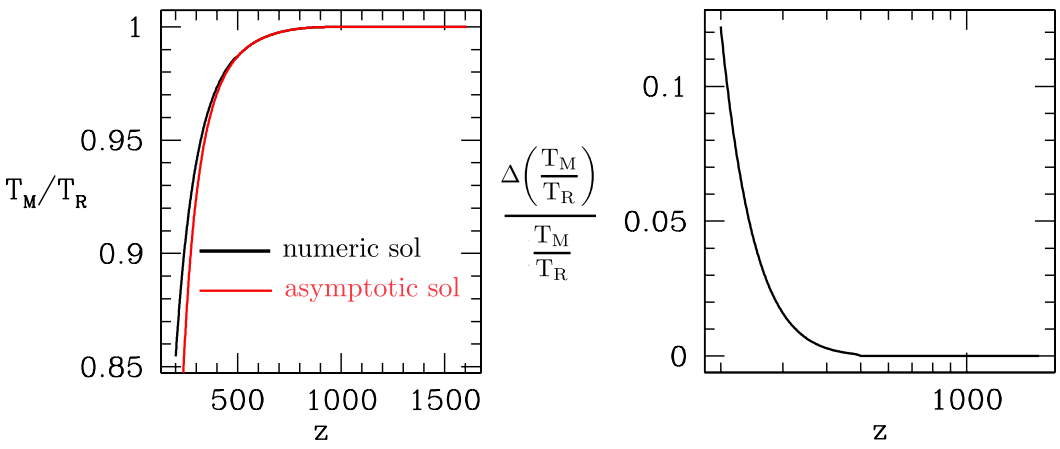

Figure 4.1 Evolution of the ratio of matter/radiation temperatures $T_{\rm M}/T_{\rm R}$ as a function of redshift z for a RecSparse run with $n_{\rm max} = 100$. The left panel shows $T_{\rm M}/T_{\rm R}$. The black curve corresponds to the asymptotic solution [Eq. (4.21)] for $z > 500$ and the numerical solution to Eq. (4.19) for $z \leq 500$. The right curve shows how the fractional error $\Delta\left(T_{\rm M}/T_{\rm R}\right)/\left(T_{\rm M}/T_{\rm R}\right)$ of the asymptotic solution evolves with z, where $\Delta\left(T_{\rm M}/T_{\rm R}\right) \equiv \left[\left(T_{\rm M}/T_{\rm R}\right)|_{\rm numeric} - \left(T_{\rm M}/T_{\rm R}\right)|_{\rm asymptotic}\right]$.

4.2.4 The steady-state approximation

The wide range of disparate time scales in this problem would naively necessitate a stiff differential equation solver. This computational expense can be avoided by repackaging Eqs. (4.1), (4.2),and (4.5)-(4.8). These equations may be rewritten for excited states as ($[n,l] \neq [1,0]$)

$$\dot{x}_{n,l} = -\sum_{n'l'} T^{l,l'}_{n,n'} x_{n',l'} + s_{n,l}, \tag{4.22}$$

with

$$T^{l,l'}_{n,n'} = \delta^{l,l'}_{n,n'} \left(\mathcal{I}_{nl} + \gamma_{nl} + \sum_{n'',l''} \Gamma^{l'',l'}_{n'',n'} \right) - \Gamma^{l,l'}_{n,n'}, \tag{4.23}$$

where the integrated photoionization rate from $[n,l]$ is

$$\mathcal{I}_{nl} = \int \beta_{nl}\left(E_e\right) I\left(E_e, T_{\rm R}\right) dE_e \tag{4.24}$$

and $\Gamma^{l,l'}_{n,n'}$ is defined in Eq. (4.2).

The downward flux to the ground state is

$$\gamma_{nl} = A^{0,1}_{1,n} P^{0,1}_{1,n} \left(1 + \mathcal{N}^{+}_{1n}\right) \delta_{l,1} + \Lambda_{2s,1s} \delta^{l,0}_{n,2}, \tag{4.25}$$

where the first term describes Lyn series transitions (stimulated and spontaneous) while the second accounts for the $[2,0] \rightarrow [1,0]$ two-photon transition. Kronecker delta symbols ($\delta^{l,l'}_{n,n'}$ and $\delta_{l,l'}$) are employed throughout to enforce $[n,l] = [n',l']$ and $l = l'$).

The source term s_{nl} includes flux from the ground state and direct recombination into the state $[n,l]$:

$$\begin{aligned} s_{n,l} &= \eta_{\rm H} x_e^2 \int \alpha_{nl}\left(E_e\right) S\left(E_e, T_{\rm M}, T_{\rm R}\right) dE_e + x_{1s}\Lambda_{2s,1s} e^{-E_{2s,1s}/(kT_{\rm R})}\delta^{l,0}_{n,2} \\ &+ x_{1s} g_l A^{0,1}_{1,n} P^{0,1}_{1,n} \mathcal{N}^{+}_{1n}\delta_{l,1}/2. \end{aligned} \tag{4.26}$$

This can also be rewritten in matrix notation: $d\vec{x}/dt = -\mathbf{T}\vec{x} + \vec{s}$, where $\mathbf{T}$ is the matrix of rates with components given by Eq. (4.23).

The left-hand side of Eq. (4.22) is associated with the recombination time scale, while both terms on the right-hand side are associated with much shorter atomic time scales. For example, the longest lifetimes in the recombination problem are those of the $2s$ and $2p$ states ($\Lambda_{2s,1s} \sim 10$ s and $A_{2p,1s}P_{2p,1s} \sim 1$ s when Ly-α optical depth peaks at $\tau \sim 6 \times 10^8$), considerably shorter than the recombination time scale of $t_{\rm rec} \sim 10^{12}$ s. Thus we make a steady-state approximation, $\dot{x}_{nl} = 0$, which is formally valid because the reciprocal of the minimum eigenvalue of $\mathbf{T}$ peaks at 0.8 s, which is $\sim 10^{-12}$ of the duration of recombination. Thus the excited-state abundances are given by

$$\vec{x} \simeq \mathbf{T}^{-1}\vec{s}. \tag{4.27}$$

The rates in $\mathbf{T}$ and $\vec{s}$ depend on x_e, x_{1s}, $T_{\rm M}$, $T_{\rm R}$, and $\mathcal{N}$. The ground-state population is given by $x_{1s} = 1 - x_e - \sum_{[n,l]\neq[1,0]} x_{n,l}$, but since excited-state populations are small ($x_{n,l} < 10^{-13}$), x_{1s} can be eliminated from Eq. (4.26) using the approximation $x_{1s} \simeq 1 - x_e$. We can then solve for the evolution of x_e, leaving out ineffective direct recombinations to the ground state:

$$\dot{x}_e \simeq -\dot{x}_{1s} = x_{1s}\Lambda_{2s,1s} e^{-E_{2s,1s}/(kT_{\rm R})} - \sum_{[n,l]\neq[1,0]} \left(\gamma_{nl} x_{n,l} - \frac{g_l}{2} A^{0,1}_{1,n} P^{0,1}_{1,n} \mathcal{N}_{1n} x_{1s}\delta_{l,1}\right). \tag{4.28}$$

The steady-state approximation thus allows us to convert a stiff system of ordinary differential equations into a large system of coupled linear algebraic equations, along with a single ordinary differential equation.

4.3 Recombination with high-n states

The original "effective 3-level atom" (TLA) treatments of cosmological recombination in Refs. [272, 273] were built on the assumption that the primary bottlenecks to effective recombination are the slow $2s \rightarrow 1s$ transition rate and the reabsorption of $2p \rightarrow 1s$ resonance photons by the optically

thick plasma. Other crucial assumptions included radiative equilibrium between excited states,

$$x_n = x_2 e^{-(E_n - E_2)/(kT_{\rm R})} n^2/4 \ \text{ if } n > 2, \tag{4.29}$$

$$x_n \equiv \sum_{l<n-1} x_{n,l}, \tag{4.30}$$

and statistical equilibrium between angular momentum sublevels:

$$x_{n,l} = x_n \frac{(2l+1)}{n^2}. \tag{4.31}$$

Recombination to higher excited states was included through an effective "Case B" total recombination constant $\alpha_B(T)$ (recombinations to the ground state are omitted) [272, 276].

As the radiation field cools and the baryon density falls at late times, the transitions coupling high-n to low-n become inefficient, as do those coupling different l sublevels with the same n. This leads to a breakdown of statistical equilibrium (note however that the steady-state approximation is still valid), and so Eqs. (4.30) and (4.31) cease to apply. In Ref. [276], Eq. (4.30) is relaxed while Eq. (4.31) is still imposed, and $\sim 10\%$ corrections to the TLA prediction for $x_e(z)$ result. At late times, nonequilibrium effects cause a net flux downward from states with quantum number n to the ground state, accelerating recombination. The inclusion of progressively more shells increases the number of downward cascade channels to the ground state for continuum electrons. Thus higher $n_{\rm max}$ leads to faster recombination and lower $x_e(z)$. Reference [276] reports results for $n_{\rm max}$ as high as 300. The Lyman ($np \to 1s$) transitions from very high-n states overlap with the Lyman continuum due to thermal broadening. Ref. [276] uses this fact to argue that the high-n *states* themselves are indistinguishable from the continuum, and that there is thus no need to go past $n = 300$. This is an incorrect line of reasoning, and it is important to correctly treat the problem of high-n convergence in cosmological recombination.

4.3.1 Are high-n states well-defined and physical?

The real question as to whether the different values of n are well defined is whether the broadening of the state, $\hbar/t$ (where t is the lifetime) is larger than the splitting of adjacent energy levels, $\Delta E^{\rm split} \approx 2 I_{\rm H} n^{-3}$. The intrinsic broadening for a typical level with $l/n \sim \mathcal{O}(1)$ is [302]

$$\Delta E \sim \hbar/t \sim \frac{\alpha^3 I_{\rm H}}{n^5}, \tag{4.32}$$

where $\alpha \simeq 1/137$ is the usual fine structure constant. For $l = 1$ states, the intrinsic width is dominated by Lyman-series transitions, and so [303]

$$\Delta E \sim \frac{\alpha^3 I_{\rm H}}{n^3}. \tag{4.33}$$

In the $l/n \sim \mathcal{O}(1)$ case, the condition $\Delta E \ll \Delta E^{\rm split}$ imposes the condition $n^2 \gg \alpha^3 \sim 10^{-6}$, which is clearly satisfied for any physical n. In the case of the $l = 1$ states, $\Delta E \ll \Delta E^{\rm split}$ imposes the consistency condition $2 \gg \alpha^3$, which is also obviously always true. Thus $\Delta E \ll \Delta E^{\rm split}$ and so these extremely high-n energy levels are well defined; indeed, transitions between highly excited states in such nonequilibrium plasmas are seen in interstellar H II regions and are a useful diagnostic of physical conditions [304]. States in the intermediate region between $l = 1$ and $l/n \sim \mathcal{O}(1)$ are bracketed by the range just described and are thus also well defined.

For extremely large n, the above physical argument may break down because of additional broadening contributed by interactions with the radiation field or the plasma. In the case of broadening due to stimulated emission and absorption, the additional (radiative) contribution to the width is

$$\Delta E \sim \hbar \sum_{n',l'=l\pm1} A^{l',l}_{n',n} \mathcal{N}\left(E_{n,n'}\right). \tag{4.34}$$

The Lyn lines are optically thick and thus $\mathcal{N}\left(E_{1,n}\right) \simeq x_{np}/\left(3x_{1s}\right)$, as can be seen from Eq. (4.14). As a result, $\mathcal{N}\left(E_{1,n}\right) < 10^{-13}$ [283] and Lyman-series transitions may be neglected from the sum in Eq. (4.34).

When $h\nu_{n',n} \gg kT_{\rm R}$, deep in the Wien tail of the microwave blackbody, photon occupation numbers are highly suppressed, and so non-Lyman transitions with $\Delta n = n' - n \gg n$ may also be neglected in Eq. (4.34). When $h\nu_{n',n} \ll kT_{\rm R}$ and $\Delta n \ll n$, the denominator of Eq. (4.4) may be expanded to yield

$$\mathcal{N}\left(E_{n',n}\right) \simeq \frac{kT_{\rm R}}{h\nu_{n',n}} \simeq \frac{kT_R}{I_{\rm H}} \frac{1}{\left|\frac{1}{n'^2} - \frac{1}{n^2}\right|} \simeq \frac{kT_{\rm R} n^3}{2I_{\rm H}\Delta n}, \tag{4.35}$$

where the last step follows from expanding $|1/n'^2 - 1/n^2|$ for $\Delta n \ll n$. Using the asymptotic expression for $\sum_{l',l} A^{l',l}_{n',n}$ (when $\Delta n \ll n$) in Ref. [305], we then obtain

$$\Delta E \sim \frac{16\alpha^3 kT_{\rm R}}{3\pi\sqrt{3}n^2} \sum_{\Delta n=1}^{\infty} \left(\frac{1}{\Delta n}\right)^2 = \frac{8\pi\alpha^3 kT_{\rm R}}{9\sqrt{3}n^2}. \tag{4.36}$$

Requiring that $\Delta E \ll \Delta E^{\rm split}$ then imposes the condition

$$\begin{aligned} n &\ll n^{\rm stim}, \\ n^{\rm stim} &\equiv \frac{9\sqrt{3}}{4\pi\alpha^3} \frac{I_{\rm H}}{kT_0\left(1+z\right)}, \end{aligned} \tag{4.37}$$

where T_0 is the CMB temperature today.

At sufficiently high distances from the atomic nucleus, the Coulomb potential from charged particles (predominantly electrons and protons in the primordial plasma) clustered around the nucleus will be comparable to the Coulomb potential of the hydrogen nucleus. This shielding occurs on the Debye length scale [306]:

$$R_D = \left(\frac{kT_{\rm M}}{4\pi\eta_e e^2}\right)^{1/2}. \tag{4.38}$$

Here e is the norm of the electron charge. This shielding may be ignored as long as the expectation value $\langle r^2\rangle_{nl} \ll R_D$. Otherwise, the contribution of free charge carriers in the plasma to the potential within the bound-electron radius may not be ignored, and for $r \gtrsim R_D$, a distorted potential, such as the Debye-Hückel potential, should be used to properly estimate transition energies and rates [307]. For a Coulomb hydrogen atom [303],

$$\langle r^2\rangle_{nl} = a_0^2 n^2 \left[\frac{5n^2 + 1 - 3l(l+1)}{2}\right]. \tag{4.39}$$

For a strict bound on the range of n for which this effect may be ignored, we wish the maximum value of $\langle r^2\rangle_{nl}$ given by Eq. (4.39) to obey the constraint $\langle r^2\rangle_{nl} \ll R_D$. We thus apply this inequality with the choice $l = 0$, yielding the constraint

$$\begin{aligned} n^4 &\ll n^4_{\rm Debye} \\ n^4_{\rm Debye} &\equiv \frac{kT_{\rm M}}{10\pi x_e \eta_{\rm H} x_e e^2 a_0^2}. \end{aligned} \tag{4.40}$$

In a sufficiently dense gas, loosely bound (high-n) electrons could find themselves close enough to nearby charge carriers that the energy shells are significantly distorted. In fact, this 'collisional broadening' may be strong enough that the energy levels become blended. This is essentially the well known Stark effect, and has been observed in spectral lines from stellar atmospheres. If the zero of a bound electron's energy is set at infinite distance from the hydrogen nucleus, the interaction energy with a neighboring charge carrier is $\Delta E \sim e^2\sqrt{\langle r^2\rangle_{nl}}/r_p^2$, where r_p is the typical distance between the perturbing charge carrier and the bound electron. If we demand, as before, that $\Delta E \ll \Delta E^{\rm split}$, then we obtain the condition [308]

$$\begin{aligned} n^5 &\ll n^5_{\rm Stark}, \\ n^5_{\rm Stark} &\equiv \sqrt{\frac{2}{5}}\frac{1}{\left(a_0^3\eta_e\right)^{2/3}}. \end{aligned} \tag{4.41}$$

In Fig. 4.2, we show $n_{\rm stim}$, $n_{\rm Debye}$ and $n_{\rm Stark}$ as computed using Eqs. (4.37), (4.40), and (4.41). Using Fig. 4.2, we verify that during the recombination epoch, radiation and plasma induced distortions of atomic energy levels may be ignored, as long as $n \lesssim 10^3$, a condition respected by all

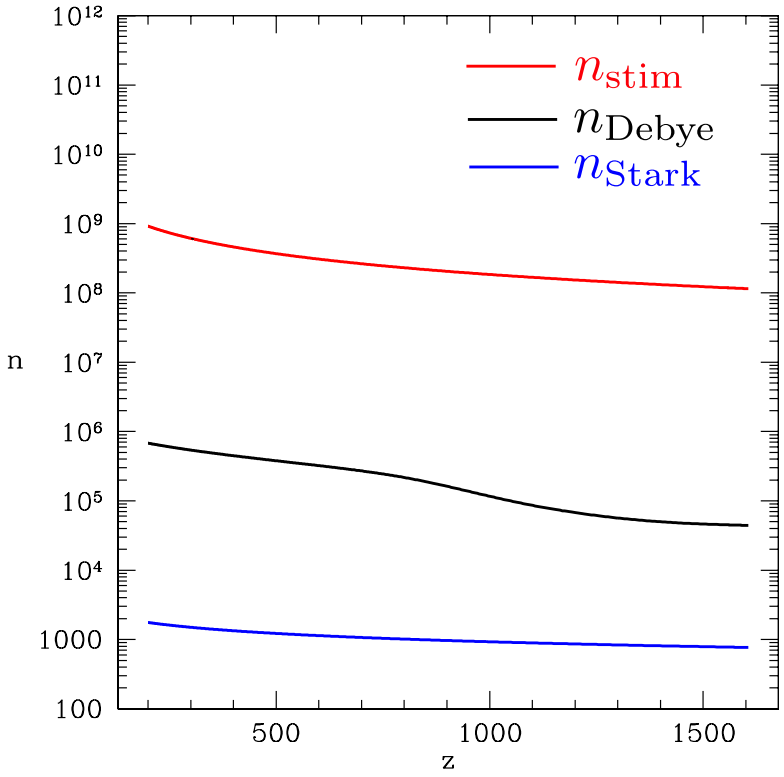

Figure 4.2 Transition shell numbers $n_{\rm stim}$, $n_{\rm Debye}$, and $n_{\rm Stark}$. For $n > n_{\rm max}$, the broadening of spectral lines due to stimulated emission/absorption, Debye screening, and collisions becomes comparable to the inter-level spacing. This plot was produced using a RecSparse run with $n_{\rm max} = 30$ and $T_{\rm M}$ given by Eq. 4.21.

RecSparse runs shown in this chapter. All the same, it is instructive to estimate the 'size' of the highly excited atoms we model in our computation. Roughly, $r \sim a_0 n^2 = 2\mu$m for $n = 200$. These are **very** big atoms! The constraints on stimulated emission and Debye screening are most easily satisfied ($n \ll 10^8$ and $n \ll 10^4$, respectively), while the constraint on collisional broadening is more marginal. For the $n_{\rm max}$ values considered in this paper, collisional broadening is still two orders of magnitude smaller than the inter-level spacing; it is conceivable, however, that future computations of recombination (with $n_{\rm max}$ higher by a factor of 3 or more) will require a more careful treatment of plasma effects. For the purposes of predicting $x_e(z)$ precisely enough for *Planck*, we may proceed onward and ignore broadening by stimulated emission/absorption, Debye screening, and collisional broadening. All we have established here is that the energy levels are well defined in spite of these potential complications. We must certainly still include stimulated emission/absorption in our rate equations [as done through Eq. (4.2)], and we may have to include l-changing collisions as well (an issue addressed in Sec. 4.5.1.2).

4.3.2 Computational challenges

Recent work [7, 8] shows that additional $\sim 1\%$ corrections to $x_e(z)$ arise when Eq. (4.31) is not imposed and the populations of l sublevels are followed separately. Bottlenecks to decays from high l imposed by $l' = l \pm 1$ slow down cascades to the ground state, and thus lead to slower recombination. In this case, the sidelength of $\mathbf{T}$ is $N = \mathcal{O}\left(n_{\rm max}^2\right)$. Since the number of computational steps needed to invert a matrix is generically a N^3 process, the computational time needed for a single ODE time step in the recombination time will be proportional to $n_{\rm max}^6$.

As noted in Ref. [8], a recombination calculation with $n_{\rm max} = 100$ already takes ~ 6 days on a standard workstation. It this thus difficult to explore how quickly $x_e\left(z\right)$ converges for progressively higher values of $n_{\rm max}$. Even between $n_{\rm max} = 80$ and $n_{\rm max} = 100$, $\sim 1\%$ changes are seen in the TT and EE multipole moments (C_ℓs) of the CMB. In Ref. [40], the results of Ref. [8] are used to explore the effect of progressively higher $n_{\rm max}$ on CMB C_ℓs. In that work, it is noted that the fractional difference between the C_ℓs for $n_{\rm max} = 60$ and $n_{\rm max} = 120$ falls within a heuristic *Planck* performance benchmark. Higher values of $n_{\rm max}$ come even closer to the fiducial case of $n_{\rm max} = 120$, a fact used to argue that even $n_{\rm max} = 60$ recombination is adequate for *Planck* data analysis.

From the Cauchy convergence criterion, however, we know that a meaningful convergence test requires a comparison between successive members in a sequence. Using the results of Ref. [8] alone, the question of convergence with $n_{\rm max}$ thus remains open. In spite of the computational challenge, it is thus crucial to push the calculation to sufficiently high $n_{\rm max}$ that corrections to $x_e(z)$ from remaining $n > n_{\rm max}$ are so small that they do not effect $C_\ell^{\rm TT}$ or $C_\ell^{\rm EE}$ at a level statistically significant compared to the predicted *Planck* sample variance (e.g., several parts in 10^4 for $l > 1000$) [299]. There are two challenges in treating such a big multilevel atom. The first is the calculation of atomic transition rates at extremely high n; this is tractable because of some convenient recursion relations. The second is simultaneously evolving the populations of $n_{\rm max}\left(n_{\rm max}+1\right)/2$ states. We discuss these in turn below.

4.3.3 Rates

Here we discuss the Einstein coefficients for dipole bound-bound and bound-free transitions in atomic hydrogen, which are used in our recombination computation. We omit reduced-mass corrections to make a consistent comparison with Refs. [302, 309–312], but include them when calculating actual recombination histories.

4.3.3.1 Bound-bound rates

The spontaneous electric dipole transition rate ${}^{(1)}A^{l',l}_{n',n}$ for a nonrelativistic hydrogen atom is given by [313]

$$ {}^{(1)}A^{l,l'}_{n,n'} = \frac{64\pi^4\nu^3_{n,n'}}{3hc^3}\frac{\max(l,l')}{2l+1}e^2a_0^2\left|{}^{(1)}X^{l,l'}_{n,n'}\right|^2, \tag{4.42} $$

$$ {}^{(1)}X^{l,l'}_{n,n'} \equiv \left[\int_0^\infty x^3 R_{n'l'}(x)R_{nl}(x)dx\right], \tag{4.43} $$

where e is the absolute value of the charge of an electron, h is Planck's constant, and ${}^{(p)}X^{l,l'}_{n,n'}$ denotes the radial matrix element between the states $[n,l]$ and $[n',l']$ at order p in the multipole expansion. For example, ${}^{(2)}A^{l',l}_{n',n}$ denotes the quadrupole rate, and so on.The restriction $l' = l \pm 1$ enforces electric dipole selection rules. Here $R_{nl}(x)$ is the radial wave function of an electron in a hydrogen atom, with principal quantum number n and angular momentum quantum number l, at a dimensionless distance x. All dimensionless distances are measured in terms of a_0. For Coulomb wave functions, this integration yields the Gordon formula [313]:

$$ {}^{(1)}X^{l,l'}_{n,n'} = \frac{(-1)^{n'-l}}{4\,(2l-1)!}\sqrt{\frac{(n+l)!\,(n'+l-1)!}{(n-l-1)!\,(n'-l)!}}\frac{(4nn')^{l+1}}{(n+n')^{n+n'}}\,(n-n')^{n+n'-2l-2}\,W\,(n,n',l)\,, \tag{4.44} $$

where $l' = l-1$,

$$ W\,(n,n',l) = {}_2F_1\,(u,-n'+l,2l,w) - \left(\frac{n-n'}{n+n'}\right)^2 {}_2F_1\,(v,-n'+l,2l,w)\,, \tag{4.45} $$

with $u = -n+l+1$, $v = -n+l-1$, and $w = -4nn'/\,(n'-n)^2$. Here ${}_2F_1\,(a,b,c;x)$ is Gauss's hypergeometric function for integer a, b, and c, evaluated using the recursion relationship

$$ \begin{aligned}(a-c)\,{}_2F_1\,(a-1,b,c;x) &= a(1-x)\,[{}_2F_1\,(a,b,c;x)\\ &-{}_2F_1\,(a+1,b,c;x)] + (a+bx-c)\,{}_2F_1\,(a,b,c;x)\,,\end{aligned} \tag{4.46} $$

with initial conditions

$$ {}_2F_1\,(0,b,c;x) = 1, \quad {}_2F_1\,(-1,b,c;x) = 1 - \frac{bx}{c}. \tag{4.47} $$

We use Eqs. (4.43)-(4.47) to calculate bound-bound transition rates at the beginning of a MLA computation, storing them for easy and repeated access.

We compared the resulting radial matrix elements with several values for high n in Ref. [309] and found agreement to all 3 published digits. We calculated oscillator strengths and compared with Ref. [310] (all transitions with n and n' were evaluated, as was the entire Balmer series for $n \leq 60$)

and found agreement to all 6 published digits. We also compared with the results in Ref. [311] (in which oscillator strengths were computed up to $n = 500$ for $\Delta n \leq 5$) and found agreement to 5 digits. We attribute the difference in oscillator strengths to the fact that a polynomial expansion of ${}_2F_1$ was used in Ref. [311], rather than the more stable recursion relationship. We also compared with the dipole one-photon rates used for the $n_{\max} = 30$ MLA computation of Ref. [283]. Most rates agreed to 7 or more significant figures. Transition rates between s and p orbitals only agreed to ~ 5 significant figures. We ran our MLA model using the rates of Ref. [283] and verified that these small disagreements do not lead to any differences in $x_e\,(z)$ at the desired level of accuracy. Given the high quantum numbers considered, it was important to verify that no numerical instability plagues our numerical implementation of these recursions. We thus checked matrix elements computed using Eqs. (4.44)-(4.47) against values estimated using the WKB approximation, as detailed in Appendix C.

4.3.3.2 Bound-free rates

Bound-free rates are evaluated using the same principle, but one of the two states used to evaluate matrix elements must be a continuum Coulomb wave function. The resulting matrix element is [314]

$$g_{n,\kappa}^{l,l'} = \frac{1}{n^2}\int_0^\infty x^3 R_{nl}(x) F_{\kappa l'}(x) dx, \tag{4.48}$$

where $F_{\kappa l'}$ is the continuum Coulomb wave function for a recombining photoelectron with angular momentum quantum number l' and dimensionless energy $\kappa^2 = E_e/I_{\rm H} = \frac{h\nu}{I_{\rm H}} - 1/n^2$. The energy of the outgoing photon is $h\nu$. This integral may also be evaluated in terms of hypergeometric functions, which in turn yields a recursion relationship for $g_{n,\kappa}^{l,l'}$ [312]:

$$\begin{aligned}
G_{n,\kappa}^{l,l'} &\equiv \frac{g_{n,\kappa}^{l,l'}}{(2n)^{l-n}\sqrt{\frac{(n+l)!}{(n-l-1)!}\prod_{s=0}^{l'}(1+s^2\kappa^2)}}, \qquad (4.49)\\
G_{n,\kappa}^{l-2,l-1} &= \left[4\left(n^2-l^2\right)+l\left(2l-1\right)\left(1+n^2\kappa^2\right)\right]G_{n,\kappa}^{l-1,l} - 4n^2\left(n^2-l^2\right)\left[1+\left(l+1\right)^2\kappa^2\right]G_{n,\kappa}^{l,l+1},\\
G_{n,\kappa}^{l-1,l-2} &= \left[4\left(n^2-l^2\right)+l\left(2l+1\right)\left(1+n^2\kappa^2\right)\right]G_{n,\kappa}^{l,l-1} - 4n^2\left[n^2-\left(l+1\right)^2\right]\left(1+l^2\kappa^2\right)G_{n,\kappa}^{l+1,l}.
\end{aligned}$$

The initial conditions of the recursion are [312]

$$\begin{aligned}
G_{n,0}^{n-1,n} &= \sqrt{\frac{\pi}{2}}\frac{8n}{(2n-1)!}\left(4n\right)^n e^{-2n}, \qquad (4.50)\\
G_{n,\kappa}^{n-1,n} &= \frac{e^{2n-2\kappa^{-1}\operatorname{atan}(n\kappa)}}{\sqrt{1-e^{-\frac{2\pi}{\kappa}}}\left(1+n^2\kappa^2\right)^{n+2}}G_{n,0}^{n-1,n},\\
G_{n,\kappa}^{n-2,n-1} &= \left(2n-1\right)\left(1+n^2\kappa^2\right)nG_{n,\kappa}^{n-1,n},\\
G_{n,\kappa}^{n-1,n-2} &= \left(\frac{1+n^2\kappa^2}{2n}\right)G_{n,\kappa}^{n-1,n}.
\end{aligned}$$

These matrix elements are tabulated at the beginning of each MLA run for all $l < n \leq n_{\max}$, and $10^{-25} \leq \kappa^2 n^2 \leq 4.96 \times 10^8$; this range of κ is partitioned into 50 logarithmically spaced bins, with each bin containing 11 equally spaced κ values. Bound-free matrix elements were compared with tabulated values for low n in Ref. [312] and agreed to all 4 listed digits. Matrix elements were also compared with those used in Ref. [283]; we found agreement to one part in 10^7, aside from $s-p$ transitions, as already discussed.

The recombination rate to $[n, l]$ as a function of energy is then

$$\alpha_{nl}\left(E_e\right) = \frac{4\sqrt{\pi}\alpha^4 a_0^2 c I_{\mathrm{H}}^{3/2}}{3n^2\left(kT_{\mathrm{M}}\right)^{3/2}} \sum_{l'=l\pm1} \max\left\{l, l'\right\} \Theta_{n,\kappa}^{l,l'}, \tag{4.51}$$

with

$$\Theta_{n,\kappa}^{l,l'} = \left(1 + \frac{n^2 E_e}{I_{\mathrm{H}}}\right)^3 \left|g_{n,\kappa}^{l,l'}\right|^2. \tag{4.52}$$

At each value of T_M, the tabulated matrix elements, Eqs. (4.6) and (4.51) are used to calculate thermally averaged recombination rates, using an 11-point Newton-Cotes [315] formula for the integration and neglecting stimulated emission. Large bins are added into the integral until it has converged to a fractional precision of 5×10^{-15}. We compared our values with integrated rates tabulated in Ref. [312] and found agreement to all 4 listed digits. Comparing with the rates used in Ref. [283], we found agreement to one part in 10^7, aside from s-p transitions.

In Saha equilibrium,

$$\eta_e^2 \alpha_{nl}\left(E_e\right)\left[1 + \mathcal{N}\left(E_\gamma, T_{\mathrm{R}}\right)\right] P_{\mathrm{M}}\left(E_e, T_{\mathrm{M}}\right) = \eta_{\mathrm{H}} x_{n,l} \mathcal{N}\left(E_\gamma, T_{\mathrm{R}}\right) \beta_{nl}\left(E_\gamma\right), \tag{4.53}$$

and so by the principle of detailed balance,

$$\int dE_e \beta_{nl}\left(E_\gamma\right) = \frac{x_e^2 \eta_{\mathrm{H}}}{x_{n,l}} \int dE_e \alpha_{nl}\left(E_e\right) \left.\frac{\left[1 + \mathcal{N}\left(E_\gamma, T_{\mathrm{R}}\right)\right]}{\mathcal{N}\left(E_\gamma, T_{\mathrm{R}}\right)}\right|_{\mathrm{eq}} P_{\mathrm{M}}\left(E_e\right). \tag{4.54}$$

We verified that our computed thermally averaged recombination and ionization rates satisfied this equality to machine precision. We also checked bound-free matrix elements computed using Eq. (4.50) against values estimated using the WKB approximation, as detailed in the Appendix C.

4.3.4 Sparse-matrix technique

The key to making the recombination problem tractable for high values of $n_{\max}$ is the sparsity of Eqs. (4.22) and (4.23). Dipole selection rules only allow coupling of states with angular momentum quantum numbers l and l' if $l' = l \pm 1$. It is easiest to understand how sparsity simplifies the

$$\mathbf{T} = \begin{pmatrix} \mathbf{M}_{0,0} & \mathbf{M}_{0,1} & \mathbf{0} & \dots & \dots & \dots & \dots & \dots & \mathbf{0} \\ \mathbf{M}_{1,0} & \mathbf{M}_{1,1} & \mathbf{M}_{1,2} & \mathbf{0} & \dots & \dots & \dots & \dots & \mathbf{0} \\ \mathbf{0} & \mathbf{M}_{2,1} & \mathbf{M}_{2,2} & \mathbf{M}_{2,3} & \mathbf{0} & \dots & \dots & \dots & \mathbf{0} \\ \dots & \dots & \dots & \dots & \dots & \dots & \dots & \dots & \dots \\ \mathbf{0} & \dots & \mathbf{0} & \mathbf{M}_{l,l-1} & \mathbf{M}_{l,l} & \mathbf{M}_{l,l+1} & \mathbf{0} & \dots & \mathbf{0} \\ \dots & \dots & \dots & \dots & \dots & \dots & \dots & \dots & \dots \\ \mathbf{0} & \dots & \dots & \dots & \dots & \mathbf{0} & \mathbf{M}_{l_{\max}-1,l_{\max}-2} & \mathbf{M}_{l_{\max}-1,l_{\max}-1} & \mathbf{M}_{l_{\max}-1,l_{\max}} \\ \mathbf{0} & \dots & \dots & \dots & \dots & \dots & \mathbf{0} & \mathbf{M}_{l_{\max},l_{\max}-1} & \mathbf{M}_{l_{\max},l_{\max}} \end{pmatrix}$$

Figure 4.3 Schematic of the sparse rate matrix $\mathbf{T}$ with components given by Eq. (4.23) and submatrix building blocks given by Eq. (4.58). Boldface zeroes denote block matrices of all zeros, and enforce the dipole selection rule that the initial state l' angular momentum obeys $l' = l \pm 1$, where l is the final state angular momentum. The submatrix $\mathbf{M}_{ll'}$ has dimension $(n_{\max} - n_{\min} + 1) \times (n_{\max} - n'_{\min} + 1)$, where $n_{\min} = 2$ if $l = 0$, and $n_{\min} = l + 1$ if $l > 0$. Note that submatrices $\mathbf{M}_{l,l}$ on the block diagonal of the larger rate matrix T are themselves diagonal, as seen from Eq. (4.58) and the fact that in the purely radiative case, $\Gamma^{l,l'}_{n,n'} = 0$ if $n \neq n'$ and $l = l'$.

problem with a slight change of notation. We can compose the vector $\vec{x}$ (with components $x_{n,l}$) of excited-state populations, as

$$\vec{x} = \begin{pmatrix} \vec{v}_0 \\ \vec{v}_1 \\ \dots \\ \vec{v}_{l_{\max}} \end{pmatrix}, \tag{4.55}$$

where $l_{\max} = n_{\max} - 1$ and $\vec{v}_l$ denotes a vector of the populations of all states with angular momentum l, except for the $1s$ state. Specifically,

$$\vec{v}_l = \begin{pmatrix} x_{n_{\min},l} \\ x_{n_{\min}+1,l} \\ \dots \\ x_{n_{\max},l} \end{pmatrix}, \tag{4.56}$$

where

$$n_{\min} = \begin{cases} 2 & \text{if } l = 0, \\ l + 1 & \text{if } l \neq 0. \end{cases} \tag{4.57}$$

The source vector $\vec{s}$ can similarly be written by concatenating source vectors $\vec{s}_l$; each $\vec{s}_l$ feeds all states with angular momentum l.

The rate matrix may be similarly built of submatrices $\mathbf{M}_{l,l'}$, as illustrated in Fig. 4.3. The complete rate matrix is block tridiagonal, and the blocks decrease in dimension as l increases. The

matrix $\mathbf{M}_{l,l'}$ has components

$$M_{l,l'}^{n,n'} = \delta_{n,n'}^{l,l'} \left(\mathcal{I}_{nl} + \gamma_{nl} + \sum_{n'',l''} \Gamma_{n'',n'}^{l'',l'} \right) - \Gamma_{n,n'}^{l,l'}. \tag{4.58}$$

In the steady-state approximation, Eq. (4.22) can be rewritten as a system of matrix equations. If $l = 0$,

$$\mathbf{M}_{0,0}\vec{v}_0 + \mathbf{M}_{0,1}\vec{v}_1 = \vec{s}_0. \tag{4.59}$$

If $0 < l < l_{\max}$,

$$\mathbf{M}_{l,l-1}\vec{v}_{l-1} + \mathbf{M}_{l,l}\vec{v}_l + \mathbf{M}_{l,l+1}\vec{v}_{l+1} = \vec{s}_l. \tag{4.60}$$

To close the system, we must truncate the hierarchy by excluding states with $n > n_{\max}$ as both sources and sinks, which is equivalent to setting $A_{n,n'}^{l,l\pm1} = 0$ for $\max\{n, n'\} > n_{\max}$. Then for $l = l_{\max}$,

$$\mathbf{M}_{l_{\max},l_{\max}-1}\vec{v}_{l_{\max}-1} + \mathbf{M}_{l_{\max},l_{\max}}\vec{v}_{l_{\max}} = \vec{s}_{l_{\max}}. \tag{4.61}$$

It might be possible to approximate the correction due to this truncation error, using asymptotic expressions for $A_{n,n'}^{l,l\pm1}$ and Saha equilibrium abundances for $n > n_{\max}$. This will only work if $n_{\max}$ is sufficiently high for nearly perfect equilibrium Saha equilibrium to hold between states with $n > n_{\max}$ and the continuum.

At any given time step, the actual quantity of interest is not the inverse $\mathbf{T}^{-1}$ of the rate matrix but the solution set $\{\vec{v}_l\}$ to the steady-state rate equations. The closed form solution to Eqs. (4.59)-(4.61) is

$$\vec{v}_l = \mathbf{K}_l \left[\vec{s}_l - \mathbf{M}_{l,l+1}\vec{v}_{l+1} + \sum_{l'=0}^{l-1} (-1)^{l'-l} \mathbf{S}_{l,l'}\vec{s}_{l'} \right], \tag{4.62}$$

if $l < l_{\max}$. If $l = l_{\max}$, then

$$\vec{v}_l = \mathbf{K}_l \left[\vec{s}_l + \sum_{l'=0}^{l-1} (-1)^{l'-l} \mathbf{S}_{l,l'}\vec{s}_{l'} \right]. \tag{4.63}$$

Here

$$\mathbf{K}_l = \begin{cases} \mathbf{M}_{00}^{-1} & \text{if } l = 0, \\ \left(\mathbf{M}_{l,l} - \mathbf{M}_{l,l-1}\mathbf{K}_{l-1}\mathbf{M}_{l-1,l}\right)^{-1} & \text{if } l > 0, \end{cases} \tag{4.64}$$

and

$$\mathbf{S}_{l,i} = \begin{cases} \mathbf{M}_{l,l-1}\mathbf{K}_{l-1} & \text{if } i = l-1, \\ \mathbf{S}_{l,i+1}\mathbf{M}_{i+1,i}\mathbf{K}_i & \text{if } i < l-1. \end{cases} \tag{4.65}$$

Our new MLA code, RecSparse, operationally implements this solution at each time step as follows:

1. Using the values of $T_{\rm R}$ and x_e, $T_{\rm M}$ is calculated using the results of Sec. 4.2.2.

2. All relevant $\mathbf{M}_{l,l'}$ and $\vec{s}_l$ are computed using Eqs. (4.58) and (4.26) and stored.

3. All $\mathbf{K}_l$ and $\mathbf{S}_{l,i}$ are computed using Eqs. (4.64)-(4.65) and stored.

4. Equation (4.63) is applied to obtain the solution for $\vec{v}_{l_{\rm max}}$.

5. Equation (4.62) is iterated to obtain the solutions for all $\vec{v}_l$.

The free-electron fraction x_e is then evolved forward in time using $\{\vec{v}_l\}$ and Eq. (4.28). It would also be interesting to compute the cumulative spectral distortion emitted by the line and continuum processes responsible for recombination [7, 8, 275, 316]. This fractional perturbation of 10^{-7} to the blackbody intensity of the CMB could be detectable with future experiments and would offer a test both of our understanding of recombination and of new physics behind the surface of last scattering (e.g., time variation of fundamental constants, energy injection by decaying/annihilating dark matter) [317–321]. This and the development of a fast code for *Planck* data analysis including all the relevant physical effects will be the subject of future work.

4.3.5 Numerical methods

RecSparse begins at $z = 1606$, assuming Saha equilibrium to compute the initial value of x_e and setting $T_{\rm M}$ as discussed in Sec. 4.2.2. Excited-state populations are obtained using the method of Sec. 4.3.4. Submatrix inversions are implemented using the double precision routine DGESVX from the LAPACK library [322]. Time evolution of $x_e(z)$ with Eq. (4.28) is implemented using the $5^{\rm th}$-order Runge-Kutta-Cash-Karp (RKCK) implementation in *Numerical Recipes* [323]. The rapid time scale for return to Saha equilibrium introduces a stiff mode into the equations at early times, necessitating care in the choice of a stepsize for the integrator. We were able to achieve relative precision of $\epsilon \sim 10^{-8}$ by placing 59 time steps at $z \geq 1538$ and 250 steps in the range $200 \leq z \leq 1538$, partitioning each interval into equally sized steps in $\Delta \ln a$; relative errors were estimated by halving step size and comparing values of $x_e(z)$ at identical time steps. The computation time $t_{\rm comp}$ for RecSparse scales as $t_{\rm comp} \propto n_{\rm max}^{\alpha}$, where $2 < \alpha < 3$. This is an empirical estimate for the range of $n_{\rm max}$ that we have explored, and may not extend to higher $n_{\rm max}$ values. In contrast, for standard MLA codes, $t_{\rm comp} \propto n_{\rm max}^6$. We can calculate recombination histories for $n_{\rm max} = 200$ in 4 days on a standard workstation; this would likely take weeks using a conventional MLA code.

4.4 Extension to electric quadrupole transitions

Early work on recombination highlighted the importance of forbidden transitions, as half of the hydrogen atoms in the Universe form by way of the $2s \rightarrow 1s$ "forbidden" transition [272, 273].

Recent work has included additional "forbidden" transitions in the MLA treatment, namely, two-photon transitions ($ns \rightarrow 1s$ and $nd \rightarrow 1s$) in H [280–283], two-photon and spin-forbidden transitions in He [284–287], as well as electric quadrupole (E2) transitions in He [299, 300].

Until this work, the impact of E2 transitions in H on recombination has not been considered, even though they are optically thick for transitions to/from the ground state. For optically thick lines, the overall transition rate is proportional to $A^{l,l'}_{n,n'}/\tau^{l,l'}_{n,n'}$. Since $\tau^{l,l'}_{n,n'} \propto A^{l,l'}_{n,n'}$, the overall transition rate is independent of the rate coefficient. Transitions such as electric quadrupoles, which seem "weaker" judging from rate coefficients alone, can thus be as important as "stronger" transitions, like the Lyn lines. For example, this is why the semiforbidden He I 591Å line is important in cosmological recombination [299, 300]. We thus include E2 quadrupole transitions in our MLA computation to properly assess their relevance for cosmological recombination. M1 (magnetic dipole) transition rates in H are typically suppressed by an additional factor of $10^7 - 10^8$, and are thus negligible [324].

4.4.1 Rates

The electric quadrupole (E2) Einstein A-coefficient for transitions from states $[n, l]$ to states $[n', l']$ is [325]:

$$ {}^{(2)}A^{l',l}_{n',n} = \frac{\alpha\omega^5_{n,n'}a_0^4}{15 g_a c^4} \left|\langle nl|\,|Q^{(2)}|\,|n'l'\rangle\right|^2, \tag{4.66}$$

where the quadrupole matrix element is

$$ \langle nl|\,Q^{(2)}\,|n'l'\rangle = \langle l|\,|C^{(2)}|\,|l'\rangle\ {}^{(2)}X^{l',l}_{n',n}. \tag{4.67}$$

The matrix elements of the reduced angular tensor operator $C^{(2)}$ are given by

$$ \langle l|\,|C^{(2)}|\,|l'\rangle = (-1)^l \sqrt{g_l g_{l'}} \begin{pmatrix} l & 2 & l' \\ 0 & 0 & 0 \end{pmatrix}, \tag{4.68}$$

where the last factor is the well-known Wigner-3J symbol. This operator is defined as

$$ \langle l|\,|C^{(k)}|\,|l'\rangle \quad = \quad (-1)^{l-m} \begin{pmatrix} l & k & l' \\ -m & q & m' \end{pmatrix}^{-1} \sqrt{\frac{4\pi}{2k+1}}\,\langle lm|\,Y_{kq}\,(\theta,\phi)\,|l'm'\rangle\,. \tag{4.69}$$

The dimensionless radial quadrupole integral is

$$ {}^{(2)}X^{l',l}_{n',n} = \int_0^\infty x^4 R_{n'l'}(x) R_{nl}(x) dx. \tag{4.70}$$

Thanks to the existence of ladder operators for the radial Coulomb wave functions $R_{nl}(x)$, these matrix elements may be derived using convenient recursion relationships [326] illustrated in Appendix

D. The radial matrix element for the $nd \to 1s$ transition is a special case of Eq. (B.13) of Ref. [326] with $n' = 1$ [Eq. (D.9) in Appendix D of this thesis]:

$$ {}^{(2)}X^{0,2}_{1,n} = (-1)^{n-1} 2^6 n^4 \left[\frac{(n+2)!}{(n-3)!}\right]^{1/2} \frac{(n-1)^{n-4}}{(n+1)^{n+4}}. \tag{4.71}$$

We numerically implemented this recursion in RecSparse. We checked special cases of ${}^{(2)}X^{l',l}_{n',n}$ against values tabulated in Ref. [326], and found agreement to all listed digits. We also compared ${}^{(2)}A^{l',l}_{n',n}$ with the rates in Ref. [324]. The rates in Ref. [324] result from numerical integration of the more precise Dirac wave function and so the resulting fractional disagreement of $\mathcal{O}\left(\alpha^2\right) \sim 5 \times 10^{-5}$ is not surprising. This is a 'correction to a correction,' and so our calculated rates should be adequate for assessing the importance of E2 transitions. We also checked our precise calculated values of ${}^{(2)}X^{l',l}_{n',n}$ against values estimated using the WKB approximation, as detailed in Appendix D.

4.4.2 Inclusion in multilevel atom code

The obvious way to include quadrupole transitions into our MLA code would be to generalize Eq. (4.60) to include $\Delta l = \pm 2$ transitions:

$$\mathbf{M}_{l,l+2}\mathbf{v}_{l+2} + \mathbf{M}_{l,l+1}\mathbf{v}_{l+1} + \mathbf{M}_{l,l}\mathbf{v}_{l} + \mathbf{M}_{l,l-1}\mathbf{v}_{l-1} + \mathbf{M}_{l,l-2}\mathbf{v}_{l-2} = \mathbf{s}_l. \tag{4.72}$$

The resulting system is obviously not as sparse as in the dipole case, and solving for all $\mathbf{v}_l$ would be computationally more expensive, slowing down the whole MLA code. Since the contribution from even the largest quadrupole rates may turn out to be small, we pursue a computationally less expensive approach.

Higher energy E2 transitions will proceed much faster than lower energy ones, since E2 rates scale as $\omega^5_{nn'}$. In particular, transitions to and from the $1s$ ground state will dominate any other quadrupole contributions to the recombination problem, since

$$\frac{{}^{(2)}A^{0,2}_{1,n}}{{}^{(2)}A^{0,2}_{q,n}} \sim \frac{\omega^5_{1n}}{\omega^5_{qn}} = \left[\frac{q^2\left(n^2-1\right)}{n^2-q^2}\right]^5 \gtrsim 10^3 \text{ if } q \geq 2. \tag{4.73}$$

Moreover, the $nd \to 1s$ lines are optically thick for small n. We thus restrict our consideration to $nd \leftrightarrow 1s$ transitions, since other quadrupole transitions are "corrections to a correction." A further simplification follows if we recall that the Lyn lines are all optically thick [283]. Thus, the transition $nd \to 1s$ is highly probable to be immediately followed by a transition $1s \to np$. This yields a net $nd \to np$ transition, analogous to an l-changing collision, which occurs with forward rate ${}^{(2)}\Gamma^{0,2}_{1,n} = x_{nd}{}^{(2)}A^{0,2}_{1,n}$. The reverse process occurs with rate ${}^{(2)}\Gamma^{0,2}_{1,n} = x_{np}{}^{(2)}A^{0,2}_{1,n}D$, where D is a factor relating forward and backward rates. If the p and d states were in equilibrium, the two rates

would cancel, so by the principle of detailed balance, $D = (x_{nd}/x_{np})_{\rm eq} = 5/3$, where "eq" denotes an equilibrium value. The net $np \leftrightarrow nd$ transition rate due to E2 transitions is thus

$$\dot{x}_{np} = -\dot{x}_{nd} = {}^{(2)}A^{0,2}_{1,n}\left(x_{nd} - \frac{5}{3}x_{np}\right). \tag{4.74}$$

Since this overall rate obeys the $\Delta l = \pm 1$ selection rule, it can be numerically implemented within the same framework as the dipole rates.

4.5 Results

We ran the RecSparse code for a variety of $n_{\rm max}$ values. Here we omitted E2 transitions to focus on the effect of deviations from statistical equilibrium and increasing $n_{\rm max}$. We begin by discussing deviations from equilibrium, and proceed to discuss the recombination history and numerical convergence with $n_{\rm max}$.

4.5.1 State of the gas

The assumptions of statistical equilibrium between different l sublevels within the same n shell and Boltzmann equilibrium between different n states fail at late times, as discussed in Sec. 4.3. Furthermore, as reactions become inefficient on the Hubble time scale and $x_e(z)$ freezes out, Saha equilibrium between the continuum and excited states of H also fails. Below, we discuss each of these failures quantitatively.

4.5.1.1 Populations of angular momentum sublevels

At early times, the populations of hydrogen atoms in states with the same n but different angular momentum l are in statistical equilibrium [see Eq. (4.31)]. Radiative transitions do not include reactions that are l changing but n conserving. The l sublevels must thus be kept in equilibrium by a combination of sequences of allowed radiative transitions and atomic collisions. These processes become inefficient at later times, leading the different l sublevels to fall out of equilibrium. Both the TLA treatment of Peebles and the later MLA treatment of Seager et al. rely on the statistical equilibrium assumption [272, 276]. Our RecSparse code relaxes this assumption and follows the populations of all l sublevels separately.

For $n > 5$, the resulting populations are marked by several features, shown in Figs. 4.4 and 4.5 at early and late times, respectively. We use

$$\Delta x_{n,l} = x_{n,l} - x^{\rm eq}_{n,l} \tag{4.75}$$

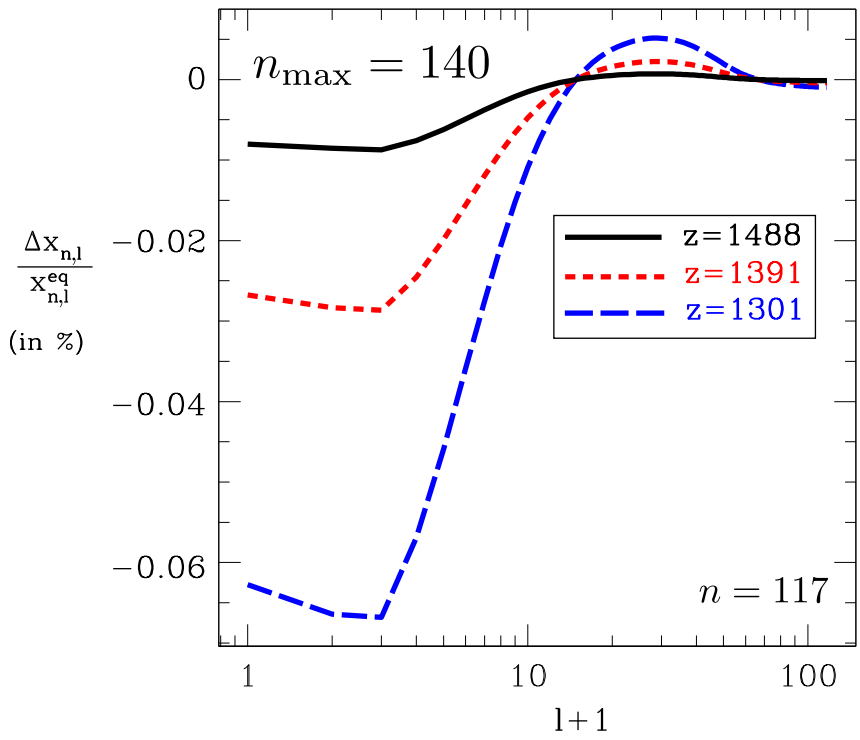

Figure 4.4 Early time deviations from statistical equilibrium between different l at fixed n and $n_{\rm max}$, as computed by RecSparse.

to compare actual with equilibrium populations, where

$$x^{\rm eq}_{n,l} \equiv x_n \frac{(2l+1)}{n^2}. \tag{4.76}$$

Deviations begin modestly at early times ($\Delta x_{n,l}/x^{\rm eq}_{n,l} \lesssim 0.1\%$ for $1300 \lesssim z \lesssim 1600$) but are quite large by late times ($\Delta x_{n,l}/x^{\rm eq}_{n,l} \sim 60\%$ by $z \lesssim 600$).

Lower l states depopulate efficiently, and are significantly underpopulated relative to statistical equilibrium expectations. States with $l = 0$ can only make downward dipole transitions in n if $l' = 1$. These rates are several order of magnitude lower than Lyman-series rates with the same Δn, and so $l = 0$ states depopulate less efficiently than other low-l states. This explains the upturn at the lowest l values. The $\Delta l = \pm 1$ selection rule implies that higher l states couple efficiently to neighboring bound states ($l' = l \pm 1$) with a limited range of accessible n', since $n' > l'$. These states thus depopulate less efficiently than states with lower l due to this bottleneck.

The recombination rate α_{nl} peaks in the range $0.3 \lesssim l/l_{\rm max} \lesssim 0.4$. Together, these facts imply the presence of a peak in $\Delta x_{n,l}/x^{\rm eq}_{n,l}$, which turns out to occur in the range $32 \lesssim l \lesssim 37$ for a wide range of n at all times. The transition to $x_{n,l}/x^{\rm eq}_{n,l} \geq 1$ occurs in the range $16 \lesssim l \lesssim 21$, also for a wide range of n at all times. At very high l, recombination rates are so slow that these states are again underpopulated relative to statistical equilibrium, though less dramatically than they are at

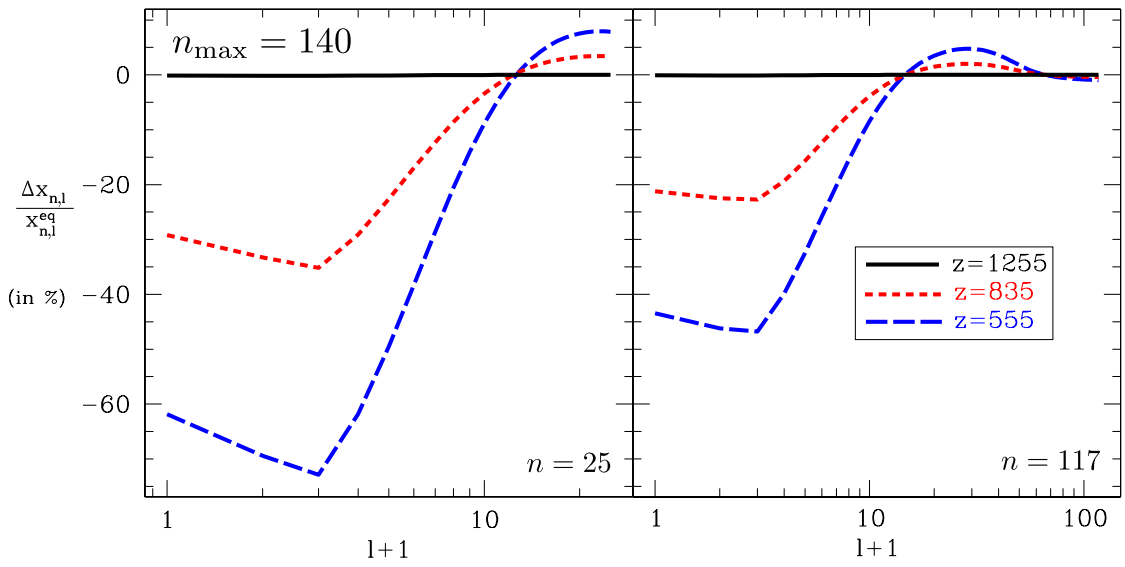

Figure 4.5 Deviations from statistical equilibrium between different l at fixed n and $n_{\max}$, shown as computed by RecSparse at a variety of times through the recombination process. The left panel shows results for states with $n = 25$, while the right panel shows results for states with $n = 140$.

low l.

The observed amplitude and shape of the curves in Figs. 4.4-4.5 qualitatively agree with the results in Refs. [7]-[8], including the upturn near the lowest l and sharp minimum at $l = 2$. The minimum is due to fast Balmer transitions out of the $l = 2$ state. When we computed a recombination history with these rates ($nd \rightarrow 2p$ for $n \geq 2$) artificially set to zero, the minimum moved to $l = 1$, as shown in Fig. 4.6. It is interesting that the curves in Figs. 4.4-4.5 exhibit the same behavior with l as the departure coefficients of Ref. [327], which describe neutral hydrogen (also in the steady-state approximation) in interstellar H II regions. RecSparse only takes into account radiative transitions, and omits l and n-changing collisions.

4.5.1.2 The effect of collisions

The inclusion of l-changing collisions would flatten all the curves in Figs. 4.4-4.6, lessening deviations from statistical equilibrium between the different l sublevels [8]. Indeed, the assumption of statistical equilibrium between these states at all times is formally equivalent to the limit of infinite l-changing collision rates. Theoretical estimates for collisional rates all depend on different assumptions and tabulated rates disagree by as much as factors of ten (see, e.g., Ref. [7–9, 328]).

The total rate for atoms to transition from the state $[n', l']$ to final states with $n = n'$ and $l = l' \pm 1$ due to collisions with the charged species labeled i is $\varphi^i_{n',l'} \eta_{n',l'} \eta_i$, where $\varphi^i_{n',l'}$ is the total thermally averaged cross section for dipole-allowed collisions with i particles, and for the primordial plasma

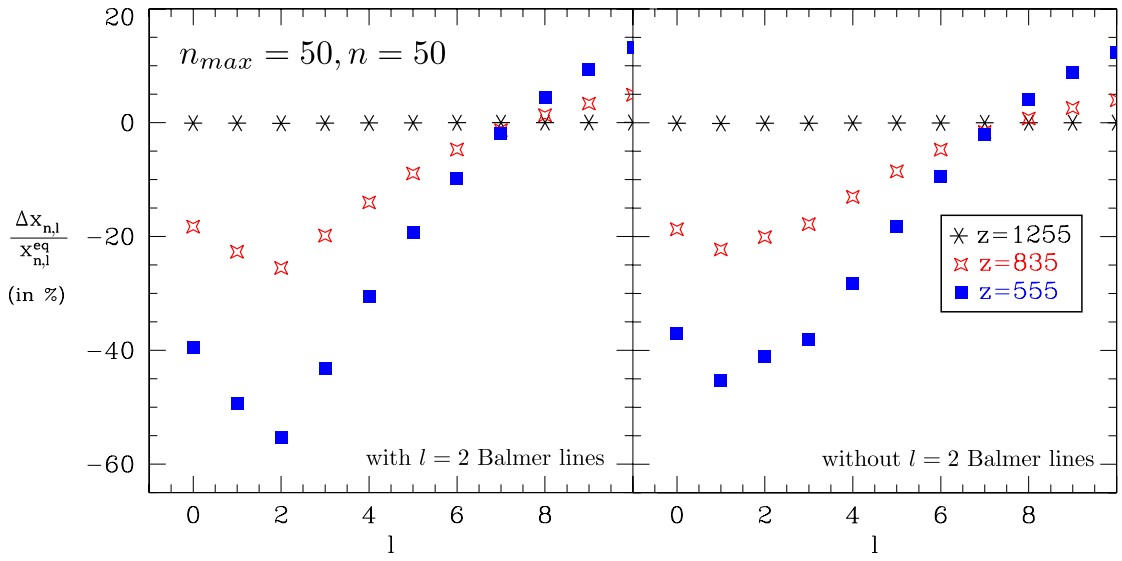

Figure 4.6 The origin of the $l = 2$ dip in Figs. 4.4 and 4.5 is illustrated. Deviations from statistical equilibrium between different l at fixed n and $n_{\rm max}$ are shown at a variety of times through the recombination process. The left panel shows standard results with RecSparse. The right panel shows the results obtained if $l = 2$ Balmer rates are artificially set to zero in the code. This figure highlights the relatively rapid $l = 2$ Balmer transitions as the origin of the $l = 2$ dip.

under consideration i stands for electrons (e^-) or protons (p). In terms of the velocity-dependent collision cross section $\sigma^i_{n',l'}(v)$, the thermally-averaged collision cross section is

$$\varphi^i_{n',l'}\left(T_{\rm M}\right) = \int \sigma^i_{n',l'}\left(v\right) v f^i\left(v, T_{\rm M}\right) dv. \tag{4.77}$$

Here $\sigma_{n',l'}(v) = \sum_{l=l'\pm1} \sigma^i_{n',l'\rightarrow n,l}(v)$, where $\sigma^i_{n',l'\rightarrow n,l}(v)$ is the collision cross-section for the indicated initial/final states. The probability density $f^i(v)$ in speed v of the $i^{\rm th}$ species is

$$f^i(v) = v^2 \sqrt{\frac{2}{\pi}\left(\frac{m_i}{kT_{\rm M}}\right)^3} e^{-\frac{m_i v^2}{2kT_{\rm M}}} \tag{4.78}$$

where m_i is the mass of a particle of species i.

In the limit that the impactor executes an unperturbed trajectory and may be treated classically (as opposed to quantum mechanically), Eq. (4.77) applied in conjunction with matrix elements (and thus cross sections) from Ref. [329] yields

$$\varphi^i_{n',l'} \simeq 9.93\times10^{-6}\mu_i^{1/2}\frac{D_{n',l'}}{T^{1/2}_{\rm M,Kelv}}\left\{11.54 + \log_{10}\left(\frac{T_{\rm M,Kelv}}{D_{n'l'}\mu_i}\right) + 2\log_{10}\left(y^i_{n',l'}\right)\right\}{\rm cm}^3\ {\rm s}^{-1}, \tag{4.79}$$

where $\mu_i = m_i/\left(m_e + m_i\right)$ is the dimensionless reduced mass of the colliding pair, $T_{\rm M,Kelv}$ is the

matter temperature in Kelvin, and

$$D_{n'l'} = 6n'^2\left(n'^2 - l'^2 - l' - 1\right), \tag{4.80}$$

arises from the evaluation of the dipole matrix element between states with $n = n'$. The collision rate in Eq. (4.79) was obtained through an integral over impact parameters which is formally infinite. The integral is requlalized by cutting of the integral at some maximum impact parameter, and the dimensionless cutoff radius $y^i_{n',l'}$ is given by

$$2\log_{10}\left(y^i_{n',l'}\right) = \begin{cases} 10.95 + \log_{10}\left(\frac{T_{\rm M,Kelv}\mathcal{L}^2_{n',l'}}{\mu_i}\right) & \text{radiative cutoff,} \\ 1.68 + \log_{10}\left(\frac{T_{\rm M,Kelv}}{\eta_e\ \rm cm^3}\right) & \text{Debye length.} \end{cases} \tag{4.81}$$

The 'radiative cutoff' corresponds to the possibility that the bound-atom makes a radiative transition during the course of a two-body encounter. On the other hand, for impact parameters $R > R_D$, the potential of a passing charged particle is screened, where R_D is the Debye length of the plasma, defined in Eq. (4.38). In this case the Debye length provides an alternative cutoff radius.

The dimensionless radiative lifetime of the state (in s) results from a sum over all allowed final states for *radiative* dipole-allowed transitions ($\Delta l = \pm 1$, $\Delta n > 0$):

$$\mathcal{L}_{n',l'} = t_{n',l'}\ \mathrm{s}^{-1}, \quad t_{n',l'} = \frac{1}{A_{n',l'}}, \quad A_{n',l'} = \sum_{n,l=l'\pm 1} \Gamma^{l,l'}_{n,n'}. \tag{4.82}$$

Stimulated and spontaneous emission are included in this sum, as can be seen from Eq. (4.2).

As a function of redshift z, we compute the ratio

$$r^{\rm coll}_{nl} \equiv \sum_{i=e^-,p} r^{{\rm coll},i}_{n,l} \tag{4.83}$$

$$r^{{\rm coll},i}_{n,l} \equiv \eta_{\rm H}\varphi^i_{n,l}x_i\mathcal{L}_{n,l} \tag{4.84}$$

of collisional to radiative transition rates out of the state $[n, l]$, summing over collisions with both electrons and protons. We can evaluate Eqs. (4.84) using either cutoff prescription. The results are shown in Figs. 4.7 and 4.8. We see that collisions are most important relative to radiative transitions at early times, unsurprising because $r^{\rm coll}_{n,l} \propto \eta_e$, whereas most downward radiative transitions proceed with rate $\propto A^{l,l'}_{n,n'}$ (with redshift dependence entering more subtly through the Sobolev probability and also the enhancement in this rate due to stimulated emission).

We may also define the quantities n_{10} and n_{100} as the lowest n values (at a given redshift) at which $r^{\rm coll}_{n,l} > 0.1$ or $r^{\rm coll}_{n,l} > 1.0$, respectively. We plot n_{10} and n_{100} in Fig. 4.9, thus showing that the transition from radiative to collisional rate dominance occurs at progressively higher n as z falls

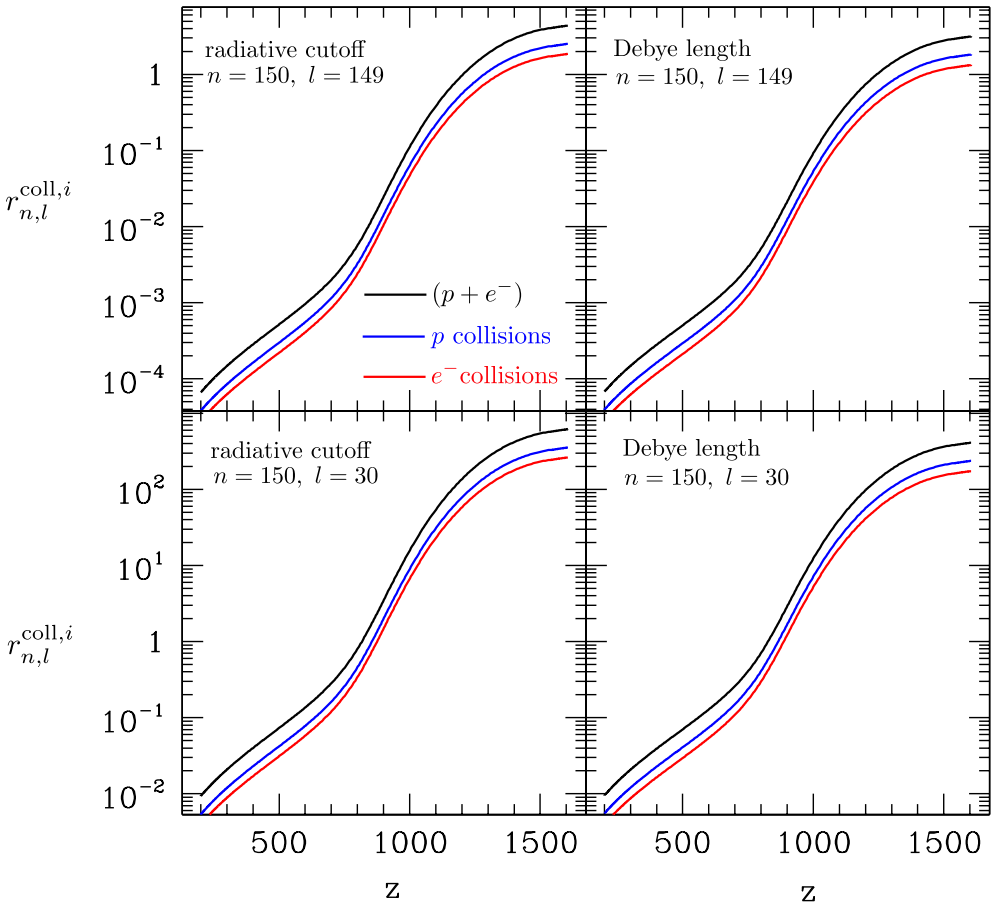

Figure 4.7 Ratio of radiative to collisional depopulation rates of the $n = 150$ energy shell ($l = 149$ and $l = 30$ angular momentum sublevels, for the upper and lower panels, respectively) as a function of redshift. Ratio is shown for atomic collisions with both protons and electrons (red and blue curves, respectively). The total value is shown in black. This ratio is evaluated using both impact parameter cutoff prescriptions described in Sec. 4.5.1.2. Results using the radiative cutoff are shown in the left panels, while those obtained using the Debye length are shown in the right panels. These curves were obtained from a RecSparse run with $n_{\mathrm{max}} = 180$ and $T_{\mathrm{M}} = T_{\mathrm{R}}$.

and the universe cools. Results are nearly independent of the impact parameter cutoff used, as seen in Fig. 4.9. Applying the n_{100} values used to generate Fig. 4.9, we estimate that collisional rates (per unit time) are of the same order of magnitude as radiative rates for $n \gtrsim 52$ at $z \sim 1600$, $n \gtrsim 83$ at $z \sim 1080$, $n \gtrsim 160$ at $z \sim 740$, and $n \gtrsim 250$ at $z \sim 200$.[2] In other words, as the primordial gas cools, collisions come to only influence the highest H energy levels, which contain the least bound electrons.

This occurs because of the exponential decrease in the free-electron density $\eta_{\mathrm{H}} x_e$ in the early

[2]The flat portion of the right panel of Fig. 4.9 at low z results from the fact that this particular RecSparse run only went up to $n = 180$. Our estimate of $n_{100} = 250$ at $z \sim 200$ is obtained by extrapolating the rising portion of the curve to lower z values than shown in the right panel of Fig. 4.9.

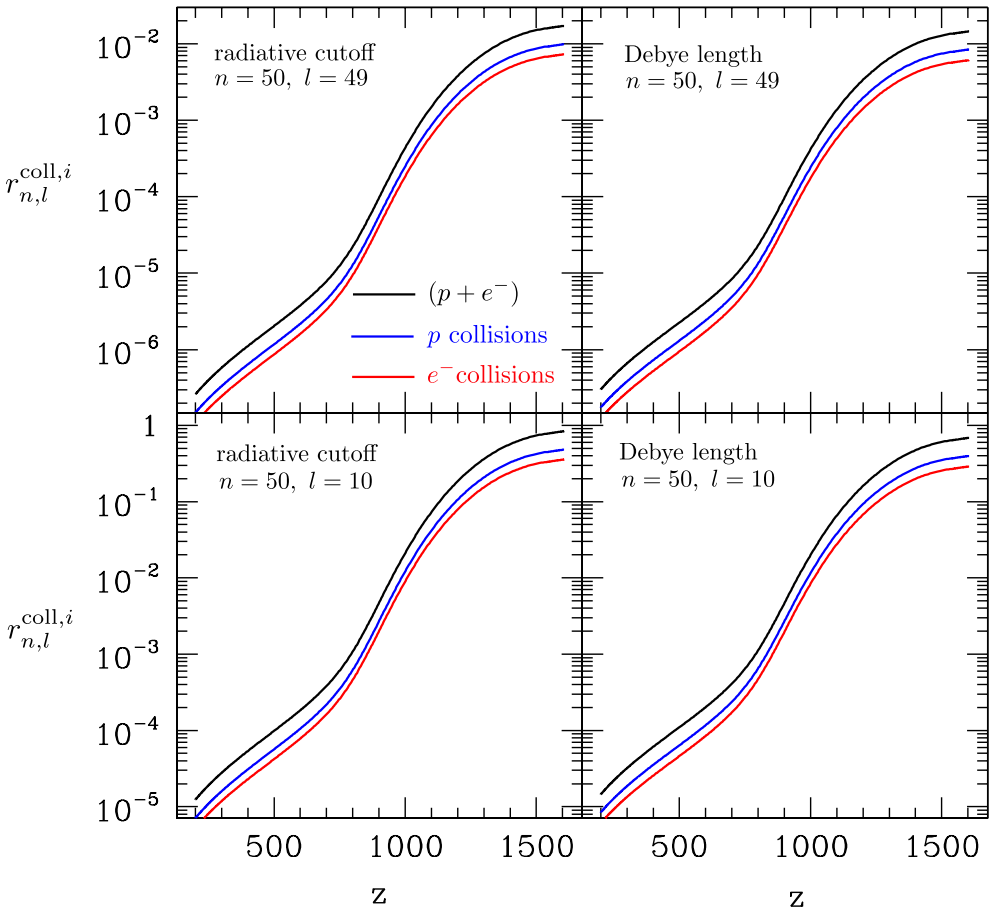

Figure 4.8 Ratio of radiative to collisional depopulation rates of the $n = 50$ energy shell ($l = 49$ and $l = 10$ angular momentum sublevels, for the upper and lower panels, respectively) as a function of redshift. Colors and panels are as in Fig. 4.7.

stages of recombination, which drives down collision rates accordingly. Near $z \sim 1600$ and shortly thereafter, radiative rates alone are high enough to keep the excited states in l-equilibrium. Collisions thus have little effect on $x_e(z)$ at early times. There may, however, be a window at some intermediate redshift, when collision rates are still relatively high, but departures from l-equilibrium are large enough to warrant including collisions in the recombination model. A full calculation is necessary to understand the actual effect. A final answer on the effect of resolving l sublevels on both the recombination history $x_e(z)$ and the recombination spectrum awaits a robust theoretical calculation of the relevant collisional rates. This is an area of future investigation.

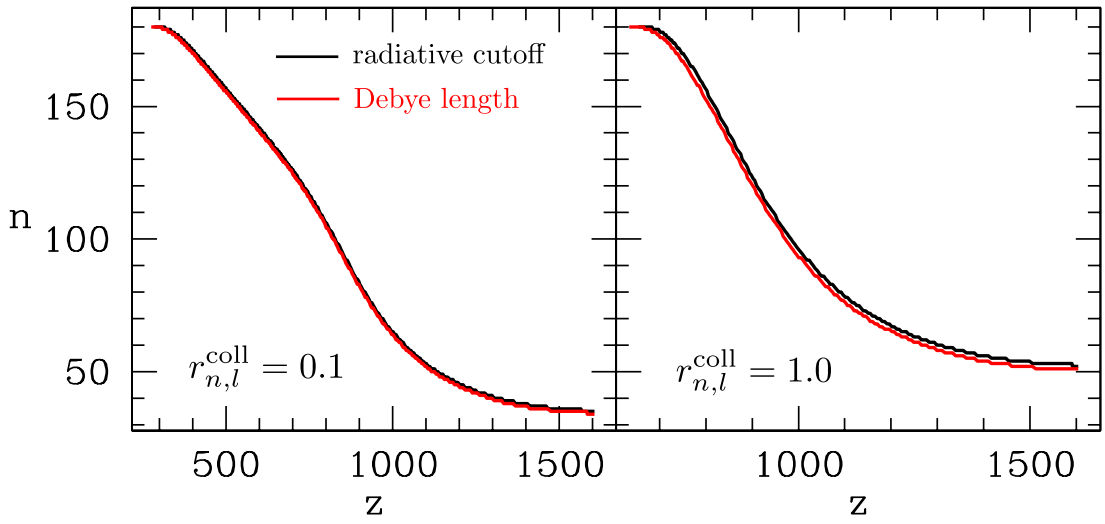

Figure 4.9 This plot shows the lowest shell number n at which the total (electron+proton) collision rate is equal to 10% (left panel) or 100% (right panel) of the radiative transition rate. The matter temperature $T_{\rm M}$ and $n_{\rm max}$ are as in Figs. 4.7 and 4.8.

4.5.1.3 Populations of Rydberg energy levels

We may also compare the total population of the $n^{\rm th}$ energy level to values in Boltzmann equilibrium with $n = 2$:

$$x_n^{\rm Boltz} \equiv x_2 e^{-(E_n - E_2)/(kT_R)} n^2/4. \tag{4.85}$$

The recombination rate to states with $n > 2$ is greater than the downward cascade rate, creating a bottleneck to depopulating these states. This bottleneck causes an over-population of the excited states compared to the equilibrium values of Eq. (4.85), as shown in Fig. 4.10. The ratio $x_n/x_n^{\rm Boltz}$ is $\mathcal{O}(1)$ at early times but grows as high as 3×10^4 by $z = 555$. The ratio approaches a constant at high n, as energy levels get closer to the continuum and the energy differences between successive levels shrink.

Relative to $n = 2$, excited states are over-populated, but there is no population inversion or cosmic maser manifest here. Excited states are still less populated than the $n = 2$ energy level, just not as dramatically as they would be if Eq. (4.85) held. Among highly excited states, some pairs of levels do exhibit population inversion. For effective maser action, inversion must occur between pairs of radiatively connected levels, and the coherence of the radiation field must not be destroyed along the line of sight. This effect will be explored in detail later in this chapter. In extremely dense structure-forming regions, more dramatic population inversion may result and lead to local masing; if these masers were observed, they could offer interesting new probes of structure formation near $z \sim 1000$ as well as the physics of reionization [330]. In this work, we restrict our attention to the

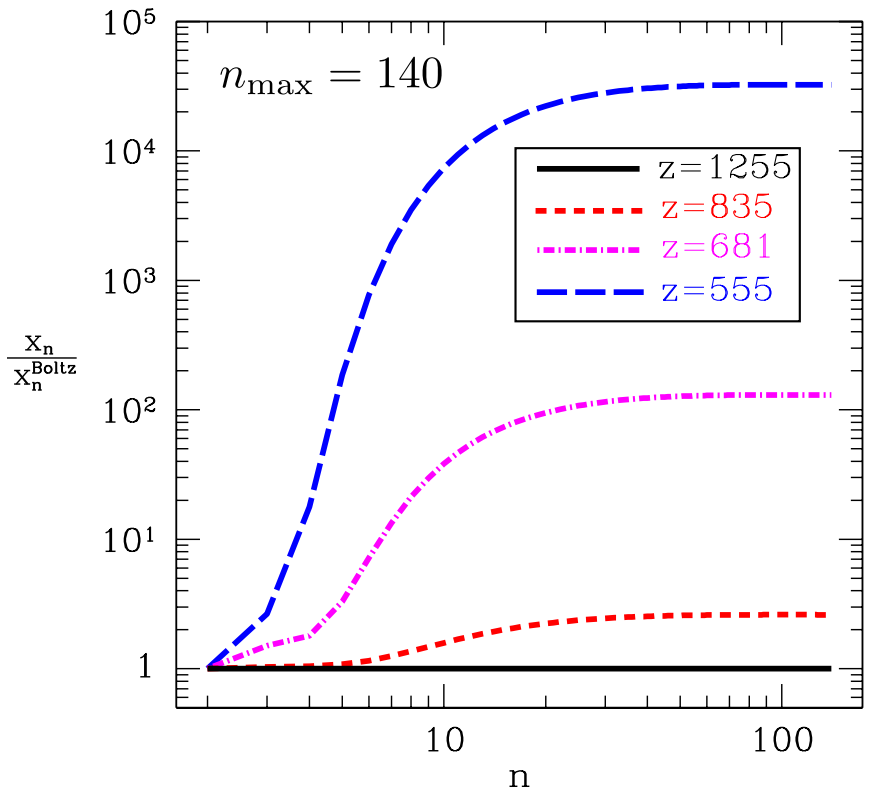

Figure 4.10 Actual population of the $n^{\rm th}$ shell compared to its population in Boltzmann equilibrium with $n = 2$, as computed by RecSparse at a variety of times through the recombination process.

possibility of a global maser in the homogeneous recombining plasma.

Recombination becomes inefficient at late times; i.e., the recombination time scale $[\alpha_{\rm B}(T) x_e n_{\rm H}]^{-1}$ becomes longer than the age of the Universe. Saha equilibrium expressions for x_e and x_{1s} fail dramatically at late times. The free-electron fraction x_e freezes out and is higher than the Saha equilibrium value, and thus x_{1s} is lower than the Saha equilibrium value. Excited states are overpopulated relative to the ground state, but still not enough to be in Saha equilibrium with the continuum. The tower of excited states is thus also underpopulated relative to Saha equilibrium, as shown in Figs. 4.11 and 4.12. Lower energy levels fall out of Saha equilibrium faster than higher energy levels. Higher energy levels are closest to Saha equilibrium, but at late times ($z \sim 200$), even the population of the $n = 250$ level is nearly 10% below its Saha equilibrium value. Modeling the effect of states with $n > n_{\rm max}$ may require Saha equilibrium abundances to hold in the regime past the cutoff. To this end, it is important to properly model atomic collisions (which would push atoms towards Saha equilibrium at a lower transitional value of $n_{\rm max}$), and apply even greater computational resources to obtain $x_e(z)$ for even higher $n_{\rm max}$.

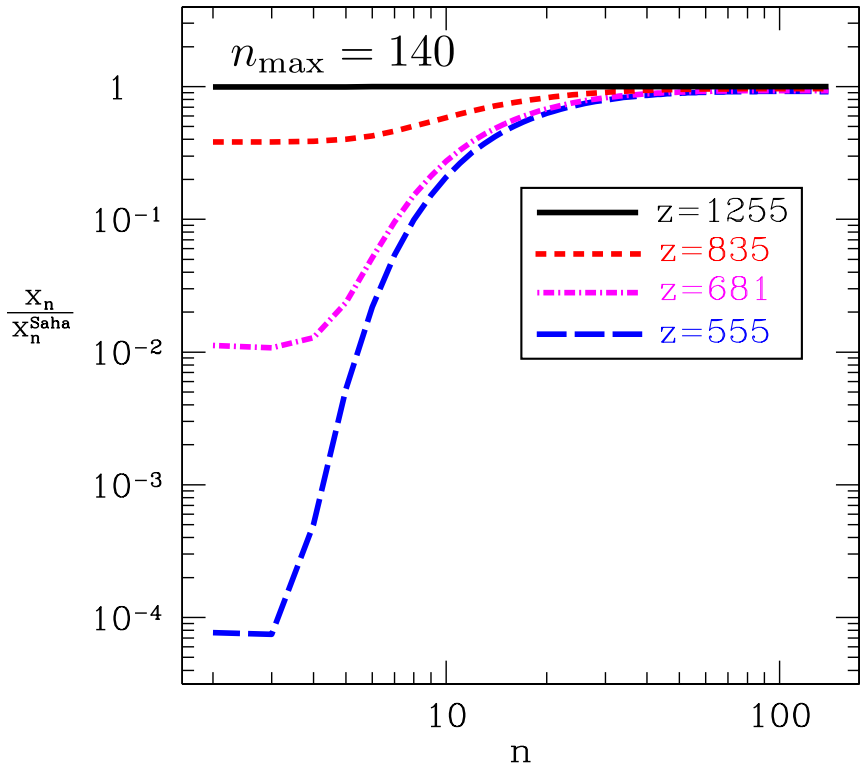

Figure 4.11 Actual population of the n^{th} shell compared to the Saha equilibrium population, as computed by RecSparse at a variety of times through the recombination process.

4.5.2 Population inversion in the primordial plasma

Appropriately bottlenecked multi-level atomic/molecular systems may develop population inversions between radiatively coupled states. If the velocity field of resonant absorbers/emitters is not overly random, the effective path length long enough (either by way of an effective cavity in a lab or a sufficiently long astrophysical column), and the density of absorbers not too high, the resulting stimulated emission may lead to enormous amplification and coherence. This may generate extremely intense and narrow line emission known as *maser* or *laser* radiation [331, 332].

Masers do exist in an astrophysical context. The list of masing species includes H_2O, OH, methanol, SiO, NH_4, CH_2O, and others. The astrophysical environments hosting masers include accretion disks around supermassive black holes at galactic centers, supernovae remnants, planetary atmospheres, plumes of water around Saturnian moons [333], giant molecular clouds, circumstellar disks and even comets [331, 332, 334]! Distances to extra-galactic mega-masers in the 22.2 Ghz H_2O line may be measured very precisely as follows: radial velocities to masing spots in extragalactic sources may be compared with proper motions [determined with very long baseline interferometry (VLBI)] and used to obtain distances. These distances are an important part of the modern

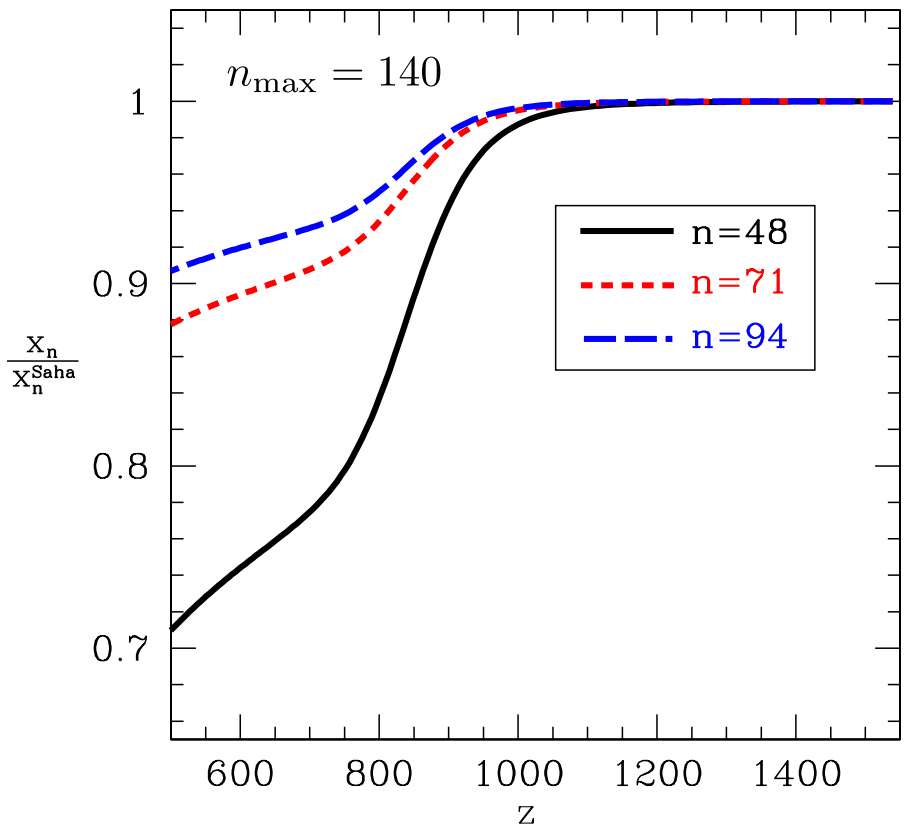

Figure 4.12 Actual population of energy shells compared to Saha equilibrium values, shown for several n values as an explicit function of cosmological redshift z.

cosmological distance ladder [331, 335–337].

One particularly interesting astrophysical maser system is the emission-line star MWC349, a hydrogen recombination line maser thought to originate from the circumstellar disk [336, 338]. Maser emission has been detected in a collection of lines in the range $12 \leq n \leq 41$, with a peak over spontaneous emission of nearly 3 orders of magnitude near $n = 26$. In light of the existence of such a system, it is at least plausible that line radiation from the cosmological recombination epoch is masing [339], and RecSparse is an ideal tool to take a first pass at the problem.

If the results show population inversion (a necessary but not a sufficient condition for maser radiation), it will be important to consider further details, such as the detailed velocity structure of the gas, radiative transfer through the closely spaced fine-structure lines, and the possibility that the maser radiation is efficiently absorbed through free-free processes. This possibility of a cosmic recombination maser is particularly enticing because it could conceivably amplify low-frequency $\nu = 100$ Mhz $\rightarrow$ Ghz spectral distortions from the recombination epoch to a more readily detectable level. The naive un-masing prediction for line distortions from recombination is that at frequencies

low enough to avoid the FIRB, the spectral distortion $\Delta I_\nu / I_\nu \sim 10^{-7}$ [7], where I_ν is the specific intensity of the radiation. It is thus unlikely that unmased recombination spectral lines could be detected with any CMB experiment in the near term. If recombination calculations predict masers, however, there could be cause for optimism.

It turns out that from $z \sim 1600$ onward, many pairs of states briefly exhibit some population inversion. To be clear, we define a population inversion ratio

$$\mathcal{R}^{l,l'}_{n,n'} \equiv \frac{x_{n',l'} g_l}{x_{n,l} g_{l'}}, \tag{4.86}$$

which turns out to rise as high as 4 for some pairs of states. Here we take $n' > n$. The real question, of course, is whether *radiatively connected* levels (potential masers) actually exhibit population inversion. They do; in particular, levels connected by $\Delta n = 1$ (α) lines display population inversion in the RecSparse output, with the most dramatic effects at low l from $z \lesssim 800$ onward, with $\mathcal{R}^{l,l'}_{n,n'}$ rising as high as 1.7 for some pairs of states. In the top panel of Fig. 4.13, we plot $\mathcal{P}^{l,l'}_{n,n'} \equiv \mathcal{R}^{l,l'}_{n,n'} - 1$ for $n = 49$, $n' = 50$, $l = 2$, $l' = 3$. We see that after an early epoch of underpopulation, the population ratio rises well into the overpopulated regime. This shape of curve is typical for radiatively connected levels.

To estimate the effect of population inversions on the radiation field, it is useful to first consider the radiative transfer equation for a single line in the Sobolev approximation [291, 300]:

$$\frac{d\mathcal{N}(\nu)}{d\nu} = \tau^{l,l'}_{n,n'} \phi^{l,l'}_{n,n'}(\nu) \left[\mathcal{N}(\nu) - \mathcal{N}^{\mathrm{eq},l,l'}_{n,n'} \right]. \tag{4.87}$$

Here $\phi^{l,l'}_{n,n'}(x)$ is the profile of the line as a function of frequency ν and the occupation number in equilibrium with the line is

$$\mathcal{N}^{\mathrm{eq},l,l'}_{n,n'} = \mathcal{R}^{l,l'}_{n,n'} = \frac{x_{n',l'} g_l}{x_{n,l} g_{l'}}. \tag{4.88}$$

We neglect free-free absorption (if our analysis predicts maser radiation, it will be important to revisit this simplification). Eq. (4.88) can be solved using the method of integrating factors in terms of a boundary condition $\mathcal{N}(\infty) = \mathcal{N}^{+}_{n,n'}$ to the far blue end of the line, yielding

$$\mathcal{N}(\nu) = \mathcal{N}^{\mathrm{eq},l,l'}_{n,n'} + \left(\mathcal{N}^{+}_{n,n'} - \mathcal{N}^{\mathrm{eq},l,l'}_{n,n'} \right) e^{-\int_\nu^\infty \tau^{l,l'}_{n,n'} \phi^{l,l'}_{n,n'}(x) dx}. \tag{4.89}$$

In the far red wing of the line, $\mathcal{N}(-\infty) = \mathcal{N}^{-}_{n,n'}$, where

$$\mathcal{N}^{-}_{n,n'} = \mathcal{N}^{\mathrm{eq},l,l'}_{n,n'} + \left(\mathcal{N}^{+}_{n,n'} - \mathcal{N}^{\mathrm{eq},l,l'}_{n,n'} \right) e^{-\tau^{l,l'}_{n,n'}}, \tag{4.90}$$

as $\int_{-\infty}^{\infty} \phi^{l,l'}_{n,n'}(x)\, dx = 1$ for the probability $\phi^{l,l'}_{n,n'}(x)$. Eq. (4.90) is the usual Sobolev expression. The

enhancement due to the line is then

$$\frac{\mathcal{N}^{-}_{n,n'}}{\mathcal{N}^{+}_{n,n'}} - 1 = \left(\frac{\mathcal{R}^{l,l'}_{n,n'}}{\mathcal{N}^{+}_{n,n'}} - 1 \right) \left(1 - e^{-\tau^{l,l'}_{n,n'}} \right), \tag{4.91}$$

$$\tau^{l,l'}_{n,n'} = \frac{c^3 \eta_{\rm H} A^{l,l'}_{n,n'} g_{l'} x_{n,l}}{8\pi H(z) g_l \nu^3_{n,n'}} \left(1 - \mathcal{R}^{l,l'}_{n,n'} \right). \tag{4.92}$$

To obtain Eq. (4.92), we have merely repackaged the definition of the Sobolev optical depth, Eq. (4.12), using Eq. (4.86). From Eq. (4.92), we may now see that there are two necessary criteria for maser amplification. First of all, the population inversion must be dramatic enough and the abundance $x_{n,l}$ high enough that both $\tau^{l,l'}_{n,n'} < 0$ and $|\tau^{l,l'}_{n,n'}| \gtrsim 1$. Second of all, for the feature to show up in emission and not absorption, we must have $\mathcal{R}^{l,l'}_{n,n'}/\mathcal{N}^{+}_{n,n'} - 1 < 0$. Strictly speaking, even if the more moderate condition $|\tau| > n^{-2}_{\rm max}$, it is conceivable that there is a significant enhancement to $\mathcal{N}(\nu)$ as photons redshift through and are enhanced by a forest of stimulated α resonances.

For the case of high-n α transitions, this argument runs into one serious complication, the fact that there is a whole forest of radiatively connected pairings $l, l' = l \pm 1$ compatible with a given pair n, n'. In other words, there are many distinct atomic transitions feeding the same spectral line. In this case, the radiative transfer equation [(Eq. (4.87)] is modified to

$$\frac{d\mathcal{N}(\nu)}{d\nu} = \sum_{l,l'} \tau^{l,l'}_{n,n'} \phi^{l,l'}_{n,n'}(\nu) \left[\mathcal{N}(\nu) - \mathcal{N}^{{\rm eq},l,l'}_{n,n'} \right], \tag{4.93}$$

where the sum is over all dipole allowed l, l' transitions corresponding to a frequency $\nu_{n,n'}$. The same technique applied earlier may be used to obtain a formal solution to Eq. (4.93), yielding

$$\mathcal{N}(\nu) = \left[\mathcal{N}^{+}_{n,n'} + \sum_{l,l'} \int_{\nu}^{\infty} dx\ \mathcal{N}^{{\rm eq},l,l'}_{n,n'} \tau^{l,l'}_{n,n'} \phi^{l,l'}_{n,n'}(x) \right] \exp \left[-\sum_{l,l'} \int_{\nu}^{\infty} dx\ \tau^{l,l'}_{n,n'} \phi^{l,l'}_{n,n'}(x) \right]. \tag{4.94}$$

Eq. (4.94) simplifies considerably if all the transitions in the $n' \to n$ line can be assumed to have the same (Doppler-broadening dominated) profile $\phi_{n,n'}(x)$. Using RecSparse and the expressions in Ref. [291] for the Voigt parameter a, we have verified that the lines under consideration $n \geq 2, n' > n$ are dominantly broadened by their common Doppler profile. The solution to Eq. (4.94) then depends on the total optical depth $\tau_{n,n'}$ and is

$$\mathcal{N}(\nu) = \left(\mathcal{N}^{+}_{n,n'} - \tilde{\mathcal{N}}^{\rm eq}_{n,n'} \right) \exp \left[-\tau_{n,n'} \int_{\nu}^{\infty} dx\ \phi_{n,n'}(x) \right] + \tilde{\mathcal{N}}^{\rm eq}_{n,n'}, \tag{4.95}$$

$$\tau_{n,n'} \equiv \sum_{l,l'} \tau^{l,l'}_{n,n'}, \tag{4.96}$$

$$\tilde{\mathcal{N}}^{\rm eq}_{n,n'} \equiv \frac{\sum_{l,l'} \tau^{l,l'}_{n,n'} \mathcal{N}^{{\rm eq},l,l'}_{n,n'}}{\sum_{l,l'} \tau^{l,l'}_{n,n'}}. \tag{4.97}$$

As before, we may now evaluate $\mathcal{N}^{-}_{n,n'} = \mathcal{N}(-\infty)$ and obtain the enhancement [e.g. Eq. (4.91)] to the radiation field due to the line:

$$\frac{\mathcal{N}^{-}_{n,n'}}{\mathcal{N}^{+}_{n,n'}} - 1 = \left(\frac{\tilde{\mathcal{N}}^{\rm eq}_{n,n'}}{\mathcal{N}^{+}_{n,n'}} - 1\right)\left(1 - e^{-\tau_{n,n'}}\right). \tag{4.98}$$

As before, for a line to mase, it is necessary (but not sufficient) that the *total* optical depth in the line $\tau_{n,n'} < 0$ and that $|\tau_{n,n'}| \gtrsim 1$. We have the same caveat as in the single-line case that the feedback of stimulated emission in a resonance line on the radiation field may be significant if $\tau_{n,n'} > n_{\rm max}^{-2}$. Using RecSparse output for same $n_{\rm max} = 180$, $T_{\rm M} = T_{\rm R}$ run used to make the plots in Sec. 4.5.1.2, we find that the most negative values of $\tau_{n,n'}$ result for $n = 49$, $n' = 50$. The redshift dependence of $|\tau_{n,n'}(z)|$ is shown in the lower panel of Fig. 4.13. We see the most negative values are $\tau_{n,n'}(z) \sim -10^{-9}$, thwarting our hopes for masing in this spectral line (and all others) in the purely radiative case. We also show $\tau^{2,3}_{49,50}$, since the indicated transition turns out to make the largest negative contribution to $\tau_{49,50}$. Other l, l' pairs make the transition from $\tau^{l,l'}_{49,50} > 0$ to $\tau^{l,l'}_{49,50} < 0$ at later z, and so the maximum value $|\tau^{\rm max}_{49,50}| < |\tau^{{\rm max},l,l'}_{49,50}|$. The only potential caveat to our conclusion of no global recombination maser is that through atomic collisions, additional pumping of atomic levels could occur. We will thus re-visit the issue of masers from cosmological recombination once collisions are properly treated.

4.5.3 The effect of extremely high-n states on recombination histories

To explore the relative convergence of $x_e(z)$ over a wide logarithmic range of $n_{\rm max}$ values, we computed $x_e(z)$ for $n_{\rm max} = 4, 8, 16, 32, 64, 128$, and 250. We define a relative error:

$$\Delta x_e^i(z) = x_e^{n^{i-1}_{\rm max}}(z) - x_e^{n^{i}_{\rm max}}(z). \tag{4.99}$$

Here $n^i_{\rm max}$ is the $i^{\rm th}$ $n_{\rm max}$ value. We show the resulting recombination histories and $\Delta x_e^i(z)$ in Fig. 4.14. As $n_{\rm max}$ increases, the larger number of pathways to the ground state makes recombination more efficient, decreasing $x_e^{n^i_{\rm max}}(z)$ and making $\Delta x_e^i(z)$ positive. The relative error $\Delta x_e^i(z)$ shrinks with $n_{\rm max}$, indicating that relative convergence is taking place, as demonstrated in Fig. 4.15. Note, however, that the relative error may not be a good proxy for the absolute error. Suppose that the absolute error is given by $x_e^{n^i_{\rm max}} = \Delta x_e^{{\rm abs},i} + x_e$, where $\Delta x_e^{{\rm abs},i} = A\left(n^i_{\rm max}\right)^p$, for some normalization A and power-law index $p < 0$. Then it is easy to show that for $n^i_{\rm max} = 2n^{i-1}_{\rm max}$, $\Delta x_e^i/\Delta x_e^{\rm abs,i} = (1 - 2^p)$. In other words, the relative error will underestimate the absolute error. To demonstrate absolute convergence, one should demonstrate that the physics neglected by ignoring transitions to $n > n_{\rm max}$ does not cause large changes in $x_e(z)$. We also calculated recombination histories for $n_{\rm max} = 20, 50, 90, 105$, and 160.

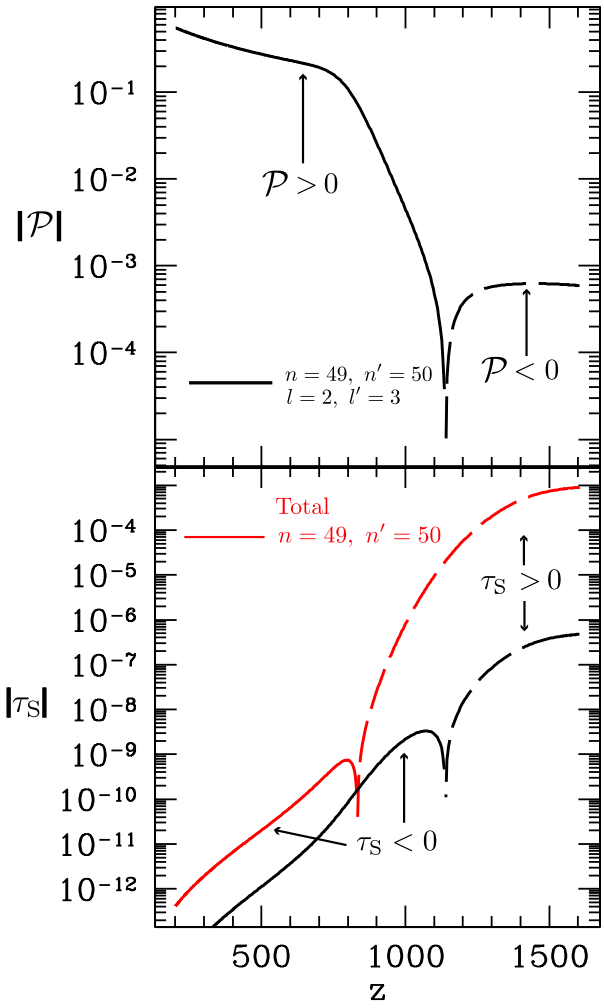

Figure 4.13 Top panel shows population inversion $\mathcal{P}^{l,l'}_{n,n'}$ as a function of redshift z for the $n = 49$, $n' = 50$, $l = 2$, $l = 3$ transition. Dashed portion of the black line indicates that the higher energy level is less populous (including degeneracy factors) than the lower energy level, while the solid portion of the black line indicates population inversion. Bottom panel shows the absolute value of the Sobolev optical depth as a function of z. The black curve shows $\tau^{2,3}_{49,50}$ with the dashed portion corresponding to $\tau^{2,3}_{49,50} > 0$ and solid portion corresponding to $\tau^{2,3}_{49,50} < 0$. The red curve shows the total Sobolev optical depth $\tau_{49,50}$ for the transition, summing over all radiatively coupled sub-levels. The dashed portion indicates $\tau^{2,3}_{49,50} > 0$ while the solid portion indicates $\tau^{2,3}_{49,50} < 0$.

4.5.4 Code comparisons

Independent of our own efforts, a team lead by J. Chluba at CITA[3] has pursued the general problem of computing $x_e(z)$ while resolving l-sublevels [7, 8]. The work described in this chapter improved upon prior work by J. Chluba and collaborators by extending $n_{\rm max}$ from 100 to 250 [44]. Following

[3]Canadian Institute for Theoretical Astrophysics

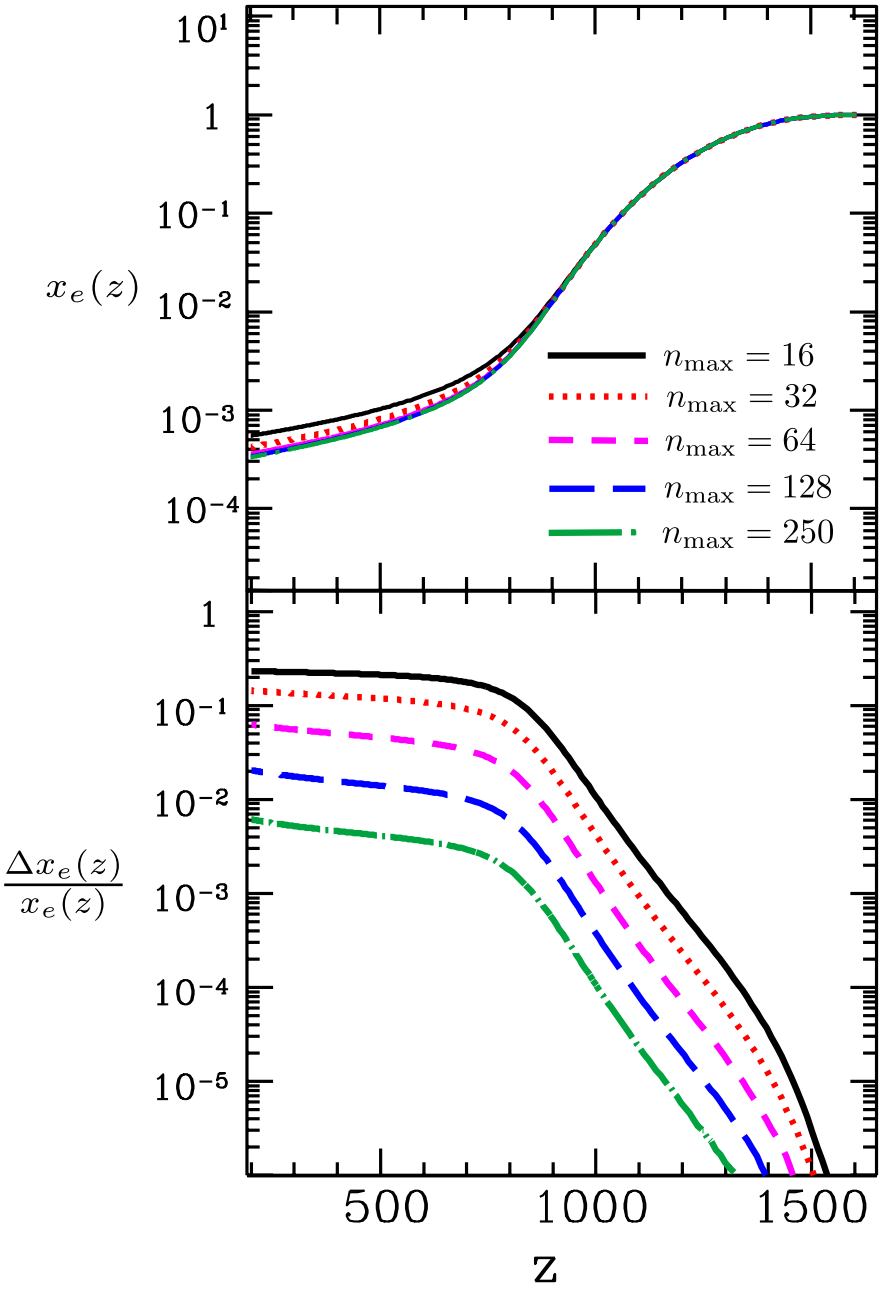

Figure 4.14 The top panel contains the recombination histories $x_e(z)$ and a legend. The bottom panel shows relative errors between successively more accurate recombination histories with the indicated values of $n_{\rm max}$. Higher values of $n_{\rm max}$ make recombination more efficient and yield lower freeze-out values of $x_e(z)$. As $n_{\rm max}$ increases, relative errors shrink, indicating that recombination is convergent with $n_{\rm max}$. The relative error Δx_e^i is defined in Eq. (4.99).

our own work [44], this team has used sophisticated parallel techniques and sparse matrix techniques to extend the reach of their recombination code to $n_{\rm max} = 350$ [9]. To build confidence in each group's techniques, we have devoted considerable effort to a careful comparison of our results. This is an

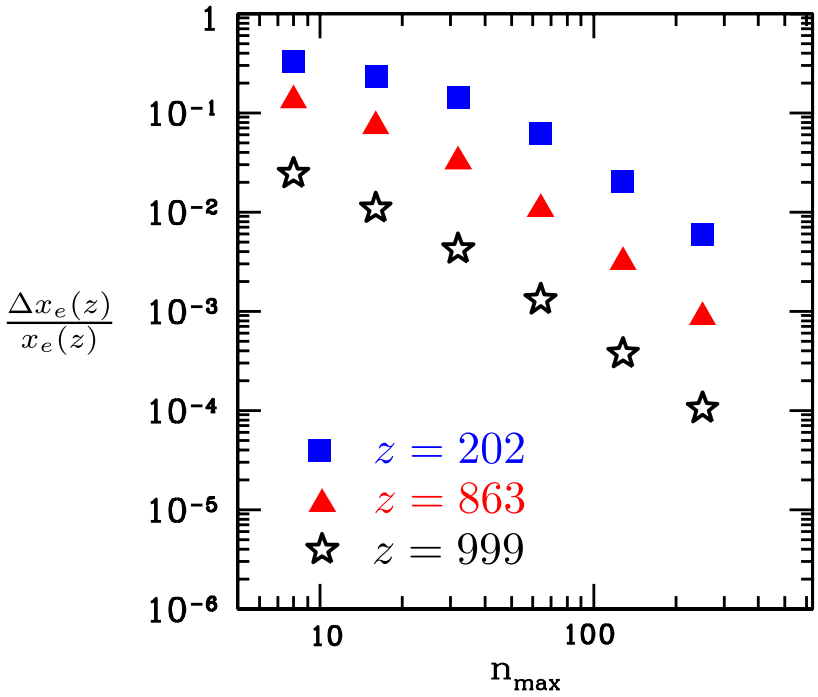

Figure 4.15 Relative errors between successively more accurate recombination histories. Values are shown here for 3 different values of redshift z. Errors shrink with $n_{\rm max}$, indicating relative convergence. Note, however, that this figure gives no scale for the absolute error.

ongoing effort. A blind first-pass comparison of results yielded a disagreement of $\Delta x_e/x_e \simeq 0.1\%$ for $n_{\rm max} = 5$. Once $T_{\rm CMB}$ and $\Omega_{\rm b}h^2$ were adjusted to the fiducial values stated earlier in this chapter and the NIST standard value ($m_{\rm He} = 3.9715\ m_{\rm H}$) adopted for the mass of helium (where m_H is the mass of a hydrogen atom), two additional causes for disagreement were identified.

All other results presented in this chapter were obtained using the theoretical value $\Lambda_{2s,1s} = 8.2246\ {\rm s}^{-1}$ for the crucial $2s \rightarrow 1s$ two-photon transition rate. On the other hand, the results presented in Refs. [7–9] used the more recent theoretical value of $\Lambda_{2s,1s} = 8.2206\ {\rm s}^{-1}$ [340]. This effect led to a discrepancy of $\Delta x_e/x_e \sim 3 \times 10^{-4}$ between the two codes.

Additionally, while we begin using the numerical solution for $T_{\rm M}/T_{\rm R}$ [Eq. (4.19)] for $z \leq 500$ and the asymptotic solution in Eq. (4.21) before that, the work presented in Ref. [8] relies on the numerical solution at all redshifts. This discrepancy is small at early times but is as large as $\Delta x_e/x_e \simeq 3 \times 10^{-3}$ for $z \lesssim 500$. This occurs because the transition from the regime $t_{\rm comp} \ll H^{-1}(z)$ to $t_{\rm comp} \gg H^{-1}(z)$ is actually rather gradual, and corrections to $T_{\rm M}/T_{\rm R}$ at the $\sim 0.1\%$ level are already present at $z = 900$. However, at these relatively early times, Eq. (4.19) is stiff enough to necessitate either using a much finer time-gridding or a stiff solver. Future implementations of RecSparse will include these improvements or perhaps a simpler method for accurately evaluat-

ing $T_{\rm M}/T_{\rm R}$. For the time being, we proceed with the code comparison by enforcing the artificial constraint $T_{\rm M} = T_{\rm R}$ to see if the two codes agree to the level of accuracy needed for *Planck*.

The results are shown in Fig. 4.16. The level of agreement for $n_{\rm max} \leq 128$ is extremely confidence building, as $|\Delta x_e|/x_e < 2 \times 10^{-5}$ when $z \gtrsim 400$. This is well within the required level of accuracy for *Planck* data analysis [40]. It would still be useful to understand the discrepancy at low z, which is likely due to discrepant bound-free transition rates. This is an area of ongoing investigation. The sharp spike at early times subsides quickly, but is likely due to numerical error propagating through the fast mode, which returns the plasma to Saha equilibrium on short time scales before recombination begins in earnest.

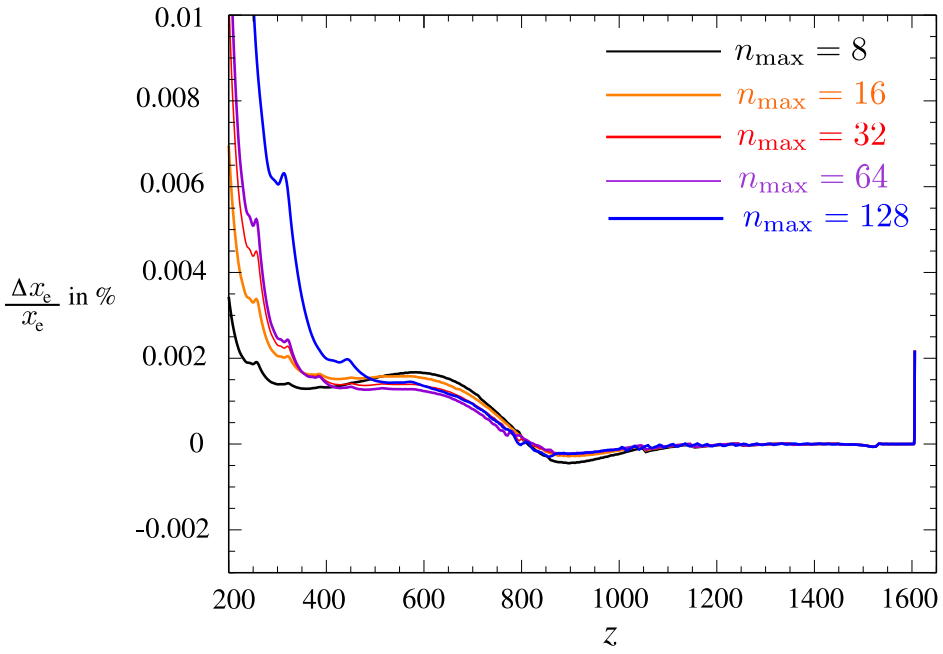

Figure 4.16 Comparison of RecSparse output for $x_e(z)$ with results obtained using the methods of Refs. [7–9], provided courtesy of Jens Chluba and reproduced here with permission.

It is also instructive to compare the relative convergence of $x_e(z)$ for different $n_{\rm max}$ using the methods of Refs. [7–9] (shown in Fig.4.17) and compare this behavior with that shown in RecSparse output. We can see that the convergence behavior agrees between the two codes, both in shape and normalization. The next step in the code comparison project will require updating RecSparse for more precise evolution of $T_{\rm M}/T_{\rm R}$ as a function of z.

4.5.5 The effect of high-n states on CMB anisotropies

We may also assess the effect of the computed changes in $x_e(z)$ on the CMB C_ℓs. To this end, we replace the usual table generated and used in the RecFast module of CMBFast with a table of

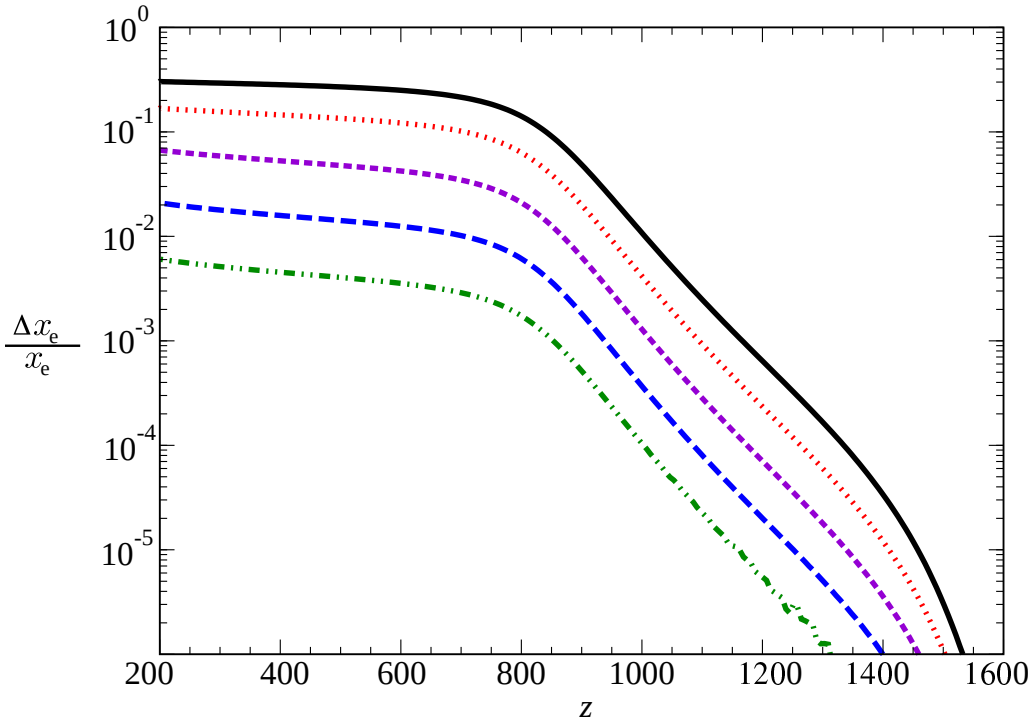

Figure 4.17 This plot shows relative errors between successively more accurate recombination histories as generated in Refs. [7–9]. Colors are as in Fig. 4.14. As $n_{\rm max}$ increases, relative errors shrink, indicating that recombination is convergent with $n_{\rm max}$. The relative error Δx_e^i is defined in Eq. (4.99). Plot provided by Jens Chluba and reproduced with permission.

our own output for different $n_{\rm max}$ values, smoothly stitching our history onto the usual RecFast history at the boundaries $z = 1606$ and $z = 200$. We ran CMBFast with scale-invariant adiabatic initial conditions, and no relic electrons from reionization. We tried a variety of smoothing schemes including no smoothing at all, and determined that the resulting error was at most 10% the change already induced by varying $n_{\rm max}$. The choice of smoothing scheme is thus a "correction to a correction" and does not alter the conclusions of our analysis. In particular, the number of sigmas at which power spectra corrected and uncorrected for higher-n levels (specifically, $n_{\rm max} = 128$ vs. $n_{\rm max} = 64$) can be distinguished will change by at most 10% of itself as a result of changing the smoothing scheme. The statistical significance of higher-n shells will thus be essentially unchanged by the choice of smoothing scheme. The results for temperature and E-mode polarization anisotropy power spectra ($C_\ell^{\rm TT}$ and $C_\ell^{\rm EE}$) are shown in Figs. 4.18 and 4.19, respectively. Here we also define a relative error:

$$\Delta C_\ell^{\rm XX,i} = C_\ell^{{\rm XX},n_{\rm max}^{i-1}} - C_\ell^{{\rm XX},n_{\rm max}^{i}}. \tag{4.100}$$

Here XX denotes the TT or EE label of the power spectrum under consideration. The relative error $\Delta C_\ell^{\rm XX,i}$ is always negative, indicating that increasing $n_{\rm max}$ also increases $C_\ell^{\rm XX}$, as shown in Figs.

4.18 and 4.19. The common (TT and EE) origin for this effect is clear from Fig. 4.14. Higher $n_{\rm max}$ makes recombination more efficient, driving down the freeze-out value of $x_e(z)$ and the residual optical depth $\tau\left(\chi_{\rm SLS}\right)$ to the SLS due to Thompson scattering, where $\tau\left(\chi\right)$ is given by

$$\tau\left(\chi\right) = -\int_{\chi_0}^{\chi} d\chi' \eta_e \sigma_{\rm T} a(\chi'). \tag{4.101}$$

Here $\chi = \int_0^t dt'/a$ is the conformal time while χ_0 denotes its value today. The familiar optical depth due to Thompson scattering is $\tau\left(\chi\right)$ and dots indicate derivatives with respect to conformal time. As a result of smaller $\tau\left(\chi_{\rm SLS}\right)$ for higher $n_{\rm max}$, the smearing out of primary CMB anisotropies by relic free electrons, $C_\ell \rightarrow C_\ell e^{-2\tau(\chi_{\rm SLS})}$ [38], is less dramatic. This suppression leads to the high-l plateaus seen in Fig. 4.18 and 4.19, as $\Delta C_\ell \propto -C_\ell \Delta\tau\left(\chi_{\rm SLS}\right)$ for small $\tau\left(\chi_{\rm SLS}\right)$. The absolute value of the fractional relative error, $|\Delta C_\ell^{\rm XX,i}|/C_\ell^{\rm XX}$ shrinks with increasing $n_{\rm max}$, due to the progressively smaller changes in x_e [and thus $\tau\left(\chi_{\rm LSS}\right)$] for successive doublings of $n_{\rm max}$.

4.4.5.1 The visibility function

We can reinforce our intuition for how including high-n states changes the CMB multipole moments by re-acquainting ourselves with the *visibility* function $g(\chi)$:

$$g(\chi) = -\dot{\tau} e^{-\tau(\eta)} \tag{4.102}$$

Physically, $g(\chi)$ is the probability that a CMB photon last scatters at conformal time χ. The visibility function appears when evaluating CMB temperature multipole moments [here we ignore contributions from time-dependence in gravitational potentials (the integrated Sachs-Wolfe effect [236]) and from the angular dependence of Compton scattering] [236]:

$$\begin{aligned} \Theta_\ell(k,\eta_0) &= \int_0^{\chi_0} d\chi g(\chi) \left[\Theta_0\left(k,\chi\right) + \Psi\left(k,\chi\right)\right] j_\ell\left[k\left(\chi_0-\chi\right)\right] \\ &- \int_0^{\chi_0} d\chi g(\chi) \frac{3\Theta_1}{k} \frac{d}{d\chi} j_\ell\left[k\left(\chi_0-\chi\right)\right]. \end{aligned} \tag{4.103}$$

Here k is the amplitude of a Fourier mode, ℓ is the multipole number, Θ_ℓ the $l^{\rm th}$ temperature multipole moment and Ψ is the Newtonian gravitational potential perturbation.

Using the Boltzmann code CAMB [341], we stitch in RECSPARSE recombination histories, smoothly joining $x_e(z)$ onto the RECSPARSE-generated histories at the boundaries $z = 200$ and $z = 1606$. Results for the $C_\ell s$ are consistent with those obtained using CMBFAST, but here we chose CAMB here due to its modular nature and the ease of obtaining numerical output for $g(z)$. The resulting $g(z)$ is shown in Fig. 4.20, along with fractional differences $\Delta g/g$ between successive increases in $n_{\rm max}$. We see that when going from $n_{\rm max} = 11$ to $n_{\rm max} = 30$, the tail of the visibility function is lowered while

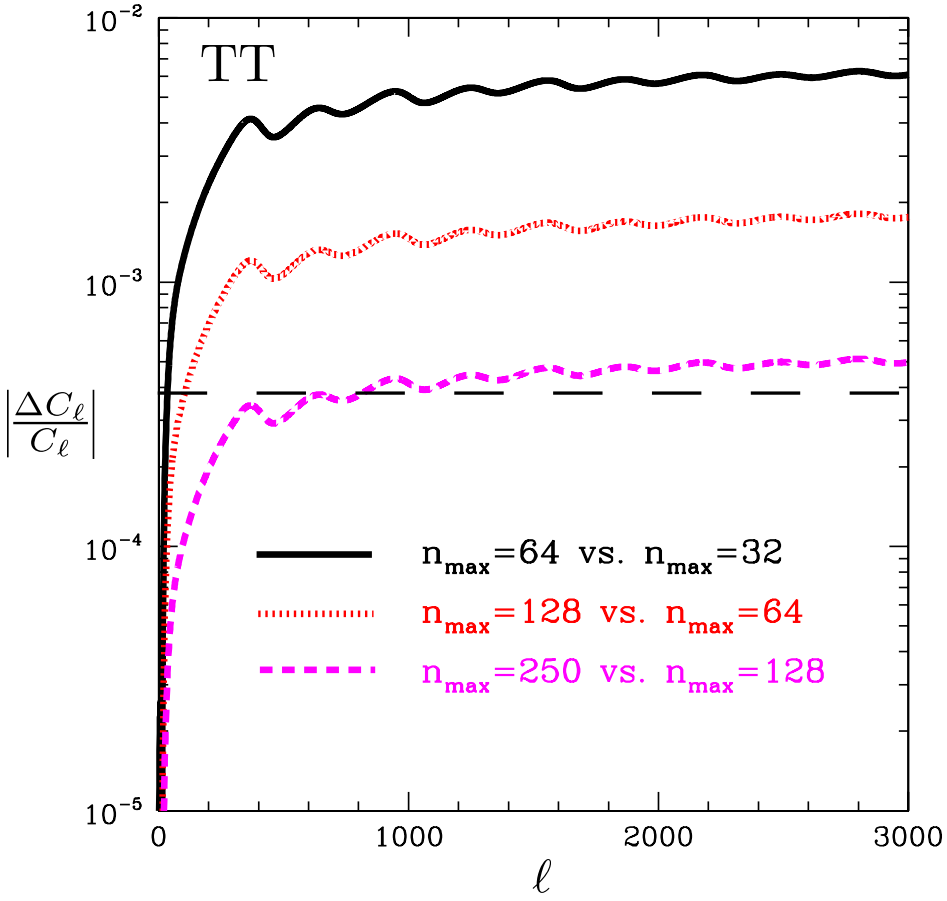

Figure 4.18 Relative errors between temperature anisotropy spectra $C_\ell^{\rm TT}$ computed using CMBFAST, modified to include successively more accurate RECSPARSE recombination histories. Pairs of $n_{\rm max}$ values used for the comparison are indicated in the legend. $C_\ell^{\rm TT}$ increases with $n_{\rm max}$, as discussed in Sec. 4.5.5. The correction shrinks with increasing $n_{\rm max}$. The long dashed line indicates the cosmic variance target for $\Delta C_\ell/C_\ell$, as discussed in the text.

its peak is raised. We see that the largest correction to $g(z)$ from including higher-n states occurs at low z, when $\Delta x_e(z)/x_e(z)$ is largest. The lower electron densities at late times that result from including higher-n states make it *less* likely that a photon will last scatter at those times, explaining the negative-sign of the correction at low z. Since the total last-scattering probability over cosmic time is $\int d\chi g(\chi) = 1$, the early-time probability of last-scattering must be correspondingly higher, explaining the positive sign of the correction at high z. This is easy to understand: if a CMB photon is less likely to *last* scatter at lower z after the putative SLS, it must be more likely to last scatter at early times. This is a result of the fact that $g(z)$ is fundamentally an integral quantity, since $\tau(\chi) = -\int_{\chi_0}^{\chi} d\chi' d\tau/d\chi'$ depends on $x_e(z)$ along the whole interval $0 < \chi' < \chi$.

The fractional change to $g(z)$ due to $n_{\rm max} \geq 100$ is quite small near the SLS [which is located at the peak of $g(z)$] at $z_{\rm SLS} \simeq 1088$, and the width of the SLS is not noticeably changed. Thus

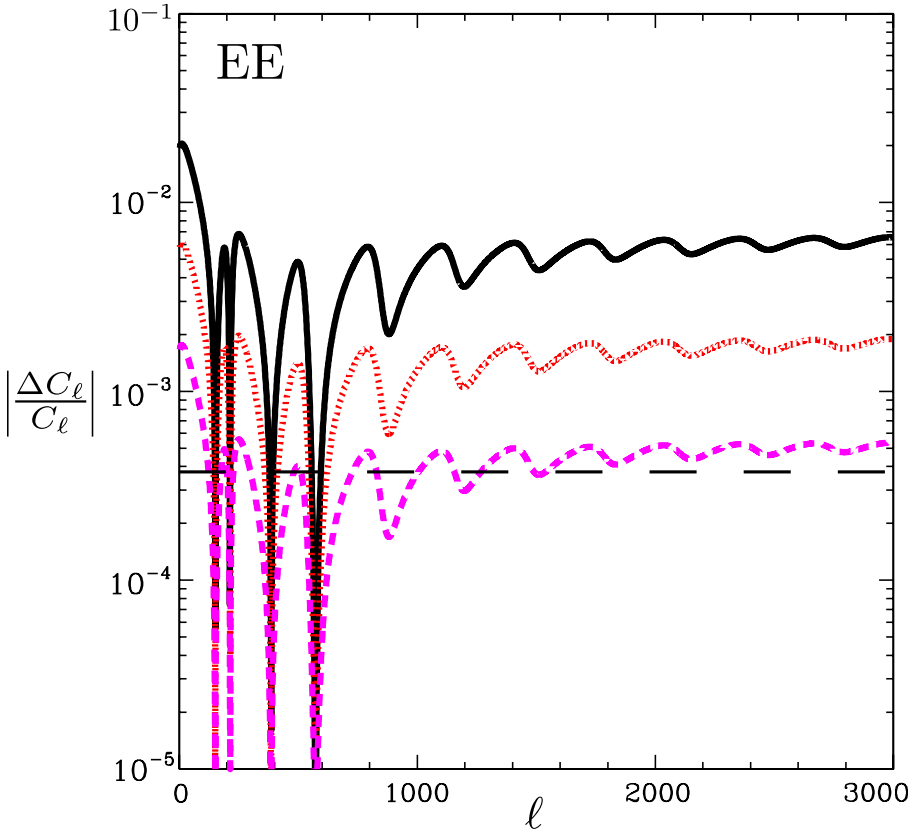

Figure 4.19 Relative errors between E-mode polarization anisotropy spectra $C_\ell^{\rm EE}$ computed using CMBFast, modified to include successively more accurate RecSparse recombination histories. Pairs of $n_{\rm max}$ values used for the comparison are indicated in the legend of Fig. 4.18. $C_\ell^{\rm EE}$ increases with $n_{\rm max}$, as discussed in Sec. 4.5.5. The correction shrinks with increasing $n_{\rm max}$. The long dashed line indicates the cosmic variance target for $\Delta C_\ell/C_\ell$, as discussed in the text.

the suppression of temperature anisotropies (and generation of polarization anisotropies) by Silk damping near the SLS is nearly unaffected by the addition of extremely high-n states, while the re-scattering of primary anisotropies by free electrons along the line of sight is noticeably perturbed. Heuristically, the total probability that a photon reaching an observer today last scattered somewhere between the observer and surface of last scattering is $\int_0^{\chi_{\rm SLS}} d\chi g(x) = 1 - e^{-\tau(\chi_{\rm SLS})}$. Thus a CMB photon leaving the surface of last scattering has a probability $e^{-\tau(\chi_{\rm LSS})}$ of traveling directly to an observer staring at the patch of sky from which the photon originates. Relic electrons along the line of sight then reduce the anisotropy from $\Theta \rightarrow \Theta e^{-\tau(\chi_{\rm SLS})}$, and the multipole moments are correspondingly reduced $C_\ell \rightarrow C_\ell e^{-2\tau(\chi_{\rm SLS})}$. Changes to the free-electron fraction due to high $n_{\rm max}$ occur predominantly at low z, and it is for this reason that the C_ℓs converge fairly quickly with $n_{\rm max}$. We now proceed to assess the significance for CMB (*Planck*) data analysis of the correction to the $C_\ell s$ resulting from the inclusion of high-n states.

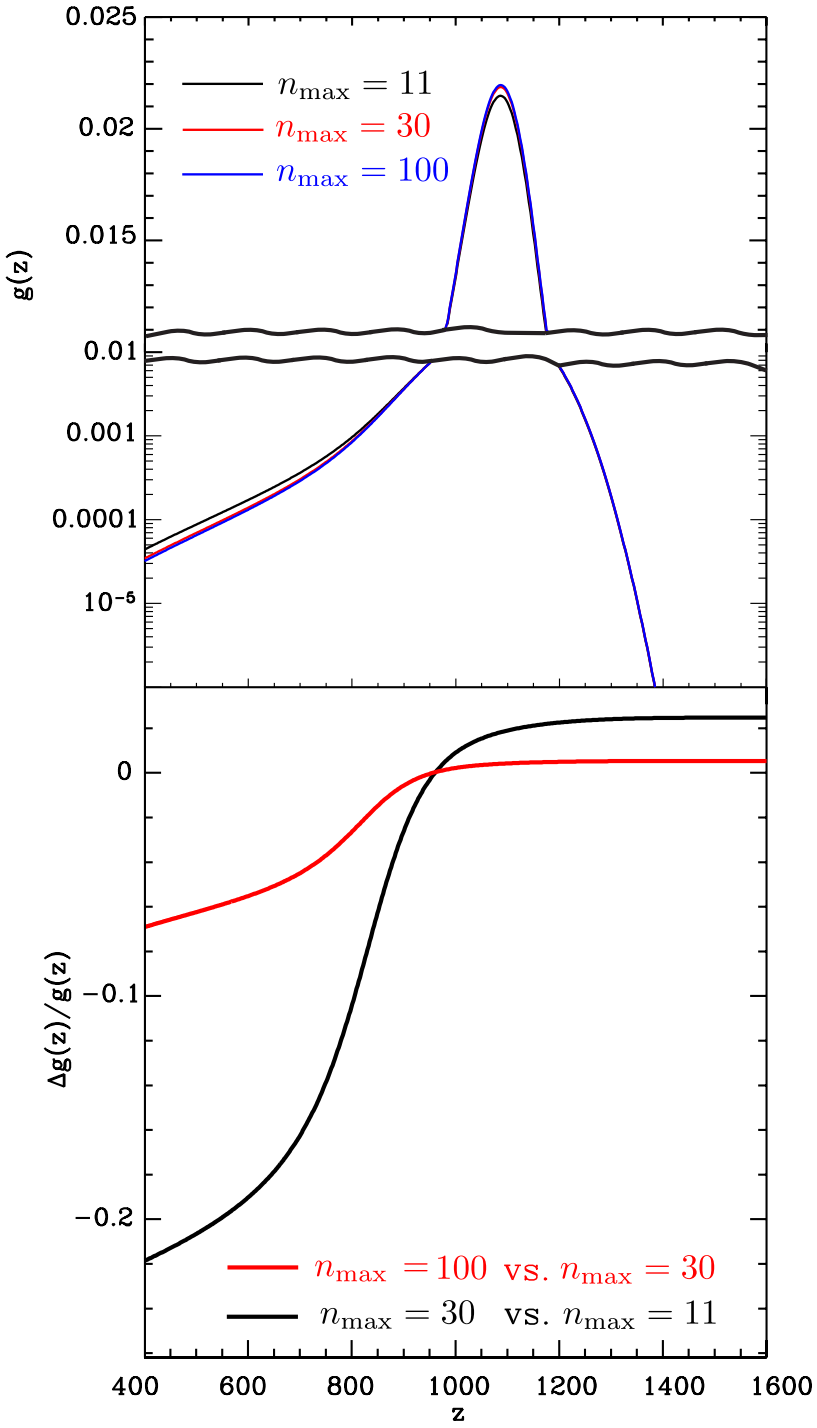

Figure 4.20 Effect of high-n states on the visibility function $g(z)$. The top panel shows the visibility function generated by the Boltzmann code CAMB using recombination histories output by RecSparse for $n_{\max} = 11$, 30, and 100. The function $g(z)$ is smooth; the double wavy lines in the middle of the top panel mark the boundary between logarithmic/linear y-axes. This is done to highlight features in the plots near the peak and tail of $g(z)$. The bottom panel shows fractional corrections that result to the visibility function when going from $n_{\max} = 11$ to $n_{\max} = 11$ (black curve), and from $n_{\max} = 30$ to $n_{\max} = 100$ (red curve).

4.5.6 Statistical significance of corrections to the recombination history

Taken as a proxy for the absolute error, $\Delta C_\ell^{\rm XX,i}$ may be compared to a crude (cosmic variance) estimate of the required accuracy of $C_\ell^{\rm XX}$ predictions in the damping tail:

$$\frac{\Delta C_\ell^{\rm XX}}{C_\ell^{\rm XX}} \sim 3\times 10^{-4} f_{\rm sky}^{-1/2}. \tag{4.104}$$

Here $f_{\rm sky}$ is the fraction of the sky covered by a CMB experiment. For $f_{\rm sky}=0.70$, results are shown in Figs. 4.18 and 4.19 and we see that only for $n_{\rm max}=250$ does the relative error shrink to a level comparable with the cosmic variance. The ultimate aim is for *the total* correction from recombination physics to be less than statistical errors, so any individual contribution such as the truncation error at $n_{\rm max}$ should be $\ll 1\sigma$. In any case, collisions must be properly included to show absolute convergence, and so this should be a key focus of future work on highly excited states in hydrogen recombination. To more realistically assess the importance of high-n states, $\Delta C_\ell^{\rm XX}$ should be compared with a realistic error estimate for *Planck*.

As a test of the importance of the modified recombination history for *Planck*, we have compared our corrections to the power spectrum ΔC_ℓ with the forecast *Planck* error bars. The comparison is done by means of the statistic

$$Z = \sqrt{\sum_{ll'} F_{ll'}\Delta C_l \Delta C_{l'}}, \tag{4.105}$$

where $F_{ll'}$ is the Fisher matrix for the CMB power spectrum. For the temperature-only case, ℓ ranges from 2 to $\ell_{\rm max}$ and hence $\mathbf{F}$ is an $(\ell_{\rm max}-1)\times(\ell_{\rm max}-1)$ matrix; when polarization is included, $\mathbf{F}$ expands to a $3(\ell_{\rm max}-1)\times 3(\ell_{\rm max}-1)$ matrix incorporating TT, EE, and TE spectra. The Z statistic is the number of sigmas at which the corrected and uncorrected power spectra could be distinguished assuming perfect knowledge of the cosmological parameters, and hence represents the largest possible bias (in sigmas) on any combination of cosmological parameters in any fit that incorporates the CMB [283]. We use the forecast noise and beam curves for *Planck* data 70 GHz (Low-Frequency Instrument) and 100 and 143 GHz (High-Frequency Instrument) channels in the Blue Book [35], and assume a usable sky fraction of $f_{\rm sky}=0.7$.

The computation considering the difference between the $n_{\rm max}=128$ and 250 curves gives a Z value of 0.36. However, the actual error in the $n_{\rm max}=128$ calculation is somewhat greater because even the $n_{\rm max}=250$ calculation is not completely converged. If the error in the C_ls scales as $\sim n_{\rm max}^p$ and has a shape that varies slowly with $n_{\rm max}$, then our value of Z should be increased by a factor of $[1-(250/128)^p]^{-1}$; for $p\approx -1.9$ (as suggested by Fig. 4.15) this is 1.39. Thus if the power-law extrapolation is to be trusted there is a 0.50σ error ($Z=0.50$) in the CMB power spectrum if one restricts attention to $n_{\rm max}=128$, and a ~ 4 times smaller error ($Z=0.14$) at $n_{\rm max}=250$. A similar comparison between $n_{\rm max}=64$ and 250 implies an error of $Z=1.79$ at $n_{\rm max}=64$. This suggests

that in the *purely radiative* problem the CMB power spectrum is converged (in the sense that our remaining errors are small compared to projected *Planck* errors) at $n_{\rm max} \geq 128$; however this issue will have to be reconsidered in future work when collisions are included.

In Ref. [40], CAMB and a recombination history generated using $n_{\rm max} = 110$ are used to create mock *Planck* data sets. These are then analyzed using standard Monte-Carlo Markov Chain (MCMC) techniques, assuming either $n_{\rm max} = 75$, or in contrast, $n_{\rm max} = 110$. This is done to assess the bias induced on cosmological parameters when using an insufficient number of levels. Using CMB data alone, no statistically significant bias is found in the scalar spectral index n_s, the optical depth $\tau\left(\chi_{\rm SLS}\right)$, the curvature parameter Ω_k, the cold dark-matter density parameter $\Omega_c h^2$, the present-day Hubble parameter H_0, the baryon density $\Omega_b h^2$, or the amplitude of the primordial power spectrum A_s.

The likely reason for the lack of bias, in spite of the results of our own Fisher analysis, is the well-known fact that using CMB data alone, A_s and $\tau\left(\chi_{\rm SLS}\right)$ are very degenerate. The corrections due to high n are corrections to $\tau\left(\chi_{\rm SLS}\right)$, as we saw in Sec. 4.5.3 (Fig. 4.14). We thus suspect that the correction due to highly excited states is lurking in the Fisher matrix, unlikely to emerge as bias into parameter estimates until the degeneracy between A_s and τ is broken by combining CMB data with a LSS data set. We will check this hypothesis in the near future by projecting our full Fisher matrix into biases/uncertainties for the cosmological parameters of interest, and perhaps also by running our own MCMC.

4.5.7 The effect of electric quadrupole transitions on recombination histories and the CMB

Using the treatment of Sec. 4.4 and an integration stepsize fine enough to obtain a fractional accuracy of 10^{-10} in x_e, we compute the effect of E2 quadrupole transitions on cosmological hydrogen recombination for several values of $n_{\rm max}$. We can parametrize this effect using

$$\Delta x_e \equiv x_e|_{\text{no E2 transitions}} - x_e|_{\text{with E2 transitions}}\,, \tag{4.106}$$

and

$$\Delta C_\ell \equiv C_\ell|_{\text{no E2 transitions}} - C_\ell|_{\text{with E2 transitions}}\,. \tag{4.107}$$

Note that unlike the case of varying $n_{\rm max}$, these are the absolute errors induced by ignoring E2 transitions.

The results are shown in Fig. 4.21. The maximum effect of E2 transitions occurs at $z \sim 800$ with a fractional enhancement of $\Delta x_e/x_e \simeq 10^{-5}$, and the calculation seems well converged by $n_{\rm max} = 30$. Corrections due to even higher excited states would be a correction to a correction, and so we ignore

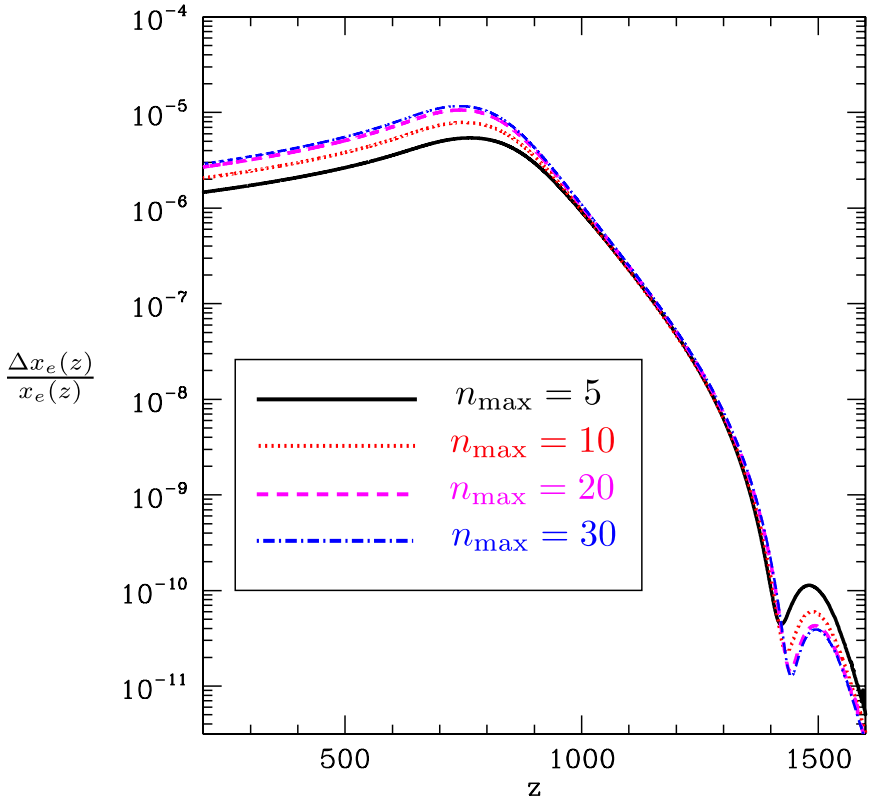

Figure 4.21 Fractional difference between recombination histories with/without E2 quadrupole transitions included for different values of $n_{\rm max}$. The net effect is always to speed up recombination.

them. We can explain features in this figure and develop some intuition for the effect of including E2 transitions.

Examining output files from RecSparse at early times and for $n < 5$, we see that $l = 2$ is less underpopulated than $l = 1$. Since $\dot{x}_{np} = -\dot{x}_{nd} \propto x_{nd} - 5x_{np}/3 > 0$ [see Eq. (4.74)], there will be an additional flux of atoms from the nd state to the np state because of E2 transitions. We can anticipate the effect on the recombination history by examining the schematic in Fig. 4.22. More atoms in the np state will decay to the $2s$ state than would otherwise. Since $2s \rightarrow 1s$ is the dominant recombination channel at early times (see Sec. 4.1), the net recombination rate will increase. Thus $x_e(z)$ will be lower than in the case with no quadrupoles, and so we expect $\Delta x_e(z) > 0$ at high z, as is indeed seen in Fig. 4.21.

At early times and for $n \geq 5$, $l = 2$ is more underpopulated than $l = 1$, as shown in Fig. 4.5. Since $\dot{x}_{nd} = -\dot{x}_{np} \propto 5x_{np}/3 - x_{nd} > 0$ [see Eq. (4.74)], there will be an additional flux of atoms from the np state to the nd state because of E2 transitions. We can anticipate the effect on the recombination history by examining the schematic in Fig. 4.23. More atoms in the nd state will decay to the $2p$ state than would otherwise. Since $2p \rightarrow 1s$ is a sub-dominant recombination channel

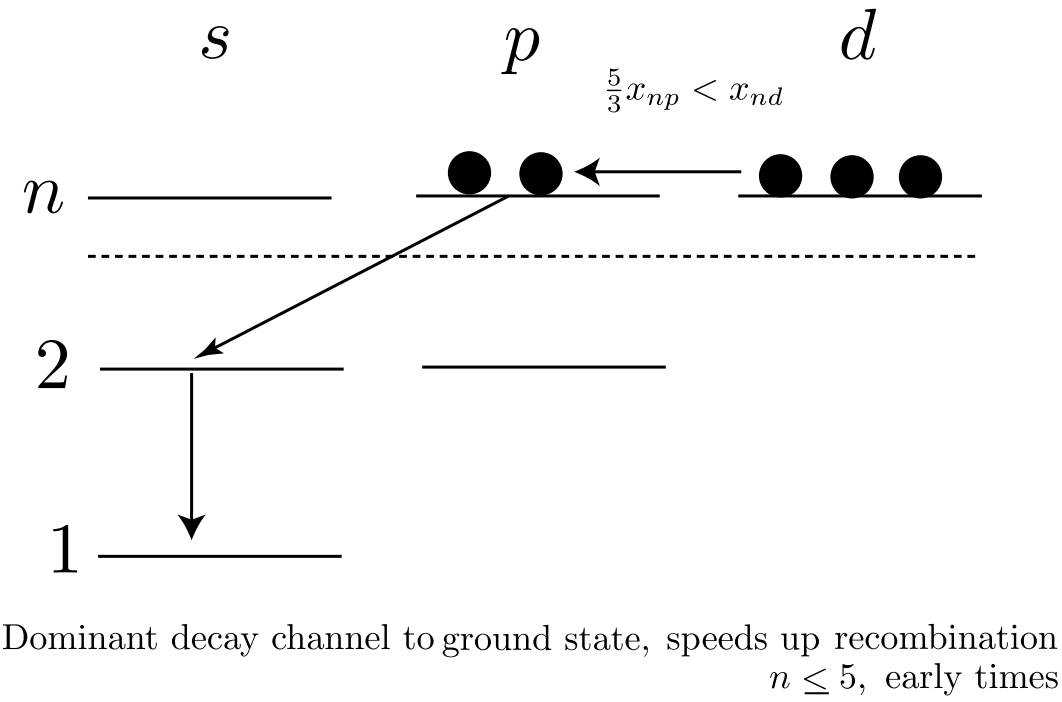

Figure 4.22 Schematic indicating the effect of hydrogen quadrupole transitions with $n < 5$ on the early cosmic recombination history. The number of black circles is proportional to the abundance $x_{n,l} = \eta_{n,l}/\eta_{\rm H}$ of a state. See text for detailed discussion.

at early times (see Sec. 4.1), the net recombination rate will be lower than it would be if only quadrupole transitions from $n < 5$ were included. Thus $x_e(z)$ will still be lower than it would if no quadrupole transitions were included, but less dramatically so, and so we expect lower $\Delta x_e(z)$ values at high z when higher-n quadrupole transitions are included, as is indeed seen in Fig. 4.21.

At late times and for $n \geq 5$, $l = 2$ is more underpopulated than $l = 1$, as shown in Fig. 4.5. Since $\dot{x}_{nd} = -\dot{x}_{np} \propto 5x_{np}/3 - x_{nd} > 0$ [see Eq. (4.74)], there will be an additional flux of atoms from the np state to the nd state because of E2 transitions. We can anticipate the effect on the recombination history by examining the schematic in Fig. 4.24. More atoms in the nd state will decay to the $2p$ state than would otherwise. Since $2p \rightarrow 1s$ is the dominant recombination channel at late times (see Sec. 4.1), the net recombination rate will increase as higher-n quadrupole transitions are included. Thus $x_e(z)$ will be get lower and lower as more quadrupole transitions are included, and so we expect higher $\Delta x_e(z)$ values at low z, as is indeed seen in Fig. 4.21.

Although the correction from E2 transitions is small, it extends over a broad epoch at late times after reaching its maximum. To determine if this could affect CMB anisotropies in an observable way, we modify and run CMBFAST [342] using recombination histories computed with/without E2 transitions. The results are shown in Figs. 4.25-4.26.

E2 transitions decrease $x_e(z)$, and so the optical depth $\tau = \int \eta_e(\chi)\, \sigma_{\rm T} a(\xi) d\xi$ to the SLSS

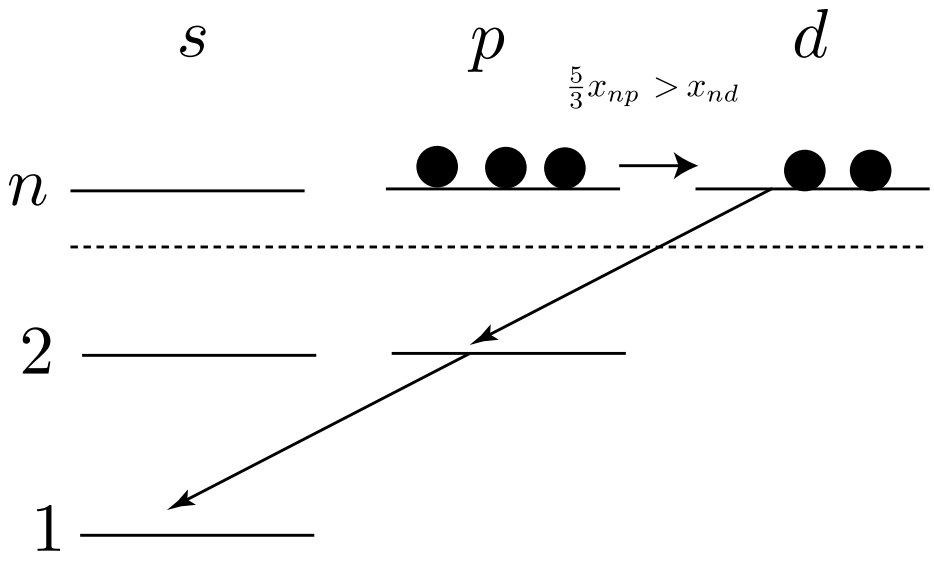

Figure 4.23 Schematic indicating the effect of hydrogen quadrupole transitions with $n \geq 5$ on the early cosmic recombination history. The number of black circles is proportional to the abundance $x_{n,l} = \eta_{n,l}/\eta_{\rm H}$ of a state. See text for detailed discussion.

decreases, where is ξ is the conformal time. At small angular scales, anisotropies are suppressed by the 'smearing factor' due to re-scattering of CMB photons by relic electrons along the line of sight, that is, $C_l^{\rm TT,EE} \rightarrow e^{-2\tau(\chi_{\rm SLS})} C_l^{\rm TT,EE}$. The smaller optical depth resulting from E2 transitions causes a slight enhancement in $C_l^{\rm TT,EE}$, as seen in Figs. 4.25-4.26. We conclude that the observed change in the anisotropy results from changes to $\tau\left(\chi_{\rm SLS}\right)$, since the lower electron densities would lead to longer mean-free paths $\lambda \sim 1/\left(\eta_e \sigma_{\rm T}\right)$ for CMB photons. The damping tail thus sets in at larger angular scales, which should lead to a *decrease* in TT power on small scales [265]. Similarly, the slightly shorter recombination epoch leaves less time for quadrupole temperature anisotropies to grow and get re-scattered into polarization anisotropies. This would cause a decrease in EE power. Since the opposite is seen for both temperature and polarization in Figs. 4.25-4.26, we conclude that the dominant effect of E2 transitions is through the 'smearing effect' [38, 236, 266] induced by a slightly lower value of τ. This is primarily a late time effect induced by a large $\tau(\chi_{\rm SLS})$, and the change to the visibility function of $g(z)$ resulting from the inclusion of E2 transitions is qualitatively similar to the effect of dipole transitions to very high $n_{\rm max}$ (as exhibited in Fig. 4.20).

Higher values of $n_{\rm max}$, with their faster net recombination rates, decrease $\tau\left(\chi_{\rm SLS}\right)$ and thus increase temperature and polarization power spectra $C_l^{\rm TT,EE}$. Large-angle modes re-enter the horizon after recombination and are unaffected by changes to the recombination history. This fact is reflected

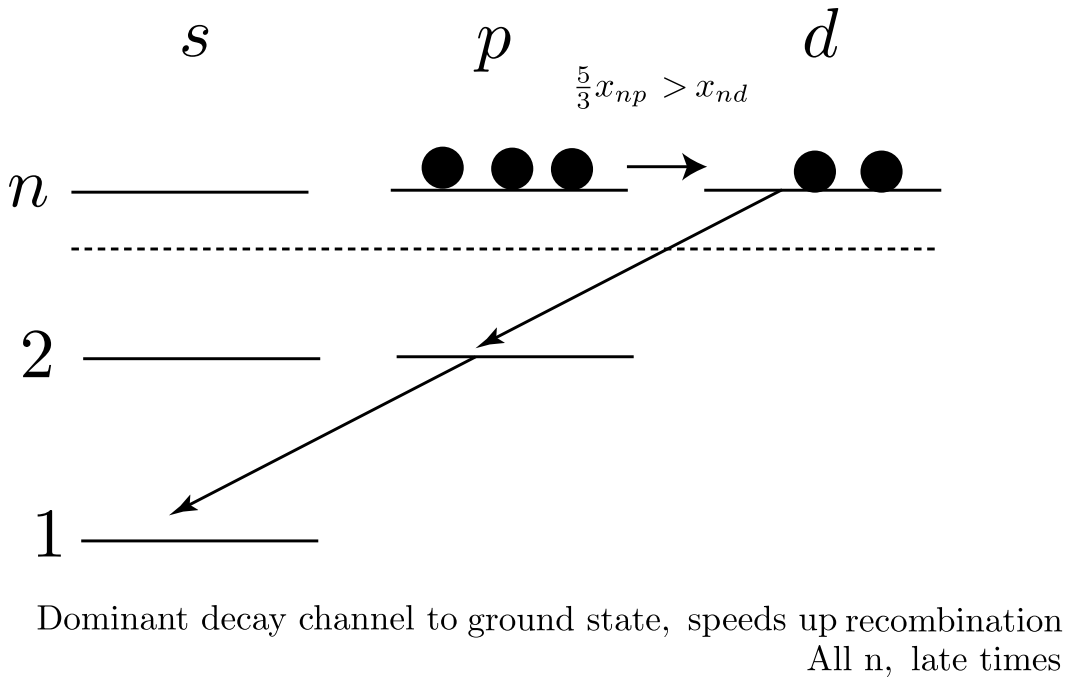

Figure 4.24 Schematic indicating the effect of hydrogen quadrupole transitions with any n on the late cosmic recombination history. The number of black circles is proportional to the abundance $x_{n,l} = \eta_{n,l}/\eta_{\rm H}$ of a state. See text for detailed discussion.

by the convergence and drop-off at low l in all the curves in Fig. 4.25. As before, we can safely neglect the effect of states with $n > n_{\rm max}$ when comparing recombination with/without quadrupole transitions, since they are a correction to a correction. The contribution of E2 quadrupole transitions to $C_l^{\rm TT,EE}$ converges to $\Delta C_l/C_l \sim 3 \times 10^{-6}$, negligible compared to the (sample variance) Planck accuracy requirement of [286]

$$\frac{\Delta C_l^{\rm TT,EE}}{C_l^{\rm TT,EE}} \lesssim 2 \times 10^{-4} f_{\rm sky}^{-1/2}, \tag{4.108}$$

where $f_{\rm sky}$ is the fraction of the sky remaining after foregrounds have been adequately masked. The changes in $C_l^{\rm TT,EE}$ due to E2 transitions are only ~ 2 orders of magnitude too low to be important for Planck; the simple order-of-magnitude estimate of Sec. 4.4 fails due to order-unity factors, motivating our detailed computation. This computation shows that the effect of E2 transitions in hydrogen on cosmological recombination may be safely ignored when analyzing Planck data. Future primary polarization anisotropy experiments will extend the cosmic-variance-limited range of l, but errors will still be bounded from below by cosmic variance. Thus E2 transitions in hydrogen are also negligible in theoretical calculations of polarization anisotropies for future experiments.

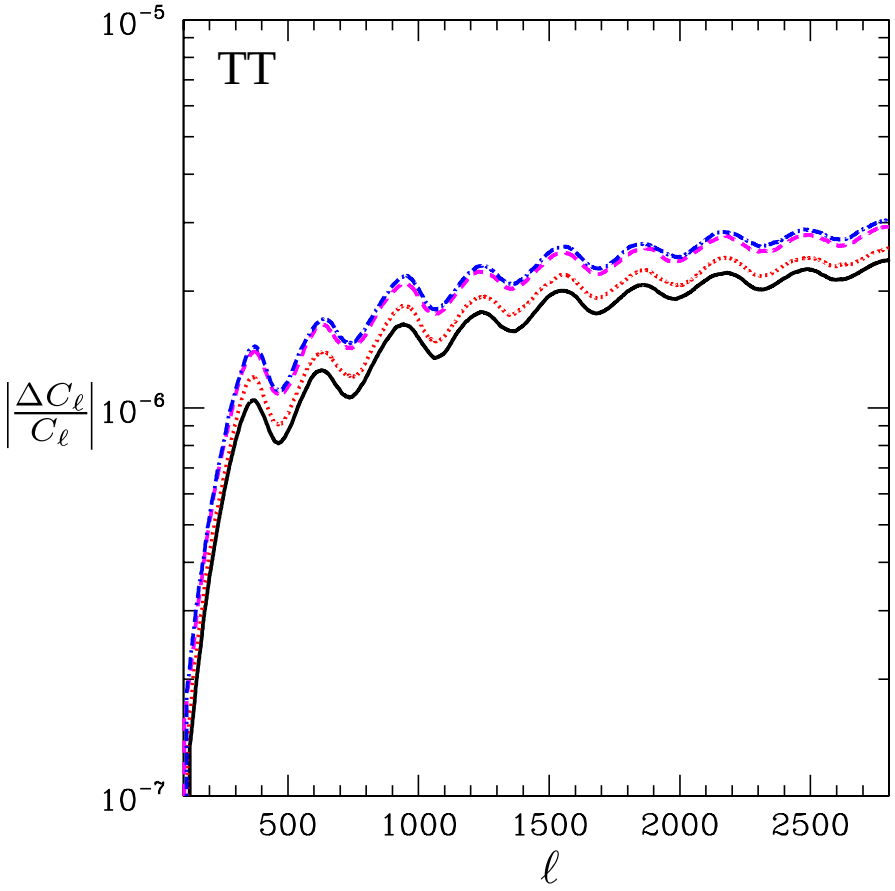

Figure 4.25 Fractional difference between temperature anisotropy angular power spectra $C_l^{\rm TT}$ with/without E2 quadrupole transitions included for different values of $n_{\rm max}$. Color code/line styles are as in Fig. 4.21.

4.6 Conclusions

We have developed a new recombination code, RecSparse, optimized for tracking the populations of many energy shells of the hydrogen atom while resolving angular momentum sublevels. The code runs more quickly than would be anticipated using simple scaling arguments, which would yield the the scaling $t_{\rm comp} \propto n_{\rm max}^6$. Using RecSparse, we find empirically that for the range of $n_{\rm max}$ values used, computation time scales as $t_{\rm comp} \propto n_{\rm max}^\alpha$, where $2 < \alpha < 3$. With this code, we have computed cosmological hydrogen recombination histories for a series of $n_{\rm max}$ values going as high as $n_{\rm max} = 250$ and explored the highly nonequilibrium state of the resulting atomic hydrogen.

The resulting correction $\Delta x_e(z)$ satisfies $\Delta x_e(z)/x_e(z) < 0.01$ for $z > 200$ when $n_{\rm max} = 250$ and converges with $\Delta x_e(z)/x_e(z) \propto n_{\rm max}^{-1.9}$. The correction to the C_ℓs becomes of order the cosmic variance when $n_{\rm max} = 250$. In light of realistic error estimates for *Planck*, the resulting CMB anisotropy spectra $C_\ell^{\rm XX}$ are converged to 0.5σ at Fisher-matrix level for $n_{\rm max} = 128$ in the purely

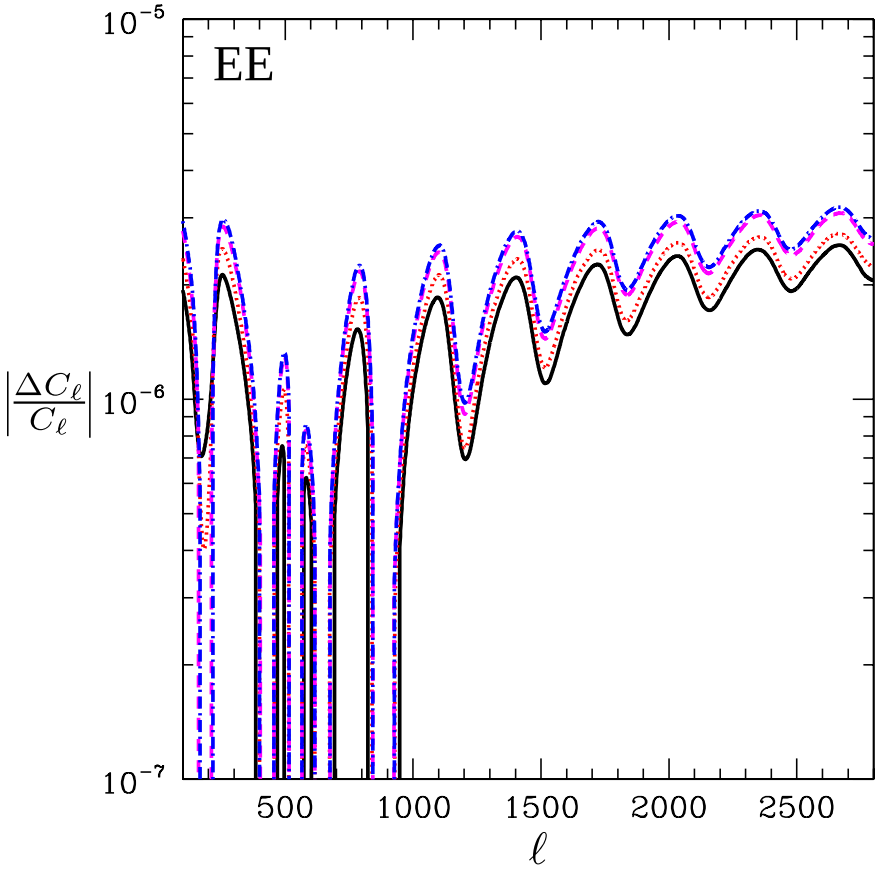

Figure 4.26 Fractional difference between E-mode polarization anisotropy angular power spectra $C_l^{\rm EE}$ with/without E2 quadrupole transitions included for different values of $n_{\rm max}$. Color code/line styles are as in Fig. 4.21.

radiative case, assuming error extrapolations may be trusted. We found E2 quadrupole transitions to make a negligible impact on the CMB power spectra, showed that no maser arises in the purely radiative case, and investigated the onset of collisional dominance of radiative rates.

To definitively answer the question of absolute convergence, collisions must be included to speed the approach to Saha equilibrium at high n, allowing a conclusive treatment of states beyond the truncation limit, with $n > n_{\rm max}$. Future work should also properly account for the overlap of the Lyman resonance line series at high n. It will also be interesting to determine if there is coherent stimulated emission between excited states, given its relevance for the detectability of faint CMB spectral distortions from the epoch of recombination. Finally, the sparse-matrix methods applied here or similar techniques could be profitably applied in the development of fast recombination codes for CMB data analysis, even at early times in recombination, when only lower values of $n_{\rm max}$ are relevant.

Acknowledgments

The author thanks Christopher Hirata for his contributions to the research described in this chapter. The author thanks Y. Ali-Haïmoud for detailed discussions about collisions and line overlap. The author acknowledges useful conversations with Y. Ali-Haïmoud, N. Bode, A. Pullen, T. L. Smith, J. Chluba, J. A. Rubiño-Martín, and the participants of the July 2009 Paris Workshop on Cosmological Recombination. The author additionally thanks Jens Chluba for useful conversations about code comparisons, and for providing two code-comparison figures for this chapter. The author thanks Jens Chluba and CITA for their hospitality during a useful visit during November 2009. This research was supported by DoE DE-FG03-92-ER40701, the National Science Foundation under Contract No. AST-0807337, the Dan David Foundation, the Gordon and Betty Moore Foundation, and the Alfred P. Sloan Foundation.

Chapter 5
Lower Limit to the Scale of an Effective Theory of Gravitation[1]

The discovery of the cosmic acceleration [22–25] has prompted speculations of new physics. A leading hypothesis is the existence of a cosmological constant, responsible for the accelerated expansion. The milli-eV energy scale implied by this phenomenon is difficult to understand in terms of a fundamental theory [343–346]. The validity of Einstein's general theory of relativity (GR) on cosmological scales has thus come under suspicion. A novel solution to this problem might be achieved if GR is a low-energy effective theory in which gravity weakens at some energy scale. In an effective theory of gravity there may exist a threshold, μ, beyond which gravitons cannot mediate momentum transfers. This behavior may be due to a "fat" graviton, a minimal length scale associated with quantum gravity, or possibly nonlinear effects which filter out high-frequency interactions [347–354]. Such theories offer a novel solution to the cosmological constant problem by regulating the contribution of vacuum fluctuations to the cosmological constant. However, we will show that this mechanism may have already been explored and ruled out by gravitational lensing on cosmological scales.

We estimate the energy scale of an effective theory of gravitation by matching the predicted quantum vacuum energy density with the energy density of a cosmological constant, Λ, necessary to explain the accelerated cosmic expansion. Following Zeldovich [355], the gravitating energy density of the particle physics vacuum as due to N equivalent, massless scalar particles, is

$$\rho_\Lambda = \frac{N}{2}\int \frac{d^3k}{(2\pi\hbar)^3}\, kc\, f(k). \tag{5.1}$$

We introduce the function $f(k) = \mathrm{e}^{-k/\mu}$ to regulate the momentum at the vertex where vacuum bubbles connect to gravitons in order to limit the gravitating energy density. We refer to μ as a "cutoff" scale in the sense that the standard gravitational interactions are severely weakened above this scale. We match $\rho_\Lambda = \Omega_\Lambda \rho_{\rm crit}$ and obtain $\mu = 0.0048(\Omega_\Lambda h^2/N)^{1/4}$ eV/c as the desired cutoff scale. Current measurements give $\Omega_\Lambda h^2 = 0.34 \pm 0.04\,(1\sigma)$ (see Ref. [356] and references therein) so that $\mu = 0.0037(1 \pm 0.03)/N^{1/4}$ eV/c. We now examine the consequences of this cutoff.

We consider weak gravitational fields described by a linearized, effective quantum theory of

[1]The material in this chapter was adapted from *Lower Limit to the Scale of an Effective Theory of Gravitation*, Robert R. Caldwell and Daniel Grin; Phys. Rev. Lett. **100**, 031301 (2008). Reproduced here with permission, copyright (2008) by the American Physical Society.

gravity [357–361]. The interaction Lagrangian at lowest order is

$$\mathcal{L}_I = -\frac{1}{2}\kappa h_{\mu\nu} T^{\mu\nu} \tag{5.2}$$

where $\kappa = \sqrt{32\pi G}$, $h_{\mu\nu}$ is the graviton field, and $T^{\mu\nu}$ is the stress-energy tensor of the gravitating sources. Here, we introduce an exponential cutoff at μ on graviton momenta.

Short-distance gravitational phenomena below the length $\ell_0 = \hbar/\mu \sim 0.05$ mm are affected by such a cutoff, which we impose on the graviton four-momentum q^μ so that $q^2 \equiv q^\mu q_\mu < \mu^2$. For real gravitons, $q^\mu q_\mu = 0$ and so the constraint is trivially satisfied. For virtual gravitons, the cutoff may be imposed by suppressing the graviton propagator in the ultraviolet [362]: $1/q^2 \to \mathcal{G}\left(q^2/\mu^2\right)/q^2$, where $\mathcal{G}$ is a function of the graviton momentum. For example, our exponential cutoff follows if $\mathcal{G}(x) = e^{-\sqrt{x}}$. Such a modified propagator follows naturally from modified gravitational Lagrangians. This is clear upon inspection of the weak-field, Coulomb gauge, gravitational Lagrangian for a "fading gravity" model [362]:

$$\mathcal{L}_g = 2\left(h^{\alpha\beta} - \frac{1}{2}\eta^{\alpha\beta}h\right)\mathcal{G}^{-1}\left(\Box/\mu^2\right)\Box h_{\alpha\beta}, \tag{5.3}$$

where $\Box$ is the D'Alembertian operator. The sum of (5.2) and (5.3) can be used to obtain the weak-field equations of motion.

An exponential cutoff to the momentum-space integral for the virtual gravitons exchanged between two static masses, m_1 and m_2, changes the Newtonian potential to

$$\begin{aligned} V &= -8\pi G m_1 m_2 \int \frac{d^3q}{(2\pi)^3\hbar}\frac{1}{2q^2} e^{\frac{i}{\hbar}\vec{q}\cdot(\vec{x}_1-\vec{x}_2)} \times f(q) \\ &= -\frac{G m_1 m_2}{r} \times \frac{2}{\pi}\arctan\frac{r}{\ell_0}. \end{aligned} \tag{5.4}$$

Relativistic corrections to the potential are similarly modified [363, 364]. The above expression asymptotes to the standard result for $r \gg \ell_0$ but reaches a finite minimum as $r/\ell_0 \to 0$. Hence, static masses become free of gravitation at short distances.

The possibility of new gravitational phenomena at submillimeter distances has motivated laboratory tests of the Newtonian force law [365–370]. These experiments look for departures from the Newtonian force law, which are interpreted as bounds on a Yukawa-type modification of the potential, $V = -\frac{Gm_1m_2}{r} \times \left(1 + \alpha \mathrm{e}^{-r/\lambda}\right)$. The potential (5.4) roughly corresponds to $\alpha \sim -1$ and $\lambda \sim \ell_0$. Recent measurements show that the Newtonian force law holds down to 56μm for $|\alpha| = 1$ so that $\mu > 0.0035$ eV/c at the 95% confidence level [370]. These efforts are at the threshold of the scale inferred from Λ.

Long-distance gravitational phenomena are also sensitive to such modifications and provide a tighter bound on μ, the scale of new physics. The key is the limited range of graviton momenta mediating the gravitational force exerted by a massive body on a test particle. Considering the de-

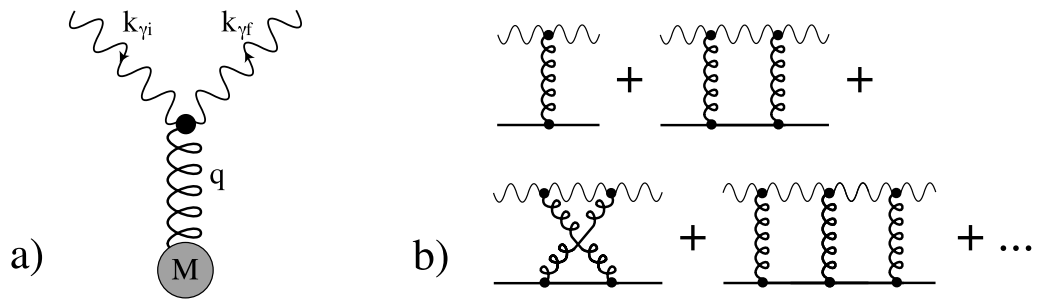

Figure 5.1 a) The Feynman diagram for the gravitational deflection of light. b) The leading ladder and crossed-ladder Feynman diagrams for graviton exchange are shown.

flection of light as an elastic, quantum mechanical scattering process, the photon energy is conserved but its momentum is redirected. A maximum graviton momentum implies a maximum deflection angle, and so $|\vec{k}_{\gamma i} - \vec{k}_{\gamma f}| \approx 2k_\gamma\theta < \mu$, where k_γ is the photon momentum.

We perform a calculation of tree-level photon scattering in linearized quantum gravity. We treat the lens as one massive particle, as many constituent particles, or as the source of an external gravitational field. All approaches yield the same result. The external field offers the clearest view. The cross section is

$$\sigma = (2\pi)^2 \int d^3k_{\gamma f}\delta(k_{\gamma i} - k_{\gamma f})|\langle k_{\gamma f}|\mathcal{M}|k_{\gamma i}\rangle|^2, \tag{5.5}$$

for a given photon polarization. The Maxwell tensor $T^{\mu\nu} = F^{\mu\rho}F^{\nu}_{\ \rho} - \frac{1}{4}\eta^{\mu\nu}F_{\alpha\beta}F^{\alpha\beta}$ is used in (5.2) to determine the scattering vertex, and the matrix element is calculated in the external-field approximation, using $h^{\mu\nu}$ for a weak gravitational field due to a point source of mass M. Following Refs. [371, 372] we obtain

$$\begin{aligned} \langle k_{\gamma f}|\mathcal{M}|k_{\gamma i}\rangle &= \frac{8\pi GM}{2(2\pi)^2}\sqrt{k_{\gamma f}k_{\gamma i}}\frac{\mathrm{e}^{-|\vec{k}_{\gamma f}-\vec{k}_{\gamma i}|/\mu}}{|\vec{k}_{\gamma f}-\vec{k}_{\gamma i}|^2}\,\Pi(e,k) \\ \Pi(e,k) &= \frac{1}{\sqrt{2}}[(\hat{e}_i\cdot\hat{e}_f^*)(3-\hat{k}_{\gamma i}\cdot\hat{k}_{\gamma i}) + (\hat{e}_f^*\cdot\hat{k}_{\gamma i})(\hat{e}_i\cdot\hat{k}_{\gamma f})] \end{aligned} \tag{5.6}$$

where $\hat{e}$ is the photon polarization vector. Averaging over incoming photon polarizations and summing over outgoing polarizations, we obtain the differential cross section in the small angle limit

$$\frac{d\sigma}{d\Omega} = \frac{(4GM)^2}{(c\theta)^4} \times \mathrm{e}^{-2\theta k_\gamma/\mu}\,. \tag{5.7}$$

In the absence of the cutoff, the cross section has the familiar θ^{-4} dependence found in Coulomb scattering. With the cutoff, we interpret the result to indicate that high-energy photons find a weaker gravitational lens, than low-energy photons. This stands in contrast with the achromatic nature of lensing in general relativity.

It is not surprising that gravitational lensing can be described by a tree-level diagram. As with

Coulomb scattering, a tree-level diagram is sufficient to reproduce the classical result. We may also calculate the contribution of higher-order Feynman diagrams in the *eikonal* limit, wherein the total energy of the colliding particles vastly exceeds the momentum transfer. This clearly applies to astrophysical gravitational lensing. In perturbative quantum gravity, graviton loop diagrams are responsible for the nonrenormalizability of the theory and lead to a loss of predictive power at high energies. In the eikonal limit, these diagrams are negligible compared to the series of ladder and crossed-ladder diagrams illustrated in Fig. 5.1. As shown in Refs. [373, 374], the amplitude for gravitational scattering of two massive scalar particles can then be summed to all orders in perturbation theory. In the absence of a cutoff on graviton momenta, this procedure yields the amplitude multiplied by a divergent phase factor. Since the cross section depends on $|\mathcal{M}|^2$, the Born approximation for the cross-section is exact. We generalize this result to the case with the cutoff. We work in the rest frame of the massive scatterer and include an exponential factor for the momentum cutoff on each graviton propagator. The photon is adequately treated as a massless scalar in the limit of small deflections. Then, following Ref. [374], the scattering amplitude due to an infinite sum of ladder graphs in the eikonal limit is

$$i\mathcal{M} = \frac{8\pi M E_\gamma}{q^2}\, \mathrm{e}^{-q/\mu} \int_0^\infty dz\; z\; J_0(z) \left[\left(k_{\mathrm{IR}}/\mu + \sqrt{(k_{\mathrm{IR}}/\mu)^2 + (z k_{\mathrm{IR}}/q)^2} \right)^{4i\eta} - 1 \right].$$

As in QED, the infrared regulator k_{IR} is necessary because the asymptotic states assumed were plane waves, rather than Coulombic wave functions. To proceed, we make a series expansion in small k_{IR}/μ. Then, because $\eta \equiv GME_\gamma \gg 1$, the integral is found to be well-approximated by

$$i\mathcal{M} = i\mathcal{M}_{\mathrm{Born,GR}}\, \mathrm{e}^{-q/\mu} \left(\frac{4k_{\mathrm{IR}}^2}{q^2} \right)^{2i\eta} \frac{\Gamma(1+2i\eta)}{\Gamma(1-2i\eta)} \mathrm{e}^{iq/\mu}, \tag{5.8}$$

where $\mathcal{M}_{\mathrm{Born,GR}} = 32\pi G M^2 E_\gamma^2/q^2$ for the gravitational scattering of these two scalar particles. This nonperturbative result consists of the exponentially suppressed Born amplitude with an additional phase which does not affect the scattering cross-section. Thus our tree-level result is exact in the eikonal limit.

As opposed to multiple graviton exchange in a single scattering interaction, we may also consider multiple encounters along the particle trajectory. For photons impinging on a target with an impact parameter b, the gravitational interaction time is $\sim b/c$. In comparison, the interval during which the photon is in the near, scattering zone of the gravitational lens is $\Delta t \sim b/c$. From the similarity of these time scales, we expect that the photon will experience but a single scattering interaction. For a non-relativistic particle of velocity v, we expect the interval $\Delta t \sim b/v$ will be much greater than b/c. We thus expect the deflection to be determined by many, successive single-graviton exchange interactions with the central mass. Hence, bound systems as well as the scattering of massive objects,

such as satellites or stars, are insensitive to the cutoff since they exchange lower momentum gravitons at each vertex.

We can also consider the photon deflection as arising from multiple scattering events off the constituent particles in the deflector mass. In QED, when an electron scatters off a heavy nucleus, it has a single photon vertex, but each charged nucleon couples coherently to a virtual photon. The total scattering matrix element is the sum of the matrix elements due to the individual scatterers [375]. If $\mathcal{M}_j$ is the matrix element for the jth scatterer, the total amplitude is $|\mathcal{M}_{\rm tot}|^2 = \sum_j |\mathcal{M}_j|^2 + \sum_{j\neq j'} \mathcal{M}_j^* \mathcal{M}_{j'}$. For Z constituent particles there are Z diagonal terms and $Z(Z-1)$ off-diagonal terms. Evaluation of the off-diagonal terms requires the correlations between j, j' pairs of particles. The incoming electron scatters coherently, as is the case for weak deflections in which the internal momenta of the nucleons are negligible, so the j particles all move with the nucleus zero mode, and the correlations are effectively delta functions. Upon integration over the phase space to obtain the differential cross section, the Z^2 diagonal and off-diagonal terms contribute equally, and so the multiple scattering approach yields the same result as scattering off the collective nucleus.

In the case of gravitational deflection, we may consider the deflector mass M as consisting of Z smaller objects of mass M/Z, which includes the gravitational binding energy. For typical gravitational lens systems, the impact parameter is much greater than the deBroglie wavelength corresponding to the total momentum transfer. Thus, we are in the limit of coherent scattering, and as in QED, the same result is obtained whether we employ the point particle or multiple scattering description. Since the scattered particle has only one vertex, the cutoff leads to the same constraint on the change in photon momentum, resulting in Eq. (5.7) for the cross section.

To interpret the cross section in terms of a deflection angle, we consider an incident beam of light at impact parameter b. The beam is deflected into an area $d\sigma = \ b\ db\ d\phi$, which gives us a differential relating θ and b. For small angles, this differential can be integrated to yield $4GM/(bc^2) = \theta/F(2\theta k_\gamma/\mu)$ where $F(x) = \sqrt{(1-x)\mathrm{e}^{-x} - x^2\mathrm{Ei}(-x)}$ and $Ei(x) \equiv -\int_{-x}^{\infty} \mathrm{e}^{-t}dt/t$ is the exponential-integral function. Defining $\theta_{GR} \equiv 4GM/(bc^2)$ for the standard result without the cutoff, then $\theta/\theta_{GR} = F(2\theta k_\gamma/\mu)$. We note that the static, frequency-independent metric potential is insufficient to describe the photon's path past the lensing source when $\theta_{GR} \gtrsim \mu/2k_\gamma$. It would be necessary to introduce an effective force into the geodesic equation, based on the modified graviton propagator. We thus find that the deflection is half the standard prediction when $2\theta k_\gamma/\mu \sim 1$. In the limit $\theta \ll \mu/2k_\gamma$, $F \to 1$, but for $\theta \gtrsim \mu/2k_\gamma$ the deflection angle is suppressed. Hence, *we would expect a dearth of gravitationally lensed images of high-frequency light if there were a cutoff in graviton momentum.*

Numerous gravitational lens systems have been observed from radio to x-ray frequencies. The tightest constraint to μ comes from x-ray observations of the gravitationally lensed system Q0957+561 [376]. For this lens system, image A due to the quasar at $z = 1.4$ appears $5.2''$ away from the pri-

mary lensing galaxy at $z = 0.36$ [377]. Using the angular-diameter distances to the source and from lens to the source, D_S, D_{LS}, to reconstruct the lensing geometry, we estimate a deflection angle of $\theta = 5.2" \times D_S/D_{LS} = 7.8''$. The lens image locations are unchanged for $E_\gamma < 5$ keV [378], which yields the lower bound $\mu > 0.38$ eV/c. This result pushes the threshold for departures from the Newtonian force law down to 0.5 μm.

This lower limit is nearly two orders of magnitude higher than, and therefore rules out, the cutoff inspired by the cosmological constant with $N > 1$. If $N \ll 1$ perhaps due to a cancellation of bosonic and fermionic contributions, then agreement is still possible. We have also tried other forms for the cutoff, including a Gaussian and a sharp power law and find that our results do not change appreciably. This bound may also constrain dark energy models, where such a cutoff prevents the spontaneous decay of the vacuum into phantom or ghost particles [379–382]. We caution the reader that our results only apply to effective theories in which gravity weakens above the cutoff scale in a way described by the implementation of the cutoff function $f(q)$. A tighter constraint may be obtained in the future from hard x-ray or gamma-ray observations of lens images.

It is instructive to compare our graviton momentum cutoff with a similar cutoff in the electron-phonon interaction. In metals, the phonon plays an important role in the dynamics of conduction electrons, conveying an attractive long-range interaction between electrons, which partially cancels the Coulomb interaction. The phonon has an effective width or frequency which characterizes the response time of the ion lattice, above which the phonon interaction is suppressed. The bare pseudo-potential extracted from the electron-phonon matrix element must be dressed by frequency-dependent factors which include the limited phonon-response, in order to produce an accurate picture of the electron dynamics (e.g. Ref. [383]). By analogy with the phonon, we expect the effective width of the graviton to lead to a dramatic change in the behavior of gravitational scattering, shifting the boundary between classical and quantum gravitational interactions. Tree-level amplitudes, which are usually regarded as classical due to the absence of any $\hbar$ factor, are quantum-corrected by the presence of the phenomenological scale μ. We expect that the static gravitational potential will be of limited use, since it may not fully capture the effects of the limited graviton response on kinematics.

We note that a graviton cutoff would lead to a suppression of the spectrum of inflationary gravitational waves. The highest frequency graviton modes allowable by the cutoff enter the horizon when $H \sim c\mu/\hbar$, at which time the cosmic temperature is ~ 2 TeV for a cutoff based on the magnitude of Λ. These waves redshift down to a frequency $\sim 2 \times 10^{-4}$ Hz by the present day. Hence, there would be no inflationary gravitational waves in the frequency range of the proposed Big Bang Observer [384] satellite gravitational wave detector.

We have explored the consequences of a simplistic treatment of the cosmological constant problem. Here, with the introduction of the momentum scale μ, the classical regime is restricted to soft interactions with low momentum transfers; hard scattering must take into account the suppression

factor on the graviton propagator. One may expect a cutoff to play some role in separating the high energy and low energy domains of the underlying, fundamental theory of gravity. At energy scales above the cutoff, gravity may weaken and then lensing imposes an important bound.

Acknowledgments

The author thanks Robert Caldwell for his contributions to the research described in this chapter. The author thanks George Chartas for sharing his Chandra results. The author also thanks the TAPIR group and Mark Wise at Caltech for useful discussions. This research was supported by the National Science Foundation under Contract No. AST-0349213 and Research Corporation RI-0887 at Dartmouth, as well as by the Gordon and Betty Moore Foundation.

Appendix A
King/NFW surface density profiles[1]

The King profile is parameterized by the expression

$$\rho(r) = \frac{9\sigma^2}{4\pi G a} \frac{1}{(1+\frac{r^2}{a^2})^{3/2}}, \tag{A.1}$$

where σ is the cluster velocity dispersion, a is its core radius, and r denotes distance from the cluster center. The surface density for a King profile is derived by integrating by Eq. (A.1) along the line of sight, and is given by

$$\Sigma(R) = \frac{9\sigma^2}{2\pi G a} \frac{1}{1+\frac{R^2}{a^2}}, \tag{A.2}$$

where R is the projected radius [385]. The projected mass density associated with the NFW mass profile,

$$\begin{aligned} \rho(r) &= \frac{\rho_s}{\left(\frac{r}{r_s}\right)\left(1+\frac{r}{r_s}\right)^2}, \\ \rho_s &= \frac{200 c_{\rm NFW}^3 \rho_{\rm crit}}{3\left[\ln(1+c_{\rm NFW}) - \frac{c_{\rm NFW}}{1+c_{\rm NFW}}\right]}, \end{aligned} \tag{A.3}$$

is $\Sigma = r_s \rho_s f(x)$, where

$$f(x) = \begin{cases} \frac{2\left\{1 - \frac{2}{\sqrt{1-x^2}} \operatorname{arctanh}\left[\left(\frac{1-x}{1+x}\right)^{1/2}\right]\right\}}{x^2-1}, & \text{if } x < 1; \\ \frac{2}{3}, & \text{if } x = 1; \\ \frac{2\left\{1 - \frac{2}{\sqrt{x^2-1}} \arctan\left[\left(\frac{x-1}{x+1}\right)^{1/2}\right]\right\}}{x^2-1}, & \text{if } x > 1, \end{cases} \tag{A.4}$$

$c_{\rm NFW}$ is the NFW concentration parameter, and $x = R/r_s$ [386–389].

[1]The material in this chapter was adapted from *Telescope search for decaying relic axions*, Daniel Grin and others; Phys. Rev. D **75**, 105018 (2006). Reproduced here with permission, copyright (2006) by the American Physical Society.

Appendix B
The effect of updated cluster mass-profiles on constraints obtained from A1413, A2256, and A2218[1]

The values of σ and a used in Refs. [10, 11] are shown in Table B-1, along with the relevant redshift values and spectral slit locations. In Refs. [10, 11], the sky background was removed by subtracting 'off' cluster spectra from 'on' cluster spectra. In general, the expected signal due to axion decay, in the observer's frame, is

$$I_{\lambda_0} = \frac{\Sigma_{\rm a}(R)c^3}{4\pi\sqrt{2\pi}\sigma\lambda_{\rm a}\tau_{\rm a}(1+z_{\rm cl})^4} e^{-\frac{(\lambda_0/(1+z_{\rm cl})-\lambda_{\rm a})^2}{\lambda_{\rm a}^2}\frac{c^2}{2\sigma^2}}. \tag{B.1}$$

This can be shown by the same arguments used to derive Eq. (2.29). Using this ratio, we can figure out the ratio in expected signals. Since $I_{\lambda_0} \propto \xi^2$, we can obtain an estimate of the upper limit implied by the results of Refs. [10, 11], given current measurements of the cluster mass-profile and cosmological parameters.

For A1413, we took best-fit values from the XMM-Newton x-ray profiles of Ref. [390], where it was found that A1413 is fit much better by an NFW profile than by a King profile. The best-fit NFW parameters are $c_{\rm NFW} = 5.82$ and $r_{200} = r_s c_{\rm NFW} = 1707$ kpc. We use $\Omega_{\rm m,new}h^2_{\rm new} = 0.15$, while $\Omega_{\rm m,old}h^2_{\rm old} = 0.25$ is the value used in Refs. [10, 11]. The projected mass density in axions is $\Sigma_{\rm a} = \left[\Omega_{\rm a}h^2/(\Omega_{\rm m}h^2)\right]\Sigma$. We define an on-off density-contrast $\tilde{\Sigma}^{\rm new}_{\rm a} \equiv \Sigma^{\rm new}_{\rm a}(R_{\rm on}) - \Sigma^{\rm new}_{\rm a}(R_{\rm off})$ using the best-fit values today. We define another, $\tilde{\Sigma}^{\rm old}_{\rm a} \equiv \Sigma^{\rm old}_{\rm a}(R_{\rm on}) - \Sigma^{\rm old}_{\rm a}(R_{\rm off})$, using the best-fit values assumed in Refs. [10, 11]. When calculating $\Sigma_{\rm new}$ at the slit locations of Refs. [10, 11], we took the slit locations in angular units and obtained physical distances using the angular-diameter distance for a ΛCDM cosmology. Applying Eq. (A.4), we obtained $\tilde{\Sigma}^{\rm new,1}_{\rm a}/\tilde{\Sigma}^{\rm old,1}_{\rm a} = 0.9853$ and $\tilde{\Sigma}^{\rm new,2}_{\rm a}/\tilde{\Sigma}^{\rm old,2}_{\rm a} = 1.449$. Using Eq. (B.1), it can be seen that this implies $\xi_{\rm new,1} = 1.104\xi_{\rm old,1}$ and $\xi_{\rm new,2} = 0.831\xi_{\rm old,2}$ for A1413.

The optical depth to lensing by A2256 is very low, because of the low redshift of the cluster. As a result, lensing derived mass models of this cluster do not exist. We took best-fit values from the

[1]The material in this chapter was adapted from *Telescope search for decaying relic axions*, Daniel Grin and others; Phys. Rev. D **75**, 105018 (2006). Reproduced here with permission, copyright (2006) by the American Physical Society.

Table B-1 Summary of observations and properties of clusters used in Refs. [10, 11]. Table entries taken from Ref. [11].

Cluster	σ (km s^{-1})	a [kpc(arcmin)]	Inner/Outer aperture (R/a)	z
A1413	1230	$400h_{50}^{-1}(2.03)$	1.11/4.64 0.65/2.94	0.143
A2218	1300	$200h_{50}^{-1}(0.88)$	0.94/5.33	0.171
A2256	1300	$473h_{50}^{-1}(5.0)$	0.484/2.96	0.0601

BeppoSAX x-ray profiles of Ref. [391], in which King profiles are parameterized via[2]

$$\Sigma^{\rm new}(R) = \frac{r_c \rho_s}{1+\frac{R^2}{r_c^2}}. \tag{B.2}$$

We then used Eqs. (B.2) and (A.2) to obtain the ratio of the best-fit on-off density contrast determined using current data to that used in Refs. [10, 11]:

$$\frac{\tilde{\Sigma}_{\rm a}^{\rm new}}{\tilde{\Sigma}_{\rm a}^{\rm old}} = \frac{50 a r_c c_{\rm NFW}^3 H^2}{9\sigma^2\left[\ln(1+c_{\rm NFW}) - \frac{c_{\rm NFW}}{1+c_{\rm NFW}}\right]} \left(\frac{\Omega_{\rm m,old}h_{\rm old}^2}{\Omega_{\rm m,new}h_{\rm new}^2}\right) \frac{\left[\frac{1}{1+\left(\frac{a}{r_c}\right)^2\left(\frac{R_{\rm on}}{a}\right)^2} - \frac{1}{1+\left(\frac{a}{r_c}\right)^2\left(\frac{R_{\rm off}}{a}\right)^2}\right]}{\left[\frac{1}{1+\left(\frac{R_{\rm on}}{a}\right)^2} - \frac{1}{1+\left(\frac{R_{\rm off}}{a}\right)^2}\right]}. \tag{B.3}$$

Here, H is the value of the Hubble constant preferred today. Using BeppoSax data, best-fit values of $c_{\rm NFW} = 4.57$ and $r_c = 570$ kpc were derived in Ref. [391], using a redshift of $z = 0.0581$, and assuming a sCDM cosmology. Rescaling this core radius for a ΛCDM universe, we obtain $r_c = 414$ kpc. Inserting these values into Eq. (B.3), we obtain $\tilde{\Sigma}_{\rm a}^{\rm new}/\tilde{\Sigma}_{\rm a}^{\rm old} = 0.5982$. For A2256, this yields $\xi_{\rm new} = 1.29\xi_{\rm old}$. If true, recent claims that A2256 is undergoing merging activity impugn the assumption that A2256 is relaxed [392, 393]. In that case, the assumption of a King profile for A2256 is invalid, and upper limits to ξ obtained from A2256 have to be revised.

The strong-lensing analyses of A2218 in Refs. [394, 395] indicate the presence of several mass clumps in the cluster, four of which have total masses comparable to the total cluster mass, and one, centered on the brightest cluster galaxy (BCG), which has a total mass comparable to a typical galaxy mass. The observed lensing configuration is well fit by the set of parameters listed in Table

[2]The factor ρ_s usually appears in NFW profiles, and its use in a King profile is unusual, but correct.

Table B-2 Best-fit parameters for the mass model of A2218, determined from a strong-lensing analysis. The table was taken from Refs. [394, 395]. Square brackets indicate a value that was not fit for, but set by hand. The quantity θ is the orientation of the ellipse's major axis relative to some horizontal in the image plane.

ΔR.A.(")	ΔDec.(")	a/b	θ(deg)	$r_{\rm core}$(kpc)	$r_{\rm cut}$(kpc)	σ_0
$+0.2$	$+0.5$	1.2	32	83	[1000]	1070
[+47.0]	[-49.4]	1.4	53	57	[500]	580
[+16.1]	[-10.4]	[1.1]	[70]	< 2	65	195
[4.8]	[-20.9]	[1.4]	[-23]	< 2	77	145
$+0.3$	$+0.1$	1.8	53	< 3	136	270

B-2. The parameters refer to a PIEMD [138], whose surface mass density is given by

$$\Sigma(x,y) = \frac{\sigma_0^2}{2G}\frac{r_{\rm cut}}{r_{\rm cut}-r_{\rm core}}\left[\frac{1}{(r_{\rm core}^2+s^2)^{1/2}}\right].$$
$$s^2 = \left[\frac{x-x_c}{1+\epsilon}\right]^2 + \left[\frac{y-y_c}{1-\epsilon}\right]^2,$$
$$\epsilon = \frac{a/b-1}{a/b+1}, \tag{B.4}$$

where a and b are the semi-major and semi-minor axes of the best-fitting ellipse, x_c and y_c are the best-fitting mass centers given in Table B-2, translated into physical units using the ΛCDM angular-diameter distance, and σ_0 is the velocity dispersion of the cluster. Although these lensing data were analyzed using a sCDM cosmology, the authors report that the best-fit parameters are insensitive at the 10% level to reasonable variations in cosmological parameters. The on-off radii are provided without orientation information in Refs. [10, 11], and so we allow the slit orientation angle ϕ to vary over the full possible range, and repeat the preceding analysis to obtain a range $0.57\xi_{\rm old} \leq \xi_{\rm new} \leq 0.71\xi_{\rm old}$. Parameters whose values are bounded from above are set to zero for our analysis. Depending on the mass bin, the upper limits of Refs. [10, 11] come from A2256 or A2218. The updated upper limits of Refs. [10, 11] must thus fall in the bracket $0.57\xi_{\rm old} \leq \xi_{\rm new} \leq 1.29\xi_{\rm old}$. This range is plotted in Fig. 2.13, and it is clear that our upper limits to ξ improve considerably on those reported in Refs. [10, 11], even when past work is reinterpreted optimistically.

Appendix C
WKB approximation for radial dipole integrals[1]

The development of laser spectroscopy of high-n states in hydrogen and other atoms, along with the study of nonlinear and multiphoton ionization, required the computation of dipole radial matrix elements for high and even fractional quantum numbers in a Coulomb or perturbed Coulomb potential [396]. Until adequate algorithms for these computations were ultimately developed, the Wentzel, Kramers, Brillouin, and Jeffreys (WKBJ) semiclassical approximation (quite accurate for $n \gg 1$) [286, 397] proved a useful tool for estimating ${}^{(n)}X^{l',l}_{n',n}$. At high n, radial wave functions in the Coulomb potential have a large number of nodes and thus a short wavelength λ. For the WKB approximation to be valid, it is necessary that $|d\lambda/dx| \ll 2\pi$. Because of the large number of nodes in the Coulomb wave functions at high n, the WKB approximation is ideally suited to estimating matrix elements for transitions between high n.

In the classically allowed region, the nonrelativistic WKB radial wave function for a hydrogen atom is

$$xR_{nl}(x) = \left(\frac{2}{\pi n^3 k(x)}\right)^{1/2} \cos\left[\int_{x_1}^{x} k_{nl}(x)dx - \frac{\pi}{4}\right] \tag{C.1}$$

with

$$k_{nl}(x) = \left[\frac{1}{n^2} + \frac{2}{x} - \frac{l\,(l+1)}{x^2}\right]^{1/2}, \tag{C.2}$$

where the inner classical turning point x_1 is a solution of the equation $k_{nl}(x) = 0$. Substituting Eq. (C.2) into Eq. (4.43) for the dipole matrix element, and making several additional approximations, the following expression is obtained if $|n' - n| \ll n, n'$ and $n, n' \gg l$ [397]:

$${}^{(1)}X^{l',l}_{n',n} = \frac{n_c^2}{2s}\left[\left(1 + \Delta l\frac{l_c}{n_c}\right) J_{s+1}(\epsilon s)\left(1 - \Delta l\frac{l_c}{n_c}\right) J_{s-1}(\epsilon s)\right]. \tag{C.3}$$

with $s = n - n'$, $\Delta l = l' - l$, $l_c = (l + l' + 1)/2$, $n_c = 2nn'/(n + n')$, and $\epsilon^2 = 1 - \left(l_c^2/n_c^2\right)$. Here ϵ is the eccentricity of a Keplerian orbit with the quantum numbers n_c and l_c, and $J_s(x)$ is a Bessel function of the first kind. These estimates agree with matrix elements computed using Eq. (4.44)

[1]The material in this chapter was adapted from *Cosmological hydrogen recombination: The effect of extremely high-n states*, Daniel Grin and Christopher M. Hirata; Phys. Rev. D **81**, 083005 (2010). Reproduced here with permission, copyright (2010) by the American Physical Society.

to a precision of 5%–50%; the agreement worsens as $|n' - n| \to n, n'$.

If $l \ll n', n$ and $s \sim n, n'$, then [398]

$$ {}^{(1)}X^{l\pm1,l}_{n',n} = 2\frac{l^2}{\pi\sqrt{3}}\left(nn'\right)^{-3/2} y^{-1}\left\{K_{2/3}\left(\frac{l^3 y}{6}\right) \mp K_{1/3}\left(\frac{l^3 y}{6}\right)\right\}, \tag{C.4} $$

with $y = \left|n^{-2} - n'^2\right|$. Here $K_s(x)$ is a modified Bessel function of the second kind. These estimates agree with matrix elements computed using Eq. (4.44) to a precision of 1%–20%; the agreement worsens as s shrinks, at which point Eq. (C.3) becomes more accurate.

A WKB estimate of bound-free matrix elements is obtained by making the substitution $n' \to i/\kappa$ in Eq. (C.4) [398]. The resulting estimate is reasonable if $l \ll n, \kappa^{-1}$ and agrees with matrix elements computed using Eq. (4.50) to a precision of 50%. This analysis confirms that the high n and l values under consideration do not afflict our evaluation of Eqs. (4.44) or (4.50) with any instability that would throw computed rates off by orders of magnitude.

Appendix D
Radial bound-bound quadrupole integrals[1]

Schrödinger, Infeld, and Hull developed a factorization of the Schrödinger equation which revealed an underlying operator algebra [399, 400]. This algebra has now been used to derive many recurrence relations for matrix elements of radial electric multipole operators. For our quadrupole matrix elements, we follow Ref. [326]. We begin by reviewing these results and follow with a discussion of the WKB estimates of these rates used to check the stability of our quadrupole rate computations.

We continue to work in units where the radial coordinate and wave function are dimensionless. The radial Schrödinger equation may then be factored to yield [326]

$$ {}^{+}\Omega_{nl}\,{}^{-}\Omega_{nl} R_{nl}(x) = R_{nl}(x), \tag{D.1} $$

with

$$ {}^{\mp}\Omega_{nl} = \frac{1}{l q_{n,l}} \left[1 \mp l \left(\frac{d}{dx} \pm \frac{l \pm 1}{x} \right) \right]. \tag{D.2} $$

The operators ${}^{-}\Omega_{nl}$ and ${}^{+}\Omega_{nl}$ satisfy the algebra

$$ \begin{aligned} {}^{-}\Omega_{nl} R_{nl}(x) &= R_{nl-1}(x) \\ {}^{+}\Omega_{nl} R_{nl-1}(x) &= R_{nl}(x) \end{aligned} \tag{D.3} $$

and the normalization constant $q_{n,l}$ is given by

$$ q_{n,l} = \frac{\sqrt{(n-l)\,(n+l)}}{nl}. \tag{D.4} $$

The diagonal matrix elements are obtained by taking appropriate expectation values and applying Eq. (D.3) repeatedly, yielding [326]:

$$ {}^{(2)}X^{l-1,l-1}_{n',n} = \frac{\left(q_{n',l}\,{}^{(2)}X^{l,l}_{n',n} + 2\,{}^{(1)}X^{l,l-1}_{n',n} \right)}{q_{n,l}}, \tag{D.5} $$

[1] The material in this chapter was adapted from *Cosmological hydrogen recombination: The effect of extremely high-n states*, Daniel Grin and Christopher M. Hirata; Phys. Rev. D **81**, 083005 (2010). Reproduced here with permission, copyright (2010) by the American Physical Society.

with the initial condition of the recursion occurring at $l = n'$ with value

$$ {}^{(2)}X^{n'-1,n'-1}_{n',n} = 2\frac{nn'}{\sqrt{n^2-n'^2}}\,{}^{(1)}X^{n'-1,n'}_{n',n}, \tag{D.6}$$

assuming $n' < n$; otherwise the arguments should be reversed to obtain correct expressions. As can be seen the recursion for diagonal quadrupole matrix elements requires the evaluation of dipole matrix elements. We calculate these using the methods of Sec. 4.3.3.1. There are also recursion relationships for *dipole* matrix elements derived using these operator algebras, and they are known to agree with the results of Ref. [311] (derived from the more familiar Gordon formula [313]) to 8 significant figures.

The off-diagonal matrix elements are derived using a similar method (where $1 \leq l \leq n'-1$) [326]:

$$\begin{aligned} l\,(2l+3)\,q_{n',l}\,{}^{(2)}X^{l-1,l+1}_{n',n} &= (2l+1)(l+2)q_{n,l+2}\,{}^{(2)}X^{l,l+2}_{n',n} + 2(l+1)q_{n',l+1}\,{}^{(2)}X^{l+1,l+1}_{n',n} \\ &+ 2(2l+1)(3l+5)\,{}^{(1)}X^{l,l+1}_{n',n}. \end{aligned} \tag{D.7}$$

$$\begin{aligned} l\,(2l+3)\,q_{n,l}\,{}^{(2)}X^{l+1,l-1}_{n',n} &= (2l+1)(l+2)q_{n',l+2}\,{}^{(2)}X^{l+2,l}_{n',n} + 2(l+1)q_{n,l+1}\,{}^{(2)}X^{l+1,l+1}_{n',n} \\ &+ 2(2l+1)(3l+5)\,{}^{(1)}X^{l+1\ l}_{n',n}. \end{aligned} \tag{D.8}$$

For Eq. (D.7), the initial condition of the recursion occurs for $l = n'$ with value [326]

$$ {}^{(2)}X^{n'-1,n'+1}_{n',n} = (-1)^{n-n'}2^{2n'+4}\,(nn')^{n'+3}\left[\frac{n'^2\,(n+n'+1)!}{(n-n'-2)!\,(2n'-1)!}\right]^{1/2}\frac{(n-n')^{n-n'-3}}{(n+n')^{n+n'+3}}. \tag{D.9}$$

For Eq. (D.8) the initial condition of the recursion occurs for $l = n'$ with value ${}^{(2)}X^{n'+1,n'-1}_{n_{\prime},n} = 0$. In deriving the complete set of quadrupole coefficients it is useful to note that [326]

$$ {}^{(2)}X^{n'-1,n'-1}_{n',n} = (-1)^{n-n'-1}2^{2n'+3}\,(nn')^{n'+3}\left[\frac{(n+n'-1)!}{(n-n')!\,(2n'-1)!}\right]^{1/2}\frac{(n-n')^{n-n'-2}}{(n+n')^{n+n'+2}}. \tag{D.10}$$

The same method described in Appendix C can be used to derive expressions for the radial quadrupole matrix element valid in the WKB approximation [397]:

$$ {}^{(2)}X^{l\pm2,l}_{n,n'} = -\frac{2n_c^4}{s^2}J_s\,(s\epsilon) + \frac{4n_c^4}{s\epsilon}\left[1-\epsilon^2 \mp \frac{\left(1-\epsilon^2\right)^{1/2}}{s}\right]\left[J_{s-1}\,(s\epsilon) - \frac{1\mp\left(1-\epsilon^2\right)^{1/2}}{\epsilon}J_s\,(s\epsilon)\right]. \tag{D.11}$$

Here ϵ, s, and n_c are defined as in Appendix C. These estimates agree with matrix elements computed using Eq. (4.71) to a precision of 5%–50%; the agreement worsens as $|n'-n|, l \to n, n'$. For $l, |n'-n| < n/10$, WKB estimates agree with Eq. (4.71) to $\sim 5\%$.

Bibliography

[1] S. Weinberg, *The First Three Minutes: A Modern View of the Origin of the Universe* (BasicBooks, 1977).

[2] K. R. Popper, *Conjectures and Refutations: The Growth of Scientific Knowledge* (Routledge and Kegan Paul, 1963).

[3] K. S. Thorne, *Black holes and time warps: Einstein's outrageous legacy* (Commonwealth Fund Book Program, New York, NY: W.W. Norton and London: Picador, 1994).

[4] G. G. Raffelt, *Stars as Laboratories for Fundamental Physics* (The University of Chicago Press, Chicago, 1996).

[5] G. G. Raffelt, in *Beyond the Desert 1997: Accelerator and Non-Accelerator Approaches*, edited by H. V. Llapdor-Kleingrothaus and H. Päs (1998), pp. 808–+.

[6] S. Hannestad, A. Mirizzi, and G. Raffelt, JCAP **0507**, 002 (2005), `arXiv:hep-ph/0504059`.

[7] J. A. Rubiño-Martín, J. Chluba, and R. A. Sunyaev, Mon. Not. R. Astron. Soc. **371**, 1939 (2006), `arXiv:astro-ph/0607373`.

[8] J. Chluba, J. A. Rubiño-Martín, and R. A. Sunyaev, Mon. Not. R. Astron. Soc. **374**, 1310 (2007), `arXiv:astro-ph/0608242`.

[9] J. Chluba, G. M. Vasil, and L. J. Dursi, ArXiv e-prints (2010), `arXiv:1003.4928`.

[10] M. T. Ressell, Phys. Rev. D **44**, 3001 (1991).

[11] M. A. Bershady, M. T. Ressell, and M. S. Turner, Phys. Rev. Lett. **66**, 1398 (1991).

[12] A. E. Lange et al. (Boomerang), Phys. Rev. D **63**, 042001 (2001), `astro-ph/0005004`.

[13] E. L. Wright et al., Astrophys. J. Lett. **396**, L13 (1992).

[14] D. N. Spergel et al. (2006), `astro-ph/0603449`.

[15] D. N. Spergel et al. (WMAP), Astrophys. J. Suppl. **148**, 175 (2003), `astro-ph/0302209`.

[16] D. N. Spergel et al. (WMAP), Astrophys. J. Suppl. Ser. **170**, 377 (2007), `astro-ph/0603449`.

[17] G. Hinshaw et al., Astrophys. J. Suppl. Ser. **180**, 225 (2009), `arXiv:0803.0732`.

[18] M. Tegmark et al. (SDSS), Phys. Rev. D **69**, 103501 (2004), `astro-ph/0310723`.

[19] M. Tegmark et al., Phys. Rev. D **69**, 103501 (2004).

[20] M. Tegmark et al., Astrophys. J. **606**, 702 (2004), arXiv:astro-ph/0310725.

[21] M. Colless et al. (2003), arXiv:astro-ph/0306581.

[22] A. G. Riess et al., Astron. J. **116**, 1009 (1998), arXiv:astro-ph/9805201.

[23] B. P. Schmidt et al., Astrophys. J. **507**, 46 (1998), arXiv:astro-ph/9805200.

[24] P. M. Garnavich et al., Astrophys. J. **509**, 74 (1998), arXiv:astro-ph/9806396.

[25] S. Perlmutter et al., Astrophys. J. **517**, 565 (1999), arXiv:astro-ph/9812133.

[26] S. Hannestad, Phys. Rev. D **D70**, 043506 (2004), astro-ph/0403291.

[27] L. J. Rosenberg, AIP Conf. Proc. **698**, 332 (2004).

[28] S. Andriamonje et al. (CAST), JCAP **0704**, 010 (2007), hep-ex/0702006.

[29] D. J. H. Chung et al., JHEP **10**, 16 (2007), arXiv:0706.2375.

[30] D. Denegri and Cms Collaboration, in *The Dark Side of the Universe; Experimental Efforts and Theoretical Framework*, edited by R. Bernabei & A. Incicchitti (1996), pp. 107–+.

[31] A. Moiseev, in *International Cosmic Ray Conference* (1999), vol. 2 of *International Cosmic Ray Conference*, pp. 273–+.

[32] P. L. Brink et al., in *Proceedings of the 22nd Texas Symposium on Relativistic Astrophysics at Stanford, Stanford California, December 13-17, 2004. Edited by Pisin Chen, Elliott Bloom, Greg Madejski (SLAC), and Vahe Patrosian (Stanford University), p.801-806*, edited by P. Chen, E. Bloom, G. Madejski, & V. Patrosian (2005), pp. 801–806.

[33] E. Aprile et al., New Astronomy Review **49**, 289 (2005), arXiv:astro-ph/0407575.

[34] V. N. Lebedenko et al., Phys. Rev. D **80**, 052010 (2009), 0812.1150.

[35] The Planck Collaboration (2006), arXiv:astro-ph/0604069.

[36] R. D. Peccei and H. R. Quinn, Phys. Rev. Lett. **38**, 1440 (1977).

[37] D. Baumann et al. (CMBPol Study Team) (2008), arXiv:0811.3911.

[38] D. Scott, in *Evolution of Large Scale Structure : From Recombination to Garching*, edited by A. J. Banday, R. K. Sheth, and L. N. da Costa (1999), pp. 30–+.

[39] J. Chluba and R. A. Sunyaev, Astron. Astrophys. **496**, 619 (2009), arXiv:0810.1045.

[40] W. A. Fendt, J. Chluba, J. A. Rubiño-Martín, and B. D. Wandelt, Astrophys. J. Suppl. Ser. **181**, 627 (2009), arXiv:0807.2577.

[41] W. Y. Wong, A. Moss, and D. Scott, Mon. Not. R. Astron. Soc. **386**, 1023 (2008), arXiv:0711.1357.

[42] D. Grin et al., Phys. Rev. D **75**, 105018 (2007), arXiv:astro-ph/0611502.

[43] D. Grin, T. L. Smith, and M. Kamionkowski, Phys. Rev. D **77**, 085020 (2008), arXiv:0711.1352.

[44] D. Grin and C. Hirata, Phys. Rev. D **81**, 083005 (2010), arXiv:0911.1359.

[45] R. R. Caldwell and D. Grin, Phys. Rev. Lett. **100**, 031301 (2008), arXiv:astro-ph/0606133.

[46] E. Leader and E. Predazzi, *An Introduction to Gauge Theories and Modern Particle Physics* (Cambridge University Press, Cambridge, 1996).

[47] V. Baluni, Phys. Rev. D **19**, 2227 (1979).

[48] R. J. Crewther, P. Di Vecchia, G. Veneziano, and E. Witten, Phys. Lett. **B88**, 123 (1979).

[49] P. G. Harris et al., Phys. Rev. Lett. **82**, 904 (1999).

[50] E. W. Kolb and M. S. Turner, *The Early Universe* (Addison-Wesley Publishing Company, Redwood City, 1990).

[51] M. S. Turner, Phys. Rev. Lett. **59**, 2489 (1987).

[52] M. S. Turner, Phys. Rev. D **33**, 889 (1986).

[53] D. B. Kaplan, Nucl. Phys. **B260**, 215 (1985).

[54] M. Dine, W. Fischler, and M. Srednicki, Phys. Lett. **B104**, 199 (1981).

[55] A. R. Zhitnitsky, Sov. J. Nucl. Phys. **31**, 260 (1980).

[56] J. E. Kim, Phys. Rev. Lett. **43**, 103 (1979).

[57] A. I. Vainshtein, V. I. Zakharov, and M. A. Shifman, Sov. Phys. Usp. **23**, 429 (1980).

[58] D. A. Dicus, E. W. Kolb, V. L. Teplitz, and R. V. Wagoner, Phys. Rev. D **22**, 839 (1980).

[59] G. Raffelt and A. Weiss, Phys. Rev. D **51**, 1495 (1995), arXIv:hep-ph/9410205.

[60] G. G. Raffelt, Phys. Rev. D **41**, 1324 (1990).

[61] G. G. Raffelt, Phys. Rept. **198**, 1 (1990).

[62] G. G. Raffelt and D. S. P. Dearborn, Phys. Rev. D **36**, 2211 (1987).

[63] K. Zioutas et al., Phys. Rev. Lett. **94**, 121301 (2005).

[64] J. M. Overduin and P. S. Wesson, Astrophys. J. **414**, 449 (1993).

[65] E. Zavattini et al. (PVLAS), Phys. Rev. Lett. **96**, 110406 (2006), arXiv:hep-ex/0507107.

[66] E. Iacopini and E. Zavattini, Phys. Lett. **B85**, 151 (1979).

[67] L. Maiani, R. Petronzio, and E. Zavattini, Phys. Lett. **B175**, 359 (1986).

[68] A. A. Anselm, Phys. Rev. D **37**, 2001 (1988).

[69] M. Gasperini, Phys. Rev. Lett. **59**, 396 (1987).

[70] G. Raffelt and L. Stodolsky, Phys. Rev. D **37**, 1237 (1988).

[71] R. Rabadan, A. Ringwald, and K. Sigurdson, Phys. Rev. Lett. **96**, 110407 (2006), arXiv:hep-ph/0511103.

[72] E. Masso and J. Redondo, J. Cosmol. Astropart. Phys. **0509**, 015 (2005), arXiv:hep-ph/0504202.

[73] P. Jain and S. Mandal (2005), arXiv:astro-ph/0512155.

[74] T. W. Kephart and T. J. Weiler, Phys. Rev. Lett. **58**, 171 (1987).

[75] Y. N. Gnedin, S. N. Dodonov, V. V. Vlasyuk, O. I. Spiridonova, and A. V. Shakhverdov, Mon. Not. R. Astron. Soc. **306**, 117 (1999).

[76] G. F. Giudice, E. W. Kolb, and A. Riotto, Phys. Rev. D **64**, 023508 (2001), arXiv:hep-ph/0005123.

[77] G. F. Giudice, E. W. Kolb, A. Riotto, D. V. Semikoz, and I. I. Tkachev, Phys. Rev. D **64**, 043512 (2001), arXiv:hep-ph/0012317.

[78] M. Kawasaki, K. Kohri, and N. Sugiyama, Phys. Rev. Lett. **82**, 4168 (1999), astro-ph/9811437.

[79] S. Dodelson and L. M. Widrow, Phys. Rev. Lett. **72**, 17 (1994), arXiv:hep-ph/9303287.

[80] A. D. Dolgov and S. H. Hansen, Astropart. Phys. **16**, 339 (2002), arXiv:hep-ph/0009083.

[81] X.-D. Shi and G. M. Fuller, Phys. Rev. Lett. **82**, 2832 (1999), astro-ph/9810076.

[82] T. Asaka, M. Shaposhnikov, and A. Kusenko, Phys. Lett. **B638**, 401 (2006), arXiv:hep-ph/0602150.

[83] J.-P. Kneib, R. S. Ellis, I. Smail, W. J. Couch, and R. M. Sharples, Astrophys. J. **471**, 643 (1996), arXiv:astro-ph/9511015.

[84] O. Le Fèvre et al., The Messenger **111**, 18 (2003).

[85] A. Zanichelli et al., Publ. Astron. Soc. Pac. **117**, 1271 (2005), arXiv:astro-ph/0509454.

[86] T. Moroi and H. Murayama, Phys. Lett. **B440**, 69 (1998), arXiv:hep-ph/9804291.

[87] S. Weinberg, Phys. Rev. Lett. **40**, 223 (1978).

[88] F. Wilczek, Phys. Rev. Lett. **40**, 279 (1978).

[89] M. R. Buckley and H. Murayama, J. Cosmol. Astropart. Phys. **7**, 12 (2007), arXiv:0705.0542.

[90] M. E. Peskin and D. V. Schroeder, *An Introduction to Quantum Field Theory* (Westview Press, 1995).

[91] W. M. Yao et al. (Particle Data Group), J. Phys. **G33**, 1 (2006).

[92] D. J. Gross, R. D. Pisarski, and L. G. Yaffe, Rev. Mod. Phys. **53**, 43 (1981).

[93] S. Chang and K. Choi, Phys. Lett. **B316**, 51 (1993), arXiv:hep-ph/9306216.

[94] P. Sikivie, ArXiv Astrophysics e-prints (2006), arXiv:astro-ph/0610440.

[95] M. S. Turner, Phys. Rev. D **33**, 889 (1986).

[96] R. L. Davis, Phys. Lett. B **180**, 225 (1986).

[97] D. Harari and P. Sikivie, Phys. Lett. B **195**, 361 (1987).

[98] R. L. Davis and E. P. S. Shellard, Nucl. Phys. **B324**, 167 (1989).

[99] R. A. Battye and E. P. S. Shellard, ArXiv Astrophysics e-prints (1999), arXiv:astro-ph/9909231.

[100] O. Wantz and E. P. S. Shellard, ArXiv e-prints (2009), arXiv:0910.1066.

[101] P. Sikivie, Phys. Rev. Lett. **48**, 1156 (1982).

[102] D. Seckel and M. S. Turner, Phys. Rev. D **32**, 3178 (1985).

[103] E. Komatsu et al., ArXiv e-prints (2010), arXiv:1001.4538.

[104] E. Komatsu et al., Astrophys. J. Suppl. Ser. **180**, 330 (2009), arXiv:0803.0547.

[105] S. Tremaine and J. E. Gunn, Phys. Rev. Lett. **42**, 407 (1979).

[106] J. Madsen, Phys. Rev. D **44**, 999 (1991).

[107] J. Madsen, Phys. Rev. D **64**, 027301 (2001).

[108] J. Isern et al., Astrophys. J. Lett. **682**, L109 (2008), 0806.2807.

[109] A. Bischoff-Kim, M. H. Montgomery, and D. E. Winget, Astrophys. J. **675**, 1512 (2008), 0711.2041.

[110] M. Kachelriess, C. Wilke, and G. Wunner, Phys. Rev. D **56**, 1313 (1997), arXiv:astro-ph/9701056.

[111] P. Sikivie, Phys. Rev. Lett. **51**, 1415 (1983).

[112] S. J. Asztalos et al., Phys. Rev. Lett. **104**, 041301 (2010), arXiv:0910.5914.

[113] S. L. Adler, Ann. Phys. **67**, 599 (1971).

[114] G. Ruoso et al., Z. Phys. **C56**, 505 (1992).

[115] A. S. Chou et al., Phys. Rev. Lett. **100**, 080402 (2008), arXiv:0710.3783.

[116] C. Robilliard et al., Physical Review Letters **99**, 190403 (2007), 0707.1296.

[117] T. Bruch and Cdms Collaboration, in *Identification of Dark Matter 2008* (2008), pp. 104–+.

[118] Y. Inoue et al., ArXiv e-prints (2010), arXIv:1002.0468.

[119] J. Carson, Journal of Physics Conference Series **60**, 115 (2007), arXiv:astro-ph/0610960.

[120] D. Hooper and P. D. Serpico, Phys. Rev. Lett. **99**, 231102 (2007), arXiv:0706.3203.

[121] A. Payez, J. R. Cudell, and D. Hutsemékers, in *American Institute of Physics Conference Series*, edited by J. Cugon, J.-P. Lansberg, & N. Matagne (2008), vol. 1038 of *American Institute of Physics Conference Series*, pp. 211–219.

[122] A. Avgoustidis et al., ArXiv e-prints (2010), arXiv:1004.2053.

[123] F. Wilczek, Proc. Nat. Acad. Sci. **102**, 8403 (2005), arXiv:hep-ph/0502113.

[124] A. Ljubicic, D. Kekez, Z. Krecak, and T. Ljubicic, Phys. Lett. **B599**, 143 (2004), arxiV:hep-ex/0403045.

[125] M. Krcmar, Z. Krecak, M. Stipcevic, A. Ljubicic, and D. A. Bradley, Phys. Lett. **B442**, 38 (1998), arXiv:nucl-ex/9801005.

[126] M. Krcmar, Z. Krecak, A. Ljubicic, M. Stipcevic, and D. A. Bradley, Phys. Rev. D **64**, 115016 (2001), hep-ex/0104035.

[127] A. V. Derbin et al., European Physical Journal C **62**, 755 (2009), arXIv:0906.0256.

[128] S. Hannestad et al., JCAP **4**, 19 (2008), arXiv:0803.1585.

[129] A. Melchiorri, O. Mena, and A. Slosar, Phys. Rev. D **76**, 041303 (2007), arXiv:0705.2695.

[130] S. Hannestad et al., ArXiv e-prints (2010), arXiv:1004.0695.

[131] G. Covone, J.-P. Kneib, G. Soucail, J. Richard, E. Jullo, and H. Ebeling, Astron. Astrophys. **456**, 409 (2006), arXiv:astro-ph/0511332.

[132] E. Jullo et al., in preparation (2007).

[133] M. Scodeggio et al., Publ. Astron. Soc. Pac. **117**, 1284 (2005), arXiv:astro-ph/0409248.

[134] S. D'Odorico et al., The Messenger **113**, 26 (2003).

[135] K. Horne, Publ. Astron. Soc. Pac. **98**, 609 (1986).

[136] M. Bershady, private correspondence (2005).

[137] G. P. Smith et al., Mon. Not. R. Astron. Soc. **359**, 417 (2005), astro-ph/0403588.

[138] A. Kassiola and I. Kovner, Astrophys. J. **417**, 450 (1993).

[139] S. M. Faber and R. E. Jackson, Astrophys. J. **204**, 668 (1976).

[140] J.-P. Kneib, Ph.D. Thesis (1993).

[141] P. Natarajan and J.-P. Kneib, Mon. Not. R. Astron. Soc. **287**, 833 (1997), arXiv:astro-ph/9609008.

[142] J. Tonry and M. Davis, Astron. J. **84**, 1511 (1979).

[143] A. de Gouvea, Phys. Rev. D **72**, 033005 (2005), arXiv:hep-ph/0501039.

[144] A. de Gouvea and C. Pena-Garay, Phys. Rev. D **64**, 113011 (2001), arXiv:hep-ph/0107186.

[145] K. Abazajian, G. M. Fuller, and M. Patel, Phys. Rev. D **64**, 023501 (2001), astro-ph/0101524.

[146] P. B. Pal and L. Wolfenstein, Phys. Rev. D **25**, 766 (1982).

[147] A. De Rujula and S. L. Glashow, Phys. Rev. Lett. **45**, 942 (1980).

[148] K. Abazajian, G. M. Fuller, and W. H. Tucker, Astrophys. J. **562**, 593 (2001), astro-ph/0106002.

[149] V. D. Barger, R. J. N. Phillips, and S. Sarkar, Phys. Lett. **B352**, 365 (1995), arXiv:hep-ph/9503295.

[150] P. Rosati, R. della Ceca, C. Norman, and R. Giacconi, Astrophys. J. Lett. **492**, L21 (1998), arXiv:astro-ph/9710308.

[151] M. Lombardi et al., Astrophys. J. **623**, 42 (2005), arXiv:astro-ph/0501150.

[152] W. Hu, D. J. Eisenstein, and M. Tegmark, Phys. Rev. Lett. **80**, 5255 (1998), astro-ph/9712057.

[153] D. J. Eisenstein and W. Hu, Astrophys. J. **511**, 5 (1997), astro-ph/9710252.

[154] S. Hannestad, Prog. Part. Nucl. Phys. **57**, 309 (2006), astro-ph/0511595.

[155] W. Hu and N. Sugiyama, Phys. Rev. D **51**, 2599 (1995).

[156] S. Hannestad, A. Mirizzi, G. G. Raffelt, and Y. Y. Y. Wong, J. Cosmol. Astropart. Phys. **8**, 15 (2007), arXiv:0706.4198.

[157] A. Melchiorri, O. Mena, and A. Slosar, Phys. Rev. D **76**, 041303 (2007), 0705.2695[astro-ph].

[158] P. Crotty, J. Lesgourgues, and S. Pastor, Phys. Rev. D **69**, 123007 (2004), arXiv:hep-ph/0402049.

[159] V. Barger, D. Marfatia, and A. Tregre, Phys. Lett. **B595**, 55 (2004), arXiv:hep-ph/0312065.

[160] U. Seljak et al. (SDSS), Phys. Rev. D **71**, 103515 (2005), astro-ph/0407372.

[161] G. L. Fogli et al., Phys. Rev. D **D75**, 053001 (2007), arXiv:hep-ph/0608060.

[162] J. R. Kristiansen, H. K. Eriksen, and O. Elgaroy (2006), astro-ph/0608017.

[163] M. Fukugita, K. Ichikawa, M. Kawasaki, and O. Lahav, Phys. Rev. D **74**, 027302 (2006), astro-ph/0605362.

[164] O. Elgaroy and O. Lahav, Phys. Scripta **t127**, 105 (2006), arXiv:hep-ph/0606007.

[165] E. Pierpaoli, Mon. Not. Roy. Astron. Soc. **342**, L63 (2003), astro-ph/0302465.

[166] M. Kamionkowski and M. S. Turner, Phys. Rev. D **42**, 3310 (1990).

[167] M. Kawasaki, K. Kohri, and N. Sugiyama, Phys. Rev. D **62**, 023506 (2000), astro-ph/0002127.

[168] K. Ichikawa, M. Kawasaki, and F. Takahashi, Phys. Rev. D **72**, 043522 (2005), astro-ph/0505395.

[169] E. W. Kolb, A. Notari, and A. Riotto, Phys. Rev. D **68**, 123505 (2003), arXiv:hep-ph/0307241.

[170] A. D. Dolgov and A. D. Linde, Phys. Lett. **B116**, 329 (1982).

[171] L. F. Abbott, E. Farhi, and M. B. Wise, Phys. Lett. **B117**, 29 (1982).

[172] L. Kofman, A. D. Linde, and A. A. Starobinsky, Phys. Rev. Lett. **73**, 3195 (1994), arXiv:hep-th/9405187.

[173] L. Kofman, A. Linde, and A. A. Starobinsky, Phys. Rev. D **56**, 3258 (1997), arXiv:hep-ph/9704452.

[174] Y. Shtanov, J. Traschen, and R. Brandenberger, Phys. Rev. D **51**, 5438 (1995), arXiv:hep-ph/9407247.

[175] D. J. H. Chung, E. W. Kolb, and A. Riotto, Phys. Rev. D **60**, 063504 (1999), arXiv:hep-ph/9809453.

[176] S. Davidson, M. Losada, and A. Riotto, Phys. Rev. Lett. **84**, 4284 (2000).

[177] J. R. Ellis, J. E. Kim, and D. V. Nanopoulos, Phys. Lett. **B145**, 181 (1984).

[178] G. F. Giudice, A. Riotto, and I. Tkachev, JHEP **8**, 9 (1999), arXiv:hep-ph/9907510.

[179] J. L. Feng and J. Kumar, Phys. Rev. Lett. **101**, 231301 (2008), arXiv:0803.4196.

[180] G. Gelmini et al., Phys. Rev. D **74**, 083514 (2006), arXiv:hep-ph/0605016.

[181] G. Kane and S. Watson, Modern Physics Letters A **23**, 2103 (2008), arXiv:0807.2244.

[182] B. S. Acharya et al., Phys. Rev. D **80**, 083529 (2009), 0908.2430.

[183] L. Visinelli and P. Gondolo, Phys. Rev. D **81**, 063508 (2010), arXiv:0912.0015.

[184] R. N. Mohapatra and G. Senjanovi, Phys. Rev. Lett.. **44**, 912 (1980).

[185] K. N. Abazajian, Astropart. Phys. **19**, 303 (2003), astro-ph/0205238.

[186] A. D. Dolgov and S. H. Hansen (2001), arXiv:hep-ph/0103118.

[187] K. Abazajian and S. M. Koushiappas, Phys. Rev. D **74**, 023527 (2006), astro-ph/0605271.

[188] C. R. Watson, J. F. Beacom, H. Yuksel, and T. P. Walker, Phys. Rev. D **74**, 033009 (2006), astro-ph/0605424.

[189] S. Riemer-Sorensen, S. H. Hansen, and K. Pedersen, Astrophys. J. **644**, L33 (2006), astro-ph/0603661.

[190] S. Hannestad and G. Raffelt, Phys. Rev. D **59**, 043001 (1999), astro-ph/9805223.

[191] A. Boyarsky, A. Neronov, O. Ruchayskiy, and M. Shaposhnikov, Mon. Not. R. Astron. Soc. **370**, 213 (2006), astro-ph/0512509.

[192] A. Boyarsky, A. Neronov, O. Ruchayskiy, and M. Shaposhnikov, Phys. Rev. D **74**, 103506 (2006), astro-ph/0603368.

[193] U. Seljak, A. Makarov, P. McDonald, and H. Trac, Phys. Rev. Lett. **97**, 191303 (2006), astro-ph/0602430.

[194] S. Dodelson, A. Melchiorri, and A. Slosar, Phys. Rev. Lett. **97**, 04301 (2006), astro-ph/0511500.

[195] C. E. Yaguna, JHEP **06**, 002 (2007), 0706.0178[hep-ph].

[196] G. Gelmini and others., ArXiv e-prints (2008), arXiv:0803.2735.

[197] G. B. Gelmini et al., Phys. Rev. D **81**, 063529 (2010), arXiv:0912.2478.

[198] B. S. Acharya et al., JHEP **6**, 64 (2008), arXiv:0804.0863.

[199] P. Salati, Phys. Lett. **B571**, 121 (2003), astro-ph/0207396.

[200] B. Spokoiny, Phys. Lett. B **315**, 40 (1993), arXiv:gr-qc/9306008.

[201] P. J. E. Peebles and A. Vilenkin, Phys. Rev. D **59**, 063505 (1999), arXiv:astro-ph/9810509.

[202] M. Peloso and F. Rosati, JHEP **12**, 26 (1999), arXiv:hep-ph/9908271.

[203] M. Joyce, Phys. Rev. D **55**, 1875 (1997), arXiv:hep-ph/9606223.

[204] P. G. Ferreira and M. Joyce, Phys. Rev. D **58**, 023503 (1998), arXiv:astro-ph/9711102.

[205] M. Joyce and T. Prokopec, Phys. Rev. D **57**, 6022 (1998), arXiv:hep-ph/9709320.

[206] M. Joyce and T. Prokopec, JHEP **10**, 30 (2000), arXiv:hep-ph/0003190.

[207] P. Salati, Phys. Lett. B **571**, 121 (2003), arXiv:astro-ph/0207396.

[208] S. Profumo and P. Ullio, JCAP **11**, 6 (2003), arXiv:hep-ph/0309220.

[209] P. Gondolo and G. Gelmini, Nucl. Phys. **B360**, 145 (1991).

[210] P. Gondolo et al., J. Cosmol. Astropart. Phys. **0407**, 008 (2004), astro-ph/0406204.

[211] E. J. Chun, D. Comelli, and D. H. Lyth, Phys. Rev. D **62**, 095013 (2000), arXiv:hep-ph/0008133.

[212] E. J. Chun, H. B. Kim, and D. H. Lyth, Phys. Rev. D **62**, 125001 (2000), arXiv:hep-ph/0008139.

[213] E. J. Chun, K. Dimopoulos, and D. H. Lyth, Phys. Rev. D **70**, 103510 (2004), arXiv:hep-ph/0402059.

[214] H. Murayama, H. Suzuki, and T. Yanagida, Phys. Lett. **B291**, 418 (1992).

[215] P. Moxhay and K. Yamamoto, Phys. Lett. **B151**, 363 (1985).

[216] Z. G. Berezhiani, A. S. Sakharov, and M. Y. Khlopov, Sov. J. Nucl. Phys. **55**, 1063 (1992).

[217] M. K. Volkov et al., Phys. Lett. B **424**, 235 (1998), arXiv:hep-ph/9706350.

[218] M. Srednicki, Nucl. Phys. **B260**, 689 (1985).

[219] S. J. Asztalos et al., Astrophys. J. **571**, L27 (2002), astro-ph/0104200.

[220] G. G. Raffelt and D. S. P. Dearborn, Phys. Rev. **D36**, 2211 (1987).

[221] W. M. Yao et al. (Particle Data Group), J. Phys. **G33**, 1 (2006).

[222] K. Maltman, J. T. Goldman, and J. Stephenson, G. J., Phys. Rev. **C41**, 2764 (1990).

[223] D. B. Kaplan and A. V. Manohar, Phys. Rev. Lett. **56**, 2004 (1986).

[224] S. Hannestad and G. Raffelt, J. Cosmol. Astropart. Phys. **0404**, 008 (2004), arXiv:hep-ph/0312154.

[225] H. Zhan, L. Knox, A. Tyson, and V. Margoniner, Astrophys. J. **640**, 8 (2006), astro-ph/0508119.

[226] J. A. Tyson (LSST), AIP Conf. Proc. **870**, 44 (2006), astro-ph/0609516.

[227] M. Tegmark et al., Phys. Rev. D **74**, 123507 (2006), astro-ph/0608632.

[228] M. Viel, M. G. Haehnelt, and V. Springel, Mon. Not. R. Astron. Soc. **354**, 684 (2004), astro-ph/0404600.

[229] C. Y. Cardall and G. M. Fuller, Phys. Rev. D **54**, 1260 (1996), astro-ph/9603105.

[230] M. Kaplinghat, L. Knox, and Y.-S. Song, Phys. Rev. Lett. **91**, 241301 (2003), astro-ph/0303344.

[231] G. Steigman, Annu. Rev. Nucl. Part. Sci. **57**, 463 (2007), arXiv:0712.1100.

[232] R. H. Cyburt, B. D. Fields, K. A. Olive, and E. Skillman, Astroparticle Physics **23**, 313 (2005), arXiv:astro-ph/0408033.

[233] K. Ichikawa and T. Takahashi, Phys. Rev. D **73**, 063528 (2006), astro-ph/0601099.

[234] K. Ichikawa, T. Sekiguchi, and T. Takahashi (2007), arXiv:0712.4327[astro-ph].

[235] R. Trotta and S. H. Hansen, Phys. Rev. D **69**, 023509 (2004), arXiv:astro-ph/0306588.

[236] S. Dodelson, *Modern cosmology* (Amsterdam, Netherlands: Academic Press., 2003).

[237] D. J. Eisenstein, W. Hu, and M. Tegmark, Astrophys. J. **518**, 2 (1999), arXiv:astro-ph/9807130.

[238] S. Perlmutter et al., Astrophys. J. **517**, 565 (1999), arXiv:astro-ph/9812133.

[239] A. G. Riess et al., Astron. J. **116**, 1009 (1998), arXiv:astro-ph/9805201.

[240] M. Tegmark et al., Astrophys. J. **606**, 702 (2004), arXiv:astro-ph/0310725.

[241] N. Padmanabhan et al., Mon. Not. R. Astron. Soc. **378**, 852 (2007), arXiv:astro-ph/0605302.

[242] S. Cole et al., Mon. Not. R. Astron. Soc. **362**, 505 (2005), arXiv:astro-ph/0501174.

[243] E. Rozo et al., Astrophys. J. **708**, 645 (2010), arXiv:0902.3702.

[244] R. R. Caldwell, R. Dave, and P. J. Steinhardt, Phys. Rev. Lett. **80**, 1582 (1998), arXiv:astro-ph/9708069.

[245] S. M. Carroll, V. Duvvuri, M. Trodden, and M. S. Turner, Phys. Rev. D **70**, 043528 (2004), arXiv:astro-ph/0306438.

[246] K. Ichikawa, M. Fukugita, and M. Kawasaki, Phys. Rev. D **71**, 043001 (2005), arXiv:astro-ph/0409768.

[247] S. Dodelson, E. Gates, and A. Stebbins, Astrophys. J. **467**, 10 (1996), arXiv:astro-ph/9509147.

[248] C.-P. Ma and E. Bertschinger, Astrophys. J. **455**, 7 (1995), arXiv:astro-ph/9506072.

[249] C. B. Netterfield et al., Astrophys. J. **571**, 604 (2002), arXiv:astro-ph/0104460.

[250] T. J. Pearson et al., Astrophys. J. **591**, 556 (2003), arXiv:astro-ph/0205388.

[251] C. L. Kuo et al., Astrophys. J. **600**, 32 (2004), arXiv:astro-ph/0212289.

[252] C. L. Reichardt et al., Astrophys. J. **694**, 1200 (2009), arXiv:0801.1491.

[253] J. M. Kovac et al., Nature (London) **420**, 772 (2002), arXiv:astro-ph/0209478.

[254] H. C. Chiang et al., Astrophys. J. **711**, 1123 (2010), arXiv:0906.1181.

[255] U. Seljak and M. Zaldarriaga, Phys. Rev. Lett. **78**, 2054 (1997), astro-ph/9609169.

[256] M. Kamionkowski, A. Kosowsky, and A. Stebbins, Phys. Rev. D **55**, 7368 (1997), astro-ph/9611125.

[257] A. Albrecht et al. (2009), arXiv:0901.0721.

[258] D. J. Eisenstein et al., Astrophys. J. **633**, 560 (2005), arXiv:astro-ph/0501171.

[259] J. Ruhl et al., in *Society of Photo-Optical Instrumentation Engineers (SPIE) Conference Series*, edited by C. M. Bradford et al. (2004), vol. 5498 of *Society of Photo-Optical Instrumentation Engineers (SPIE) Conference Series*, pp. 11–29.

[260] A. Kosowsky, New Astron. Rev. **47**, 939 (2003), arXiv:astro-ph/0402234.

[261] M. Zaldarriaga et al. (2008), arXiv:0811.3918.

[262] D. Baumann et al. (CMBPol Study Team), AIP Conf. Proc. **1141**, 10 (2009), arXiv:0811.3919.

[263] J. R. Bond and G. Efstathiou, Mon. Not. R. Astron. Soc. **226**, 655 (1987).

[264] P. J. E. Peebles and J. T. Yu, Astrophys. J. **162**, 815 (1970).

[265] J. Silk, Astrophys. J. **151**, 459 (1968).

[266] W. Hu, Nature (London) **386**, 37 (1997), arXiv:astro-ph/9504057.

[267] J. R. Bond and G. Efstathiou, Astrophys. J. Lett. **285**, L45 (1984).

[268] A. G. Polnarev, Sov. Astron. Lett. **29**, 607 (1985).

[269] S. Seager, D. D. Sasselov, and D. Scott, Astrophys. J. Lett. **523**, L1 (1999), arXiv:astro-ph/9909275.

[270] A. Lewis, J. Weller, and R. Battye, Mon. Not. R. Astron. Soc. **373**, 561 (2006), arXiv:astro-ph/0606552.

[271] W. Y. Wong and D. Scott, in *Bull. Am. Astron. Soc.* (2006), vol. 38 of *Bulletin of the American Astronomical Society*, pp. 1210–+.

[272] P. J. E. Peebles, Astrophys. J. **153**, 1 (1968).

[273] Y. B. Zel'dovich, V. G. Kurt, and R. A. Sunyaev, Sov. Phys. JETP **28**, 146 (1968).

[274] G. B. Rybicki and I. P. dell'Antonio, in *Observational Cosmology*, edited by G. L. Chincarini, A. Iovino, T. Maccacaro, and D. Maccagni (1993), vol. 51 of *Astronomical Society of the Pacific Conference Series*, pp. 548–+.

[275] V. K. Dubrovich, Sov. Astron. Lett. **1**, 3 (1975).

[276] S. Seager, D. D. Sasselov, and D. Scott, Astrophys. J. Suppl. Ser. **128**, 407 (2000), arXiv:astro-ph/9912182.

[277] R. Weymann, Phys. Fluids **8**, 2112 (1965), URL http://link.aip.org/link/?PFL/8/2112/1.

[278] R. A. Sunyaev and Y. B. Zel'dovich, Astrophys. Space Sci. **7**, 20 (1970).

[279] V. V. Sobolev, Sov. Astron. Lett. **1**, 332 (1957).

[280] E. E. Kholupenko and A. V. Ivanchik, Astron. Lett. **32**, 795 (2006), arXiv:astro-ph/0611395.

[281] J. Chluba and R. A. Sunyaev, Astron. Astrophys. **446**, 39 (2006), arXiv:astro-ph/0508144.

[282] J. Chluba and R. A. Sunyaev, Astron. Astrophys. **480**, 629 (2008), arXiv:0705.3033.

[283] C. M. Hirata, Phys. Rev. D **78**, 023001 (2008), arXiv:0803.0808.

[284] J. Chluba and R. A. Sunyaev (2009), arXiv:0904.0460.

[285] W. Y. Wong and D. Scott, Mon. Not. R. Astron. Soc. **375**, 1441 (2007), arXiv:astro-ph/0610691.

[286] C. M. Hirata and E. R. Switzer, Phys. Rev. D **77**, 083007 (2008), astro-ph/0702144.

[287] V. K. Dubrovich and S. I. Grachev, Astron. Lett. **31**, 359 (2005), {arXiv:astro-ph/0501672}.

[288] J. Chluba and R. A. Sunyaev, Astron. Astrophys. **475**, 109 (2007), arXiv:astro-ph/0702531.

[289] E. E. Kholupenko, A. V. Ivanchik, and D. A. Varshalovich, Mon. Not. R. Astron. Soc. **378**, L39 (2007), arXiv:astro-ph/0703438.

[290] R. A. Sunyaev and J. Chluba, Nuovo Cimento B **122**, 919 (2007), arXiv:0802.0772.

[291] Y. Ali-Haïmoud, D. Grin, and C. H. Hirata, in preparation (2010).

[292] C. M. Hirata and J. Forbes, Phys. Rev. D **80**, 023001 (2009), arXiv:0903.4925.

[293] P. J. Mohr, B. N. Taylor, and D. B. Newell, Rev. Mod. Phys. **80**, 633 (2008), arXiv:0801.0028.

[294] S. P. Goldman, Phys. Rev. A **40**, 1185 (1989).

[295] J. H. Krolik, Astrophys. J. **338**, 594 (1989).

[296] G. B. Rybicki and I. P. dell'Antonio, in *Bull. Am. Astron. Soc.* (1990), vol. 22, pp. 1214–+.

[297] S. I. Grachev and V. K. Dubrovich, Astron. Lett. **34**, 439 (2008), arXiv:0801.3347.

[298] J. Chluba and R. A. Sunyaev (2009), arXiv:0904.2220.

[299] E. R. Switzer and C. M. Hirata, Phys. Rev. D **77**, 083008 (2008), arXiv:astro-ph/0702145.

[300] E. R. Switzer and C. M. Hirata, Phys. Rev. D **77**, 083006 (2008), arXiv:astro-ph/0702143.

[301] H. Dreicer, Physics of Fluids **7**, 735 (1964).

[302] M. Brocklehurst, Mon. Not. R. Astron. Soc. **148**, 417 (1970).

[303] H. A. Bethe and E. E. Salpeter, *Quantum Mechanics of One- and Two-Electron Atoms* (New York: Academic Press, 1957).

[304] L. Goldberg, Astrophys. J. **144**, 1225 (1966).

[305] M. J. Seaton, Mon. Not. R. Astron. Soc. **127**, 177 (1964).

[306] F. F. Chen, *Introduction to plasma physics* (New York: Plenum Press, 1974).

[307] F. E. Hohne and R. Zimmermann, J. Phys. B. **15**, 2551 (1982).

[308] H. R. Griem, M. Baranger, A. C. Kolb, and G. Oertel, Physical Review **125**, 177 (1962).

[309] D. Hoang-Binh, Astron. Astrophys. **238**, 449 (1990).

[310] L. C. Green, P. P. Rush, and C. D. Chandler, Astrophys. J. Suppl. Ser. **3**, 37 (1957).

[311] H. C. Goldwire, Jr., Astrophys. J. Suppl. Ser. **17**, 445 (1968).

[312] A. Burgess, Mem. R. Astron. Soc. **69**, 1 (1965).

[313] W. Gordon, Ann. Phys. **394**, 1031 (1929).

[314] M. Brocklehurst, Mon. Not. R. Astron. Soc. **153**, 471 (1971).

[315] C. Ueberhuber, *Numerical Computation 2: Methods, Software, and Analysis* (Berlin: Springer, 1997).

[316] J. Chluba and R. A. Sunyaev, Astron. Astrophys. **501**, 29 (2009), arXiv:0803.3584.

[317] N. Padmanabhan and D. P. Finkbeiner, Phys. Rev. D **72**, 023508 (2005), arXiv:astro-ph/0503486.

[318] X.-L. Chen and M. Kamionkowski, Phys. Rev. D **70**, 043502 (2004), arXiv:astro-ph/0310473.

[319] X. Wang and M. Li (2009), arXiv:0904.1061.

[320] T. R. Slatyer, N. Padmanabhan, and D. P. Finkbeiner (2009), arXiv:0906.1197.

[321] O. Zahn and M. Zaldarriaga, Phys. Rev. D **67**, 063002 (2003), arXiv:astro-ph/0212360.

[322] E. Anderson et al., *LAPACK Users' Guide* (Society for Industrial and Applied Mathematics, Philadelphia, PA, 1999), 3rd ed., ISBN 0-89871-447-8 (paperback).

[323] W. H. Press, B. P. Flannery, and S. A. Teukolsky, *Numerical recipes. The art of scientific computing* (Cambridge: University Press, 1986, 1986).

[324] O. Jitrik and C. F. Bunge, J. Phys. Chem. Ref. Data **33**, 1059 (2004), URL http://link.aip.org/link/?JPR/33/1059/1.

[325] W. R. Johnson, *Atomic Structure Theory* (Berlin: Springer, 2007).

[326] J. D. Hey, J. Phys. B. **39**, 2641 (2006).

[327] V. S. Strelnitski, V. O. Ponomarev, and H. A. Smith, Astrophys. J. **470**, 1118 (1996), arXiv:astro-ph/9511118.

[328] L. Vriens, Phys. Rev. **141**, 88 (1966).

[329] R. M. Pengelly and M. J. Seaton, Mon. Not. R. Astron. Soc. **127**, 165 (1964).

[330] M. Spaans and C. A. Norman, Astrophys. J. **488**, 27 (1997).

[331] M. Elitzur, Annual Rev. Astron. Astrophys. **30**, 75 (1992).

[332] K. Y. Lo, Annual Rev. Astron. Astrophys. **43**, 625 (2005).

[333] S. V. Pogrebenko et al., in *IAU Symposium*, edited by J. A. Fernández, D. Lazzaro, D. Prialnik, & R. Schulz (2010), vol. 263 of *IAU Symposium*, pp. 147–150.

[334] C. B. Cosmovici et al., in *Bulletin of the American Astronomical Society* (1995), vol. 27 of *Bulletin of the American Astronomical Society*, pp. 1133–+.

[335] J. Binney and M. Merrifield, *Galactic astronomy* (Princeton University Press: Princeton, N.J., 1998).

[336] V. S. Strelnitski, V. O. Ponomarev, and H. A. Smith, Astrophys. J. **470**, 1118 (1996), arXiv:astro-ph/9511118.

[337] W. L. Freedman and B. F. Madore, ArXiv e-prints (2010), arXiv:1004.1856.

[338] V. Strelnitski et al., Science **272**, 1459 (1996).

[339] S. Daniel and V. Strelnitski, in *Bulletin of the American Astronomical Society* (2002), vol. 34 of *Bulletin of the American Astronomical Society*, pp. 1217–+.

[340] L. N. Labzowsky, A. V. Shonin, and D. A. Solovyev, J. Phys. B. **38**, 265 (2005), URL http://stacks.iop.org/0953-4075/38/i=3/a=010.

[341] A. Lewis and A. Challinor, Phys. Rev. D **66**, 023531 (2002), arXiv:astro-ph/0203507.

[342] U. Seljak and M. Zaldarriaga, Astrophys. J. **469**, 437 (1996), arXiv:astro-ph/9603033.

[343] S. Weinberg, Reviews of Modern Physics **61**, 1 (1989).

[344] S. M. Carroll, Living Reviews in Relativity **4**, 1 (2001), arXiv:astro-ph/0004075.

[345] P. J. Peebles and B. Ratra, Reviews of Modern Physics **75**, 559 (2003), arXiv:astro-ph/0207347.

[346] T. Padmanabhan, Physics Reports **380**, 235 (2003), arXiv:hep-th/0212290.

[347] A. Zee, Phys. Lett. B **594**, 8 (2004), arXiv:hep-th/0309032.

[348] R. Sundrum, Phys. Rev. D **69**, 044014 (2004), arXiv:hep-th/0306106.

[349] R. Sundrum, Nuclear Physics B **690**, 302 (2004), arXiv:hep-th/0310251.

[350] S. Hossenfelder, Phys. Rev. D **73**, 105013 (2006), arXiv:hep-th/0603032.

[351] T. Padmanabhan, Physical Review Letters **78**, 1854 (1997), arXiv:hep-th/9608182.

[352] M. Reuter and J. Schwindt, JHEP **1**, 49 (2007), arXiv:hep-th/0611294.

[353] M. Reuter and J. Schwindt, JHEP **1**, 70 (2006), arXiv:hep-th/0511021.

[354] G. Dvali, S. Hofmann, and J. Khoury, Phys. Rev. D **76**, 084006 (2007), arXiv:hep-th/0703027.

[355] Y. B. Zel'Dovich, Soviet Journal of Experimental and Theoretical Physics Letters **6**, 316 (1967).

[356] M. Roos, ArXiv Astrophysics e-prints (2005), arXiv:astro-ph/0509089.

[357] R. P. Feynman, Acta Phys. Polon. **24**, 697 (1963).

[358] B. S. Dewitt, Physical Review **160**, 1113 (1967).

[359] M. J. G. Veltman, in *Proceedings of the Les Houches Summer School, Session XXVII*, edited by R. Balian and J. Zinn-Justin (North-Holland, Amsterdam, 1976).

[360] G. Papini and S. R. Valluri, Physics Reports **33**, 51 (1977).

[361] J. F. Donoghue, Phys. Rev. D **50**, 3874 (1994), arXiv:gr-qc/9405057.

[362] J. Khoury, Phys. Rev. D **76**, 123513 (2007), arXiv:hep-th/0612052.

[363] E. Corinaldesi, Proceedings of the Physical Society A **69**, 189 (1956).

[364] B. M. Barker, S. N. Gupta, and R. D. Haracz, Physical Review **149**, 1027 (1966).

[365] C. D. Hoyle et al., Physical Review Letters **86**, 1418 (2001), arXiv:hep-ph/0011014.

[366] J. Chiaverini et al., Physical Review Letters **90**, 151101 (2003), arXiv:hep-ph/0209325.

[367] J. C. Long et al., Nature **421**, 922 (2003).

[368] C. D. Hoyle et al., Phys. Rev. D **70**, 042004 (2004), arXiv:hep-ph/0405262.

[369] S. J. Smullin et al., Phys. Rev. D **72**, 122001 (2005), arXiv:hep-ph/0508204.

[370] D. J. Kapner et al., Physical Review Letters **98**, 021101 (2007), arXiv:hep-ph/0611184.

[371] D. Boccaletti, V. Sabbata, C. Gualdi, and P. Fortini, Nuovo Cimento A Serie **48**, 58 (1967).

[372] W. K. de Logi and S. J. Kovacs, Jr., Phys. Rev. D **16**, 237 (1977).

[373] G. 't Hooft, Phys. Lett. B **198**, 61 (1987).

[374] D. Kabat and M. Ortiz, Nuclear Physics B **388**, 570 (1992), arXiv:hep-th/9203082.

[375] M. Lax, Reviews of Modern Physics **23**, 287 (1951).

[376] G. Chartas et al., Astrophys. J. **565**, 96 (2002), arXiv:astro-ph/0108277.

[377] J. A. Muñoz et al., Ap&SS **263**, 51 (1998), arXiv:astro-ph/9902131.

[378] G. Chartas, private correspondence (2005).

[379] S. M. Carroll, M. Hoffman, and M. Trodden, Phys. Rev. D **68**, 023509 (2003), arXiv:astro-ph/0301273.

[380] J. M. Cline, S. Jeon, and G. D. Moore, Phys. Rev. D **70**, 043543 (2004), arXiv:hep-ph/0311312.

[381] S. D. H. Hsu, A. Jenkins, and M. B. Wise, Phys. Lett. B **597**, 270 (2004), arXiv:astro-ph/0406043.

[382] D. E. Kaplan and R. Sundrum, JHEP **7**, 42 (2006), arXiv:hep-th/0505265.

[383] D. J. Scalapino, in *Superconductivity*, edited by R. D. Parks (Marcel Dekker, Inc., New York, 1969).

[384] V. Corbin and N. J. Cornish, ArXiv General Relativity and Quantum Cosmology e-prints (2005), arXiv:gr-qc/0512039.

[385] J. Binney and S. Tremaine, *Galactic dynamics* (Princeton University Press, Princeton, 1987).

[386] J. F. Navarro, C. S. Frenk, and S. D. M. White, Mon. Not. R. Astron. Soc. **275**, 720 (1995), arXiv:astro-ph/9408069.

[387] J. F. Navarro, C. S. Frenk, and S. D. M. White, Astrophys. J. **462**, 563 (1996), arXiv:astro-ph/9508025.

[388] J. F. Navarro, C. S. Frenk, and S. D. M. White, Astrophys. J. **490**, 493 (1997), arXiv:astro-ph/9611107.

[389] C. O. Wright and T. G. Brainerd, Astrophys. J. **534**, 34 (2000), arXiv:astro-ph/9908213.

[390] E. Pointecouteau, M. Arnaud, and G. W. Pratt, Astron. Astrophys. **435**, 1 (2005), arXiv:astro-ph/0501635.

[391] S. Ettori, S. De Grandi, and S. Molendi, Astron. Astrophys. **391**, 841 (2002), arXiv:astro-ph/0206120.

[392] U. G. Briel et al., Astron. Astrophys. **246**, L10 (1991).

[393] M. Sun, S. S. Murray, M. Markevitch, and A. Vikhlinin, Astrophys. J. **565**, 867 (2002), arXiv:astro-ph/0103103.

[394] J.-P. Kneib et al., Astrophys. J. **471**, 643 (1996), arXiv:astro-ph/9511015.

[395] G. P. Smith et al., Mon. Not. R. Astron. Soc. **359**, 417 (2005), arXiv:astro-ph/0403588.

[396] B. Kaulakys (1996), arXiv:physics/9610018.

[397] T. A. Heim, D. Trautmann, and G. Baur, J. Phys. B. **22**, 727 (1989), URL http://stacks.iop.org/0953-4075/22/727.

[398] N. B. Delone, S. P. Goreslavsky, and V. P. Krainov, J. Phys. B. **15**, L421 (1982), URL http://stacks.iop.org/0022-3700/15/L421.

[399] E. Schrodinger, Proc. Roy. Irish Acad. (Sect. A) **46**, 9 (1940).

[400] L. Infeld and T. E. Hull, Rev. Mod. Phys. **23**, 21 (1951).